CO2 methanation via Nickel based catalysts : on the influence of the supports and the promoters

Chao Sun

Sorbonne Université

École doctorale SMAER (ED391), Sciences Mécaniques Acoustique Électronique Robotique

Programme Doctoral Génie des Procédés

Institut Jean Le Rond D'Alembert, Equipe Combustion Energie Propre et Turbulence, CNRS UMR 7190,

CO_2 methanation via Nickel based catalysts: On the influence of the supports and the promoters

Méthanation du CO_2 par des catalyseurs à base de Nickel : Effet des Supports et des Promoteurs

By Mr. CHAO SUN

Doctoral thesis in Chemical Engineering-Chemical Technology

Supervised by Prof. Patrick DA COSTA

Presented and publicly supported on September XX, 2021

The scientific committee:

Prof. Catherine Batiot Dupeyrat, Full Professor, Université de Poitiers, France, **Reviewer**

Prof. Augustin Bueno-Lopez, Universidad de Alicante, Spain, **Reviewer**

Prof. Patrick Da Costa, Full Professor, Sorbonne Université, France, **Supervisor**

Prof. Ioana Fechete, UTT - Université de Technologie de Troyes, France, Examinator

Prof. Anne Giroir Fendler, Full Professor, Université de Lyon, France, Examinator

Mr. Philippe Guibert, Full Professor, Sorbonne Université, France, Examinator

Dédicace

Acknowledgments

I sincerely thank China and China Scholarship Council (CSC) for the scholarship during my studies at Sorbonne Université, France.

Firstly, this thesis was finished under the supervision of Prof. Patrick Da Costa. I would like to sincerely thank Prof. Da Costa's help in the studying. His extensive expertise, strict academic attitudes, and sagacious perception help me greatly in my research. The strict attitude and scientific spirit will still help me both in life and academic activities in the future. Herein, I would like to express my gratitude to Prof. Da Costa. I also want to thank the cooperators in the thesis. They are Patricia Beaunier, Prof. Leonarda F. Liotta, Prof. Monika Motak, Prof. Changwei Hu and Prof. Teresa Grzybek.

Secondly, I also want to appreciate Prof. Ioana Fechete and Prof. Agustín Bueno López for their meticulous reviews of the thesis. Meanwhile, Prof. Fechete also contributes to my annual defenses in the Ph.D. I would like to thank their professional comments and suggestions for the thesis.

Thirdly, I would like to thank Prof. Philipe Guibert,… etc. for the examination of my thesis. Also, I would like to thank all the committee members to attend my defense, especially in this hard time.

I also want to thank the doctors and Ph.D. candidates in the lab that help me a lot. They are Dr. Ye Wang, Dr. Hailong Zhang, Dr. Hongrui Liu, Dr. Mira Ibrahim, Dr. Katarzyna Świrk, Dr. Dominik Wierzbicki, Dr. Bo Wang, Dr. Armando Izquierdo, Maria Mikhail, Yutao Li, Paulina Summa, Golshid Hasrack, Renaud Jalain, and Marcellin Perceau.

I would like to thank all professors, researchers, engineers, administrators, and technicians in Institut Jean le Rond d'Alembert. They are Prof. Stéphane ZALESKI, Prof. Philippe GUIBERT,

Prof. Guillaume LEGROS, Dr. Alexis MATYNIA, Evelyne MIGNON, Anne MARCHAL, Jérôme BONNETY, Hugo DUTILLEUL, Christian OLLIVON, Jêrome PÉQUIN, etc. Thank all of you for providing supports in my doctoral studies. I especially want to give my gratitude to Jérôme BONNETY for his hardworking in our experimental apparatuses and Evelyne MIGNON for the help in work and life.

Thanks to Chunqiao Wang in Bureau de l'éducation de l'ambassade en France and friends in Association des Boursiers CSC en Ile de France.

In the end, I want to thank my dear friend Dr. Wei Zhang from Université de Rennes 1. Also, thanks to my whole family's supports and understandings especially my mother Jing Xu.

Résumé

Abstract

摘要

Abstract

Résumé

Les émissions de CO_2 dues aux activités anthropogéniques causent de graves problèmes environnementaux, qui exigent le développement de technologies de réduction du CO_2. L'utilisation chimique du CO_2, en particulier la méthanisation du CO_2 ($CO_2 + 4H_2 = CH_4 + 2H_2O$, ΔH_{298k}=-165 kJ/mol), offre une voie pour convertir l'excès de CO_2 en gaz naturel synthétique (CH_4) en utilisant des énergies renouvelables. Les métaux de transition, tel que le nickel (Ni), ont été intensivement utilisés pour catalyser la réaction de méthanation du CO_2 grâce à leurs hautes performances, leurs faibles coûts et leur grande accessibilité. Cependant, les catalyseurs à base de nickel rencontrent toujours des problèmes de frittage du métal et de stabilité dans le temps, ce qui limite leur application à grande échelle. Dans ce sens, des recherches se sont concentrées, ces dernières années sur le développement de catalyseurs à base de Ni très actifs et plus stables.

Dans ce but, dans cette thèse, les effets du support et des promoteurs sur la performance des catalyseurs à base de Ni ont été étudiés pour la méthanation du CO_2. Les études ont consisté en la préparation de nouveaux supports avec une structure et une morphologie unique et de catalyseurs supportés dopés par différents promoteurs. Les techniques de caractérisation telles que H_2-TPR, CO_2-TPD, physisorption de N_2, XRD petit angle/grand angle, TEM, HRTEM, EDX, XPS, TGA-MS, TPO, etc. ont été utilisées pour analyser les propriétés des catalyseurs et des supports. Ainsi, l'activité en méthanation a pu être corrélée aux propriétés physico-chimiques.

Tout d'abord, des matériaux à faible coût tels que des catalyseurs Ni-Mg supportés sur de la diatomite et des oxydes mixtes dérivés d’hydrotalcites promus par l'yttrium ont été préparés par la méthode de précipitation-déposition et la méthode de coprécipitation. Leurs activités ont été

étudiées dans la méthanation du CO_2. Ensuite une corrélation entre l'activité et les propriétés physico-chimiques a été proposée.

Dans un second temps, des nanoparticules de CeO_2 ont été synthétisées par la méthode hydrothermique. Celles-ci ont été ensuite imprégnées par des sels de Ni. Les catalyseurs Ni/CeO_2 dopés par différentes charges d'yttrium, ainsi obtenus, ont été étudiés en méthanation du CO_2. La H_2-TPR, l'XPS et les TGA ont confirmé l'augmentation des lacunes d'oxygène sur le support CeO_2 en raison de l'incorporation de Y. En outre, l'augmentation de la charge de Y peut favoriser la formation de « nano tiges » de CeO_2 sur Ni/CeO_2-Y par rapport aux « nano cubes » formés sur le catalyseur Ni/CeO_2, ce qui pourrait expliquer l'augmentation des lacunes d'oxygène et de la surface spécifique. Enfin, la basicité des catalyseurs Ni/CeO_2-Y a également été améliorée grâce à la présence de Y. Enfin, les catalyseurs Ni/CeO_2-Y ont montré des performances catalytiques supérieures à celles du catalyseur Ni/CeO_2.

Enfin, des matériaux mésoporeux ordonnés avec une morphologie unique, tels que des SBA-15 et SBA-16, ont été synthétisés et utilisés pour préparer les catalyseurs Ni/SBA-15 et Ni/SBA-16. Des promoteurs tels que Ce, Y et Ce-Y ont été utilisés pour modifier ces catalyseurs Ni/SBA-15 et Ni/SBA-16. En présence de promoteurs, les performances des catalyseurs Ni/SBA-15 et Ni/SBA-16 ont été améliorés pour la réaction de méthanation du CO_2. Dans ces études, les activités de ces catalyseurs ont été corrélées aux propriétés physico-chimiques.

En un mot, le support peut affecter de manière significative les performances des catalyseurs au Ni dans la méthanisation du CO_2 en raison de sa texture, de sa structure, de sa morphologie, de ses propriétés redox, etc. Le dopage par des promoteurs peut apparemment améliorer l'activité de ces mêmes catalyseurs contenant du Ni et supportés. L'augmentation de leur activité peut être

corrélée la modification de la basicité, à la taille des cristallites de Ni, à la présence de lacunes d'oxygène et enfin à la morphologie des supports et des catalyseurs finaux.

Mots clés : Méthanation du CO_2, catalyseurs à base de Ni, diatomite, hydrotalcite, CeO_2, yttrium, cérium, Ce-Y, SBA-15, SBA-16.

Abstract

The CO_2 emissions from anthropogenic activities have caused severe environmental problems, which demand the development of CO_2 reduction technologies. CO_2 chemically utilization especially CO_2 methanation ($CO_2 + 4H_2 = CH_4 + 2H_2O$, ΔH_{298k}=-165 kJ/mol) provides a route to convert the excess CO_2 to synthetic natural gas (CH_4) using renewable energy. Transition metal e.g., Ni has been intensively used to catalyze CO_2 methanation reaction thanks to its high performance, low cost, and high accessibility. Nevertheless, Ni-based catalysts still encounter metal sintering and low stability problems, which limit their large-scale application. In such a case, the development of highly active and stable Ni catalysts has been the research focus.

In this thesis, the effects of support and promoters on the performance of Ni catalysts in CO_2 methanation were studied. The studies consist of the preparation of supports with unique structure and morphology and supported Ni catalysts doped by different promoters. The characterization techniques such as H_2-TPR, CO_2-TPD, N_2 physisorption, small-angle/large-angle XRD, TEM, HRTEM, EDX, XPS, TGA-MS, TPO, etc. were used to analyze the properties of catalysts and supports. Meanwhile, the methanation activity was correlated to the physicochemical properties.

First, the low-cost materials like diatomite-supported Ni-Mg catalysts and LDH derived mixed oxides promoted by yttrium were prepared by the precipitation-deposition method and co-precipitation method, respectively. Afterward, the activities of catalysts were investigated in CO_2 methanation. The correlation between activity and physicochemical properties was investigated.

Secondly, the CeO_2 nanoparticles were synthesized by the hydrothermal method followed by the Ni catalysts prepared by wet impregnation. The Ni/CeO_2 catalysts doped by different loading of yttrium were investigated in CO_2 methanation. The H_2-TPR, XPS, and TGA confirmed the

increased oxygen vacancies over CeO_2 due to the incorporation of Y. Also, the increase of Y loading could promote the formation of CeO_2 nanorods over Ni/CeO_2-Y compared to the nanocubes formed over Ni/CeO_2 catalyst, which could account for the increased oxygen vacancies and surface area. The moderate basicity of Ni/CeO_2-Y catalysts was also improved due to the presence of Y. In the activity test, Ni/CeO_2-Y catalysts performed superior performance compared to Ni/CeO_2 catalyst.

Thirdly, the ordered mesoporous materials with unique morphology e.g, SBA-15 and SBA-16 were synthesized and employed to prepare Ni/SBA-15 and Ni/SBA-16 catalysts. The promoters such as Ce, Y, and Ce-Y were used to modify the Ni/SBA-15 and Ni/SBA-16 catalysts. In the presence of promoters, both Ni/SBA-15 and Ni/SBA-16 catalysts were improved in CO_2 methanation reaction. The activities of such modified catalysts were correlated to the modified physicochemical properties.

In a word, support can significantly affect the performance of Ni catalysts in CO_2 methanation due to their texture, structure, morphology, and redox properties, etc. Doping by promoters can improve the activity of supported Ni catalysts, which are attributed to the modification of basicity, Ni crystal size, oxygen vacancies, and morphology.

Keywords: CO_2 methanation, Ni catalysts, diatomite, hydrotalcite, CeO_2, yttrium, ceria, Ce-Y, SBA-15, SBA-16.

摘要

人类起源的二氧化碳排放已经引起了严重的环境问题，例如全球变暖。这使得开发二氧化碳减排技术变得越来越重要。CO_2 的化学利用，尤其是 CO_2 的甲烷化（$CO_2 + 4H_2 = CH_4 + 2H_2O$, ΔH_{298k}= -165 kJ/mol）提供了使用可再生能源将过量的 CO_2 转化为合成天然气（CH_4）的技术路径。由于过渡金属镍 (Ni) 的高性能，低成本和高可获得性等特点，它已经被广泛用于催化 CO_2 甲烷化反应。然而，Ni 基催化剂仍然遭遇金属烧结和低稳定性的等问题，这限制了它们的大规模应用。在这种情况下，开发高活性和高稳定性的 Ni 催化剂成为了 CO_2 甲烷化反应的研究重点。

本文研究了载体和助剂对 Ni 催化剂在 CO_2 甲烷化反应中性能的影响。这些研究包括制备具有独特结构和形态的载体，以及不同助剂改性的负载型 Ni 催化剂。使用 H_2-TPR，CO_2-TPD，N_2 物理吸附，小角/大角 XRD，TEM，HRTEM，EDX，XPS，TGA-MS，TPO 等表征技术来分析催化剂和载体的性能。同时，催化剂的活性和催化剂的理化性质也被关联起来。

首先，通过沉淀沉积法和共沉淀法分别制备了廉价载体负载的催化剂，如硅藻土负载的 Ni-Mg 催化剂和稀土元素钇改性的水滑石(LDH) 衍生的混合氧化物 Ni 催化剂。然后，考察了催化剂在 CO_2 甲烷化反应中的活性。催化剂的活性变化被归于理化性质的改变。

其次，通过水热法合成了 CeO_2 纳米颗粒。然后用湿浸渍法制备了 Ni 催化剂。研究了钇对于 Ni/CeO_2 催化剂在 CO_2 甲烷化反应中的影响。 H_2-TPR，XPS 和 TGA 表征证实了，掺入 Y 使得 CeO_2 上的氧空位数量增加。而且，与在 Ni/CeO_2 上形成的 CeO_2 纳米方块相比，

Y 的添加可以促进 CeO_2 纳米棒在 Ni/CeO_2-Y 催化剂上的形成。 这解释了催化剂上氧空位和表面积的增加。由于添加 Y，Ni/CeO_2-Y 催化剂的中等强度碱性也增加了。在活性测试中，Ni/CeO_2-Y 催化剂的性能显著优于 Ni/CeO_2 催化剂。

第三，合成了具有独特形貌的有序介孔材料，例如 SBA-15 和 SBA-16。并用合成的介孔硅材料制备了 Ni/SBA-15 和 Ni/SBA-16 催化剂。同时，使用 Ce，Y 和 Ce-Y 等助剂改性 Ni/SBA-15 和 Ni/SBA-16 催化剂。在助剂改性下，Ni/SBA-15 和 Ni/SBA-16 催化剂在 CO_2 甲烷化反应中的活性均得到显著改善。这种改性的催化剂的活性与被改变的催化剂的理化性质相关。

总而言之，载体由于其织构，结构，形态和氧化还原特性等，会显著影响 Ni 催化剂在 CO_2 甲烷化反应中的性能。掺杂助剂可以显著改善负载型 Ni 催化剂的活性，这可以归因于碱性，Ni 晶粒大小，氧空穴数量和形貌的变化。

关键字：CO_2 甲烷化，Ni 催化剂，硅藻土 (diatomite)，前驱体，水滑石 (hydrotalcite)，钇 (Y)，二氧化铈 (CeO_2)，Ce-Y，SBA-15，SBA-16。

Sommaire

Outline

Outline

Outline

Outline

Chapter I

General Introduction

1. General Introduction

The combustion of fossil fuels and other industrial activities result in abundant emissions of greenhouse gases (GHGs), which consist of carbon dioxide (CO_2), methane and nitrous oxide, etc. CO_2 emission accounts for the majority of the GHGs emissions. The high CO_2 concentration from anthropogenic activities in the atmosphere has resulted in serious environmental problems e.g. global warming. To mitigate the CO_2 emissions, CO_2 capture and storage (CCS) technologies have been developed to capture and store the CO_2 from the atmosphere or industrial sectors. The captured CO_2 can be stored underground or undersea. Besides storage, CO_2 can also be utilized in many ways. The CO_2 capture and utilization (CCU) technologies are developed to use the CO_2 as feedstock to produce valuable products like fuels, chemicals, and materials, etc. The CCU routes like CO_2-Enhanced Oil Recovery Technology (EOR) [1], chemical conversion [2,3], photochemical[4], electrochemical [5], and biochemical process [4], etc. have been widely studied aim to mitigate the CO_2 emission and produce value-added products. Among these routes, the CO_2 chemical utilization methods received intensive attention due to their potential/present industrial application [3]. CO_2 can be converted to methanol, formic acid, formaldehyde, methane, hydrocarbon, higher alcohol, syngas (CO and H_2), etc. by CO_2 hydrogenation [6–11]. The CO_2 hydrogenation to methane or CO_2 methanation is considered the most potent method for CO_2 chemical conversion due to its several advantages.

The CO_2 methanation ($CO_2 + 4H_2 = CH_4 + 2H_2O$) is a thermodynamic favorable and exothermic reaction [12]. The reaction is favored at a low-temperature range under atmospheric pressure. Also, the high CO_2 conversion and CH_4 selectivity can be reached thermodynamically at moderate conditions. However, good catalytic systems are still needed to catalyze the reaction due to the dynamic barrier. The transition metals-based catalysts e.g. Pd, Rh, Ru, Pt, Ni, and Co were

developed to catalyze the CO_2 methanation reaction. The noble metal-based catalysts such as Rh and Ru showed superior performance at low temperatures. However, the high cost and low availability limit their potential commercialization. In such a case, the Ni-based catalysts had been widely studied as to their low cost, high availability, and comparable activity compared to noble metals-based catalysts [13]. The activity and stability of the Ni-based catalysts depend on the properties of the catalysts such as active metal dispersion, Ni particle size, specific surface area, porosity, redox property, oxygen storage ability, and basicity, etc. As support, promoter, and preparation method have significant effects on the physicochemical properties of Ni-based catalysts, the researches on such aspects have attracted intensive attention to obtain catalysts with high activity and stability.

In this thesis, the different supports like diatomite, hydrotalcite-derived mixed oxides, cerium oxide (CeO_2), and mesoporous silica were used. All these supports were loaded with nickel to be used in the methanation process. Furthermore, promoters such as Y, Ce, and Y-Ce were selected to improve the performance of catalysts in CO_2 methanation.

This doctoral thesis consists of 7 chapters including a General Introduction, the presentation of the State-of-Art concerning the CO_2 Utilization, the Experimental part. The Results start with the presentation of the possible use of Low-Cost Supports for CO_2 Methanation. Then, Y-Promoted Novel Ceria Supported Ni Catalysts for CO_2 Methanation are reported. Moreover, Mesoporous Silica Materials supported Ni catalysts are discussed. Finally, the Conclusion and Prospect are presented.

Thus, in the second chapter, a thorough literature review of the CO_2 utilization routes is made including the comparison of different CO_2 reduction technologies and CO_2 chemical utilization routes are presented. Then Catalysts of CO_2 methanation with Noble metal-based catalytic systems

are discussed. The thermodynamics is then reported. Another sub-chapter deal with Transition metal-based catalytic systems, the Mechanisms of CO_2 methanation. And, finally Assisted catalysis for CO_2 methanation is presented.

The third chapter introduces the experimental parts, which consist of the set-up for catalytic test and a large variety of physicochemical characterizations used to drive the structure-reactivity of the different studied catalysts.

The fourth chapter deals with the low-cost supports prepared Ni catalysts for CO_2 methanation. In detail, the diatomite-supported Ni-Mg catalysts are used to catalyze the reaction. Besides, the mixed oxides derived from layered-double hydrotalcite-based Ni catalysts are studied in the reaction.

The fifth chapter investigated Y promoted novel ceria supported Ni catalysts for CO_2 methanation. The positive effects of the yttrium are then studied in detail.

The sixth chapter concentrates on two types of mesoporous silica SBA-15 and SBA-16 supported Ni catalysts. The promotion effect is also presented. Thus, the SBA-15 supported Ni catalysts promoted by Ce and Y are introduced. Meanwhile, the SBA-16 supported Ni catalysts doped by Ce or Y are also investigated.

At last, in chapter 7 the conclusion of this thesis is presented and perspectives are reported.

Thus, the aims of this thesis are:

- Investigate the effect of precursors on the performance of Ni-Mg catalysts supported on the low-cost support-diatomite for CO_2 methanation to find a good Ni salt for the preparation of Ni catalyst.
- Study the promotion effect of yttrium on the activity and physicochemical properties of hydrotalcite-derived mixed oxides for CO_2 methanation to establish activity-physicochemical relations on mixed oxides catalysts.
- Design novel Ni/CeO_2 catalysts and investigate the influence of yttrium loading on the performance of Ni/CeO_2-Y catalysts in CO_2 methanation.
- Synthesize mesoporous silica materials and used them as supports of Ni catalysts to investigate the effects of mesoporous silica materials for methanation reaction. The effects of promoters like Ce, Y, and Y-Ce are also studied.

Such results were used to evaluate the effects of support and promoter selections. The important influence of yttrium or ceria was emphasized. And the appropriate content of Y or Ce loading can be found to significantly improve the performance of Ni catalysts. At last, the dual promotion of Y-Ce additives was also demonstrated.

Chapter II

State-of-Art for the CO_2 Utilization

2. State-of-Art for the CO_2 Utilization

2.1 CO_2 emissions and impacts

Since the industrial revolution time, the consumption of energy especially fossil fuels (coal, oil, and natural gas) had been increasing significantly. Although new energy resources e.g. nuclear energy, solar, and hydropower, etc. have been developed to reduce the dependence on fossil energy, Most of the energy consumption is still based on fossil fuels. As shown in Fig.2.1, the primary energy supply from 1971 to 2018 nearly kept stable with the fossil fuels (coal, oil, and natural gas) accounting for the majority part (International Energy Agency, IEA). Meanwhile, the combustion of fossil fuels and other industrial activities resulted in the fast increase of CO_2 concentration in the atmosphere. According to the world meteorological organization (WMO) greenhouse gas bulletin report in 2019, the atmospheric CO_2 concentration has been increasing annually by 2-3 ppm over the last decade [14]. In Fig.2.2, it can be seen that the annual worldwide CO_2 emission has been increasing sharply since the last century and the peak of CO_2 emission has not been reached until 2019. The quick increase of atmospheric CO_2 concentration has caused many severe environmental problems e.g. global warming, climate change, sea level rising, and ocean acidification [15]. In Fig.2.3, it can be seen that the average global temperature has been increasing gradually since the 19^{th} century. The international panel on climate change (IPCC) commission reported that human-induced GHGs emissions had caused the average temperature to increase approximately 1 °C above pre-industrial levels in 2017 and the temperature is increasing at 0.2°C per decade. To mitigate global warming, human society has been taking action to reduce CO_2 emissions. In 2015, the Paris Agreement aimed at reducing the CO_2 emissions had been adopted by 196 parties in which the goal of the agreement is to limit global warming to 1.5 degrees Celsius compared to pre-industrial levels [16]. In order to reach this long-term target, the international

community needs to reach global peaking of GHGs emissions to achieve a climate-neutral world by mid-century. To achieve sustainable development for the human community, many countries have implemented emission reduction policies. For example, China has promised to achieve a carbon-neutral goal in 2060.

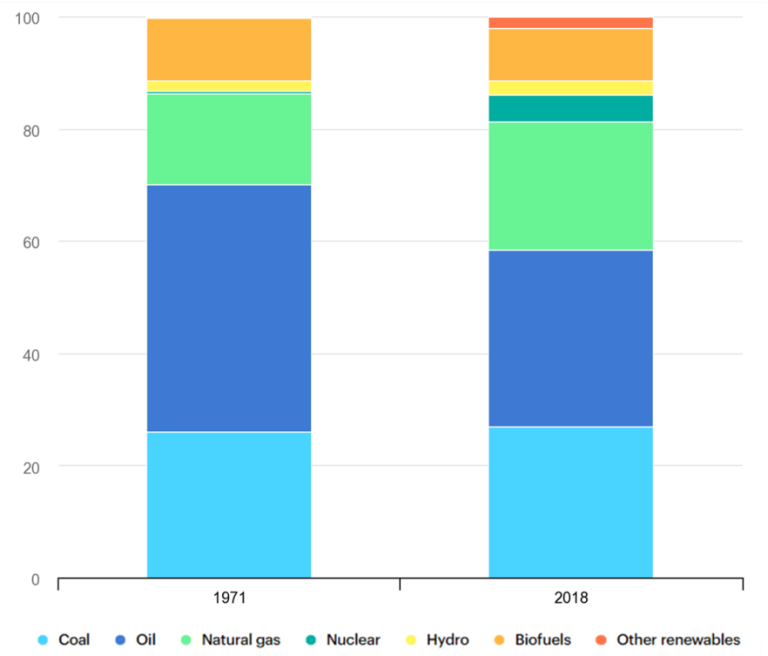

Figure. 2.1. Total primary energy supply by fuel, 1971 and 2018. Adapted from [17].

Regarding the CO_2 emissions reduction, besides limiting the consumption of fossil fuels, the CCS and CCU technologies also help to mitigate the emission. The CCS technology can use the CO_2 capture technology to concentrate the CO_2 and store the resource in geologic ways. The CCU route can use renewable energy to convert CO_2 to valuable resources.

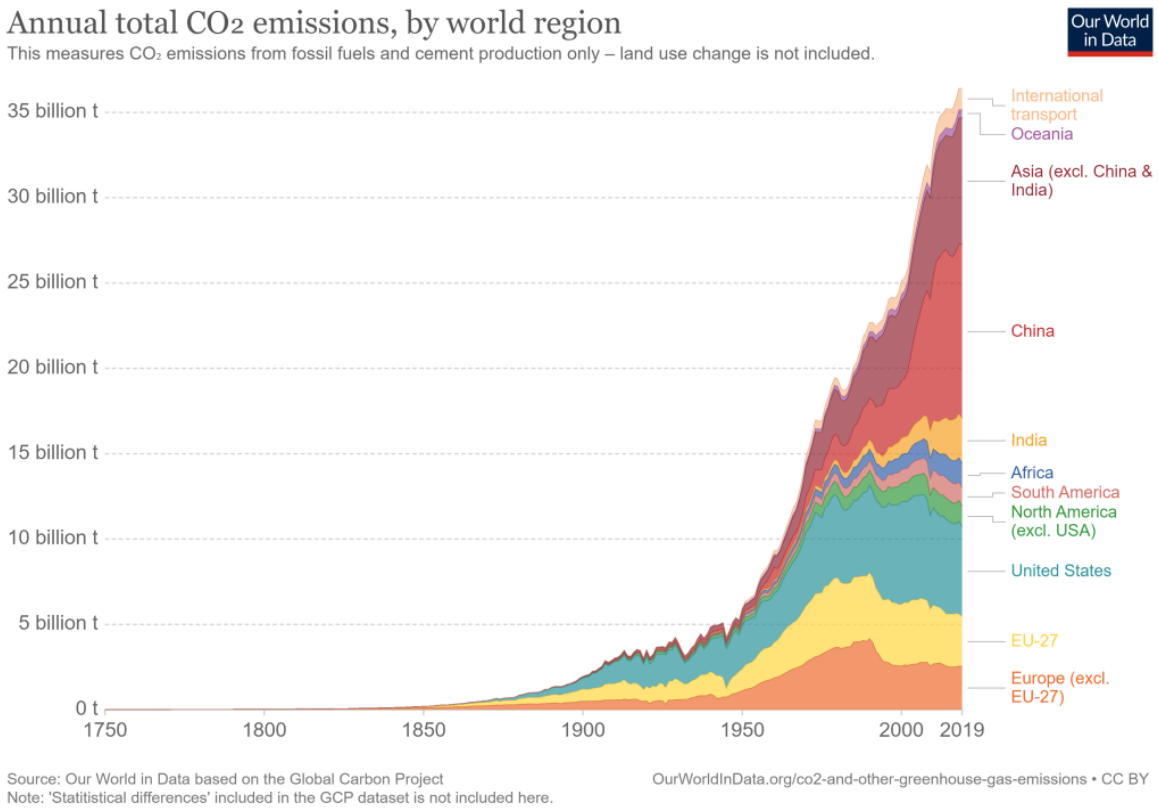

Figure. 2.2. Annual total CO_2 emissions by world region. Global Carbon Project; Adapted from [18].

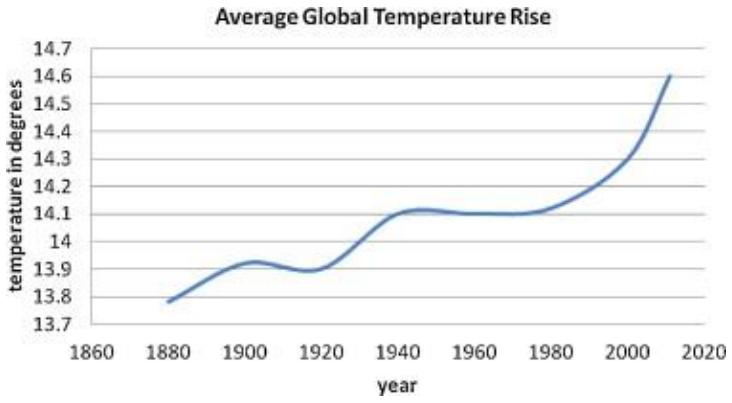

Figure. 2.3. Average global temperature rise, adapted from [15]

2.2 The routes for CO_2 storage and utilization

2.2.1 The CO_2 capture and storage (CCS).

CO_2 sources can be divided into CO_2 point sources and atmospheric CO_2 sources [19]. CO_2 point sources mainly come from the fossil-fueling power plant, petroleum refining, ethylene production, cement production, iron and steel production, ethylene oxide production, hydrogen production, ammonia processing, natural gas processing, and ethanol production chemical plants, paper mills, and fermentation, etc. [20,21]. The CO_2 capture routes consist of capturing CO_2 from the atmosphere i.e. direct air capture (DAC) and CO_2 point sources like the industry sector [21–25].

Fig.2.4 shows a future scenario regarding the capture of CO_2 sources in which the capture from fossil fuels accounts for the overwhelming majority. The CO_2 emissions from the combustion of coal, oil, and gas accounted for nearly half of the fossil fuel CO_2 emissions (30 gigatons annually) or a quarter of the GHGs emissions [22,23]. CO_2 emission from the combustion of fossil fuels including mobile and stationary emissions accounts for 93.74% of the total industrial emissions [21].

For the capture from air, the atmospheric CO_2 can be immobilized by biomass e.g. vegetation, plankton, and algae, etc., or chemical absorbents [22,26]. The direct capture of CO_2 (DAC) by technological systems has been developed and applied in the production of CO_2-free air, which is widely used in the industrial sector e.g. dry ice production and air separation plants [22]. In these routes, the sorbents like sodium hydroxide (NaOH), potassium hydroxide (KOH), sodium carbonate (Na_2CO_3), amines are needed to sorb the CO_2 and the captured CO_2 is concentrated for storage (geologic or undersea storage [27]) or recycling. For the strong chemical bases such as NaOH and KOH, their regeneration needs high temperature, which costs abundant energy [22].

The regeneration of amines needs lower temperatures, making them appropriate absorbents. Besides these materials, the novel metal-organic-framework (MOF) materials hybrid ultra-microporous materials (HUMs) were also been used to capture CO_2 [28,29]. Such new materials can serve as physisorbed in DAC, which needs low temperature in the regeneration process [28].

Generally, the purer the CO_2 emission streams are the lower cost the separation systems are. Thus, capturing CO_2 from stationary sites that have purer CO_2 could significantly decrease the cost of the CCS system and improving the economic viability for CCS and climate change mitigation.

A typical CCS system from the power plant diagram is displayed in Fig.2.5. It shows the different components of a CCS system and their consequential effects on electricity production. The CO_2 was captured from the fossil fuel combustion in the power plant followed by compressing and transporting to storage sites e.g., underground or in salts [30,31]. The captured CO_2 can also be directly used in technological applications like dry ice, soft drinks, and supercritical fluid, etc. [1,32,33].

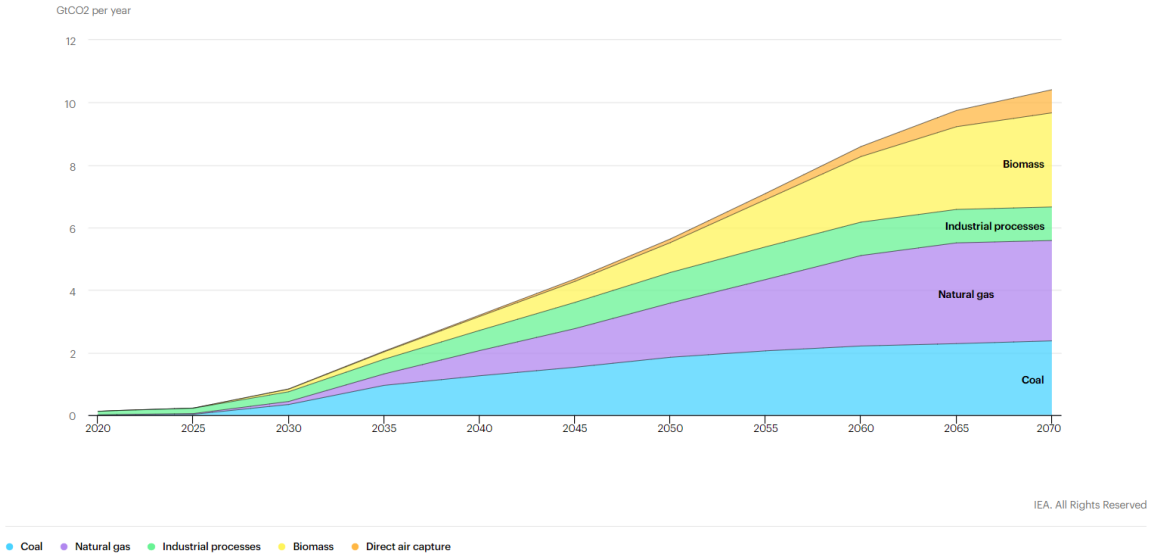

Figure. 2.4. The world captured CO_2 by source in the Sustainable Development Scenario, 2020-2070; IEA, Paris. Adapted from [34]

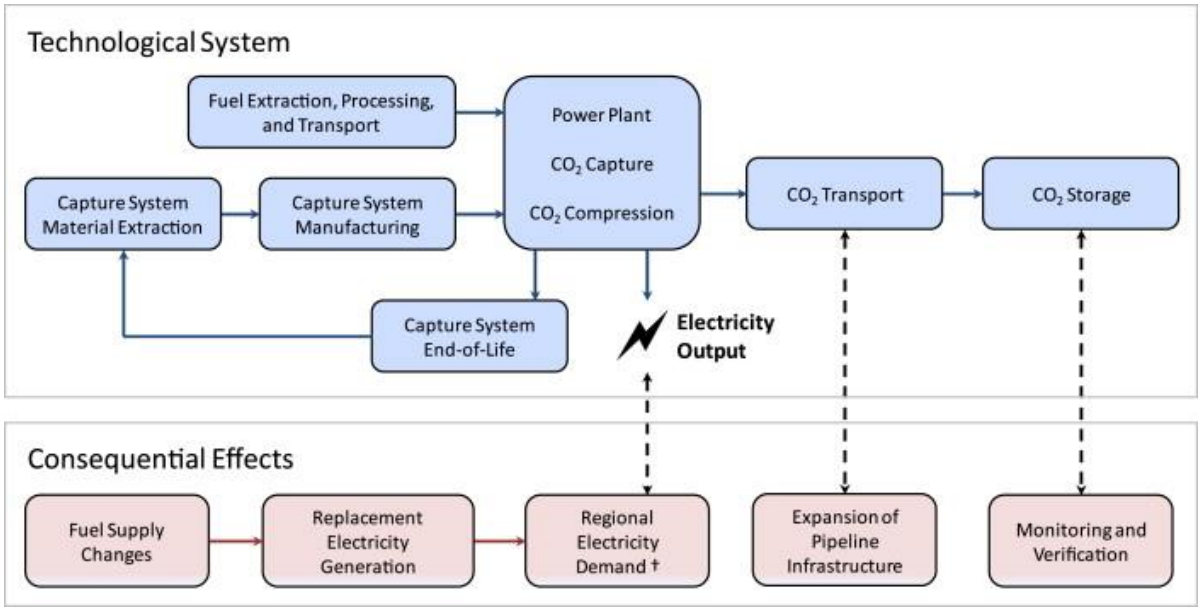

Figure. 2.5. Components of a CCS system, get permission and reproduce from the literature ref. [23]; Elsevier 2012 copyright.

2.2.2 The CO_2 capture and utilization (CCU) and why is CO_2 utilization important?

Besides the CCS technology, the CO_2 capture and utilization (CCU) technologies also play very important roles in CO_2 emissions control. The CCS technology normally needs heavy investment especially for the CCS from the air. For example, it will lead to a sharp increase in electricity cost (5-57%) from power plants using CCS [31]. In such cases, the CCU technologies have attracted intensive attention in academic and industrial areas based on their benefits. The CCU technologies can not only help to reduce CO_2 emissions but also produce valuable products.

The CCU route is a technology that uses the captured CO_2 to produce useful fuels, chemicals, and materials [33]. The CO_2 chemical utilization technologies can directly convert the CO_2 to fuels, chemicals, and materials [11,33]. The chemicals like urea, salicylic acid, and inorganic carbonates can be obtained by thermal processes. The chemicals/materials that needed catalytic processes concern the production of formic acid, other carboxylates, organic carbonates, carbamates, acrylates from ethene and CO_2, and products from olefins, dienes, and alkynes reacting with CO_2. The fuel production concentrates on syngas, methanol, higher alcohols, methane, and long-carbon chain hydrocarbon compounds.

In addition to thermal catalysis, electro-catalysis, photo-catalysis, plasma-assisted catalysis, and biochemical routes concerning CO_2 conversion have been also developed [4,35–37]. For instance, the production of biofuel via photocatalysis from microalgae using captured CO_2 seems to be an alternative route [38]. Among these routes, the CO_2 chemical utilization technologies have received the most intensive research interests due to mature technologies and high efficiency [33]. Meanwhile, the other novel approaches are still under research.

Table 2.1 lists various routes towards CO_2 chemical utilization. Six criteria such as Potential development and Economic perspectives, which influence the industrial application of CO_2 utilization technologies, were taken into account. Their degree of development was evaluated by the number from 1 to 4 and colors. The study was from the French Environment and Energy Management Agency (ADEME) [39]. The criteria used to investigate different CO_2 utilization routes were as follow [2,39]:

- Potential development: it indicates the time for the practical industrial facility, which is up to the lab research and development results.
- Economic perspective: it shows the future of obtaining an economic value and reflects the difficulty to achieve economic value.
- External use of energy: it indicates the cost of energy consumption per cost of the product. The energy cost can significantly affect the potential commercialization of the technology, which mainly refers to endothermic processes such as dry methane reforming.
- Potential volume of use of CO_2: it indicates the maximum annual amount of CO_2 that can be transferred by the year 2050.
- Time of sequestration: it refers to the time of CO_2 fixation before it is emitted to the atmosphere.
- Other environmental impacts: they indicate the application of toxic chemicals in the process and hazardous catalysts etc.

Table 2.1 Summary of the different routes in the CO_2 utilization (adapted and modified from [2])

Progress		Potential development	Economic perspectives	External use of energy	Potential volume of CO_2	Time of CO_2 sequestration	Impacts on environment
Industrialization	EOR	4	4	3	2	4	4
	Industrial use	4	4	3	2	1.5	4
	Organic synthesis	4	3	2	3	3	3
Short term	Hydrogenation	3	3	2	4	2	3
	Algae open ponds	3	3	4	4	2	4
Medium term	C_XH_y reforming	2	uncertain	1	4	2	1
	Algae reactor	2	2	4	4	2	4
Long term	Mineralization	1	1	1	3	4	3
	Thermochemical	1	2	4	4	2	3
	Electrolysis	1	uncertain	2	4	2	2
	Photo Electro Catalysis	1	uncertain	4	4	2	2
	Biochemical	1	uncertain	4	4	2	3

Potential development: 1, more than 10 years → 4, industrial
Economic perspectives: 1, difficult to estimate → 4, available industrial data
External use of energy: 1, difficult to decrease → 4, no need
Potential volume of CO_2: 1, less than 10 million tons (Mt) → 4, more than 500 Mt
Time of CO_2 sequestration: 1, very short → 4, long term
Impacts on the environment: 1, significant → 4, low (solvents or toxic chemicals, metal resources)

The CO_2 conversion to fuels can convert CO_2 to energy-rich fuels at the expense of energy. However, energy consumption today still relies on fossil energy. Thus, the conversion of CO_2 to fuels requires utilizing renewable energy rather than fossil energy for the sake of reducing CO_2 emissions.

CO_2 hydrogenation reactions and CO_2 reforming of methane had been studied intensively thanks to their high feasibility towards application. In these reactions, the H_2 can be produced by water electrolysis or photocatalysis by using renewable energy like solar [40]. Then, the captured CO_2 reacts with H_2 to form fuels like methane or methanol, etc. [41,42]. In these ways, the fluctuant renewable energy can be stored in the form of fuels/chemicals at the expense of CO_2.

2.3 Dry reforming of methane by CO_2

2.3.1 Introduction

The dry reforming of methane reaction (DRM) can convert two types of GHGs to syngas (CO and H_2). The dry reforming of methane ($CH_4 + CO_2 = 2CO + 2H_2$; ΔH_{298K}=247 kJ/mol) is an endothermic reaction [43]. The obtained syngas from dry reforming can be used in Fisher-Tropsch synthesis or the production of oxygenated organic compounds [43,44]. However, as the extremely endothermic property of the reaction, it needs a reaction temperature higher than 700 ℃ to obtain a good conversion of CO_2 and CH_4 in the presence of catalyst [44]. At a low temperature e.g. 450 ℃, the conversions of reactants were very low [11]. Meanwhile, the high temperature can result in the sintering of active metal and carbon deposition due to the occurrence of the side reactions, leading to the deactivation of catalyst [43].

The CO/H_2 molar ratio of syngas produced in DRM is close to 1, making the produced syngas appropriate for F-T synthesis. Nevertheless, the RWGS ($CO_2 + H_2 = CO + H_2O$; ΔH_{298K}=41.2 kJ/mol) can result in the molar ratio of CO/H_2 less than 1 [43]. The CH_4 decomposition reaction ($CH_4 = C(s) + 2H_2$; ΔH_{298K}=75 kJ/mol) and Boudouard reaction ($2CO = C(s) + CO_2$; ΔH_{298K}=-171 kJ/mol) can cause the coking formation on the surface of the catalyst, leading to the

deactivation of the catalyst [43]. Due to the endothermal property and high-temperature operation, the development of DRM catalysts focuses on the catalysts with good activity, high coke resistance, and anti-sintering properties.

Many catalysts e.g. Pt [45], Rh [46], Ru [47], and Ni [11,48–51] had been carried out in the DRM reaction [43]. The noble catalysts like Pt and Rh have a high resistance to coke formation and exhibit high activity and stability. But their high cost and low availability limit the possible large-scale application [52]. On the other hand, the non-noble catalysts like Ni or Co were also developed to catalyze the DRM reaction in which the Ni-based catalysts received extensive research interests [52,53]. The activity and stability of Ni catalysts depend on the properties of active metal, support, and promoters.

The Ni catalysts supported on Al_2O_3 [54], CeO_2 [55], ZrO_2 [56], KIT-6 [50], SBA-15 [57], hydrotalcite [58], etc. were widely studied in DRM reaction. A good dispersion of the active metal leads to the high DRM activity of Ni catalysts. The textural property of the support and the metal-support interaction play important roles in the activity and stability of Ni catalysts. A good selection of support needs to consider the porosity, surface area, robust ability, oxygen vacancies, redox ability, and basicity, etc. [52].

Promoters were also used to improve the activity and stability of the catalysts. The promoters e.g. Y [51,59], Ce [49,51,60], Zr [61,62], La [63], Ce-Zr [62], etc. were investigated in the Ni catalysts for DRM. Li et al. [64] studied the effect of Y_2O_3 on the SBA-15 supported Ni catalysts for DRM reaction. It was found that the adding of Y_2O_3 promoted the dispersion of Ni nanoparticles on the support and enhanced the Ni-support interaction. Thus, high activity and good stability were observed on 9 wt.% Y_2O_3 promoted catalyst. Zhang et al. [65] found that the presence of ceria on Ni/SBA-16 catalyst resulted in the uniformly dispersed Ni particles inside the mesopores and

enhanced Ni-Ce interaction. The adding of ceria results in increased Ce^{3+} concentration and improved structural stability of the catalysts. The DRM test showed that the NiCe/SBA-16 kept stable conversion during the 100 h TOS test.

Apart from the support and promoters, the preparation methods and novel materials were also studied to improve the activity and stability [66,67]. However, the advances in DRM reaction are far from commercialization. The coke deposition is still a major obstacle for industrial applications [52].

2.3.2 Power-to-syngas

The methane reforming reactions can also be integrated into the PtG processes to produce syngas or hydrogen [68,69]. In the power-to-syngas (PtS) concept, the syngas is produced by reverse water gas shift (RWGS) and dry reforming of methane (DRM) reactions powered by renewable energy like solar. The flowcharts of power-to-syngas are displayed in Fig.2.6 in which the power-to-methane route and conventional routes are also displayed. Compared to conventional syngas or synthetic natural gas production, the Power-to-syngas/methane showed less environmental impacts [69]. The PtS process showed more environmental benefits and economic viability than the PtM process under existing conditions [69,70]. However, the PtM process can be more potential if more renewable electricity is used.

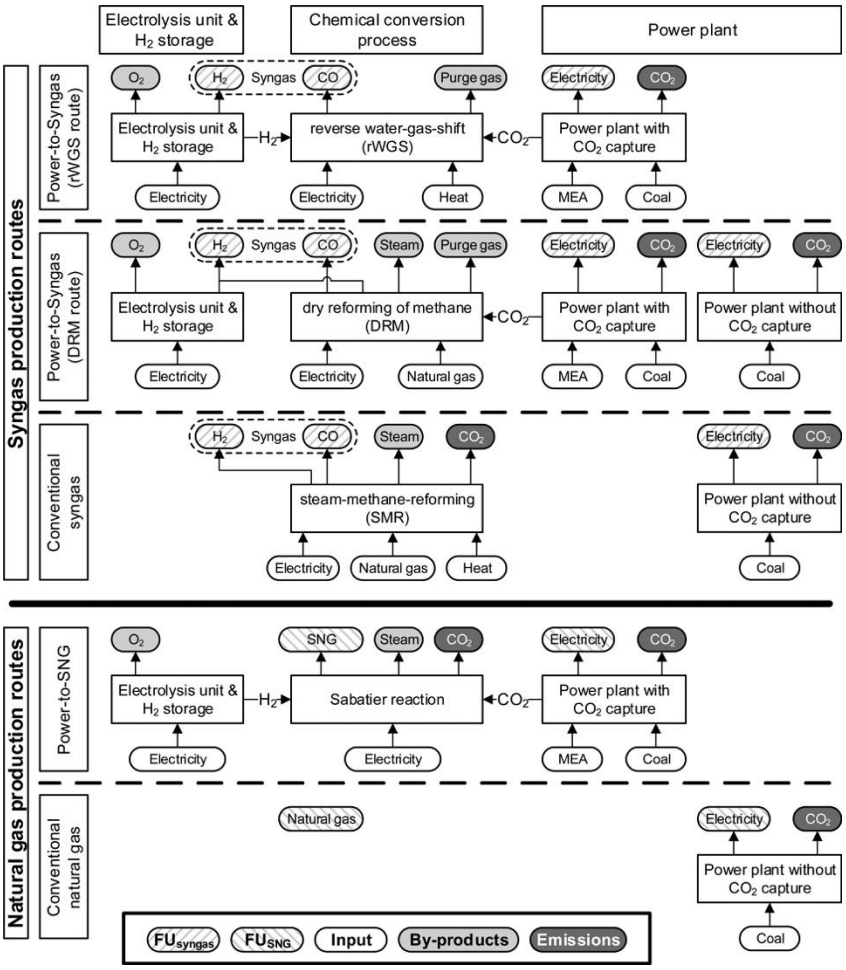

Figure. 2.6. Flowchart of Power-to-Syngas processes (rWGS and DRM) and Power to methane processes as compared with conventional routes; Adapted form [69]

2.4 CO_2 hydrogenation to methanol

2.4.1 Introduction

The CO_2 hydrogenation reactions can produce various chemicals by changing the condition and catalysts [33]. A variety of reactions are shown in Table 2.2. The syntheses of formic acid, methanol, methane, higher alcohols, and higher hydrocarbon are exothermic reactions [8,71–73]. Meanwhile, the formation of formaldehyde and CO is endothermic [72]. Among these reactions,

the CO_2 hydrogenation to methane and methanol attracted intensive interest. In this subchapter, the hydrogenation of CO_2 to methanol is discussed.

Table 2.2. Different CO_2 hydrogenation reactions.

Number	Reaction Formula	Product
(1)	$CO_2 + H_2 \rightarrow HCOOH$	Formic acid
(2)	$CO_2 + 2H_2 \rightarrow H_2CO + H_2O$	formaldehyde
(3)	$CO_2 + 3H_2 \rightarrow CH_3OH + H_2O$	methanol
(4)	$CO_2 + 4H_2 \rightarrow CH_4 + 2H_2O$	methane
(5)	$CO_2 + H_2 \rightarrow C_nH_m + H_2O$	hydrocarbon
(6)	$CO_2 + H_2 \rightarrow CO + H_2O$	Reverse-water-gas-shift
(7)	$CO_2 + H_2 \rightarrow C_nH_mOH + H_2O$	Higher alcohol

The reactions involved in CO_2 hydrogenation to methanol were listed in Table 2.3. It can be seen from Table 2.3 that both the CO_2 methanolization and CO methanolization are exothermic reactions, which are favored at low temperatures. The reverse water-gas-shift reaction, which is endothermic, also exists in the CO_2 hydrogenation to methanol process [74]. From the thermodynamic calculation results of CO_2 methanolization, the reaction is favored at low temperature, high pressure, and high H_2/CO_2 ratio [74]. However, the actual CO_2 methanolization reaction also generally needs a temperature of higher than 50 ℃ and the presence of an appropriate catalyst [75]. Even in harsh conditions, the CO_2 conversion and CH_3OH selectivity were still very low [75].

Table 2.3. Reactions involved in CO_2 hydrogenation to methanol process

Type	Formula	ΔH_{298K} (kJ·mol^{-1})	Definition
1	$CO_2 + 3H_2 = CH_3OH + H_2O$	−49.4	CO_2 methanolization
2	$CO + 2H_2 = CH_3OH$	-90.4	CO methanolization
3	$CO_2 + H_2 = CO + H_2O$	41.0	Reverse water-gas shift

Methanol can be used as fuel directly for transportation or act as a chemical feedstock. CO_2 hydrogenation to methanol technology can not only alleviate the CO_2 emissions but also produce value-added methanol. The heterogeneous catalysis on this reaction received intensive research interests. The catalytic systems mainly consist of transition metal-based catalysts and main group metal-based catalysts. The transition metal-based catalysts mainly focus on Cu-based catalyst and noble metal-based catalyst e.g., Pt and Pd [76–78]. Meanwhile, the main group of metal-based catalysts is made up of In_2O_3 catalysts and Ga-based catalysts [79,80]. Among them, the Cu-based catalyst was regarded as the most potential candidate for industrial application due to the low cost and high availability.

The studies for Cu-based catalysts mostly focused on the active sites of catalyst, the effect of catalyst structure, and activation and deactivation mechanisms [74]. It was found that the synergistic effect between Cu and ZnO contributed to the formation of methanol over $Cu/ZnO/Al_2O_3$ catalyst in CO_2 hydrogenation to methanol, in which the formate was considered as the reaction intermediate [76]. Sittichai et al. [81] studied the active sites of Cu catalysts in methanol synthesis. The XPS characterization revealed that only metallic Cu species existed on the surface of the catalysts. The Cu^0 particle size and ZnO crystallinity were directly linked with the activity of such catalysts. Smaller Cu particles resulted in a higher TOF value in methanol

production. The Cu-ZnO synergy was also a key parameter for the methanol formation. Also, the Cu structure was demonstrated to be an important factor in methanol synthesis [74]. Thus Cu atomic plane can affect the catalytic activity of Cu catalysts in methanol synthesis in which the Cu(110) orientation plane was found more active in methanol formation rate compared to that on Cu(100) and polycrystalline copper, indicating the structural sensitivity of Cu catalysts [82]. Over the time on stream (TOS) process, as for methanation, a deactivation can occur for methanolization reaction. Thus, on $Cu/ZnO/Al_2O_3$ catalyst after a long TOS run, the agglomeration of ZnO particles and partial oxidation of metallic Cu were observed and were presented as key parameters for the deactivation of the studied catalysts in methanol synthesis [83].

Furthermore, to improve the catalytic performance of catalysts in CO_2 hydrogenation to methanol reaction, intensive research had been done regarding promoters, support, and preparation methods. Alkali and alkaline earth oxides had been reported to have a positive effect on Cu catalysts in methanol production [84]. It was found that the Ba promoter can improve the activity of Cu/Al_2O_3 catalyst towards methanol synthesis while the potassium (K) promoter prefers to RWGS reaction [84]. Support oxides such as Al_2O_3, ZrO_2, Ga_2O_3, and Cr_2O_3 were also used as modifiers or promoters for Cu/ZnO catalysts [85]. The other studies on additives mainly concentrate on the study of rare earth oxides (La or Ce) [86], amphoteric oxides (e.g., TiO_2 and ZrO_2) [87], noble metal like Ag or Au [88,89], main group oxides (e.g., SiO_2) [90], and materials with semiconductor properties e.g., g-C_3N_4, etc. [91].

Regarding support, metal oxides like Al_2O_3, ZrO_2, CeO_2, and SiO_2 are then the most studied materials. The properties of the support, which consist of texture, structure, acidity/basicity, and electronic property, can have a significant effect on the performance of the catalyst [74]. Moreover, it has been reported that the porosity of the support with ordered or unordered porosities can

significantly affect the stability of for example CuZnO/SiO_2 methanol synthesis catalysts [92]. The narrowest pore constrictions of the support can mitigate the growth of metal particle size and improve catalyst stability. The other materials such as layered double hydroxides (LDHs) and carbon nanotubes (CNTs) also receive more attention recently.

The preparation method can change the catalyst structure and distribution of active sites over methanol synthesis catalysts. The most common method is the precipitation method, which allows high metal loadings and well-defined metal particles. Other methods such as the sol-gel method, liquid reduction, ammonia evaporation, microwave, and combustion method, etc. were also studied in these years [74,93,94].

Although many efforts have been devoted to the development of methanol synthesis catalysts, the activity and yield of methanol are still not very high due to the thermodynamic and dynamic barrier.

2.4.2 Power-to-methanol systems

The conventional methanol synthesis consists of the coal gasification and subsequent syngas to methanol reaction. However, this route results in severe environmental problems like CO_2 emission and sulfur pollutants [95]. Therefore, the low carbon synthesis of methanol was studied to replace the conventional way. The CO_2 hydrogenation to methanol route using solar energy attracted intensive attention due to its economic and environmental performance. For example, the solar energy-biomass-assisted CO_2 hydrogenation to methanol system can reduce the environmental impacts to 57.5% compared to that of coal gasification system [95]. As displayed in Fig.2.7, the system uses the CO_2 from the biomass power plant and H_2 from biomass combined with the solar power plant to produce methanol. However, the cost of methanol by this system is

5 times more than that of coal gasification way. Thus, the studies focus on decreasing the cost of photovoltaic electricity and improving the efficiency of water electrolysis [95].

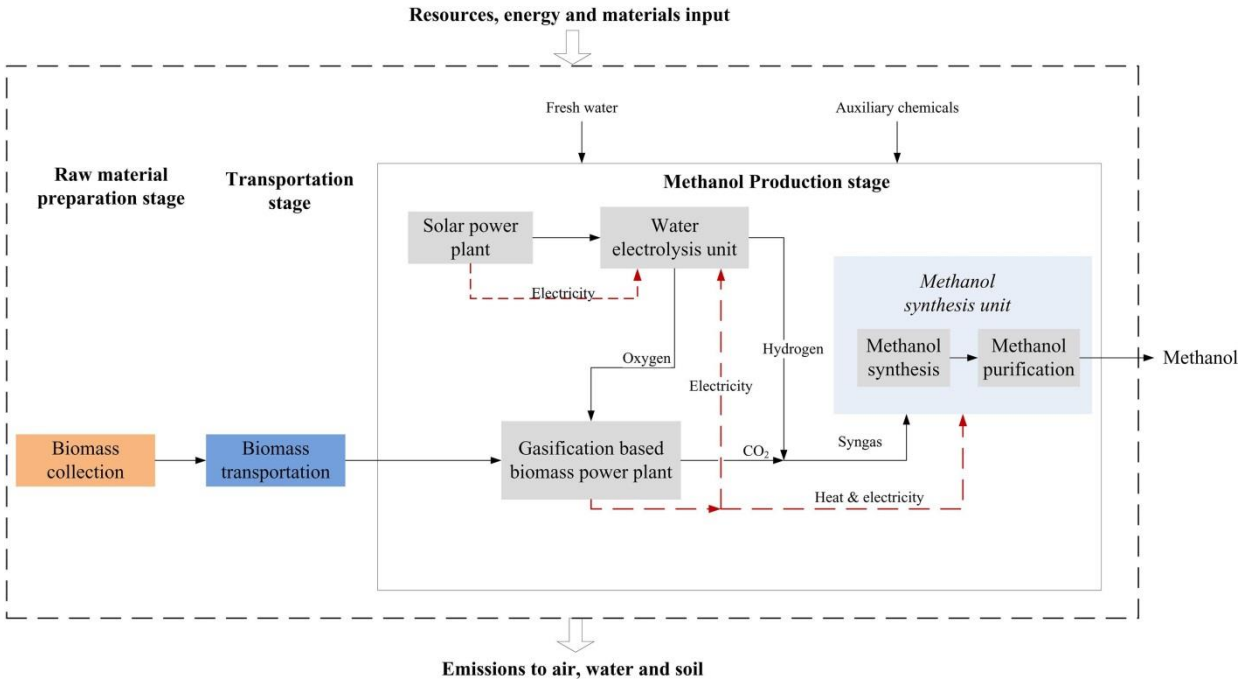

Figure. 2.7. Diagram of solar energy-biomass assisted CO_2 hydrogenation to methanol system; adapted from [95]

Liquid sunshine is a concept that uses solar energy to chemically synthesize liquid fuels e.g. methanol [96]. Methanol can be used as vehicle fuel [97]. The studies on this topic hope to produce clean energy as an alternative fuel. Regarding the application possibilities, the large-scale liquid sunshine project was tested in China in 2020.

Although many benefits of methanol, until now, the methanol production from CO_2 hydrogenation using solar energy still encounters high capital cost and running cost. Thus, the power-to-gas e.g. syngas and methane routes have attracted intensive attention.

2.5 CO_2 methanation

2.5.1 Introduction

CO_2 methanation, also known as Sabatier reaction, was found by Paul Sabatier [98].

$$CO_2 + 4H_2 = CH_4 + 2H_2O \ (\Delta H_{298k}=-165 \text{ kJ/mol}, \Delta G_{298k}=-114 \text{ kJ/mol})$$

This reaction is thermodynamically favorable and exothermic. Thus, this reaction can be carried out in moderate conditions with a high CO_2 conversion [99]. Also, the produced methane can be transported by established pipeline systems. This technology can be used in the Renewable Power-to-Gas (PtG) concept, which uses renewable energy to convert CO_2 to CH_4 [100]. By this route, the fluctuant renewable energy e.g. wind, solar, and hydropower can be stored in the form of CH_4 by PtG route.

The CO_2 reduction to CH_4 pathways consists of thermochemical, electrochemical, photochemical, and biological conversion processes [99,101]. The thermal catalysis of CO_2 reduction received the most intensive research attention because of the mild reaction condition, simple reaction set-up, high activity, and high feasibility towards commercialization. The other pathways are still under research period. The catalytic low-temperature CO_2 methanation is regarded as a potential route towards the large-scale application of CCU.

Although the CO_2 methanation reaction can reach a high activity and selectivity of CH_4 at low temperature in the thermodynamic simulation process, it needs the presence of appropriate catalytic systems under practical conditions due to the existence of a dynamic barrier. Thus, the presence of catalysts is indispensable in this reaction. The VIII group transition metal-based catalysts e.g. Pd [102–104], Rh [105–110], Ru [111–118], Pt [119,120], Fe [109,121], Co [122–129], and Ni [130,131,140–144,132–139] have been developed by scientists to catalyze the

reaction. For noble metal-based catalysts, the Ru and Ru-based catalysts generally showed superior activity. The studies regarding TiO_2 supported catalysts found that the CO_2 conversion or turnover frequency (TOF) followed the order of Rh>Ru>Pt>Pd [145]. The noble metal-based catalysts can catalyze the reaction at low temperatures (<200 ℃) under atmospheric pressure [102,106,146]. The studies on Rh/γ-Al_2O_3 catalyst for CO_2 methanation found that the reaction could happen at as low as 100 ℃ with nearly 100% of CH_4 selectivity [106]. The in situ diffuse reflectance infrared Fourier transform spectroscopy (DRIFTS) results confirmed that the CO was the main intermediate during the reaction[106].

As the high cost and low availability of noble metals, the potential commercialization of the CO_2 methanation needs to find materials that possess the properties such as low cost, high availability, high activity, and CH_4 selectivity as well as high stability. In such a case, the other transition metals e.g. Co and Ni have attracted more attention both in academic and commercial aspects [147].

2.5.2 Thermodynamic aspects of CO_2 methanation

2.5.2.1. The effect of temperature in CO_2 methanation simulation

The effects of temperature towards CO_2 conversion and CH_4 selectivity in CO_2 methanation were simulated by the HSC Chemistry 5.0 software using the Gibbs free energy minimization method. The CO_2 conversion and CH_4 selectivity are calculated following Equation (1) and (2):

$$X_{CO2}(\%) = \frac{F_{CO2,in} - F_{CO2,out}}{F_{CO2,in}} \times 100\% \qquad (1)$$

$$S_{CH4}(\%) = \frac{F_{CH4,out}}{F_{CO2,in} - F_{CO2,out}} \times 100\% \qquad (2)$$

The X_{CO2} and S_{CH4} represent the CO_2 conversion and CH_4 selectivity. The $F_{CO2,in}$, $F_{CO2,out,}$ and $F_{CH4,out}$ represent the molar flow of CO_2 or CH_4 in which the "in" and "out" mean inlet and outlet, respectively.

The possible reactions in CO_2 methanation reactions were displayed in Table 2.4. We can List eight reactions that probably happened during the CO_2 methanation process. Two of them are endothermic reactions and 6 reactions are exothermic thermodynamically.

The results of the effect of temperature at 1 bar in methanation were displayed in Fig.2.8. The molar ratio of H_2/CO_2 was controlled at 4 with a gas hourly space velocity (GHSV) of 12,000. As shown in Fig.2.8a, the CO_2 conversion decreases with the increase of temperature until 839 K and then increases gradually at atmospheric pressure. As displayed in Table 2.4, the methanation reaction is an exothermic reaction, which is favored under low temperatures. In Fig.2.8b, the CH_4 selectivity decreases gradually with the increase of temperature up to 773 K and then decreases sharply until nearly zero. Meanwhile, the selectivity of CO increases to nearly 100% as the temperature increasing up to 1173 K. The presence of CO, which is the main by-product in methanation reaction, was caused by the reversed water gas shift reaction (Table 2.4, $CO_2 + H_2 = H_2O + CO$) [148].

Table 2.4. Reactions involved in the CO_2 methanation process.

Type	Formula	ΔH_{298K} (kJ·mol^{-1})	Definition
1	$CO_2 + 4H_2 = CH_4 + 2H_2O$	−165.0	CO_2 methanation
2	$CO_2 + H_2 = CO + H_2O$	41.2	Reverse water-gas shift
3	$CO_2 + 2H_2 = C + 2H_2O$	−90.1	CO_2 reduction
4	$CO + 3H_2 = CH_4 + H_2O$	−206.2	CO methanation
5	$2CO + 2H_2 = CH_4 + CO_2$	−247.3	Reverse CH_4 dry reforming
6	$2CO = C + CO_2$	−172.4	Boudouard reaction
7	$CO + H_2 = C + H_2O$	−131.3	CO reduction
8	$CH_4 = 2H_2 + C$	74.8	CH_4 cracking

The molar ratio changes of the species were shown in Fig.2.8c. It can be seen from Fig.2.8c that the molar fraction of CH_4 decreases to nearly zero as the temperature increases up to 973 K and then keep stable. A similar evolution trend is also found over the molar fraction of H_2O, with a molar ratio of 12% found after 973 K. The change in the concentration of CH_4 and H_2O with the increase of temperature also proves that methanation reaction is favored in low temperature. The molar fraction of CO_2 increases gradually up to 823 K and then decreases with the increase of temperature. The concentration trends of H_2 and CO experience a slow, sharp, and stable increasing trend individually during the temperature range. In the calculation, nearly no carbon was formed in the chosen conditions. As reported by Jung-Nam Park [103], the methanation reaction may experience the route CO, in which CO is the main intermediate, in which the CO_2 reacts with H_2 to produce CO by reverse water gas shift, and the CH_4 is formed by CO methanation [148]. The thermodynamic results reveal that the reaction temperature should not be very high to reach a high CO_2 conversion at ambient pressure. However, the kinetic barriers determine that the

CO_2 activation is too difficult at low temperatures, which means the presence of an appropriate catalyst is necessary for the reaction to take place [148,149].

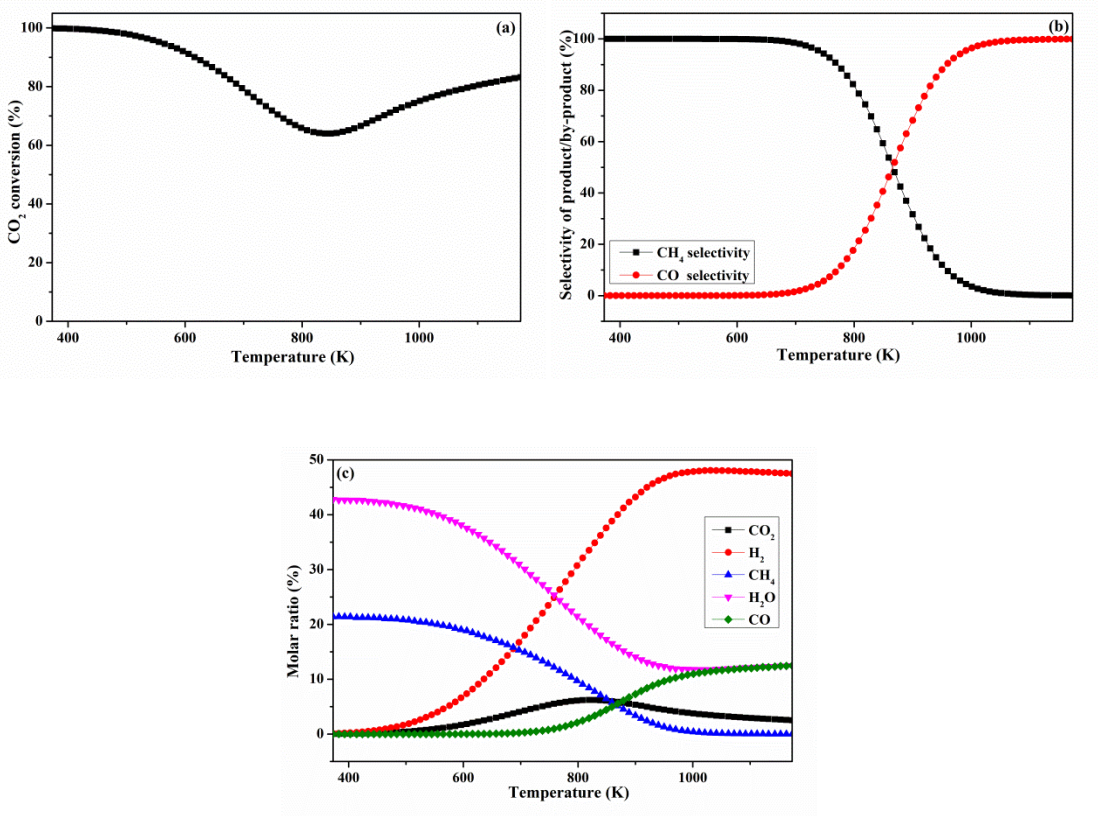

Figure. 2.8. Effect of temperature on CO_2 conversion (a), CH_4/CO selectivity (b), and molar ratio of specie (c) in methanation; Condition: 1 bar, H_2/CO_2/Ar (molar ratio)=60/15/25, GHSV=12,000 h^{-1} [141,142].

2.5.2.2. The effect of the pressure in CO_2 methanation

The thermodynamic effect of the Pressure on CO_2 conversion and CH_4 selectivity in CO_2 methanation were calculated and displayed in Fig.2.9. As shown in Fig.2.9a, the CO_2 conversion at each pressure presents a gradually decreasing trend below 873 K. The increase of pressure causes the increase of CO_2 conversion because the CO_2 methanation reaction is a volume reducing

reaction, with the gas volume changing from 5 to 3 units. Thus, the increase of pressure can promote the reaction thermodynamically. However, when the reaction temperature exceeds 873 K at 1 bar, the CO_2 starts to be converted through the reverse water-gas-shift reaction (Table 2.4, $CO_2 + H_2 = CO + H_2O$) dominates the reaction [148]. The effect on CH_4 selectivity is shown in Fig.2.9b. It is found that the CH_4 selectivity decreases slowly when the temperature increases until 773 K because of the exothermicity of methanation. Beyond 773 K, the sharp decrease of CH_4 selectivity is registered at each pressure, which is attributed to the effect of reverse water-gas-shift reaction. However, the increase of pressure can significantly promote the CH_4 selectivity, which is attributed to the volume reducing property of methanation. Meanwhile, no carbon was registered in the studied pressure range. This can be explained by the effect of H_2O formed in the reaction, which can suppress the formation of coke [148].

The calculation results in this study are well consistent with the calculation results carried out elsewhere [106,148,150].

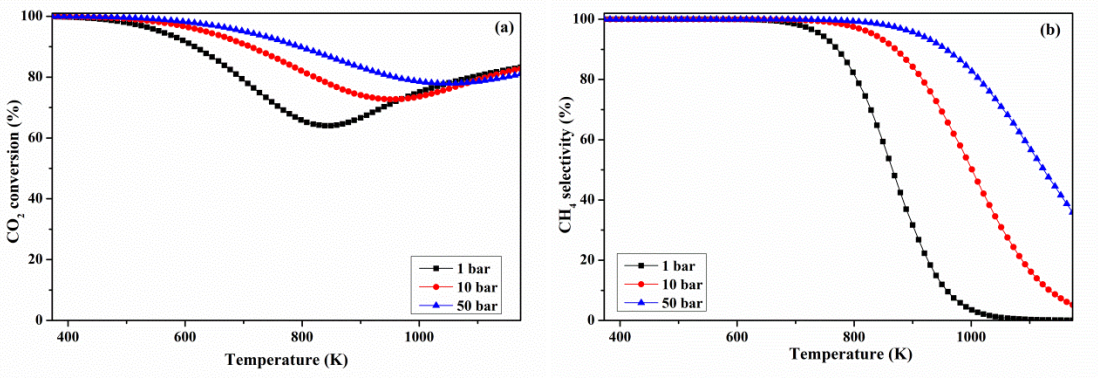

Figure. 2.9. Effect of pressure on CO_2 conversion (a) and CH_4 selectivity (b) in methanation; Condition: $H_2/CO_2/Ar$ (molar ratio)=60/15/25, GHSV=12,000 h^{-1}

2.5.2.3. The effect of H_2/CO_2 ratio in CO_2 methanation simulation

The effect of the H_2/CO_2 ratio on methanation reaction was calculated and shown in Fig.2.10. It can be seen from Fig.2.10a that the H_2/CO_2 ratio notably affects the CO_2 conversion. The increase in H_2/CO_2 ratio leads to a significant increase in CO_2 conversion. The same phenomenon is also found for CH_4 selectivity. In the case of the H_2/CO_2 ratio being 2, the CO_2 conversion and CH_4 selectivity are just 75% and 30%, separately. Meanwhile, the CO_2 conversion and CH_4 selectivity are nearly 100% when H_2/CO_2 ratio reaches 4. A lot of carbon was formed below 773 K when the H_2/CO_2 ratio is 2. Almost no carbon deposition is registered when the H_2/CO_2 ratio exceeds 2. The CO_2 reduction reaction (Table 2.4, $CO_2 + 2H_2 = C + 2H_2O$) appeared when the H_2/CO_2 ratio is 2, which results in the abundant formation of carbon.

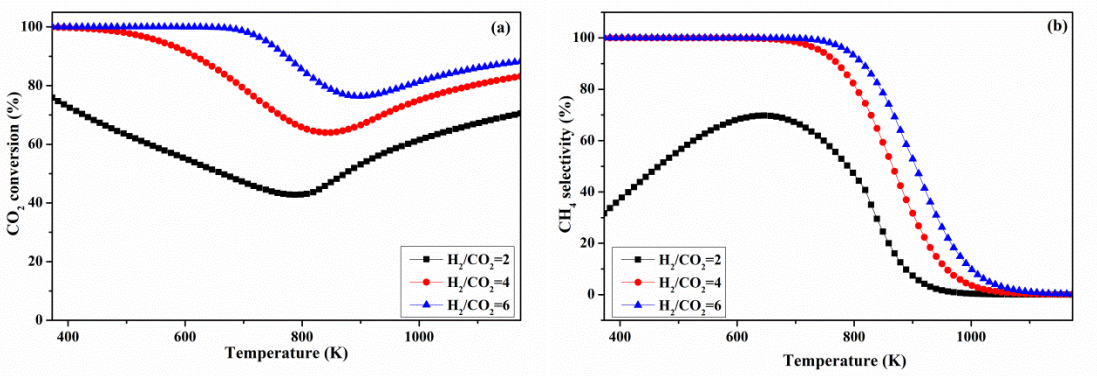

Figure. 2.10. Effect of H_2/CO_2 ratio on CO_2 conversion (a) and CH_4 slectivity (b) in methanation; Condition: 1 bar, GHSV=12,000 h^{-1}

2.5.3 Mechanisms of CO_2 methanation

2.5.3.1 The CO as intermediate of CO_2 hydrogenation mechanism

Nowadays the mechanism of CO_2 methanation remains unclear. Regarding the intermediate that account for the formation of methane, there are mainly two mechanisms proposed [151]. One of them is the mechanism that carbon oxide plays as an intermediate in which CO_2 is reduced to CO and subsequently the methane is produced by CO methanation [152]. The density functional theory on Ni(111) surfaces proposed three mechanisms in which the mechanism with a rate-determining step of CO→C+O has the lowest energy barrier [153]. The diagram of the scheme is shown in Scheme 1.

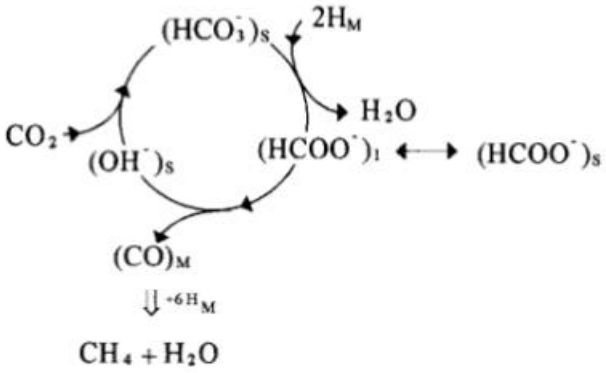

Scheme 1. Mechanism of CO_2 methanation with CO as an intermediate (M: metal, S: support); Reproduced with permission from ref [154]. Copyright Elsevier 1997.

The experimental studies on the Ni catalysts supported on activated carbon for CO_2 methanation also confirmed that the CO was an indispensable intermediate in the formation process of methane [152].

Zhou et al. [155] studied the effect of TiO_2 structure on Ni/TiO_2 for CO_2 methanation. The methanation over Ni/TiO_2 catalyst with principle Ni (111) facet experienced the CO intermediate pathway. However, the catalyst with multi-planes of Ni followed the mechanism of formate species as an intermediate pathway in which the Ni only accounted for H_2 dissociation.

The mechanism study on the noble metal-based catalyst ($Rh/\gamma\text{-}Al_2O_3$) at low temperature and ambient pressure revealed that the methanation process followed the pathway without the formation of formate species [156,157]. Three steps can be listed as follows:

$$CO_2\ (g) \rightarrow CO_2\ (ads) \quad (1)$$

$$CO_2\ (ads) \rightarrow CO\ (ads) + O\ (ads) \quad (2)$$

$$CO\ (ads) + H\ (ads) \rightarrow\cdots\rightarrow CH_4\ (ads) + H_2O\ (ads) \quad (3)$$

The H(ads) species were formed in the dissociation process of H_2. However, it was also noted that CO_2 adsorption could be a complicated process [157]. The oxidation of part of rhodium particles was also registered, which was attributed to its oxidation by O(ads).

2.5.3.2 The formate intermediate mechanism

The other proposed mechanism involves the formation of formate species during the reaction; this latter species is subsequently hydrogenated to methane [158,159]. This mechanism needs both the participation of support and active metal. It was reported that many intermediates e.g., hydrogen carbonate, bidentate carbonate, monodentate carbonate, bridged carbonate, formate, and nickel carbonyl hydride can be formed [158]. The properties of support can affect the variety of intermediates. As presented in Scheme 2 for the mechanism over $Ni/Ce_{0.5}Zr_{0.5}O_2$ and $Ni/\gamma\text{-}Al_2O_3$ catalysts, the H_2 gas is adsorbed and dissociated on the surface of the Ni atom to produce H while

the CO_2 molecules are adsorbed and dissociated on the support surface to form carbonate species. The carbonate (bidentate or monodentate) and hydrocarbonate species subsequently react with the H to form formate (bidentate or monodentate) species, which will be hydrogenated by H to produced methane as reported elsewhere [158]. For the Ni/γ-Al_2O_3 catalyst, it was demonstrated by FTIR that more hydrogen carbonates formed over the catalyst [160]. The hydrogen carbonate species were hydrogenated to bidentate formate species, which were hydrogenated to methane. For Ni/$Ce_{0.5}Zr_{0.5}O_2$ catalyst, more monodentate carbonate rather than hydrogen carbonate species formed, thus leading to more monodentate formate species, which were hydrogenated to methane. The pathway of methane formation over Ni/$Ce_{0.5}Zr_{0.5}O_2$ is faster than that over Ni/γ-Al_2O_3 catalyst [160]. This latter result is attributed to the difference of basicity, in which more medium basic sites over Ni/$Ce_{0.5}Zr_{0.5}O_2$ are favorable for the formation of monodentate carbonate.

Another important parameter is the nickel particle size. In the literature, the study on the effect of Ni particle size over Ni/SiO_2 catalysts showed that the particle size of Ni also had significant effects on the pathway of methane formation [161].

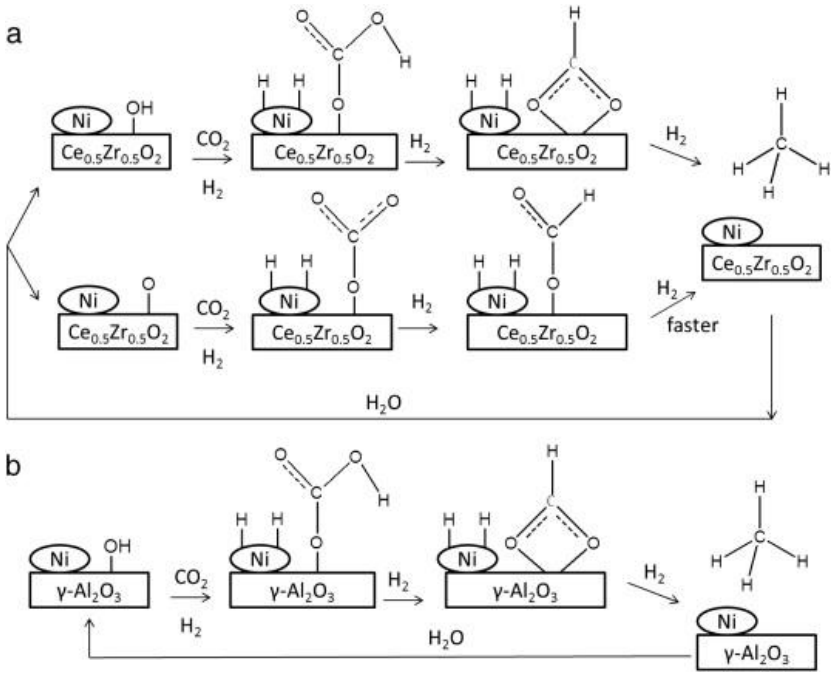

Scheme 2. Proposed mechanisms over $Ni/Ce_{0.5}Zr_{0.5}O_2$ and Ni/γ-Al_2O_3 catalysts; Reproduced with permission from ref. [160]; Copyright Elsevier 2014.

2.5.3.3 On the important presence of side reactions in CO_2 methanation reaction

In the thermodynamic analyses of CO_2 methanation, it has been demonstrated that the species formed during the methanation process depend significantly on the reaction conditions. Under atmospheric pressure, the main by-product in thermodynamic analyses is carbon monoxide (CO), which originates from the RWGS reaction ($H_2 + CO_2 \rightarrow CO + H_2O$) or reforming reactions [48,161]. Besides, the CO species can also be formed by the hydrogenation of formate species as intermediates [161]. The presence of CO can also cause the sintering of active metals (Ni, etc.), which is caused by the formation of $Ni(CO)_x$ species, leading to the agglomeration of Ni particles [162].

The H_2O formed in methanation reaction can induce the formation of Ni-hydroxide at low temperature, which results in the consequent decrease of metallic nickel. The Ni-hydroxide species cannot be reduced to Ni metal fast and contribute to the sintering of Ni and the formation of hardly reducible Ni-aluminate, leading to partial deactivation of catalysts [163].

When the ratio H_2/CO_2 decreases, the carbon can also be formed due to parallel reactions such as the Boudouard reaction or/and CO_2 reduction. It is worth noting that carbon deposition also occurs at high pressure over some catalytic systems [121].

2.5.4 The catalysts for CO_2 methanation

2.5.4.1 Noble metal-based catalysts

The noble metal-based catalysts such as Pt [145], Rh [107], Ru [118,164,165], and Pd [103,104] were also studied in CO_2 methanation. Table 2.5 summarized some noble-metal-based catalysts as compared to transition metal catalysts in CO_2 methanation. The noble metal-based catalysts could be very active at low temperatures.

Paraskevi et al. [145] studied the catalytic performance of supported noble metal-based catalysts for CO_2 methanation. It was then showed that the CO_2 conversion of TiO_2 supported noble metal catalysts decreased following the order Rh>Ru>Pt>Pd, with the Rh/TiO_2 catalyst having the higher activity and selectivity of CH_4. The Pt and Pd catalysts were mainly known to promote the RWGS reaction to produce CO. The Ru crystallite size had a significant effect on the performance of Ru/TiO_2 and Ru/Al_2O_3 catalysts for CO_2 methanation. Also, the CO acted as an important intermediate for Ru catalysts during the formation of methane [145].

For noble metal-based catalysts, the CO_2 methanation is known to be structure sensitive reaction, which means the metal crystallite size has significant effects on the performance of the catalysts. The investigation of Rh/γ-Al_2O_3 for CO_2 methanation showed that the larger particle size could promote the activity of the catalyst at a temperature lower than 458 K [107]. However, the activity of the catalyst could not be related to the particle size of the metal. The DRIFTS experiments showed that the CO was an active intermediate while the formate did not involve in the formation of methane. The doping of the additive can change the pathway of CO_2 methanation for noble metal-based catalysts. It has been reported that the doping of Ce on Ru/Al_2O_3 catalyst can significantly improve the activity and selectivity of the catalysts, 30% Ce modified catalyst possessing the best performance, which could be attributed to the formation of intermediates like formate and carbonate [112]. These species can then react with H_2 faster than with CO.

The addition of Mg onto Pd/SiO_2 catalyst could promote the formation of methane in CO_2 methanation reaction due to the stabilization of CO_2 on MgO [103]. Also, the CO acts then as an important intermediate in the reaction.

In conclusion, the Ru and Rh-based catalysts are most active for the noble metal catalysts in CO_2 methanation. The Ru and Rh catalysts are even active at a very low temperature near to ambient temperature with a very high CH_4 selectivity [156,166]. The CO acts as a main intermediate in the methanation process [156]. Although the excellent properties of Ru/Rh catalyst, their potential commercialization is limited due to their low availability and high cost.

Table 2.5 Summary of the noble-metal-based catalysts as compared to transition metal catalysts in CO_2 methanation.

Catalyst[a]	Metal content (wt.%)	Preparation method[b]	Reaction condition			CO_2 conversion (%)	CH_4 selectivity (%)	Ref.
			Temperature (°C)	H_2/CO_2 ratio	GHSV/WHSV			
Rh/MSN	5	WI	350	4	50,000 ml $g_{cat}^{-1} \cdot h^{-1}$	99.5	100	[109]
Ru/MSN						95.7	100	
Ir/MSN						9.5	83	
Ni/MSN						85.4	99.9	
Fe/MSN						4	92	
Cu/MSN						3.3	79	
Rh/TiO_2	0.5	WI	350	4	90,000 ml $g_{cat}^{-1} \cdot h^{-1}$	72	99	[145]
Ru/TiO_2						19	86	
Pd/TiO_2						6	99	
Pt/TiO_2						16	98	
Rh/SiO_2	3	WI	350	5	60, 000 h^{-1}	Ni=Rh>Pd	Rh>Ni>Pd	[71]
Pd/SiO_2								
Ni/SiO_2								
Rh/Al_2O_3	3	WI	350	5	60, 000 h^{-1}	Rh>Pd>Ni	Rh>Pd>Ni	
Pd/Al_2O_3								
Ni/Al_2O_3								
Rh/CeO_2	3	WI	350	5	60, 000 h^{-1}	Rh>Ni>Pd	Rh>Ni>Pd	
Pd/CeO_2								
Ni/CeO_2								

[a] MSN: mesostructured silica nanoparticles; [b] WI-wet impregnation.

2.5.4.2 Ni catalysts and other non-noble metal-based catalysts

2.5.4.2.1. Ni-based catalysts

Ni-based catalysts were widely investigated in CO_2 methanation regarding their superiorities like good activity and CH_4 selectivity, low cost, high availability, and high accessibility making it appropriate in potential commercial applications [142,167]. A variety of Ni catalysts with good activity and selectivity e.g. Ni/CeO_2 [141], Ni/ZrO_2 [168], Ni/CeO_2-ZrO_2 [150], Ni/SBA-15 [169], and Ni/SBA-16 [142] have been developed for CO_2 methanation. Shohei et al. [170] synthesized the Ni/CeO_2 catalyst by wet impregnation method and compared its activity and selectivity with Ni/α-Al_2O_3, Ni/TiO_2, and Ni/MgO. It was found that the Ni/CeO_2 catalyst showed the highest CO_2 conversion with CH_4 selectivity reaching nearly 1. Zhao et al. [168] prepared the Ni/ZrO_2 catalysts via combustion method using different combustion mediums and tested their activity in CO_2 methanation. It was shown that the combustion medium could significantly affect the physiochemical properties regarding Ni metal size, Ni dispersion, the crystal structure of the support, and Ni-support interaction of the catalyst, which significantly affected the activity and stability of the Ni/ZrO_2 catalyst. The CO_2 conversion of Ni/ZrO_2 synthesized by the urea medium reached 60% at 573 K under ambient pressure.

Although the superior performance of Ni-based catalysts, the problems of deactivation and poor stability still exist [171,172]. Thus, it is still a challenge to develop a highly stable Ni catalyst for CO_2 methanation [173]. At a low-temperature range lower than 573 K, the deactivation of Ni catalysts in CO_2 methanation was mostly caused by the sintering of Ni metal during the reaction process, which was caused by the formation of mobile nickel carbonyl originated from the interaction between Ni and CO [151,174–176]. At a high-temperature range of 623-723 K, the

coke may form owing to the Boudouard reaction and methane cracking. Apart from sintering of Ni metal and coke, the formation of Ni-hydroxide at low temperature was also found, which caused the decrease of the active phase of Ni [163]. Possible solutions toward tackling the problem were: (i) in adding promoter to improve the dispersion of Ni over the support or promote the formation of solid solution, (ii) in doping a metal to form an alloy, (iii) in modifying the support to obtain high surface area and pore volume, (iv) in making the catalyst with special structure, (v) in enhancing the metal-support interaction, and (vi) in changing the preparation method [173].

In the literature, it was also reported the addition of a second metal (Fe, Co, Cu) on Ni/ZrO_2 catalysts for CO_2 methanation [177]. Thus, the Fe-doped Ni/ZrO_2 catalyst significantly enhanced the activity of Ni/ZrO_2 catalyst at a low-temperature range when compared to the Co and Cu metals. The promotion of Fe could improve the dispersion and reducibility of Ni species and even promote the reduction of ZrO_2, which enhanced the adsorption and dissociation of CO_2 and H_2. Thus, the activity of Ni/ZrO_2 was improved. Moreover, the cerium had been reported to have positive effects on the mesoporous materials supported by Ni catalysts in CO_2 methanation [142,178].

Ewald et al. [172] studied the deactivation behavior of Ni-Al catalysts at 8 bar in CO_2 methanation. In the latter study, it was found that the $Ni/\gamma\text{-}Al_2O_3$ catalyst synthesized by the impregnation method exhibited lower stability compared with the Ni-Al catalysts prepared by the co-precipitation method. The stability of the Ni-Al mixed oxides increased with the decrease of Ni content, but the activity of the mixed oxides showed a reversed trend. The deactivation mechanisms found over the Ni-Al catalysts were caused by the Ni metal sintering, a loss of specific surface area, a decrease of CO_2 adsorption capacity, decreasing medium basic sites, and structure change of the mixed oxide phase [172]. Moreover, the main deactivation reasons of impregnated catalysts were attributed to increased Ni particle size and decreased surface area. Also, the structure

and metal-support interaction could play predominant effects over some structure-sensitive catalysts in methanation. The special structure like hydrotalcite, phyllosilicate, and perovskite was reported to have good activity and stability towards CO_2 methanation [131,138,144,179,180]. By tuning the metal-support interaction, a stronger metal-support interaction can promote the Ni dispersion and thus promote the activity and stability of Ni catalysts in CO_2 methanation [181].

Ye et al. [173] synthesized a series of Ni/SiO_2 catalysts by different methods i.e. wet impregnation and ammonia evaporation method. The Ni/SiO_2 (AEM) catalyst prepared by the ammonia evaporation method exhibited Ni phyllosilicate with the lamellar structure, which enhanced the Ni-support interaction of the catalyst. It also had a high BET surface area, good dispersion of Ni, and small Ni particle size. The stability test for CO_2 methanation showed a higher yield of methane and better long-term stability than the impregnated Ni/SiO_2 catalyst. Liu et al. [171] prepared the Ni/SBA-15-op catalyst by one-pot hydrothermal method and compared its activity with the Ni/SBA-15-im synthesized by conventional wet impregnation method. It was revealed that the Ni/SBA-15-op catalyst showed higher surface area, larger pore volume, and higher Ni dispersion compared to Ni/SBA-15-im. Thus, both better activity and stability were obtained over Ni/SBA-15-op catalyst.

A) On the effect of the Ni loading and Ni dispersion

The performance of the Ni-based catalysts in CO_2 methanation depends on Ni metal size and Ni dispersion [167,182]. The nickel particle size can be affected by the Ni loading, the preparation method, and the support properties. Thus, the Ni particle size of the Ni/SiO_2 catalyst prepared by the deposition-precipitation method was affected by the parameters of the preparation method

[183]. The average Ni particle size of the catalyst derived from the Ni phyllosilicate phase was smaller than that of the Ni hydroxide derived catalyst. The Ni loading also has a significant effect on many Ni-based catalysts. Generally, the Ni particle size of the supported catalysts is smaller at low Ni loading and tends to increase for high Ni loadings [167]. For example, Ni nanoparticles supported over mesoporous SBA-16 reported in literature showed a decreasing trend towards Ni particle size as the increase of Ni loading [182]. In the same study, a catalyst with Ni loading of 5.9 wt.% showed the smallest Ni particle size and exhibited the highest turnover frequency (TOF) in CO_2 methanation reaction.

Herein, we have listed the effect of Ni loading on the Ni particle sizes of some supported catalysts and illustrated the influence of Ni particle size on the activity of the catalyst in methanation. As shown in Fig.2.11, the Ni particle size of Ni/MSN catalyst (mesostructured silica nanoparticle) increases with the increase of Ni loading, with the biggest particle obtained on the sample of 10 wt.% Ni loading [184]. The TOF and CO_2 conversion showed sharply increased trends with the increase of Ni loading until 5 wt.% of Ni and then only increased a little.

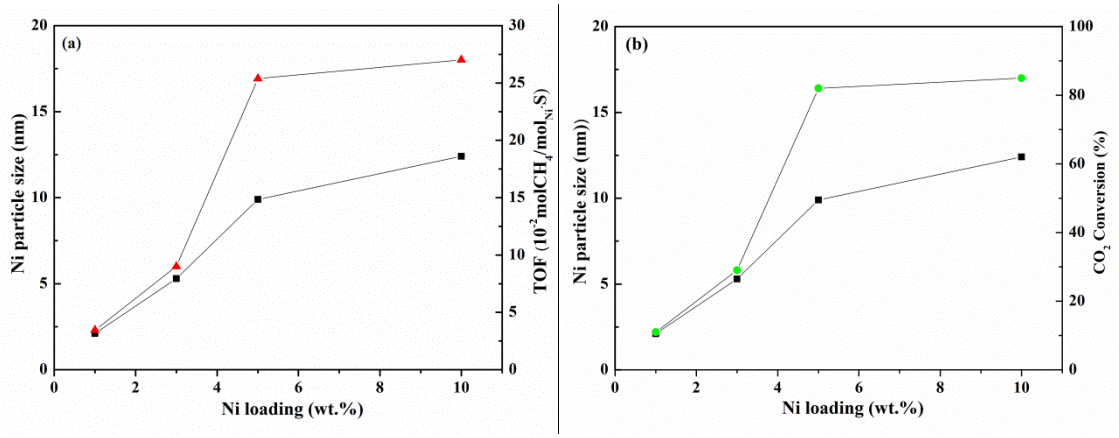

Figure. 2.11. Effect of Ni loading on the particle size and activity of Ni/MSN catalysts; Condition: GHSV = 50,000 $mL \bullet g_{cat}^{-1}h^{-1}$; H_2/CO_2 = 4/1; reaction temperature: 623 K [184].

A similar trend was also found on Ni/γ-Al_2O_3 catalyst [185]. The increase of Ni loading resulted in the increase of Ni crystalline size from 10 to 25 wt.%, with the highest CO_2 conversion obtained over 20Ni/γ-Al_2O_3 at 573 K. Generally, the increase of Ni loading can promote the activity of the catalyst due to more active metals for the reactant, but a high Ni loading may result in the aggregation of Ni species and decrease of Ni dispersion, which leads to the decrease of activity. Nevertheless, the effect of Ni content on the Ni crystalline size depends on the type of support. The increase of Ni content in hydrotalcite derived catalysts can lead to the decrease of Ni crystalline size for the reduced and spent catalysts [131]. In the CO_2 methanation reaction, the activity of the catalyst increased as an increase of Ni content until 42.5 wt.% at the temperature range of 523-923 K.

The preparation method also plays an important role in the dispersion of Ni catalysts. The Ni/Al_2O_3 catalysts prepared by the co-precipitation method showed a higher Ni dispersion compared to the one prepared by the impregnation method due to the formation of surface $NiAl_2O_4$ spinel phase [186].

B) On the Influence of the support on the performance of Ni-based catalysts

The support itself has a significant effect on the performance and stability of catalysts. The dispersion of Ni, the basicity, the metal-support interaction, and the morphology of the catalyst can be affected by the used support [160,167,187]. The support with high surface area and pore volume can confine the Ni particles inside the porous structure and thus improve the dispersion of Ni [142]. The mesoporous support like SBA-15, SBA-16, or KIT-6 with high surface area and

pore volume had been reported to promote the dispersion of Ni and lead to small Ni particles [60,179,188–190].

The basicity of supported catalyst plays an important role because the support can also participate in the reaction due to its CO_2 adsorption/desorption capacity. It has been reported that the $Ni/Ce_{0.5}Zr_{0.5}O_2$ catalyst exhibited more medium basic sites compared to that of $Ni/\gamma\text{-}Al_2O_3$ catalyst. This medium basicity promoted the formation of monodentate carbonate, thus resulting in the formation of monodentate formate species, which was hydrogenated to methane with a higher rate [160]. Also, $Ni/\gamma\text{-}Al_2O_3$ catalysts showed lower performance than the $Ni/Ce_{0.5}Zr_{0.5}O_2$ catalysts due to the lack of medium basic sites. CeO_2 supported nickel catalysts were intensively studied in CO_2 methanation because of their superior performance and selectivity toward CH_4, which could be attributed to the unique redox properties of cerium oxide [191]. The cerium oxide can be reduced partially to form defective sites on the support, which resulted in the formation of oxygen vacancies, which will promote CO_2 adsorption and dissociation [192].

The metal-support interaction is also controlling Ni particle size and oxygen availability of Ni-based catalysts. The small particle size could be favored under strong metal-support interaction [193,194]. Lin et al. [195] investigated the effect of activation treatment on the metal-support interactions (MSI) of Ni/CeO_2 catalysts. It was found that the Ni/CeO_2 catalyst pre-treated under H_2 atmosphere showed better activity and high selectivity compared to catalysts pre-treated under N_2 or air atmosphere, which was attributed to the appropriate MSI generated in the pre-treatment, leading to the high dispersion of Ni, high amount of oxygen vacancies, and abundant weak basic sites on the catalyst [195]. Regarding regulating the MSI of the catalyst, the preparation method also plays a key role. Yan et al. [187] reported the Ni/Y_2O_3 catalyst prepared by impregnating Ni onto different Y precursors like Y_2O_3, $Y_4O(OH)_9(NO_3)$, and $YO(NO_3)$ for CO_2 methanation. The

MSI of the catalyst was changed because of different Y precursors, in which the $YO(NO_3)$ material supported Ni catalyst showed the moderate metal-support interaction between Ni and Y_2O_3, leading to superior activity for CO_2 methanation and good stability in CO-containing reactants [187]. In conclusion, a moderate metal-support interaction can thus improve the dispersion of Ni, and increase basicity and oxygen vacancies of Ni catalysts, leading then to a better activity and stability in CO_2 methanation.

The morphology of Ni-based catalysts also contributes to the activity and stability of catalysts in CO_2 methanation. Bian et al. [196] prepared the Ni/CeO_2 catalyst with different CeO_2 morphologies and carried it out in low-temperature CO_2 methanation. The Ni/CeO_2 (NR) catalyst with nanorod structure exhibited superior performance than Ni/CeO_2 (NC) catalyst with nanocube structure. This high activity was attributed to the higher Ce^{3+} ratio on the surface of the catalyst. Zhou et al. [192] synthesized the CeO_2 materials by hard-template, soft-template, and precipitation method and used them to prepare Ni/CeO_2 catalysts. It was shown that the hard-template method prepared sample (NCT) showed a well-developed mesoporous structure with the highest SSA. Meanwhile, the soft-template prepared sample (NCS) displayed a disordered structure with a smaller pore diameter. The precipitation method prepared sample (NCP) only showed the nanoparticles with disordered structure. The NCT catalyst performed the highest CO_2 conversion among the studied catalysts in methanation reaction. NCP catalyst showed then lower activity, which could be attributed to the low surface area and poor porosity.

The most intensively used support such as CeO_2 [158,191,196], ZrO_2 [197], SiO_2 [197], Al_2O_3 [198], MgO [191,199], Y_2O_3 [187,198], $Ce_{0.5}Zr_{0.5}O_2$ [200], TiO_2 [147], carbon nanotube [201], zeolite [202], clays [203], SBA-15 [171], SBA-16 [142,204], and hydrotalcite [131,138,144,205–208] were widely reported in the literature. Other transition metal oxide supports such as : Sm_2O_3

[198], ZrO_2 [168], CeO_2 [192], $Ce_xZr_{1-x}O_2$ [209], Y_2O_3[210], have shown superior activity and stability when compared to Al_2O_3 based-catalyst. However, these supports contain VIII group metals which are not abundant and have high cost.

Table 2.6 summarizes the main supports that have been studied intensively in CO_2 methanation. As shown in the table, Ni catalysts supported on different support showed very different performance in CO_2 methanation. As the difference of physicochemical properties for various supports, the physicochemical parameters of Ni catalysts were also deeply changed by the support. Therefore, the activity and selectivity of the catalysts were significantly affected.

Hiroki et al. [198] synthesized the Ni catalysts supported on various supports by conventional incipient wet impregnation method and investigated their performance in CO_2 methanation. The CO_2 conversion comparison at 548 K under atmospheric pressure was displayed in Fig.2.12. The Y_2O_3 supported Ni catalyst showed the highest CO_2 conversion compared to other metal oxide supported Ni catalysts, which could be partly attributed to the effects of basicity and surface intermediates during the reaction that presented on the materials [198]. By FTIR technology, the Ni/Al_2O_3 catalyst proceeded by a CO methanation process. Only carbonates were found on Ni/La_2O_3 catalyst. Meanwhile, the formate species from the carbonates were detected on Ni/Y_2O_3 catalyst.

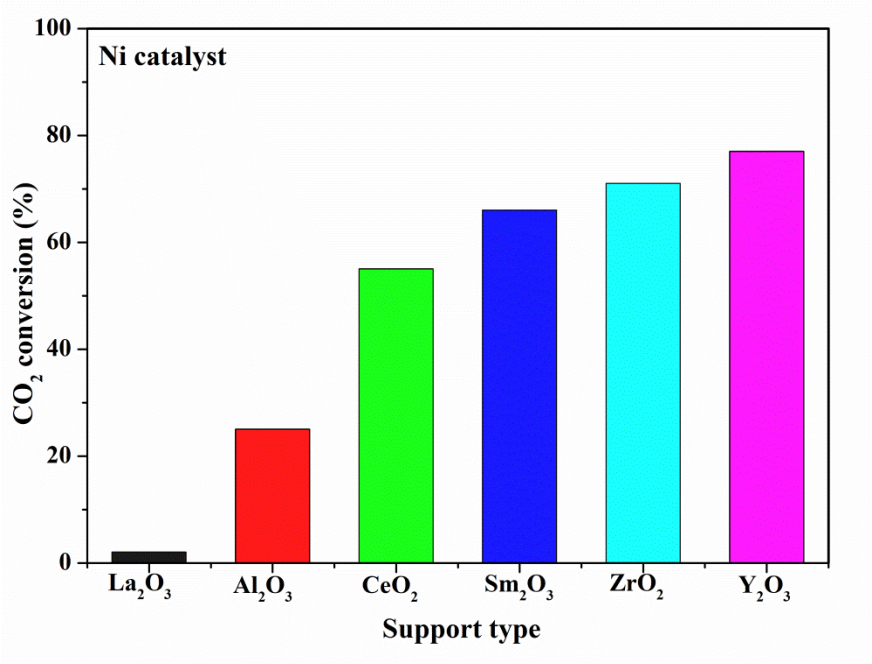

Figure. 2.12. Comparison of CO_2 conversion for Ni catalysts supported on different metal oxides; Condition: 548 K, atmospheric pressure, WHSV= 20,000 $kg^{-1}h^{-1}$.

The CeO_2 supported Ni catalysts reported in other literature exhibits superior activity and stability due to their effects of morphology and oxygen mobility property [196]. Furthermore, the ZrO_2 and $Ce_{0.5}Zr_{0.5}O_2$ also showed good activity because they also had oxygen storage capability. Jia et al. [136] prepared the Ni/ZrO_2 catalyst by plasma decomposition of Ni precursor and compared its activity to that of Ni Ni/ZrO_2 catalyst obtained by a conventional thermal decomposition. It was revealed that the plasma decomposition derived catalyst higher Ni dispersion, high concentration of Ni(111) plane, and stronger coordination between Ni and interfacial sites, leading to a fast H_2 dissociation and more oxygen vacancies, thus a higher activity was obtained compared to the thermally processed catalyst. Also, the mechanism in methanation was different regarding different catalysts; the plasma processed catalyst experienced a carbon oxide hydrogenation route while the thermally processed catalyst had a formate hydrogenation pathway. Regarding

$Ni/Ce_xZr_yO_2$ catalyst, it also proceeds through the formate species originated from carbonate hydrogenation with the CO species as a by-product [211].

Ordered mesoporous silica such as SBA-15/16 can also be potential thanks to their high surface area and confinement of porous structure, making it possible to obtain small nanoparticles of Ni. The Ni nanoparticles over Ni/SBA-16 catalyst can reach 4.3 nm with a high surface area [142]. With the incorporation of Ce, good activity and stability can be obtained over the Ni/Ce/SBA-16 catalyst.

The hydrotalcite-derived mixed oxides catalysts also attracted attention because they not only generate small particles of active metals but also maintain high stability in the high-temperature range. For instance, the low loading of yttrium doped hydrotalcite derived Ni catalyst reached a CO_2 conversion of 81% at 523 K under atmosphere pressure [144]. Its higher performance was attributed to the strong metal-support interaction, the high ratio of medium basic sites, and the small Ni particle size.

Other novel materials were also applied as Ni-based catalysts for methanation. Thus, metal-organic framework (MOF) materials were used as support to prepare catalysts due to their high surface area of more than 1,000 $m^2 \bullet g^{-1}$. Lin et al. [212] synthesized the Ni@C (designated name by author) catalyst from MOF-derived hierarchical hollow spheres and used it in CO_2 methanation. The as-prepared catalyst possessed a high surface area and rich isolated active sites. The methanation test showed that the catalyst achieved a CO_2 conversion of 100% and CH_4 selectivity of 99.9% at 598 K under atmospheric pressure and it also exhibited good stability at 523 K.

In conclusion, the activity, selectivity, and stability of the Ni catalysts deeply depended on the properties of the support. Thus, the basicity, porosity, and redox property of the support can

substantially influence the methanation reaction. For example, over hydrotalcite-derived Ni catalysts, a linear correlation was found between the basicity of the catalysts and CO_2 activity in methanation [131].

Table 2.6 Catalytic performance of the Ni catalysts supported on different materials for CO_2 methanation.

Material	Ni content (wt.%)	Preparation method*	Reaction condition			CO_2 conversion (%)	CH_4 selectivity (%)	Ref.
			Temperature (°C)	H_2/CO_2 ratio	GHSV/ WHSV			
γ-Al_2O_3	10	WI	300	4	5700 h^{-1}	82	99	[213]
Mesoporous γ-Al_2O_3	15	WI	300	3.5	9000 $mL/g_{cat}·h$	46	99	[185]
Mesoporous γ-Al_2O_3	20	WI	300	3.5	9000 $mL/g_{cat}·h$	73	99	[185]
Mesoporous γ-Al_2O_3	25	WI	300	3.5	9000 $mL/g_{cat}·h$	63	98	[185]
No support	100	WI	400	5	52,300 h^{-1}	44	58	[214]
Al_2O_3	125	WI	400	5	52,300 h^{-1}	42	81	[214]
Al_2O_3	16	WI	500	5	52,300 h^{-1}	75	100	[214]
Al_2O_3	39	WI	500	5	52,300 h^{-1}	81	93	[214]
MgO	5.8	sonochemical	400	8	47,760 h^{-1}	85	98	[215]
MgO	5.8	co-precipitation	400	8	47,760 h^{-1}	63	-	[215]

MgO	5.8	solution combustion	400	8	47,760 h^{-1}	71	-	[215]
TiO_2	10	WI	350	4	60,000 h^{-1}	42	74	[216]
TiO_2	10	DBD-plasma	350	4	60,000 h^{-1}	60	98	[216]
TiO_2	6.17	DBD-plasma-rinse	350	4	60,000 h^{-1}	72	99	[216]
SiO_2	5	WI	350	4	60,000 $mL/g_{cat}·h$	48	94	[217]
SiO_2	10	WI	350	4	60,000 $mL/g_{cat}·h$	53	95	[217]
SiO_2	15	WI	350	4	60,000 $mL/g_{cat}·h$	54	95	[217]
La_2O_3	50	CSCM	400	4	120,000 $mL/g_{cat}·h$	60	88	[218]
ZrO_2	10	WI	350	4	60,000 $mL/g_{cat}·h$	66	97	[136]
ZrO_2	8.68	DBD-plasma	350	4	60,000 $mL/g_{cat}·h$	77	99	[136]
CeO_2	10	WI-CP	340	4	45,000 $mL/g_{cat}·h$	67	100	[192]
CeO_2	10	WI-HTM	340	4	45,000 $mL/g_{cat}·h$	90	100	[192]
Ce-Zr	10	WI	300	4	20,000 $mL/g_{cat}·h$	48	99	[219]
SBA-15	15	OP	420	4	10,000 $mL/g_{cat}·h$	75	99	[171]
SBA-15	15	WI	420	4	10,000 $mL/g_{cat}·h$	68	99	[171]
MCM-41	20	precipitation	420	4	9,000 $mL/g_{cat}·h$	72	98	[220]
SBA-16	10	WI	400	4	12,000 h^{-1}	73	98	[142]
USY	15	WI	400	4	43000 $mL/g_{cat}·h$	68	93	[221]

hydrotalcite	20	precipitation	300	4	12,000 h^{-1}	87	99	[144]

*WI-wet impregnation; DBD-plasma-rinse: rinse after dielectric barrier discharge (DBD) plasma decomposition; CSCM: colloidal solution combustion method; WI-CP: Support prepared by precipitation method with the catalyst prepared by wet impregnation; WI-HTM: HTM-KIT-6 hard template method for support, wet impregnation for catalyst; OP: one-pot hydrothermal method

C) On the effect of the promotion on the performance of Ni-based catalysts in methanation reaction

It is well reported that Ni catalysts without additives suffered from low CH_4 selectivity, poor stability, and deactivation problems due to the metal sintering at high temperatures [222]. Thus, promoter elements such as: Mg [179], La [169,208,223], Ce [142,224,225], Zr [226], Y [141,227], Co [228,229], Fe [203,229] and Cu [215,229] etc. had been applied to improve the performance of Ni catalysts. The Ni/Al_2O_3, as a commonly studied catalyst in CO_2 methanation due to its economic advantage, was doped by CeO_2, La_2O_3, Sm_2O_3, Y_2O_3, and ZrO_2. The catalytic performance of the synthesized catalysts was investigated by a series of technologies [230]. It was found that the addition of these promoters had a positive effect on the performance of the Ni/Al_2O_3 catalyst, and the La-promoted catalyst showing the best activity and stability. At 573 K, the CO_2 conversion decreased as the following sequence: NiLa>NiCe>NiSm>NiY>NiZr>Ni/Al_2O_3. The authors attributed these results to the improvement of nickel reducibility, nickel dispersion, and the presence of moderate basic sites. The La additive is a very promising promoter for $Ni/\gamma\text{-}Al_2O_3$ catalysts in CO_2 methanation. Furthermore, the effect of La content on the performance of Ni/La-$\gamma\text{-}Al_2O_3$ catalysts for CO_2 methanation was also studied, in which the 14 wt.% La-doped Ni/La-$\gamma\text{-}Al_2O_3$ catalyst showed the best performance with nearly 100% of CH_4 selectivity at low

temperature [231]. This latter result was assigned to the enhanced basicity of La-γ-Al_2O_3 support and the reducibility of NiO. The presence of La also showed a good improvement in CO_2 methanation for the Ni/SBA-15 catalyst, which was also a widely investigated catalytic system [169]. The perovskite structure of $LaNiO_3$ was formed on Ni-La_2O_3/SBA-15(C) catalyst prepared by citrate complex method, leading to the enhanced interaction between La_2O_3 and Ni. Thus, high dispersion of Ni and small Ni particles (less than 5 nm) were obtained. In CO_2 methanation, the Ni-La_2O_3/SBA-15(C) catalyst showed a high CO_2 conversion of 90.7% and CH_4 selectivity of 99.5% at 593 K [169]. The La-modified mesostructured cellular foam (MCF) supported Ni catalyst with phyllosilicate structure also showed a good performance in CO_2 methanation as reported in a new study [223]. This is attributed to the small Ni particle size, high capacity of H_2 and CO_2 adsorption, and low activation energy.

In Table 2.7, the Ni catalysts supported on different materials doped by various promoters for CO_2 methanation were summarized. As shown in Table 2.7, the adding of the promoter can cause a significant effect on the physicochemical properties of the Ni catalysts. The parameters like dispersion of Ni, the reducibility of Ni, the basicity of catalyst, metal-support interaction, oxygen vacancies, anti-sintering of Ni particles, etc. have been changed by the promoters. Thus, the activity, selectivity, and stability of catalysts were affected significantly.

Table 2.7 Ni catalysts promoted by different additives reported in the literature.

Catalyst	Promoter	Loading (wt.%)	Ni (wt.%)	Effect of promoter addition	Ref.
NiUSY	Ce	15	5	A large number of carbonates, promoting CO_2 conversion to CO.	[225]
Ni/SBA-16		10	10	Increased Ce^{3+} ratio and oxygen vacancies, enhanced moderate basicity	[142]

Ni/γ-Al_2O_3		15	15	Increased metal-support interaction, medium basic sites, and adsorbed CO_2. More Ni metal species and oxygen defects on the surface	[232]
Ni/MCM-41	Zr	n_{Zr}/n_{Si}=0.01, 0.03, 0.1, 0.15	10	Strengthened Ni-Zr interaction which favored the spillover of H, increased surface oxygen species. 0.01 is the best Zr content, which showed the best performance	[233]
Ni/CeO_2	Y	2	5	The decreased particle size of CeO_2, increased specific surface area and the number of oxygen vacancies, enhanced metal-support interaction, promoted the formation of CeO_2 nanorods.	[141]
Ni/SBA-15	Mg	5	10	Increased medium basic sites and promoted the formation of monodentate formate.	[179]
Ni/Al@Al_2O_3	K	0.5	10	Decreased activity was attributed to decreased amount of Ni active sites and basic sites.	[234]
Ni-Al ordered mesoporous composite	Ca	N_{Ca}/n_{Al}=1, 3,5,8,10	n_{Ni}/n_{Al} =10	Enhanced surface basicity and decreased active energy.	[235]
Ni/SiO_2	La	10	10	Better dispersion of Ni and a higher proportion of moderate strength basic sites.	[236]
Ni/SiO_2	Cu	1	10	Increased CO selectivity indicates favoring the RWGS reaction. Slightly increased the resistance of metal sintering	[217]
Ni/Zr-clay	Co	1	15	Promoted the dispersion of NiO nanoparticles, increased quantity of the reduced active nickel species.	[203]
Ni-MgO		2	4.3	Decreased active energy, more active sites.	[215]
Ni/Zr-clay	Fe	1	15	Increased dispersion of Ni, increased Ni reducibility	[203]
Ni/(Mg, Al)O_x hydrotalcite		1.2-18	12	Increased Ni nanoparticle size, decreased Ni dispersion, enhanced CO dissociation, and basicity.	[237]
Ni-Al		10	44	The formation of a Ni-Fe alloy increased the thermal stability of catalysts.	[238]
Ni-Al	Mn	10	44	A higher density of medium basic sites and an enhanced CO_2 adsorption capacity.	[238]
Ni/bentonite	V	3,5,8	20	Enhanced H_2 uptake and Ni dispersion, promoted the dissociation ability of CO.	[239]

Besides the aforementioned catalytic systems, Lathanum was also used to improve the activity of hydrotalcite-derived Ni catalysts (HTN) in CO_2 methanation [206,208]. It was found that the 2 wt.% of La-doped HTN catalyst showed the highest CO_2 conversion at low temperature, which could be attributed to the increase of basicity caused by La incorporation. The different methods of promoter incorporation also have a significant effect on the performance of the La-doped HTN catalyst. The catalyst prepared by the ion-exchange method showed both the higher CO_2 conversion and CH_4 selectivity at low temperature (573 K) as well as superior stability. This remarkable activity was attributed to the increase of medium basic sites and the presence of smaller Ni crystal size [206].

Ceria (cerium oxide) is also known to be an important additive for Ni-based catalysts in various CO_2 utilization reactions [142,232]. As for Ni/Al_2O_3 catalyst, it has been reported that the adding of Ce on Ni/Al_2O_3 catalyst can significantly promote the activity and CH_4 selectivity in methanation. The optimum promotion was found with 15 wt.% of CeO_2. This catalyst showed the best CO_2 conversion and high CH_4 selectivity at the temperature range from 523 to 673 K. In such catalysts, the presence of ceria promoted the higher dispersion of Ni, the smaller Ni particle size, the higher amount of medium basic sites, the higher oxygen deficiencies, and finally the higher surface ratio of Ni^0 and Ce^{3+}, all which contribute to a better activity and stability of the catalyst. Also, in such catalyst, the Ce^{4+} cation can be reduced to Ce^{3+} state under the pre-treatment of hydrogen, leading to the formation of oxygen vacancies, which can then lead to a promotion of the adsorption and dissociation of CO_2 species [141]. Due to the unique redox and oxygen deficiency properties, the ceria is widely used as a promoter in the preparation of Ni catalysts.

In the literature, the Ce doped Ni/SBA-16 catalysts were prepared and their catalytic performance was evaluated in CO_2 methanation [142]. The results indicated that the presence of Ce led to the formation of oxygen vacancies, which could significantly promote the CH_4 selectivity. The

mesoporous SBA-16 can disperse the Ni and Ce species well and confine the Ni and Ce particles inside the mesoporous channels. The highest ratio of Ce^{3+}, highest amount of medium basic sites, and good dispersion of Ce have been obtained over 10 wt.% Ce-doped Ni/SBA-16 catalyst, leading to the best activity and high CH_4 selectivity.

Zirconia or zirconium oxide also can act as the oxygen storage material and has been intensively studied in many CO_2 utilization reactions [226,233]. Yang et al. [233] studied the effect of Zr on MCM-41 supported Ni catalyst for CO_2 methanation. It was found that the adding of Zr strengthened interaction between Ni and Zr, leading to the spillover of H species adsorbed on the surface of Ni to the support, which is favorable for the hydrogenation of CO_2-derived intermediates [233]. Also, the addition of Zr promoted the increase of oxygen species at the surface, and the decrease of strong basicity, which contribute to hinder the carbon deposition and the removal of deposited coke under reaction. However, an excess Zr on the support would be harmful to the activity of the catalyst due to the destruction of the ordered structure of the support.

The alkaline earth like Mg can also be a good additive alternative for Ni catalyst [179,240]. Plaifa et al. [179] Ni-Mg phyllosilicate mesoporous SBA-15 catalysts with different Mg loading by ammonia evaporation method and applied them in CO_2 methanation reaction. It was found that the presence of Mg of 5 wt.% onto Ni/SBA-15 catalyst could improve the increase of medium basic sites, which enhanced the methanation activity at low temperature. Also, the phyllosilicate structure could enhance the metal-support interaction, which suppressed the metal sintering, leading to good stability of the catalysts. The other alkaline earth metal oxides like Ca, Sr, and Ba were also studied for Ni catalysts [240]. The incorporation of alkaline earth on Ni/CeO_2 catalysts can promote the dispersion of Ni, an increase of moderate basic sites, and more oxygen deficiencies of the catalyst, thus improve the activity of the catalysts. The activity test showed that

the Ca doped Ni/CeO_2 catalyst performed the best activity due to the highest Ni dispersion and largest moderate basicity. Besides the promotion of individual additives, the addition of two additives like Ce-Zr is also widely studied for Ni catalyst, which shows good modification [241]. Thus, the addition of Ce-Zr solid solution on activated carbon (AC) supported Ni catalyst can result in stronger interaction between Ni and Ce-Zr, higher dispersion of Ni, and high CO_2 adsorption ability, leading to high CO_2 conversion and CH_4 selectivity [241]. Li et al. [242] studied the effect of ceria promotion on the performance of Ni-La/ZrO_2 catalyst in CO_2 methanation. The results revealed that the Ni-Ce-La/ZrO_2 catalyst showed better activity and high stability than the Ce or La modified Ni/ZrO_2 and the non-modified Ni/ZrO_2 catalyst. The adding of Ce on Ni-La/ZrO_2 catalyst could promote the activation of CO_2 and the Ni nanoparticles of Ni-Ce-La/ZrO_2 catalyst had a high resistance to metal sintering.

The additives with more than two metal oxides also had attracted intensive attention. The Ni catalysts supported on γ-Al_2O_3 based on composite oxide were employed in CO_2 methanation [243]. The γ-Al_2O_3–ZrO_2–TiO_2–CeO_2 (equivalent loading for the additive, 15%) composite oxide supported Ni catalyst possessed higher Ni dispersion and better reducibility, leading to higher activity compared to that of Ni/γ-Al_2O_3 catalyst.

2.5.4.2.2. Other non-noble metal-based catalysts for CO_2 methanation

Besides Ni catalyst, Iron (Fe) [121] and cobalt (Co) [29,244–246] catalysts were also studied in CO_2 methanation. Zeynep et al. [121] studied Fe catalyst promoted by different additives in CO_2 methanation. It was found that the bare Fe catalysts showed very poor activity and CH_4 selectivity and the Fe catalysts doped by promoters did not perform a comparable activity and CH_4 selectivity as a comparison to Ni-based catalyst. Among the promoters, the Mg of 2 wt.% modified Fe catalyst

exhibited the best positive effect. At a harsh condition (8 bar), the highest CH_4 yield reached 32% at 673 K for $2Mg/Fe_2O_3$ sample.

Co-based catalysts can exhibit comparable activity in comparison to Ni ones in CO_2 methanation. Liang et al. [123] investigated alumina-supported Ni and Co catalysts in CO_2 methanation. It was found that the Co/Al_2O_3 catalyst showed higher activity than that of Ni/Al_2O_3. This is attributed to the better coordination effect between Co and alumina when compared to Ni on Al_2O_3. This coordination effect can promote the hydrogenation of intermediates such as bicarbonate, formate, and carbonate species. The CO_2 can be activated on the surface of Co metal and subsequently mitigate and react with the hydroxyl in the alumina to form the intermediates. Such intermediates can be hydrogenated to methane over cobalt sites. Also, ZrO_2 supported cobalt catalysts were also employed to catalyze the CO_2 methanation reaction. It was reported that the Co/ZrO_2 catalysts prepared by the organic acid-assisted impregnation method could exhibit superior activity compared to the catalyst prepared without organic acid [127]. Within these organic acids, carboxylic acids with a longer chain containing more carboxyl and hydroxyl groups showed good improvement for the catalytic performance of Co/ZrO_2 catalysts as compared to the convention method prepared catalyst. Meanwhile, the amino acid could change the charge properties of the surface of ZrO_2 by changing the pH and increase the Co dispersion, thus exhibited better performance than the conventional one. In all the organic acids, the Co/ZrO_2 catalysts derived from the citric acid-assisted impregnation exhibited the best activity and the highest TOF value with a CO_2 conversion of 85% and a CH_4 selectivity of 99% as well as TOF of 1116 h^{-1} at 673 K and 30 bars. This high activity was attributed to the improved Co dispersion and enhanced Co-ZrO_2 interaction, resulting in more oxygen vacancies and high CO_2 adsorption capacity. The Co-based

catalysts prepared by the liquid reduction method can even reach high activity that is comparable to the noble metal-based catalysts at low temperature (<473 K) recently in the literature [126].

Apart from being a catalyst itself, cobalt can also play an important role as a promoter in improving the performance of the Ni-based catalysts. Liu et al. [228] reported that the addition of Co could improve the activity of ordered mesoporous Ni-Co/Al_2O_3 catalyst, which was attributed to the enhanced H_2 sorption capacity. Also, the ordered mesoporous structure contributed to achieving high stability. In conclusion, the Co-based catalysts can exhibit good performance in CO_2 methanation. However, Ni-based ones remained the most promising.

2.5.6 Power-to-gas system (PtG)

The flow chart of the PtG project was shown in Fig.2.13. The electricity from the renewable energy power plant or conventional power plant was used to electrolyze water to produce H_2. The captured CO_2 reacted with H_2 to produce CH_4. Then, CH_4 was transported and used as fuel or raw material. The PtG process can act as an important energy storage route. Compared to existing storage ways, the PtG route has a longer discharge time as shown in Fig.2.14.

The main energy consumption parts of the PtG route are the electrolysis part and the methanation part. For the electrolysis, it can be improved by applying a new electrolytic method like the solid oxides method. The methanation process can be promoted by controlling the reaction parameters and applying high-performance catalysts.

The development of novel CO_2 methanation catalysts is then the main topic of this thesis.

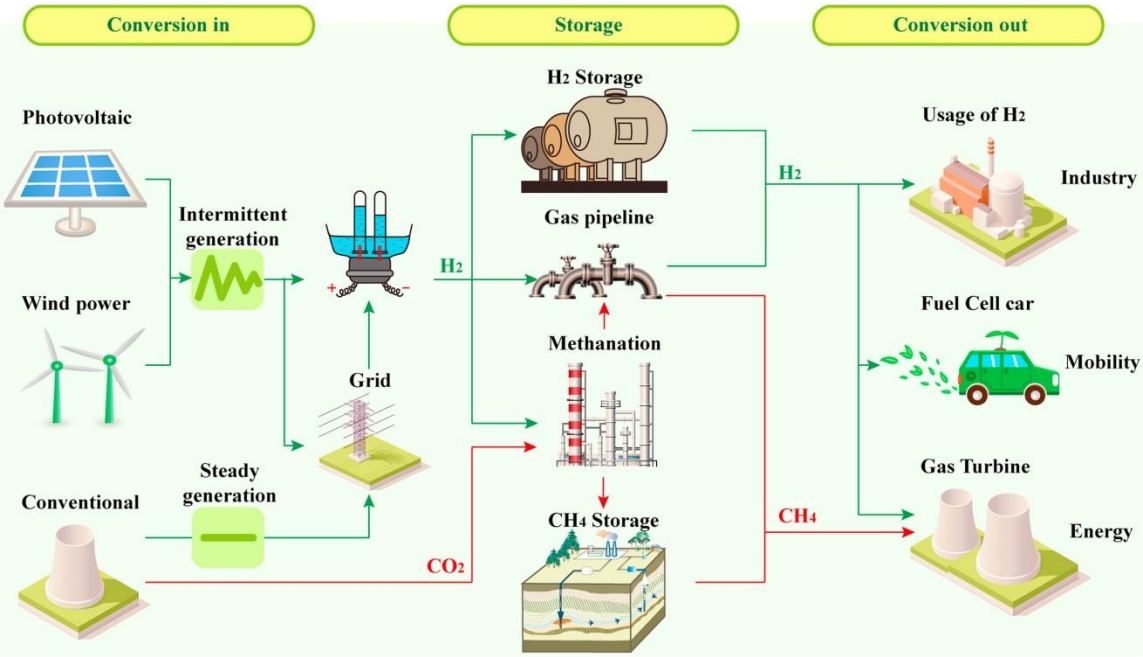

Figure 2.13. PtG technology flow chart; Adapted from [247]

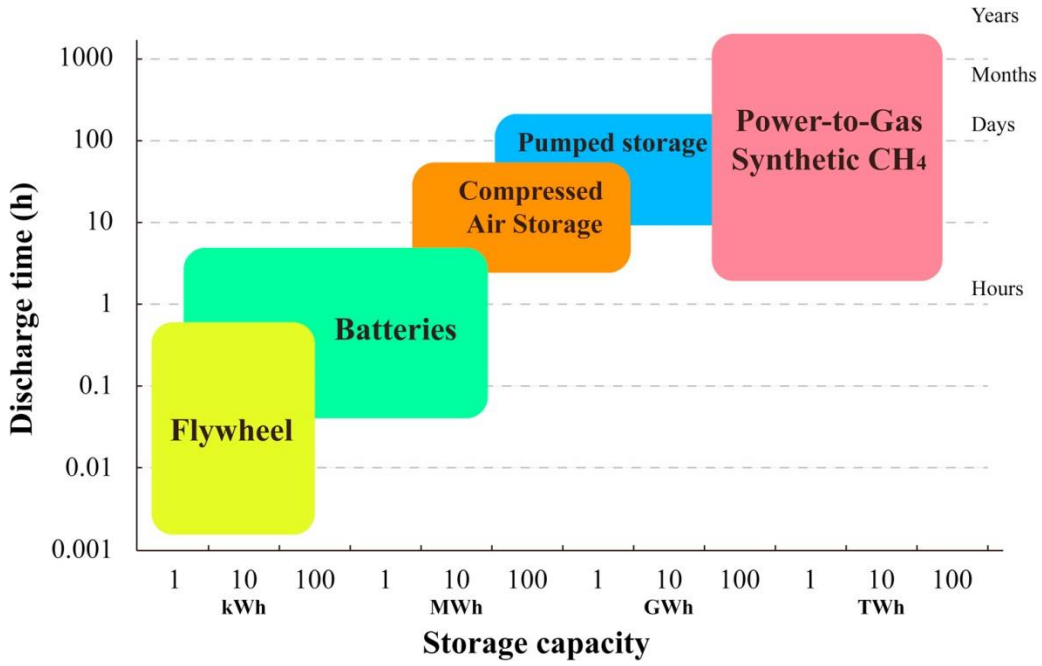

Figure 2.14. Storage routes for excess energy with the relationship between discharge time and storage capacity.

Adapted from [247].

2.5.6.1. The PtG projects in European Union

Table 2.8 lists some PtG projects in Europe, which use chemical/biological conversion systems. The European Union (EU) has the most PtG plants in the world now.

Table 2.8 Power-to-Methane plants in European Union. Adapted and modified from [248]

Installation	Methanation principle	Power [kW]	*Electrolysis	Status (Spring 2021)
Etogas - Audi AG	Chemical	6300	Alkaline	Operational
Solothurn (Store&Go project)	Biological	700	PEM	Planned
Niederaussem	Chemical	300	PEM	Finished
Foulum - Electrochaea	Biological	250	PEM	Finished
Alzey - Exytron (Exytron GmbH)	Unknown	63	Alkaline	Planned
Rostock – Exytron Demonstrations	Unknown	twenty one	Unkown	Operational
Stralsund (University of Applied Sciences Stralsund)	Unknown	20	Alkaline	Planned
Rozenburg	Chemical	10	PEM	Operational

*PEM – Polymer electrolyte membrane electrolysis.

2.5.6.2. Non- European Union: The example of China

As shown in Fig.2.15, the top 6 countries which have the highest renewable energy power generation capacities in the world were displayed. It can be seen that China has the biggest renewable energy power generation capacities. Although the biggest share of renewable energy, there are relatively few PtG (CH_4) demonstration plants in China. Until now, there is only one PtG (H_2) plant located in the province of Hebei, which uses surplus wind energy to produce hydrogen.

Even in EU, the most plants are located in Germany. However, given the ecological and economic benefits of the PtG route, there are plenty of potentials of such route in the storage of renewable energy. For example, wind and solar energy abandonment have been serious in China, which PtG technology can help to alleviate this situation. Moreover, if the carbon tax is considered in the future, policy factors and economic factors will be very beneficial to the development of PtG [247]. With the rapid development of renewable energy, the PtG process will be necessary to solve the storage problem.

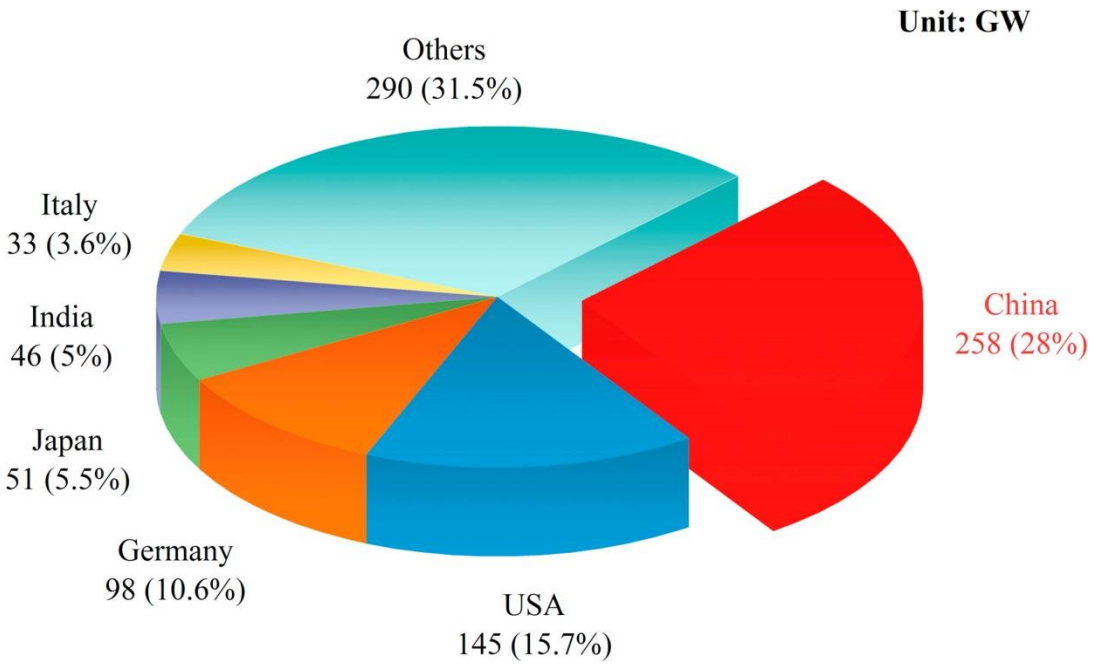

Figure 2.15. Renewable energy power generation capacities distribution in the world in 2016; adapted from [247]

Chapter III

Experimental part

3. Experimental part

3.1 Catalyst preparation

In this thesis, different catalysts were prepared by different synthesis strategies as shown in Fig.3.1.

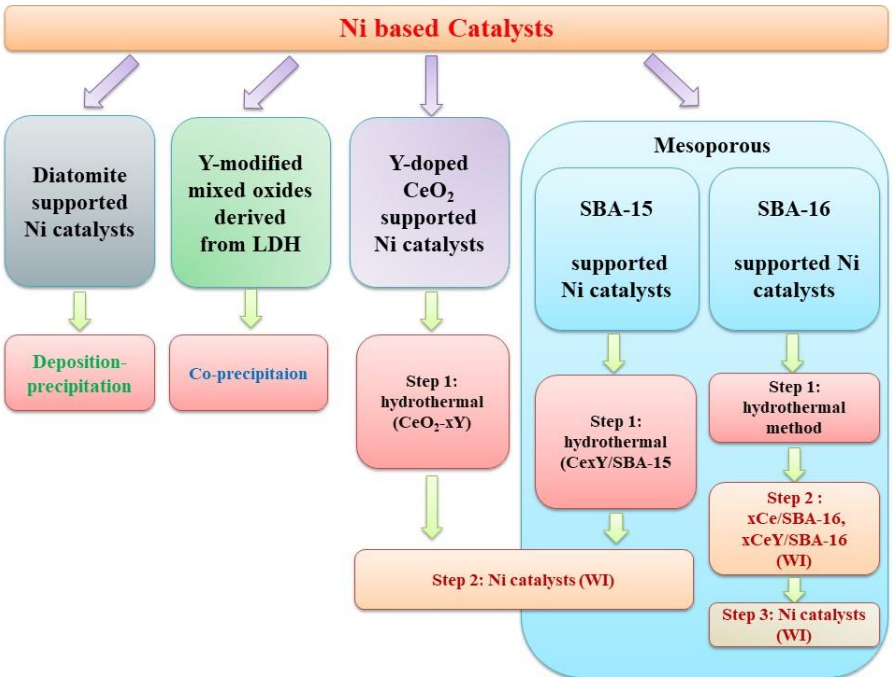

Figure 3.1. Syntheses strategies of the Ni catalysts in the thesis.

Thus, depending on the synthesized catalyst we used deposition-precipitation, co-precipitation, hydrothermal synthesis, wet impregnation, etc.

3.1.1 Low-cost diatomite supported catalysts

This work was carried out during collaboration with the University of Belgrade. The preparation of support and catalysts was thus carried out in Serbia [249]. Crude diatomite material was supplied from Prilep (The Republic of North Macedonia). The crude material was mechanically, chemically,

and thermally treated to obtain the desired support properties. The supported Ni-Mg catalysts were prepared using the precipitation-deposition (PD) method.

Precipitation of Ni and Mg species was performed by addition of anhydrous Na_2CO_3 to a salt solution containing $Ni(SO_3NH_2)_2$, $Ni(NO_3)_2$, or $Ni(CH_3COO)_2$, and $Mg(NO_3)_2$ in a molar ratio of Ni/Mg=10. The resulting suspension was vigorously stirred and heated up to 90°C. The deposition of formed Ni-precipitates onto diatomite support (D) was carried out by the addition of hot (90°C) aqueous suspension of D to a slurry containing precipitates of Ni and Mg in molar ratio SiO_2:Ni =1. The obtained suspension was aged again for 1 h under the same temperature after which it was vacuum filtered and thoroughly washed with hot (80°C) distilled water until neutral pH. Finally, the precipitates were dried in an air oven at 110 °C for 24 h and grounded to powder. After that, the samples were calcined at 550°C for 5 h. The same preparation procedure was employed for all the samples. The samples were designated as the NiMg/D-X (X=S-sulfamate, N-nitrate, or A-acetate) according to the kinds of nickel salts. The Ni content (weight percent) of the samples determined by the ICP-OES method for NiMg/D-S, NiMg/D-N, and NiMg/D-A were 35.0 wt.%, 36.3 wt. % and 36.6 wt. %, respectively.

3.1.2 Mixed oxides derived from layered-double hydrotalcite (LDH) materials

The co-precipitation method with sodium carbonate (Na_2CO_3) was carried out for the mixed oxides catalysts preparation based on the report [250]. The mixed oxides doped by different loading of yttrium were prepared. In detail, an aqueous solution of the following nitrates was used: Ni, Y, Al, and Mg, and added dropwise into Na_2CO_3 solution. NaOH (2 M) was also dripped into the mixture to adjust pH to 10±0.2. The ratio of M^{2+}/M^{3+} was assumed as 3. The assumed loading of yttrium

was 0.4 wt.%, 2.0 wt.% or 4.0 wt.%. After co-precipitation, the suspension was left to react at 65 ºC for 24 h. Then, this mixture was filtered under vacuum and washed with distilled water thoroughly. After filtration, the obtained cake was dried at 80 °C overnight and calcined in static air at 550 °C for 5 h with a heating rate of 5 °C/min. The samples were designated as MO-0Y, MO-0.4Y, MO-2.0Y, and MO-4.0Y. This work was done in the framework in collaboration with the AGH University.

3.1.3 Y-promoted novel ceria supported Ni catalysts

The catalysts were synthesized by a two steps method. First, CeO_2, Y_2O_3, and yttrium-promoted CeO_2 (denoted as CeO_2-YX%) supports were prepared by the hydrothermal method. In a typical procedure, 6 g of cerium nitrate, $Ce(NO_3)_3 \cdot 6H_2O$ (Aldrich, 99%) and an appropriate amount of yttrium nitrate hexahydrate, $Y(NO_3)_3 \cdot 6H_2O$, (Aldrich, 99%)were dissolved in 30 mL of H_2O, then, 40 mL of NaOH (2.5 mol L^{-1}; Aldrich, >98%) were added to the solution under vigorous stirring. The resulting suspension was rapidly transferred into a 100 mL Teflon autoclave and heated in an oven at 120 °C for 24 h. After aging, the obtained precipitate was filtered and washed with deionized water until neutral pH. The resulting powder was dried at 80 °C overnight and calcined at 550 °C for 5 h in static air with a heating rate of 2 °C/min. The Y loadings with respect to CeO_2 are 0.5, 1.0, 2.0, 5.0 weight percent, respectively. CeO_2 and Y_2O_3 pure oxides were prepared by the same method, starting from $Ce(NO_3)_3 \cdot 6H_2O$ (Aldrich, 99%) or $Y(NO_3)_3 \cdot 6H_2O$ precursors.

The nickel catalysts were synthesized by the wetness impregnation method of the so prepared supports with an aqueous solution of $Ni(NO_3)_2 \cdot 6H_2O$. After the impregnation process, the solids were dried at 100 °C overnight and calcined at 550 °C for 5 h with a heating rate of 2 °C/min. The

nickel loading for all the samples is 5 wt.%. The resulting catalysts were labeled according to the weight loading of Ni and Y, i.e., 5Ni/CeO_2, 5Ni/Y_2O_3, 5Ni/CeO_2-Y0.5%, 5Ni/CeO_2-Y1.0%, 5Ni/CeO_2-Y2.0%, and 5Ni/CeO_2-Y5.0%. The samples were synthesized in the framework of collaboration with Prof. Liotta from CNR Italy.

3.1.4 Ordered mesoporous SBA-15 and SBA-16 materials supported catalysts

The mesoporous materials including SBA-15 and SBA-16 were prepared by hydrothermal method using Teflon bottler or a PTFE lined stainless steel hydrothermal autoclave as shown in Annex 2.

SBA-15. Thus, SBA-15 was synthesized by the hydrothermal synthesis method as described by Han et al. [251]. In brief, Pluronic P123 (PEG-PPG-PEG, average molar weight=5800 g/mol, BASF) was dissolved in distilled water and the pH value of the aqueous solution was adjusted by adding HCl (37%, Sigma-Aldrich). After mixing thoroughly (45 min), TEOS (Tetraethyl orthosilicate, 98%, Sigma-Aldrich) was added dropwise to the above-mentioned solution and then stirred magnetically at 40 °C for 24 h. The molar ratio of the reaction mixture was controlled as TEOS/P123/HCl/H_2O=1/0.0168/5.8/155. The resulting mixture was aged at 65°C for 120 h. Then, the precipitate was filtered and washed with distilled water followed by drying in an oven at 110°C for 12 h. The obtained solids were calcined at 550 °C for 5 h in flow air (20 ml/min) with a heating rate of 1 °C/min.

3.1.4.1. Synthesis of NiY/SBA-15 and NiCexY/SBA-15 catalysts

Ni/SBA-15 catalysts doped by Y were prepared by a co-impregnation method in the presence of the surfactant cetyltrimethylammonium bromide (CTAB). The Y content (x) was controlled as 5, 10, and 20 wt.% relative to SBA-15 support. The Ni content was chosen as 15 wt.% for all samples. Typically, a certain quality of nickel nitrate ($Ni(NO_3)_2 \cdot 6H_2O$, >99%, Sigma-Aldrich), yttrium nitrate ($Y(NO_3)_3 \cdot 6H_2O$, >99%, Sigma-Aldrich), and CTAB (>99%, Sigma-Aldrich) were dissolved in distilled water and magnetically stirring for 30 min. Subsequently, the SBA-15 powder was added to the prepared solution and the magnetic stirring was maintained for 12h at ambient temperature. The CTAB/Ni molar ratio was controlled at 0.3. Afterward, the obtained slurry was evaporated in a rotary evaporator (60°C, 110r/min). After that, the material was dried in an oven at 100 °C for 12h and calcined at 550 °C under flow air for 5h with a heating rate of 5 °C/min (20 mL/min).

NiCe/SBA-15 catalysts modified with Y were prepared by the same technique as NiY/SBA-15 with the presence of cerium nitrate ($Ce(NO_3)_3 \cdot 6H_2O$, >99%, Sigma-Aldrich). The yttrium content (x) in the NiCexY/SBA-15 catalysts varied from 2 to 10 wt.%, whereas a fixed amount of Ni (15 wt.%) and Ce (10 wt.%) was adjusted. The as-prepared catalysts were labeled as 15Ni10Ce/SBA-15 and 15Ni10CexY/SBA-15 (x= 2, 4, 10).

3.1.4.2. Synthesis of SBA-16 supports

SBA-16 materials were synthesized based on an improved method presented elsewhere [252]. Typically, 3 g of Pluronic F127 ($EO_{106}PO_{70}EO_{106}$) copolymer (BASF) was dissolved with 144 g of distilled water in a Teflon bottle followed by adding 5.94 g of concentrated hydrochloric acid (HCl, 37 wt.%, Sigma Aldrich). After stirring for 20-30 min, 9 g of butanol-1 (BuOH, Sigma

Aldrich) was added into the aforementioned solution as a co-surfactant. The molar ratio of F127/BuOH was controlled as 1/3. After stirring for 1 h, 14.2 g of tetraethyl orthosilicate (TEOS, Sigma Aldrich) was added into the solution above at 40 °C, then the mixture was kept at 40 °C for 24 h. Afterward, the container of the solution was placed under a static condition (electrical oven) at 80 °C for 48 h for the hydrothermal process. After that, the mixture was filtered and washed by distilled water thoroughly. Subsequently, the precipitant was dried at 100 °C for 12 h. Finally, the solid was calcined at 550 °C for 5 h with a heating rate of 5 °C/min under flowing air (20 mL/min) to remove the copolymer template F127.

3.1.4.3. Ni/xCe/SBA-16 catalysts preparation

Ni/SBA-16 and Ce-promoted Ni/Ce/SBA-16 catalysts with different Ce content were prepared by a two-step incipient wetness impregnation method assisted by ultrasonic considering its advantages compared to the co-impregnation method [253]. As reported in the literature, the Ni-Ce/SBA-15 catalyst prepared by impregnating of Ce then by Ni presented smaller NiO particles and porosity compared with the co-impregnated catalyst and the catalyst impregnated first by Ni [254]. In the current work, cerium nitrate ($Ce(NO_3)_3 \cdot 6H_2O$, >99%, Sigma-Aldrich) was dissolved in distilled water, and then the SBA-16 support was added into the solution. The suspension was processed by ultrasonic for 1 h, after that, the mixture was placed at ambient temperature for 24 h to optimize the diffusion of ions inside the pores of the support. Afterward, the mixture was dried at 80 °C for 12 h. Finally, the material was calcined in an electrical furnace at 550 °C for 5 h with a heating rate of 5 °C/min in airflow (20 mL/min). Eventually, the as-synthesized SBA-16 and Ce/SBA-16 were used to prepared Ni/SBA-16 and Ni/Ce/SBA-16 catalysts. The same

impregnation method was used to prepare the catalyst, with replacing the solvent with ethanol (99%), which showed better performance for supported Ni catalysts relative to H_2O [255]. The content of Ni was 10 wt.% relative to the support. The catalysts were then designated as 10Ni/SBA-16 or 10Ni/xCe/SBA-16, where x represents the content of Ce, varying from 10 to 20 wt.%. All the reagents were purchased from Sigma-Aldrich or BASF (F127).

3.1.4.4. Synthesis of Ni/xCeY/SBA-16 catalysts

The Ni/xCeY/SBA-16 catalysts were prepared by a two steps impregnation method as introduced above. Firstly, the xCeY/SBA-16 materials were prepared by wet impregnation of an aqueous solution of nitrate salts ($Ce(NO_3)_3 \cdot 6H_2O$, $Y(NO_3)_3 \cdot 6H_2O$, >99%, Sigma-Aldrich) on SBA-16. After impregnation, dry, and calcination, the obtained xCeY/SBA-16 samples were impregnated by the ethanol solution of $Ni(NO_3)_2 \cdot 6H_2O$ with/without the presence of citric acid (>99%, Sigma-Aldrich). The final catalyst precursors were obtained after subsequent impregnation, dry, and calcination. The weight content Ce and Ni was 10 wt.% with Y content varying from 2 to 10 wt.%. The samples were denoted as 10Ni/10Ce/SBA-16 and 10Ni/10CexY/SBA-16, respectively. The 10Ni/SBA-16 sample was also prepared by the same process as a reference.

3.2 Catalytic CO_2 methanation

3.2.1 Activity test

The catalytic test was carried out in a fixed-bed reactor (Inner diameter of 10 mm). The catalyst (0.5 mL, density measured by a measuring cylinder of 5 mL) was loaded into the reactor under the

protection of quartz wool. A K-type thermocouple in contact with the catalyst bed was used to monitor the temperature. Before the test, the catalyst was pretreated in a gas mixture of Ar and H_2 (H_2/Ar=5%, vol./vol.) with a flow rate of 100 mL/min for 1 h. After reduction and cooling down to the desired temperature, the activity test was performed from 200 to 450 ℃ in a reactive gas mixture (CO_2/H_2/Ar=60/15/25, 100 mL/min) with a temperature ramp of 10 ℃ per min (Fig.3.2a). At each step, the temperature was kept for 30 min for the steady-state test. The gas/weight hourly space velocity (GHSV/WHSV) is 12, 000 h^{-1} (per hour)/60, 000 g_{cat}^{-1}•h^{-1}(per gram of catalyst per hour). The outlet gases were analyzed by a gas chromatograph equipped with a thermal conductivity detector (TCD) (490 Varian Micro-GC) from Agilent.

The time-on-stream (TOS) test was performed on the same set-up. The feed gas with the same composition was fed into the catalyst after the reduction step. As shown in Fig.3.2b, the isothermal test was carried out at 350 ℃ and kept for 6-7 h.

The design drawing and the assembled real profile of the set-up were shown in Fig.3.3.

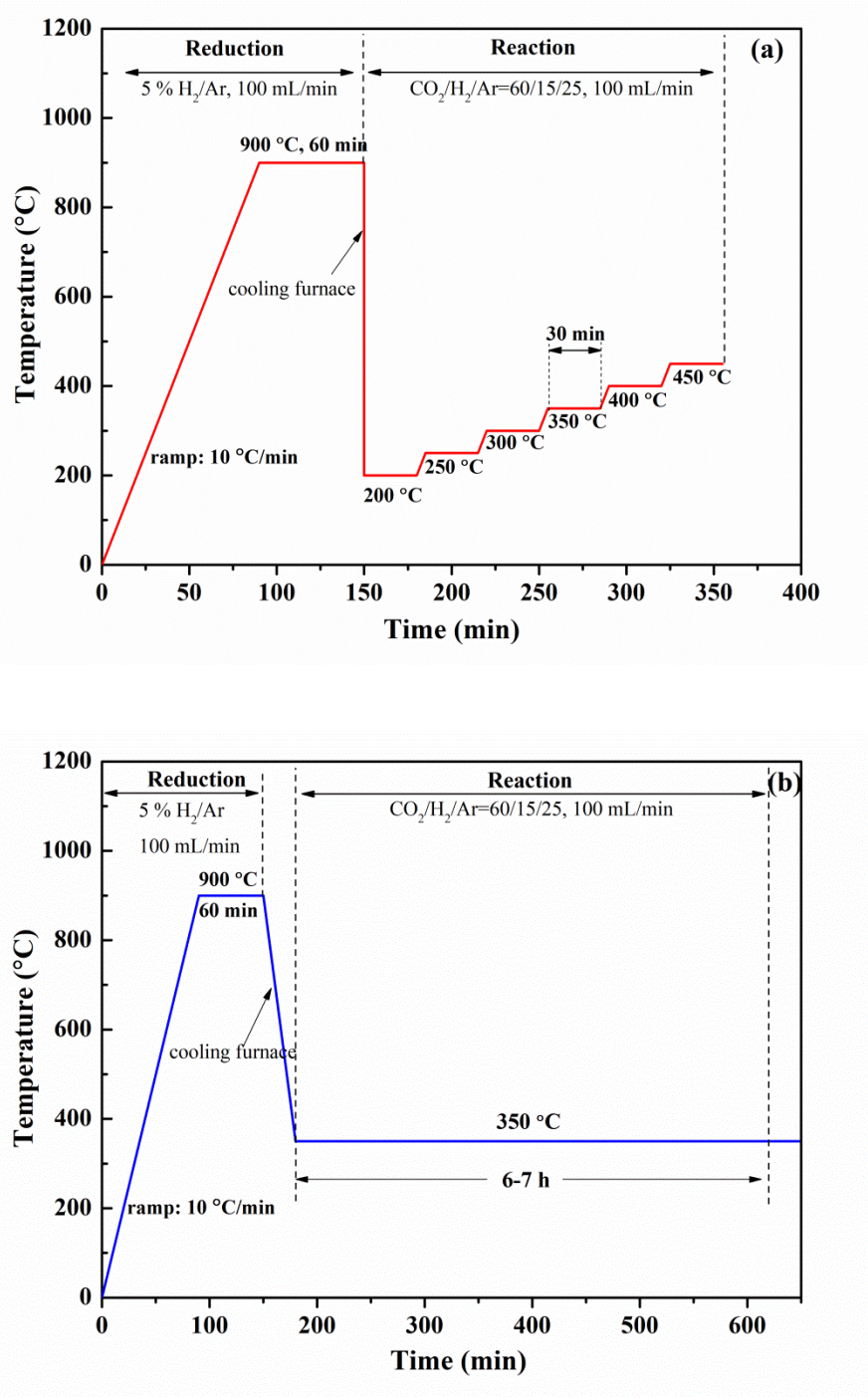

Figure. 3.2. Temperature programs used in activity test (a) and isothermal test of time-on-stream (b) for CO_2 methanation.

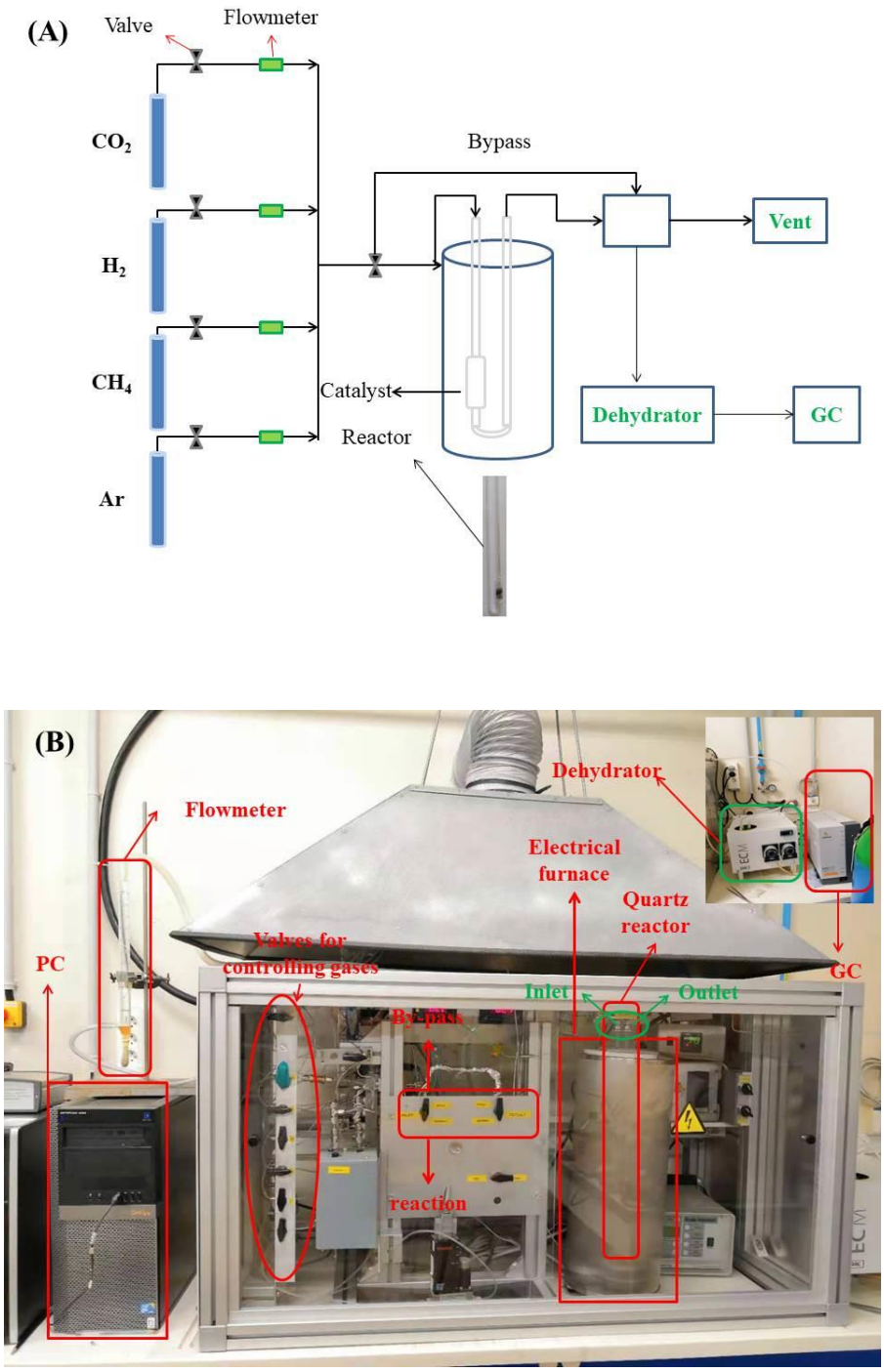

Figure. 3.3. Scheme (A) and real profile (B) for the CO_2 methanation set-up.

3.2.2 Calculations

The CO_2 conversion (X_{CO2}) and CH_4 (S_{CH4}) selectivity were calculated by the following equations:

$$X_{CO2}\,(\%) = \frac{[CO2]in-[CO2]out}{[CO2]in} = \frac{nCO2,in \times Qin - nCO2,out \times Qout}{nCO2,in \times Qin} \times 100 \qquad \text{(Equation 1)}$$

$$S_{CH4}\,(\%) = \frac{[CH4]out}{[CO2]in-[CO2]out} = \frac{nCH4,out \times Qout}{nCO2,in \times Qin - nCO2,out \times Qout} \times 100 \qquad \text{(Equation 2)}$$

Which the $[CO_2]$in and $[CO_2]$out represent the gas molar flow of CO_2 in inlet and outlet, respectively; $[CH_4]$out is the gas molar flow of CH_4 in the outlet; the $n_{CO2,\,in}$ and $n_{CO2,\,out}$ refers to the molar concentration of CO_2 in inlet and outlet, respectively. The Q_{in} and Q_{out} represent the flow rate measured by a flowmeter (Fig. 3.3b) of inlet and outlet, respectively.

The gas hourly space velocity (GHSV, h^{-1}) of weight hourly space velocity (WHSV, $mL/g_{cat}{\cdot}h^{-1}$) value was calculated following the equation below (Equation 3 and 4):

$$\text{GHSV}\,(h^{-1}) = \frac{Total\ volumetric\ \boldsymbol{flow}\ rate\ of\ the\ inlet\ gases}{Volume\ of\ the\ loaded\ sample} = \frac{Qin}{Vcat} \quad \text{(Equation 3)}$$

$$\text{WHSV}\,(g_{cat}{\cdot}h^{-1}) = \frac{Total\ volumetric\ \boldsymbol{flow}\ rate\ of\ the\ inlet\ gases}{weight\ of\ the\ loaded\ sample} = \frac{Qin}{mcat} \quad \text{(Equation 4)}$$

TOF (S^{-1}) value was calculated supposing that all the exposed Ni atoms participate in the reaction using the following equation (Equation 5)

$$\text{TOF}(S^{-1}) = \frac{nCH_4(mol)}{nNi\ (mol) * t(s)} \quad \text{(Equation 5)}$$

3.3 Characterization of the supports and catalysts

3.3.1 Temperature-programmed reduction in hydrogen (H_2-TPR)

In order to study the reducibility, metal particle distribution, and metal-support interaction [250,256], etc. of the catalyst or support, the temperature-programmed reduction in hydrogen (H_2-TPR) experiment was carried out for supports and catalysts. As the difference of interaction intensity between metal oxides and support and the particle size of crystallite, the metal oxides can be reduced by H_2 at different temperatures. Besides, some materials like CeO_2 and ZrO_2 can also be reduced by H_2 due to their redox properties [257].

The experiment program, scheme, and set-up used in this thesis were shown in Fig.3.4. The apparatus from BEL Japan Inc. shown in Fig.3.4c was equipped with a thermal conductivity detector (TCD).

As shown in Fig.3.4a, the sample was pretreated at 350℃ by helium (He) to blow out the impurities adsorbed on the surface of the sample before reduction. After pretreatment, a gas mixture of 5% H_2/Ar was fed into the sample. When the baseline of the TCD signal was stable, the sample was heated to 900 ℃ (ramp: 10 ℃/min) and kept at 900 ℃ for 30 min. At last, the furnace was cooled down to ambient temperature.

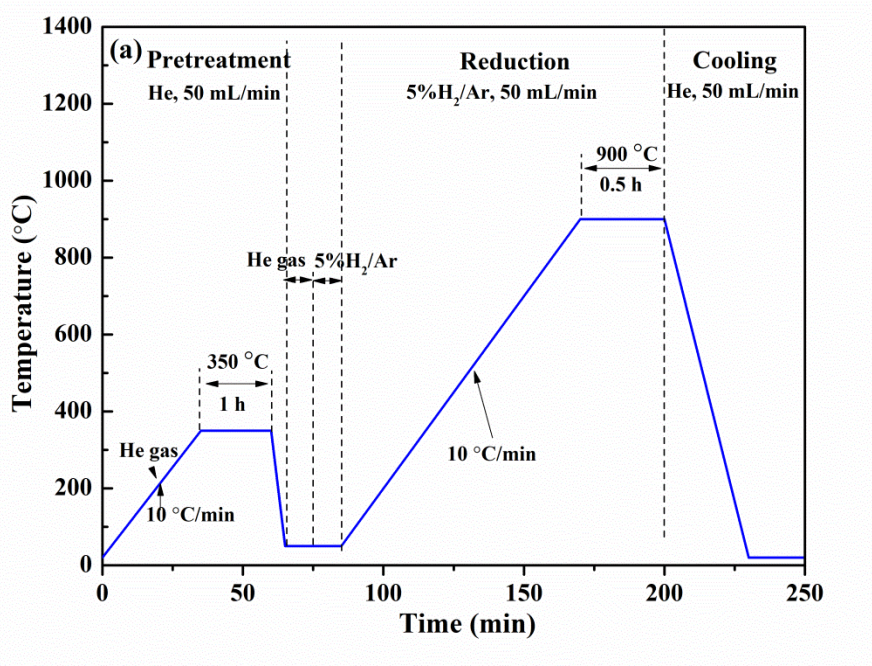
(a)
Pretreatment
He, 50 mL/min
Reduction
5%H2/Ar, 50 mL/min
Cooling
He, 50 mL/min
900 °C
0.5 h
He gas
5%H2/Ar
350 °C
1 h
He gas
10 °C/min
10 °C/min
Temperature (°C)
Time (min)
0
200
400
600
800
1000
1200
1400
0
50
100
150
200
250

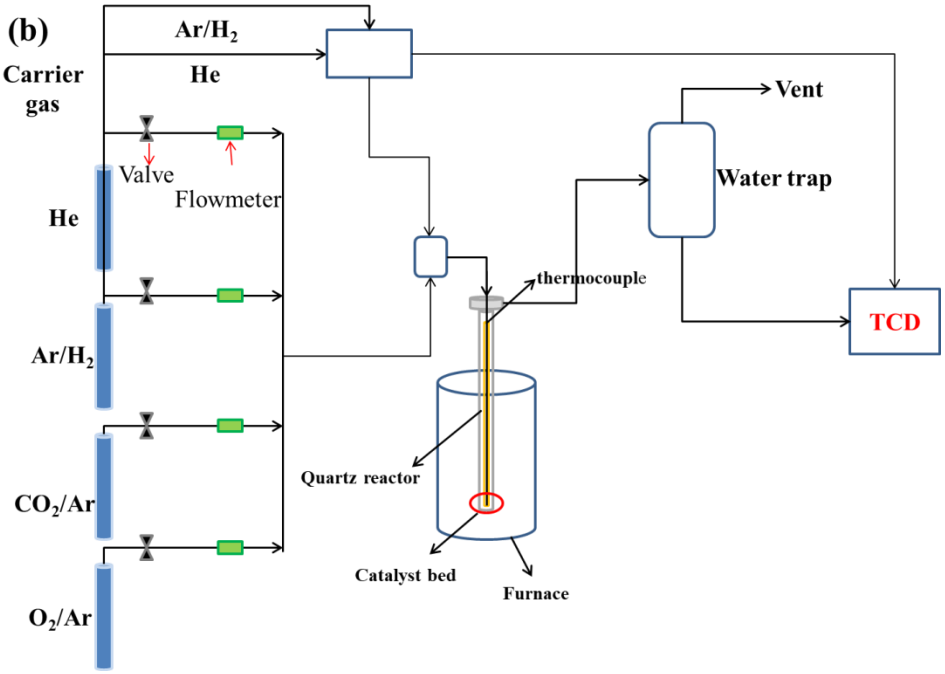
(b)
Ar/H2
Carrier gas
He
Valve
Flowmeter
He
Ar/H2
CO2/Ar
O2/Ar
Vent
Water trap
thermocouple
TCD
Quartz reactor
Catalyst bed
Furnace

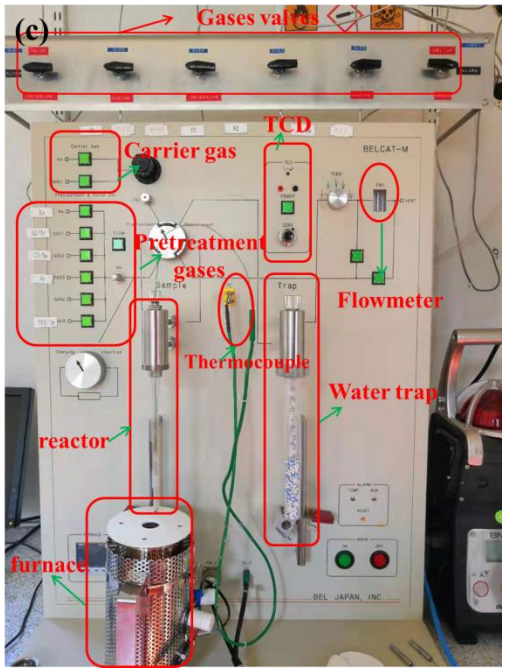

Figure. 3.4. Experimental program (a), scheme (b), and set-up (c) used in the TPR process.

3.3.2 Temperature-programmed desorption in CO_2 (CO_2-TPD)

To obtain the basicity and CO_2 adsorption ability on the surface of the sample, temperature-programmed desorption in CO_2 (CO_2-TPD) experiment was performed. This technology allows getting the total basicity and basic site distribution of the samples. According to the desorption temperature, the basic sites were divided into 3 types i.e. weak (T<150 °C), medium (T=150-550 °C), and strong basic sites (T>550 °C) [160,208,258,259]. The weak basic sites are attributed to CO_2 desorption from adsorbed CO_2 on the surface hydroxyl (OH^-) species [258,259]. The medium was assigned to Lewis acid-base pairs [258]. The strong basic sites were attributed to bulk carbonate decomposition [258,260]. Given the FTIR results reported, the weak, medium, and strong basic sites were caused by the chemisorbed CO_2 in the form of bicarbonate, bidentate carbonate, and unidentate carbonate, respectively [260].

The TPD experiments were carried out in the same apparatus as TPR and the scheme of the experiment was shown in Fig.3.5. At first, the sample was reduced at the desired temperature (550 ℃) for 1 h under a gas mixture of 5% H_2/Ar (50 mL/min). Then, the reduced sample was cooling down under H_2 to 50 ℃ and blew by He to clean the surface followed by the adsorption of CO_2 at the same temperature (10% CO_2/Ar, 50 mL/min). After that, the adsorbed CO_2 was blown by He (50 mL/min). At last, the TPD process was performed from 50 to 900 ℃ under He.

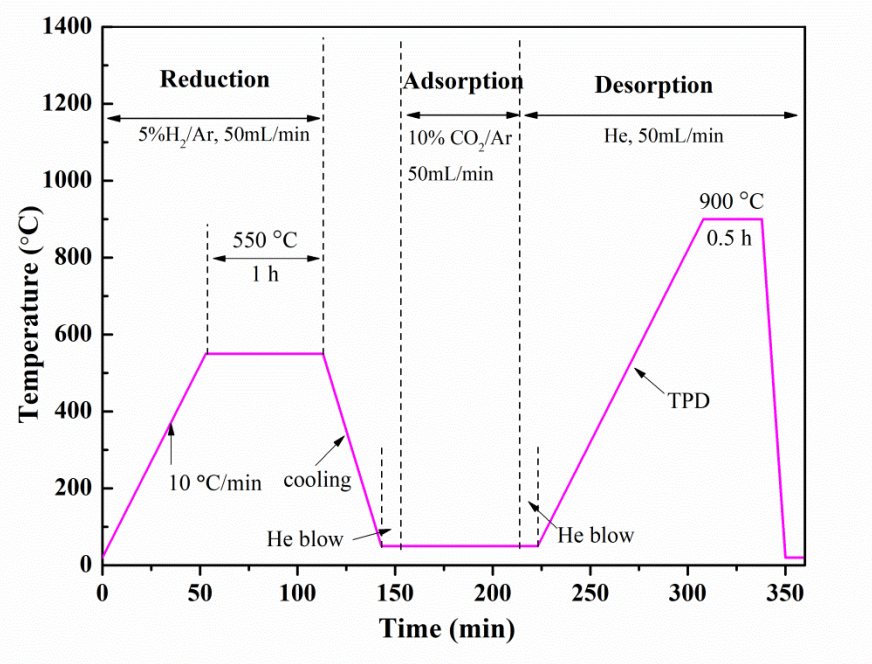

Figure. 3.5. The experimental program of temperature-programmed desorption of CO_2 (CO_2-TPD).

3.3.3 Physical adsorption of nitrogen (N_2)

The physical adsorptions of nitrogen (N_2) experiments were carried out to obtain the textural properties like specific surface area (SSA), pore volume (V_p), and average pore size (D_p). The experiments were performed in a Belsorp Mini II apparatus (Fig.3.4) from BEL Japan Inc. Before measurement, the sample was degassed at 200 ℃ under vacuum conditions for 4 h. After that, the

N_2 physical adsorption was carried out under liquid N_2 temperature (-196 ℃). The SSA was calculated by the Brunauer-Emmett-Teller method (BET) using equation 6 [261,262]:

$$\frac{p}{V(p0-p)} = \frac{(c-1)}{VmC} \times \frac{p}{p0} + \frac{1}{VmC} \quad \text{(Equation 6)}$$

$$S_g = \frac{V_m N_A A_m}{2240W} \times 10^{-18} \quad \text{(Equation 7)}$$

$$S_g\ (m_2/g) = 4.36 \times V_m/W \quad \text{(Equation 8)}$$

P represents the partial pressure of N_2 (Pa); P_0 represents the saturated vapor pressure of liquid N_2 (Pa) at adsorption temperature; V_m is the monolayer adsorbed gas quantity (mL); V is adsorbed gas quantity; C is BET constant. S_g is the SSA of the sample (m_2/g); N_A is Avogadro's constant (6.02×10^{23}); A_m is the Equivalent maximum cross-sectional area of N_2 molecules (0.162 nm^2); W is the weight of the sample (g). When the N_2 is used as adsorbate, the S_g can be calculated by equation 7.

Figure. 3.6. BELSORB MINI Apparatus used in the physical adsorption of nitrogen (N_2).

The pore volume and average pore diameter were calculated by the Barrett-Joyner-Halenda (BJH) method, which implements two fundamental assumptions i.e. the shape of the pore is cylindrical, and the adsorbed amount results from both physical adsorption on the pore walls and capillary condensation in mesopores [263]. Pore size distribution (PSD, nm) uses the classical Kelvin equation (equation 9);

$$\ln\frac{P}{P0} = \frac{2\gamma Vm}{rRT} \quad \text{(Equation 9)}$$

where P/P_0 is the relative pressure; γ is the surface tension of the adsorbate in the liquid form (N_2); V_m (mol/L) is the molar volume of the liquid; R is the universal gas constant; r is the radius of the meniscus formed in the mesopore; T is temperature [263,264].

N_2 physisorption isotherms can be classified into 6 types (Fig.3.7). As shown in Fig.3.7, the type I isotherm, also called Langmuir isotherm, was assigned to the adsorption in which pores were filled at low relative pressure with a cliffy uptake owing to the significant adsorbent-adsorbate interaction [263]. The type II isotherm normally happens on the non-porous materials and macroporous materials, where N_2 molecules are absorbed in mono/multi-layers without restriction [263]. The type IV isotherm that has a hysteresis loop is often found on materials with micropores and mesopores in which capillary condensation happens due to the interactions between gas molecules and adsorbent mesopore surface [263]. The type III and V isotherms with initial zero slopes correspond to weak adsorbate-adsorbent interactions on the materials (e.g. polyethylene). Type VI refers to stepwise multilayer adsorption on a uniform non-porous sur- face that usually happens on graphite carbon [263].

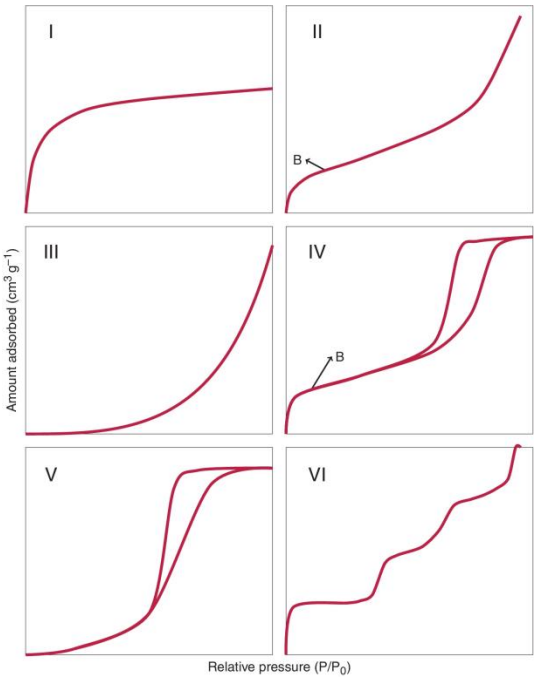

Figure. 3.7. The N_2 adsorption-desorption isotherms; Adapted from [263].

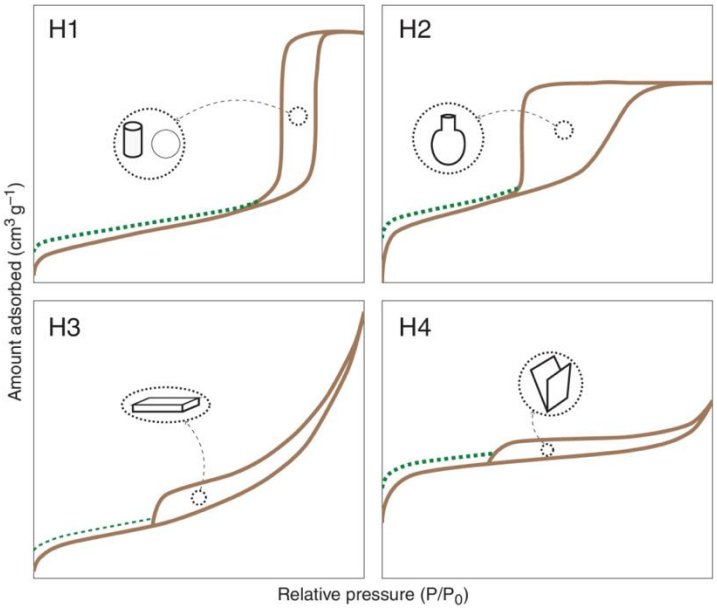

Figure. 3.8. Types of hysteresis loops obtained by N_2 physisorption; Adapted from [263].

According to the occurrence of capillary condensation in mesopores, the desorption isotherm is different from the adsorption one resulting in the formation of hysteresis loops. The loops consist

of 4 types as shown in Fig.3.8, which are associated with the pore shapes. The H1 is attributed to the uniform distribution of spherical and cylindrical narrow mesopores. H2 exists in inorganic oxides with a complex network of interconnected narrow pores. H3 are found in materials that have aggregated non-rigid plate-like particles (e.g. clay) [265]. Type H4 is characteristic of microporous materials that have narrow slit-like pores with type I isotherms [263].

Besides the BJH method, PSD (nm) is also often calculated by density function theory (DFT). The equation is below:

$$N_{exp}(P/P_0)=\int_{Dm}^{DM} N\mathrm{DFT}(\frac{P}{P0}, D) \times f(D)dD \quad \text{(Equation 10)}$$

Where f(D) is an unknown PSD function; D_m and D_M correspond to the minimum and maximum pore sizes in the kernel, respectively [263].

3.3.4 Chemisorption of hydrogen (H_2 chemisorption)

In order to obtain the active metal distribution, the H_2 chemisorption was employed to determine nickel dispersion (Micromeritics, ASAP 2020). Before analysis, about 0.2 g of calcined sample was evacuated in helium at 40°C. The sample was subsequently reduced in situ at 550°C for 1.5 h in the flow of H_2 (30 mL/min). The temperature was cooled down to 40°C, followed by the volumetric H_2 chemisorption with pure hydrogen. The metal distribution (D) is calculated by the following equation [266]:

$$D\ (\%) = \frac{1.17X}{Wf} \quad \text{(Equation 11)}$$

The average nickel crystallite diameter (surface-averaged, nm) was calculated using the equation 12 [266]:

$$d_{Ni}\,(nm) = \frac{971}{D} \quad \text{(Equation 12)}$$

Where the X is chemisorbed H_2 in micromoles per gram of catalyst, W represents the weight percentage of Ni, and f is the fraction of Ni reduced to the metal.

The Ni surface area was calculated by assuming that one hydrogen atom corresponds to one Ni atom and that the cross-sectional area of the Ni atoms is 6.49×10^{-20} m^2 [267].

3.3.5 X-ray diffraction (Small-angle and Wide-angle)

To obtain the structural properties e.g. phase composition and crystallite size of the samples, the X-ray diffraction technologies including small-angle and large-angle (SAXRD and WAXRD) were performed for the studied materials. The SAXRD was used to confirm the ordered structure of the ordered mesoporous materials. The samples after calcination (550 ℃, 5 h), reduction, and catalytic tests were characterized by WAXRD experiments.

XRD measurements were carried out on PANalytical-Empyrean diffractometer equipped with Cu K_α (λ=1.5406Å) radiation source, with the scanning range of 2 theta (θ) range from 5 to 90°, with a 0.02°/min step size. The WAXRD experiments were carried out with the 2θ range of 0.5-6.0° by a stepwise of 0.01°. Fig.3.8 shows a set-up, schematic diagram, and principles of X-ray diffractometer with main components.

The average crystallite size (D, nm) of Ni metal and support were calculated by Scherrer equation:

$$D_{hkl}(nm) = \frac{K\lambda}{\beta_{hkl}cos\theta} \quad \text{(Equation 13)}$$

In which k is Scherrer parameter (0.9); λ is the radiation wavelength (λ=1.5406Å), β_{hkl} refers to the full width at half maximum of the reflection peak, and θ represents the Bragg diffraction angle.

(A)

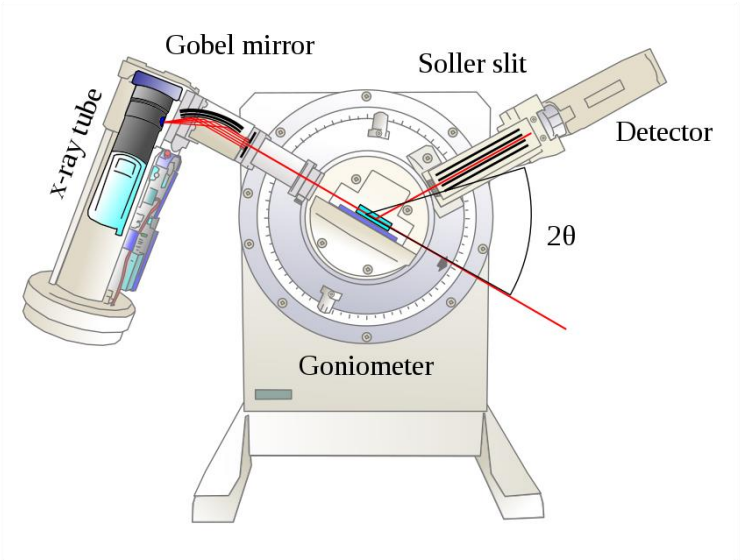

(B)

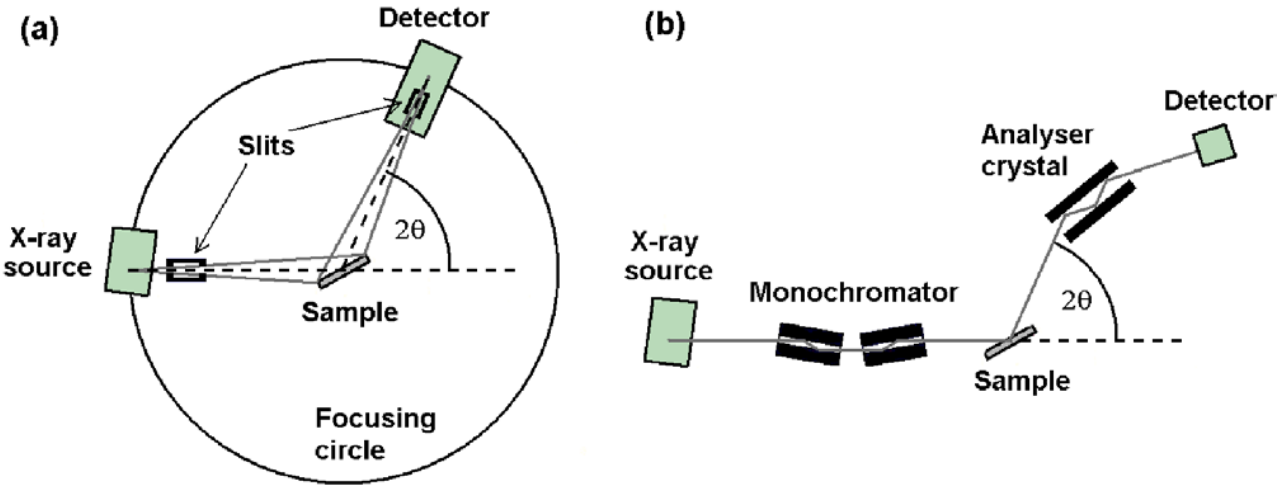

(C)

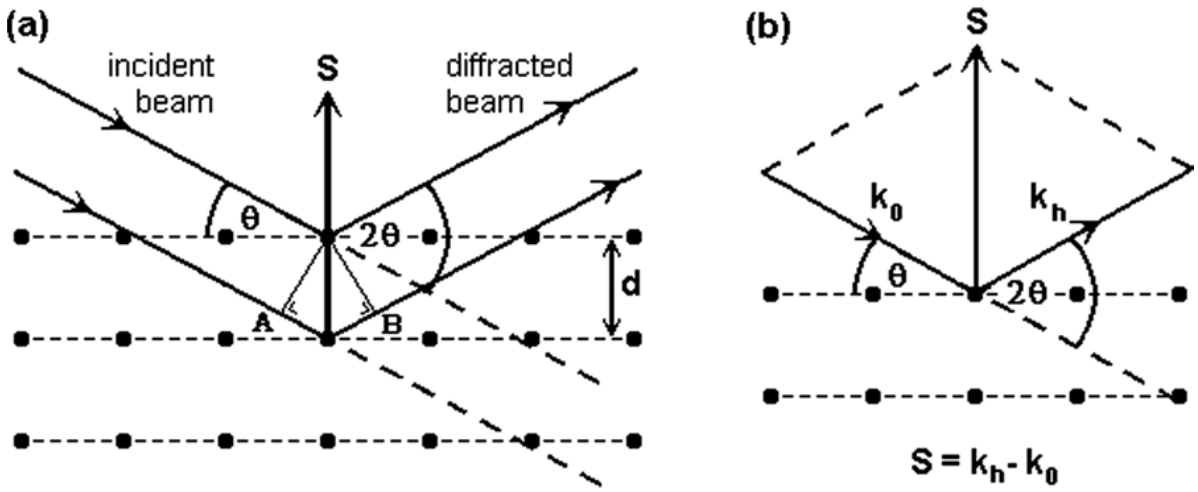

Figure. 3.8. A set-up (A), schematic diagram (B), and principles (C) of x-ray diffractometer with main components; Adapted from [268]

3.3.6 Elemental composition analysis

To obtain the element composition of catalysts, the X-Ray Fluorescence (XRF) in a Rigaku Supermini200 analyzer or XRF 1800 Shimadzu was used to evaluate the elemental composition of the studied catalysts. The experiment was performed under vacuum at 36.5 ºC in the presence of P-10 gas (a mixture of 10% CH_4/Ar, flow 24.7 mL/min). A pulse height analyzer was used to calibrate the proportional counter (PC) detector. The calcined sample was homogeneously mixed with boric acid and pelletized under 10 bar. So prepared pellet was then covered by polypropylene film (6 μm) and put into a sample holder for analysis.

3.3.7 Transmission electron microscopy and Energy Dispersive X-ray spectroscopy

To acquire the morphology information and metal size of the catalyst, the Transmission electron microscopy (TEM) and Energy Dispersive X-ray spectroscopy (EDX) analyses were carried out with JEM-2010 and JEM-2100Plus (JEOL, Tokyo, Japan) transmission electron microscopes for the reduced catalysts. Before measurement, the reduced samples were dispersed in ethanol, following the suspension being added dropwise on a copper grid covering with carbon film, then the prepared materials were used for the microscopy measurement.

3.3.8 X-ray photoelectron spectroscopy

To obtain the surface compositions and oxidation states of the catalysts, the X-ray photoelectron spectroscopy (XPS) measurements were performed with a VG Microtech ESCA 3000Multilab spectrometer, equipped with a dual Mg/Al anode, with an excitation source of unmonochromatized Al Kα radiation (1486.6 eV). The sample powders as received were analyzed as pellets, mounted on a double-sided adhesive tape. The pressure in the analysis chamber was in the range of 10^{-8} Torr during data collection. The constant charging of the samples was removed by referencing all the energies to the $Ce3d_{5/2}$ component at 882.1eV or C1s peak to 284.6 eV. Quick scans of the Ce3d region were performed before each analysis to evaluate possible reduction under the beam. Analyses of the peaks were performed with the software CasaXPS. Atomic concentrations were calculated from peak intensity using the sensitivity factors provided by the software. The binding energy values are quoted with a precision of ±0.15 eV and the atomic percentage with a precision of ±10 %.

3.3.9 Thermogravimetric analyses-mass spectrometer (TGA-MS)

To obtain the information of possible carbon deposition on the spent catalysts, the thermogravimetric analysis (TGA) was performed on the spent catalysts by the Q5000 IR apparatus. Around 25 mg of material was heated starting from room temperature to 750 °C (heating rate of 10 °C/min). The measurements were performed in synthetic air. The amount of H_2O and adsorbed CO_2 were estimated by the mass loss registered in the TGA plots and mass spectrometer (MS) signal.

3.3.10 Temperature-programmed oxidation (TPO)

To investigate the possible surface carbon deposition effects on the catalysts, the temperature-programmed oxidation (TPO) analyses were carried out on the spent catalysts by Quadstar Mass equipped with a Pfeiffer Vacuum. Around 30 mg of a sample was heated from ambient temperature to 800 °C with a heating rate of 5 °C/min. The measurements were performed in a 5% O_2/Ar gas mixture (Volumetric percentage, 200 ml/min). During the mass spectroscopy analysis, the following desorbed species were recorded; mass-to-charge ratio (m/z): 44 (CO_2) and 18 (H_2O). The CO_2 signal in the graph was enlarged 10 times for the analysis.

Chapter IV

Low-cost materials for CO_2 methanation

4. Low-cost materials for CO_2 methanation

4.1 Ni-Mg catalysts supported on diatomite

4.1.1 Introduction

In the past decades, climate changes caused by global warming had brought about serious impacts on the natural system and human society [15]. The reduction of CO_2 emissions has gained legislative importance [33]. The greenhouse gases e.g. CO_2, CH_4, and nitrous gases, mainly come from industrial activities and population growth. CO_2 emission, which mainly comes from fossil fuel consumption, accounts for most greenhouse gas emissions [269]. To mitigate climate change, the reduction of CO_2 emissions is important to protect the environment and achieve sustainable development [4,15]. It is impossible for human societies to stop consuming fossil fuels soon. Thus, the technologies to capture, store, and utilize CO_2 from the atmosphere or industrial plants would bring both economic and environmental benefits [270,271].

CO_2 reduction technologies can be divided into CO_2 capture and storage (CCS) and CO_2 capture and utilization (CCU) routes [272]. The CCU technologies consist of chemical and biological methods in which the chemical methods show the most potential now [38]. Catalytic CO_2 conversion routes to fuels and chemicals e.g. methane, methanol, or dimethyl ether received much interest due to their high value [3,4,269]. They can not only provide an alternative route to reuse the fossil carbon resources and closed the anthropogenic carbon cycle but also synthesized high-value chemicals and fuels [3]. CO_2 hydrogenation into methane over transition metal-based catalysts using renewable hydrogen from water electrolysis as an example has a huge potential to reduce the emissions and, at the same time, to store the excess renewable energy to equalize the

demand and capacity in a power to gas (PtG) process, which a few plants were already operated in European Union [100,165,230,273,274].

CO_2 methanation, also called Sabatier reaction, i.e. $CO_2 + 4H_2 \rightarrow CH_4 + 2H_2O$ (ΔG_{298K} = -130.8 kJ/mol), was a thermodynamically favorable and exothermic reaction [98]. Compared to other chemical reactions of CO_2 conversion, it showed more feasible potentials towards commercialization due to the high activity and moderate running conditions [7]. Moreover, the resulting CH_4 or synthetic/substitute natural gas (SNG) can be directly injected into the existing infrastructure for storage, transportation, and usage [7,137,167]. However, the presence of appropriate catalytic systems is indispensable due to the kinetic barriers [126].

Transition metals mainly VIII metals such as Rh, Ru, Pd, Co, Ni, Pt, and Fe [71,119,230,275–283,121,122,124,137,145,164,210,228] have been used for the formulation of supported metal catalysts. The noble metal-based catalysts like Rh and Ru showed high low-temperature activity and long-term stability, but their high cost limits the utilization on an industrial scale [258,284]. The Ni-based catalysts are much suitable due to their excellent CO_2 conversion and CH_4 selectivity, high availability, and low cost compared to the noble metal catalysts [123,137,288,289,145,167,274,279,280,285–287]. However, Ni-based catalysts still have drawbacks like poor stability, sintering of active metals, or chemical poisoning [173].

Numerous efforts have been devoted to promoting the activity and stability of Ni-based catalysts. The doping of other metals in the preparation of Ni-based catalysts e.g. Fe, Ce, Y, and Mg, etc. [142,144,290,291] had been reported to enhance the activity and stability of Ni-based catalysts towards methanation. Among the dopants, Mg seems to be a good modifying promoter since it affects the activation of CO_2 on Mg^{2+} and promotes the dispersion of Ni particles on the support, resulting in improved stability and carbon resistance [179].

Besides, the support also plays a decisive role in the metal-support interaction, which determined significantly the catalytic performance in CO_2 methanation [179]. Many materials such as SiO_2, Al_2O_3, TiO_2, CeO_2, ZrO_2 [141,147,168,173,214] have been used for the preparation of Ni-based catalyst for CO_2 methanation. It is proposed to design a Ni-based catalyst with special structures such as hydrotalcite and perovskite, which have a very high thermal stability against sintering [179,292]. Diatomite is a natural siliceous, porous, low density, hydrophobic material with high adsorption ability and thermal stability [293].

Diatomite had been used in the synthesis of catalysts for different applications as described in Table 4.1.

Table 4.1 Possible applications for Diatomite materials used as catalysts

Number	Reaction	Reference
1)	CO oxidation	[294]
2)	Degradation of organic pollutants	[295]
3)	Transesterification of vegetable oil	[296]
4)	Hydrogenation of vegetable oils	[297]
5)	Photocatalytic activity	[298,299]
6)	Heck and Suzuki reactions	[300]

However, until now the application of diatomite-supported nickel catalysts for CO_2 methanation has not been attempted. Therefore, for the first time, the capability of diatomite-supported Ni catalyst for CO_2 methanation was investigated.

The present chapter aimed to investigate the effect of three different nickel precursor salts on the textural, phase-structural, reducibility, and basicity properties of diatomite supported Ni-Mg catalysts obtained by the same precipitation-deposition (PD) method, as well as their catalytic performance in the CO_2 methanation.

4.1.2. Catalyst preparation and Physicochemical techniques

The detailed preparation process was depicted in 3.1.1 of chapter 3. The calcined samples were denoted as Ni-Mg/D-S, Ni-Mg/D-N, and Ni-Mg/D-A (X=S-sulfamate, N-nitrate, or A-acetate) based on the nickel precursors.

The textural properties of reduced and spent catalysts were analyzed by N_2 adsorption-desorption in a BELSORP Mini II-BEL Japan instrument. Before measurement, the samples (60 mg) were degassed at 200 °C for 2 h aiming at cleaning the surface, then the measurement was conducted at liquid N_2 temperature.

The structural parameters of catalysts (reduced and after methanation) were examined by X-ray diffraction (XRD) method in a PANalytical-Empyrean diffractometer equipped with Cu Kα radiation source (λ=1.5406 Å) within 2θ range from 10 to 90°, with a step-size of 0.02°/min. The reduced samples were obtained from the same reduction condition as the reaction, after the reduction, the samples were cooled down under Ar flow (100 mL/min) to ambient temperature.

The reducibility of catalysts was studied by H_2-TPR by a BELCAT-M type (BEL Japan Inc.) set-up equipped with a conductivity detector (TCD). The samples (60 mg) were pretreated in helium (50 mL/min) at 100 °C for 2 h, and then the TPR experiment was carried out in a 5% H_2/Ar mixture (50 mL/min) up to 700 °C by a heating rate of 10 °C/min.

The basicity distribution of samples was measured by CO_2-TPD in the same apparatus as TPR-H_2, and the sample after TPR was pretreated by He at 80 °C for half an hour following the adsorption of CO_2 (10% CO_2/He, 50 mL/min) for 1 h, then the TPD was performed after desorbing the physically adsorbed CO_2 in 30 min at 80 °C.

4.1.3 Texture properties and structural parameters of catalysts

The textural properties of reduced and spent catalysts were displayed in Table 4.1. It can be seen from Table 4.1 that the highest specific surface area (SSA) was obtained on both reduced and spent Ni-Mg/D-N samples compared to the other two samples.

Table 4.1 BET specific surface area, pore volume and mean pore size of the catalysts

Sample	[a]SSA [m^2g^{-1}]		[b]V_p [cm^3g^{-1}]		[c]r_p [nm]		[d]d_{Ni} [nm]	
	reduced	spent	reduced	spent	reduced	spent	reduced	spent
Ni-Mg/D-S	48.4	54.4	0.12	0.26	2.1	1.6	10.9	8.5
Ni-Mg/D-N	81.0	73.3	0.11	0.20	1.9	1.9	11.1	8.5
Ni-Mg/D-A	42.9	45.0	0.10	0.10	1.9	1.2	11.5	8.1

[a] Calculated from BET method
[b,c] Calculated from BJH method
[d] Calculated from the three strongest peaks of XRD by Scherrer equation

Moreover, no large differences regarding SSA were observed between the reduced and spent catalysts, indicating that the surface of catalysts was not modified strongly during the reaction. Meanwhile, there were slight mesopore enlargements between the reduced and spent catalysts on Ni-Mg/D-S and Ni-Mg/D-N samples, meaning the internal pores may be modified during the reaction. The mean pore sizes of the catalysts had not changed largely after the reaction. In conclusion, the Ni-Mg/D-N sample possesses the highest SSA, leading to more exposure of active sites.

The X-ray diffraction (XRD) patterns of the catalysts after reduction and test were shown in Fig. 4.1. As shown in the patterns, the small broad diffraction peak at 2θ=21.5° for all samples is attributed to the diffraction of amorphous silica, and the weak peaks at 2θ=26.7° and 28° are assigned to the diffraction of quartz phase, and the three strongest peaks located at 2θ=44.6°, 51.9°, 76.5° correspond to the metallic Ni planes of (1 1 1), (2 0 0) and (2 2 0) [301,302]. The particle

sizes of crystalline Ni^0 were calculated in Table 4.1. It can be seen there is nearly no difference of metallic Ni for reduced or spent catalysts when the nickel salt was changed. After the reaction, the crystal size of Ni^0 became smaller compared to the reduced catalysts, meaning the redistribution of Ni^0 during reaction [144].

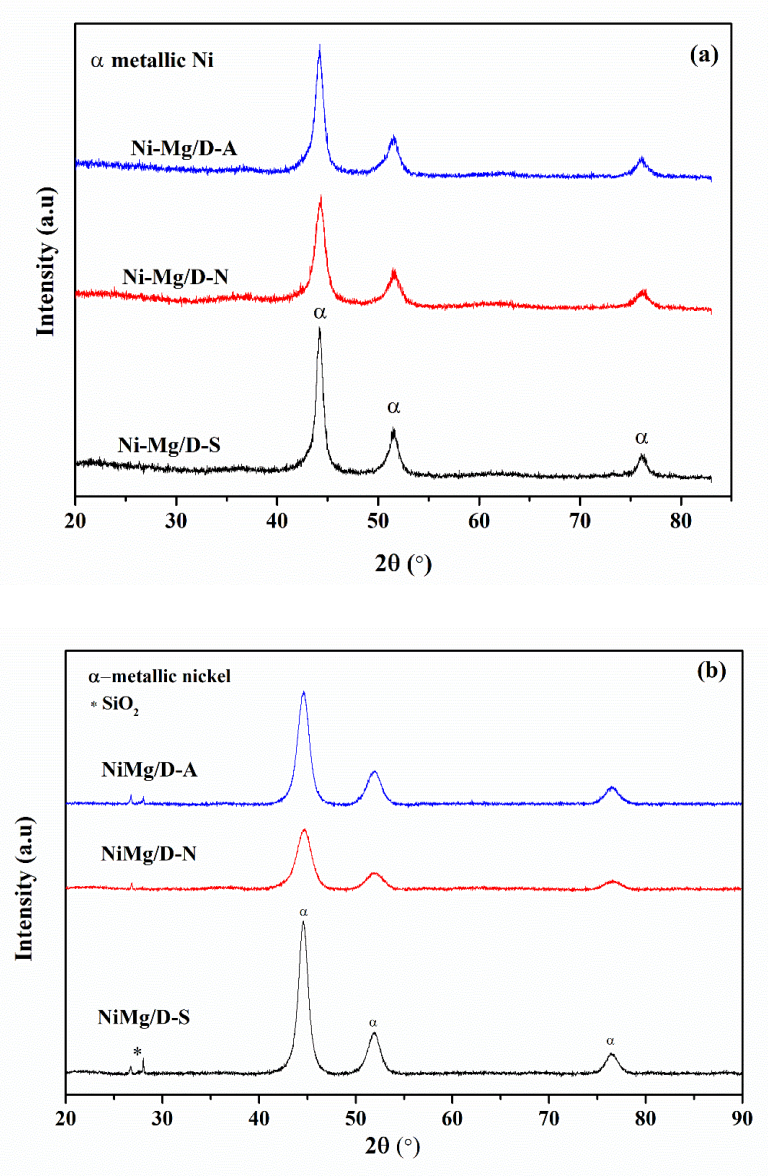

Figure. 4.1. XRD pattern of the reduced (a) and spent (b) catalysts.

4.1.4. Reducibility, basicity distribution of catalysts

The reducibility and basicity of catalysts were measured by H_2-TPR and CO_2-TPD. The profiles are displayed in Fig.4.2a and Fig.4.2b, respectively. Also, the H_2 consumption amount and basic site distribution are calculated in Table 4.2 and Table 4.3. For the TPR-H_2, the curves of all samples can be divided into 3 peaks i.e. α, β, and γ, corresponding to the reduction of small NiO on the surface (Ca.300-400 °C), bulk NiO weakly interacting with the support (Ca.400-500 °C) and nickel silicate or small NiO particles in the pore that are difficult to reduce [303]. As shown in Table 4.2, compared to the Ni-Mg/D-S, temperatures of β and γ peaks for the other samples are higher, indicating stronger Ni-support interaction. The total H_2 consumptions were similar, indicating that the reducible nickel species for the catalysts are similar.

The desorption peaks of CO_2 (Fig.4.2b) can be fitted into three peaks, representing weak, medium, and strong basic sites of the catalyst, respectively [160,258,259,303]. The highest basic sites of weak or medium and lowest strong basic sites (Table 4.3) were observed on NiMg/D-N catalyst. And the medium or weak basic sites of the other two samples are similar.

Table 4.2 H_2 consumption of catalysts calculated according to H_2-TPR

Catalyst	Temperature [°C]			H_2 consumption [mmolH_2/g]			Total [mmolH_2/g]
	α	β	γ	α	β	γ	
NiMg/D-S	353	425	520	0.22	1.41	1.44	3.07
NiMg/D-N	369	464	578	0.09	1.02	1.85	2.96
NiMg/D-A	343	479	599	0.14	1.31	1.32	2.77

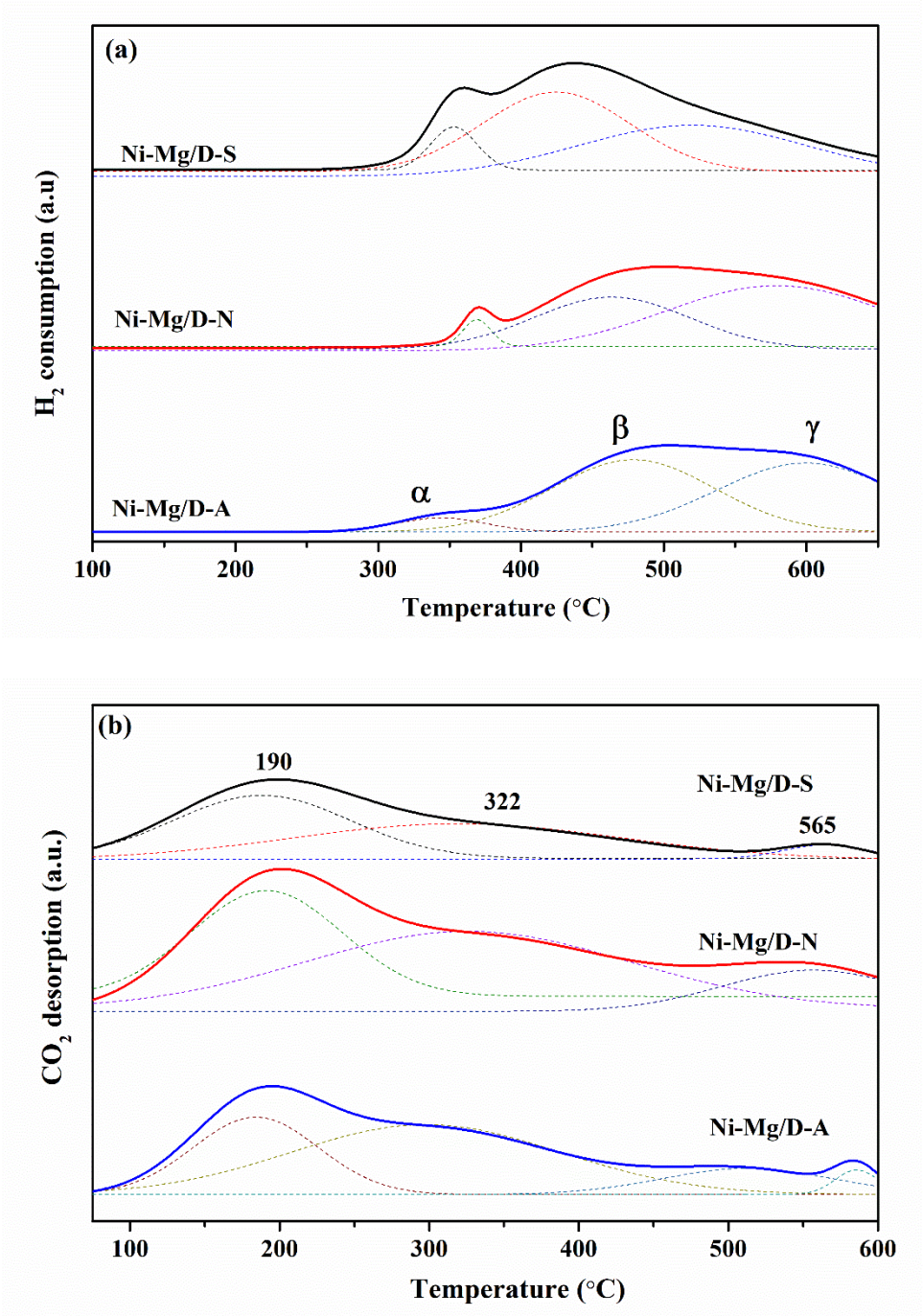

Figure. 4.2. (a) H_2-TPR profiles of fresh catalysts; (b) CO_2-TPD profiles of reduced catalysts;

Table 4.3 Basic site distribution calculated from TPD-CO_2 on reduced catalysts.

Catalyst	Basic sites [μmol/g]				Distribution of basic sites [%]		
	Weak	Medium	Strong	Total basicity	Weak	Medium	Strong
NiMg/D-S	30.5	35.5	6.6	72.7	42.0	48.9	9.1
NiMg/D-N	35.6	48.9	9.3	93.8	37.9	52.2	9.9
NiMg/D-A	32.8	36.9	12.1	81.8	40.1	45.0	14.8

4.1.5. Catalytic performance of catalysts for CO_2 methanation

The catalytic activity of catalysts in CO_2 methanation reaction was performed in a tubular U-type quartz reactor under ambient pressure, the temperature of catalyst was monitored by a K-type thermocouple. Before the reaction, the sample (100 mg) was reduced in-situ by the H_2 mixture (5% H_2/Ar, 100 mL/min) at 700 °C with a ramp of 10 °C/min for 1 h. After the reduction, the furnace was cooled down to 250 °C, then the gas mixture (CO_2/H_2/Ar=15/60/25, 100 mL/min, WHSV=60,000 $h^{-1}\cdot g_{cat}^{-1}$) was fed into the reactor. The products were analyzed in an Agilent Varian 4900 online micro chromatograph. The reaction was conducted from 250 °C to 450 °C with a step of 50 °C with a duration time of 30 min at each temperature. The CO_2 conversion and CH_4 selectivity were calculated based on Equations 1 and 2 in chapter 3, respectively.

The activities of the catalysts are thus presented in Fig.4.3 in which the thick black lines represent the thermodynamic plots of CO_2 conversion and CH_4 selectivity. The CO_2 conversion for all catalysts at the range of 250-300 °C seems very low and it increases with the rising temperature. The CO_2 conversion of Ni-Mg/D-N is higher than that of others at each temperature step. Regarding the CH_4 selectivity, there is no large difference for all catalysts at the range of 250-300 °C. However, the Ni-Mg/D-N sample always possesses the highest selectivity when temperature excesses 350 °C. Ni-Mg/D-A shows the worst CH_4 selectivity at the running temperature range.

Correlating the medium basic sites of catalysts with the CO_2 conversion values at 350-450 °C, it can be found that the CO_2 conversion increases with the increase of medium basic sites. The crystalline size of Ni^0 after the test as shown in Table 4.1 decreased compared with that of reduced catalysts, indicating no sintering happened during the reaction. Ni-Mg/D-N shows the best CO_2 conversion and CH_4 selectivity. Thus, it can be deduced that the nitrate nickel salt is the best candidate for diatomite-supported Ni catalysts for CO_2 methanation.

The highest activity of Ni-Mg/D-N catalyst could be attributed to the highest SSA, the small Ni^0 particle size, the highest medium/total basic sites, and good reducibility. It is reported that the H_2 dissociates on the surface of Ni^0 and the CO_2 adsorbs and dissociates on the weak or medium basic sites [160]. For Ni-Mg/D-N, the small Ni^0 particle could provide more active sites for H_2 dissociation, and the high basic sites, especially the medium sites, are beneficial for the adsorption and dissociation of CO_2, thus promote the activity in CO_2 methanation [160].

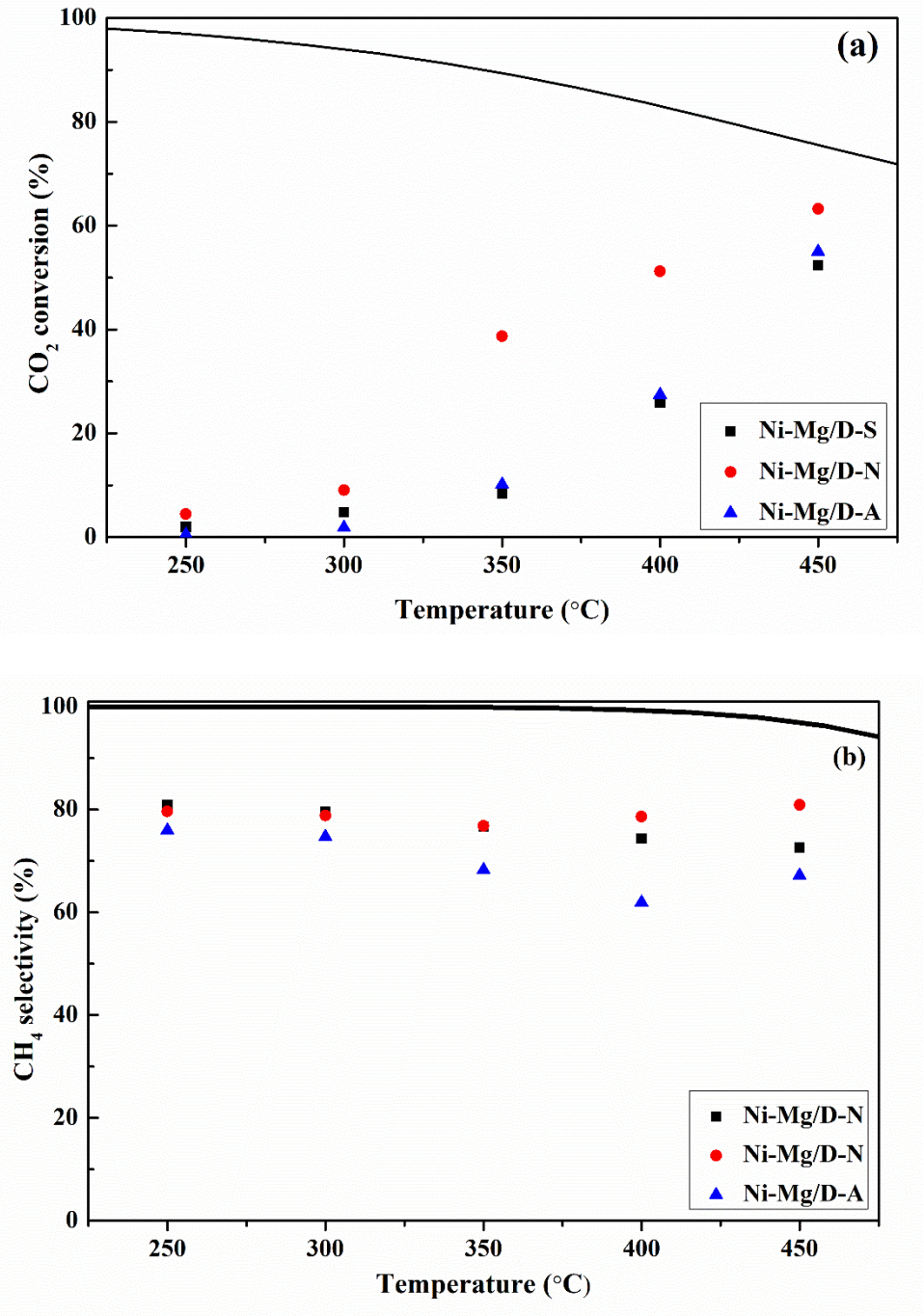

Figure. 4.3. CO_2 methanation results on the catalysts ($H_2/CO_2/Ar$=60/15/25, WHSV=60,000 $h^{-1}g_{cat}^{-1}$), (a) CO_2 conversion; (b) CH_4 selectivity

4.1.6 Conclusions of diatomite supported Ni-Mg catalysts

In this study, the Ni-Mg catalysts supported on diatomite were prepared by the precipitation-deposition method with different nickel salts. The effect of nickel salts on the performance of Ni catalysts in CO_2 methanation was investigated by H_2-TPR, CO_2-TPD, N_2 physisorption, and XRD methods. It was found that the Ni-Mg/D-N catalyst presented the best activity and selectivity, which could be ascribed to the small Ni^0 particle, good reducibility, and the highest medium basic sites.

However, the activity results of diatomite-based Ni catalysts in this chapter seem not satisfactory. The diatomite-supported catalysts in CO_2 methanation still need more development to improve the activity.

4.2 Nickel-based mixed oxides derived from layered-double hydrotalcite (LDH)

4.2.1 Introduction

Layered double hydroxides (LDH) or hydrotalcite (HT) are materials with di- and tri-valent cations incorporated into the brucite-like layers. The layers of hydrotalcite are positively charged and anions present in the interlayer spaces are compensating the charge. It was reported in the literature that there is a wide range of cations that may be incorporated into the hydrotalcite structure, e.g., Li^+, Ti^{4+}, Sn^{4+}, or Zr^{4+} [304]. The calcination of such materials leads to the formation of mixed nano-oxides with periclase-like structures, which show very interesting features [58,63,167,305–307]. Redox or acid-base properties of such materials may be tailored to some extent by controlling hydrotalcite composition, as shown e.g. in NH_3-SCR [308–312] or DRM [44,250,307,313–315] reactions. Another advantage of double-layered hydroxides is that the incorporated cations are usually homogenously distributed due to their random arrangement in the brucite-like layers. Moreover, such materials exhibit basic properties, which are of great interest when used as catalysts for the reaction of CO_2 methanation [131,138,205,206,208,250,308,316].

Several aspects were already investigated in the case of hydrotalcite-derived catalysts for CO_2 methanation reaction such as (i) the effect of nickel content, (ii) the particle size of nickel crystallites, (iii) the reducibility of nickel species, (iv) the number and distribution of basic sites, and (v) the promotion with other metals such as La, Fe, etc. or the new preparation method [131,138,206,317–320].

Fan et al. [321] studied Ni impregnated $MgAl_2O_4$ derived from hydrotalcite followed by calcination at 500 °C or treated by DBD plasma to decompose Ni precursor. The plasma treatment resulted in higher nickel dispersion of 7.1% for the plasma decomposition method prepared sample, compared to 6.0% for the traditionally calcined material. The authors claimed that smaller

metallic nickel particles resulted in enhanced activity in the reaction of CO_2 methanation. Wang et al. [319] studied Ni/Al HTs promoted with 0.05 and 0.25% molar ratio of Fe and found that the introduction of Fe effectively enhanced the H_2 adsorption capacity. Ni/Mg/Al hydrotalcite promoted with a wide range of Fe content (1.2-18 wt.% of Fe) were examined by Mebrahtu et al. [237]. It was found that the activity in CO_2 methanation was effectively increased in the low-temperature region when low amounts of iron were introduced. In our previous reports, we investigated the influence of Ni loading and the effect of La introduction on the catalytic activity of LDHs catalysts in CO_2 methanation [131,206,208]. The incorporation of higher amounts of nickel, as well as the introduction of lanthanum, significantly enhanced the activity in CO_2 methanation reaction. This could be correlated with the increased number of medium-strength basic sites, which in the case of La-promoted catalysts was strongly dependent on the method of promoter introduction [131,160,322]. According to the study of Pan et al. [160] CO_2 adsorbed on $Ni/Ce_{0.5}Zr_{0.5}O_2$ may undergo hydrogenation easier than on Ni/Al_2O_3 because of the higher content of medium basic sites.

Yttrium had been reported in the literature as a promising dopant in methane dry reforming (DRM) reaction ($CO_2 + CH_4 = 2H_2 + 2CO$) [44,50,51,64,250,316,323,324]. The increased activity of the Ni-containing hydrotalcite was attributed to the enhanced dispersion of the active phase in comparison with the un-promoted materials [51,250,316]. The stability of the Zr- containing catalysts in DRM reaction was also enhanced by the introduction of Y, which was assigned to the formation of a solid-solution ZrO_2-Y_2O_3, leading to the increased reducibility of bulk NiO [44]. Moreover, Bellido et al. [325] reported that ceria doped with yttrium showed enhanced oxygen mobility and oxygen vacancies. For CO_2 methanation, Muroyama et al. [198] reported that Y_2O_3 impregnated with Ni revealed very high activity in the low-temperature region in CO_2 methanation

when compared to Ni supported on Al_2O_3, ZrO_2, and CeO_2 catalysts. It was attributed to the promoted decomposition of formate species formed during the reaction over Ni/Y_2O_3 catalysts.

The purpose of this part is to study yttrium promoted Ni-containing hydrotalcite-derived catalysts for CO_2 hydrogenation to methane. Our study is focused on the determination of the influence of Y introduction to Ni-containing layered double hydroxides on the catalytic performance in CO_2 methanation. The catalysts were synthesized using the co-precipitation method at a constant pH and with a fixed molar ratio of M^{II+}/M^{III+} =3.0. The assumed loading of yttrium introduced into hydrotalcite was 0.4, 2.0, and 4.0 wt.%. To correlate the changes in activity with the Physico-chemical properties, the studied materials were characterized using various techniques such as X-ray diffraction (XRD), low-temperature N_2 sorption, X-ray fluorescence (XRF), temperature-programmed reduction in H_2 (H_2-TPR), temperature-programmed desorption of CO_2 (CO_2-TPD), thermogravimetric analysis (TGA) and temperature-programmed oxidation (TPO).

4.2.2 Catalyst preparation

The Layered-double hydrotalcite incorporated with or without yttrium were prepared by the co-precipitation method. The as-synthesized materials were calcined to obtain the mixed nano-oxides. The particular preparation process was described in 3.1.2 of Chapter 3. The samples were denoted as MO-0Y, MO-0.4Y, MO-2.0Y, and MO-4.0Y. The Characterization techniques used in this chapter are detailed in chapter 3.

4.2.3 Structural parameters, elemental composition, and textural properties of nano-mixed oxides derived from hydrotalcite

Structural parameters calculated from the XRD diffractograms acquired for as-synthesized materials are reported in Table 4.4. The structural parameters *a* and *c* were obtained by the equations of $a=2d_{(110)}$ and $c=d_{(003)}+2d_{(006)}+3d_{(009)}$. The crystallographic parameter *a* ($2d_{110}$) is associated with the average cation-cation distance in the hydroxide layers [63]. The parameter *a* is stable for all materials (3.06 Å), indicating the lack of possible distortions of the lattice. As stated by García-García et al. [326], yttrium can be incorporated into layers of double-layered hydroxides, though its ionic radius is somewhat larger than that of Al and Mg (Mg^{3+}=0.86 Å, Al^{3+}=0.675 Å, Y^{3+}=1.04 Å) [250,327]. The obtained parameter *c* ($d_{003} + 2d_{006}+ 3d_{009}$), which refers to the triple thickness between brucite layers in hydrotalcite structure, decreased for low Y (under 2 wt.%) modified samples in comparison to the non-modified material, except for MO-4.0Y, which increased to 23.51 Å (Table 4.4). For the MO-4.0Y, some deposition of Yttrium on the external surface may be assumed. Moreover, the distance between the brucite-like layers (*c´=c/3*) is in the range of 7.79-7.84 Å, showing the presence of interlayer anions, such as e.g. CO_3^{2-} (7.65 Å) and NO_3^- (8.79 Å) [304,328,329]. The structural parameters revealed that the yttrium loading up to 2.0 wt.% could result in the introduction of this metal into the periclase-like structure. However, the higher content of the yttrium led to the increase of the interlayer space, which was possibly linked with the deposition of the metal on the surface of the layers. This agrees with the textural properties, as the specific surface area of MO-4.0Y significantly decreased compared with that of MO-2.0Y due to their partial blockage.

The elemental composition of nano-mixed oxides obtained by calcination acquired from the XRF method is presented in Table 4.4. All samples revealed nickel content between 16 and 20 wt.%, whereas the content of yttrium was either the same (MO-0.4Y) or close to the nominal amount (MO-2.0Y and MO-4.0Y). According to Li et al. [64], Ni^{2+} can be substituted by Y^{3+}, similarly as

observed in our study (Table 4.4). The calculated M^{2+}/M^{3+} atomic ratios were fairly close to those assumed during the materials synthesis, indicating that the composition of LDHs may be easily controlled as reported before [62].

Table 4.4 Structural parameters (XRD), elemental composition (XRF), and textural properties (BET analysis) of yttrium modified nano-mixed oxides derived from hydrotalcite. Additionally, the nominal values are reported in brackets.

Catalyst	Structural parameters		Elemental composition of the calcined materials			Textural properties of the calcined materials		
	a [Å][a)]	c [Å][b)]	Ni [wt.%]	Y [wt.%]	M^{2+}/M^{3+} [-]	S_{BET} [m^2/g][c)]	V_p [cm^3/g][d)]	d_p [nm][e)]
MO-0Y	3.06	23.45	20	-	3.6 (3.0)	120	0.6	19
MO-0.4Y	3.06	23.38	21	0.4 (0.4)	3.5 (3.0)	120	0.5	15
MO-2.0Y	3.06	23.42	18	1.8 (2.0)	3.4 (3.0)	192	0.6	14
MO-4.0Y	3.06	23.51	16	3.4 (4.0)	3.7 (3.0)	153	0.7	18

[a)] calculated from d-spacing of (110) plane; $a = 2d_{110}$
[b)] calculated from appropriate d-spacings of (003), (006) and (009) planes; $c = d_{003} + 2d_{006} + 3d_{009}$
[c)] specific surface areas calculated from the BET equation
[d)] mesopore volumes obtained from the BJH desorption calculation method
[e)] pore size distribution derived from the BJH desorption calculation method

The textural parameters obtained from the N_2 sorption isotherms for the calcined materials are listed in Table 4.4. All values agree with those previously reported in the literature [44,51,131,138,208,250,304,308,316,322]. The obtained specific surface areas ranged between 120 and 192 $m^2.g^{-1}$ and the highest area was found for the MO-2.0Y catalyst. There are no significant differences regarding BET surface area and pore volume of Ni-containing double-layered hydroxides-derived catalyst when the loading of yttrium is low (≤0.4%) compared with Y-free sample, only the average pore size decreases as the increase of yttrium at a low loading of

yttrium [250,316]. As described in the section before, the structural parameters showed that the yttrium loading up to 2.0 wt.% could result in the introduction of this metal into the periclase-like structure. However, the higher content of the yttrium increased the interlayer space, which was possibly linked with the deposition of the metal on the outer surface of the layers. This agrees with the textural properties, as the specific surface area of MO-4.0 Y significantly decreased due to their partial blockage. The volume of mesopores did not change significantly after yttrium promotion. However, pore diameters diminished for MO-0.4Y and MO-2.0Y catalysts, as compared to the non-promoted material, pointing to the formation of a higher number of smaller pores when yttrium was introduced into the brucite-like layers.

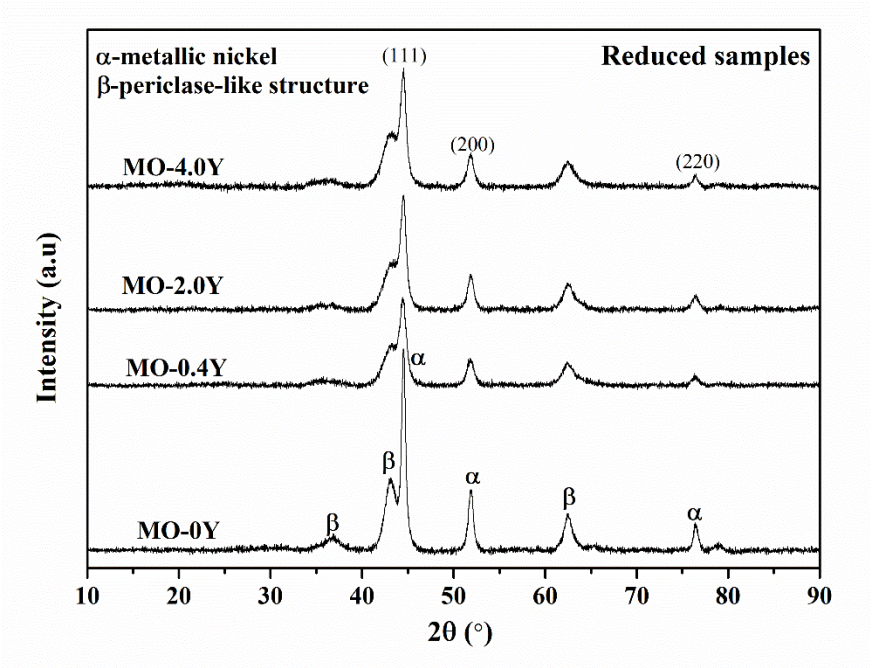

Figure. 4.4. XRD profiles for reduced nano-mixed oxides modified with different yttrium loadings (0.4, 2.0, or 4.0 wt.%) and compared to the un-promoted catalyst (MO-0Y).

Fig.4.4 shows XRD diffractograms of the reduced catalysts, in which metallic nickel phase (ICOD 01-087-0712) is evidenced by the presence of reflections at 2θ ca. 44.5, 53 and 76.5°, corresponding to crystal planes of (111), (200) and (220), respectively. Moreover, reflections arising from the periclase-like structure at 2θ ca. 36.7, 43 and 62.5° are observed, which corresponds to mixed oxides obtained after thermal treatment of double-layered hydroxides [44,250,316]. Table 4.5 reports the size of Ni^0 crystallites, calculated from the 2θ diffraction peak at ca. 52° (corresponding to (200) crystal plane of Ni^0) using the Scherrer equation. The yttrium promotion resulted in a decrease of nickel crystallites size from ca. 13.7 nm for the parent MO to ca. 9.2 nm for MO-0.4Y. The values obtained for MO-2.0Y and MO-4.0Y catalysts were close to the one registered for the un-promoted catalyst, i.e. 12.5 and 12.3 nm, respectively.

Table 4.5 Ni^0 crystallite size for the reduced and spent materials calculated from XRD

Catalyst	Ni^0 crystallite size	
	Reduced samples [nm] [a)]	Spent samples [nm] [a)]
MO-0Y	13.7	9.3
MO-0.4Y	9.2	7.9
MO-2.0Y	12.5	7.6
MO-4.0Y	12.3	7.5

[a)] Calculated from the Scherrer equation at 2θ =52°

4.2.4 Reducibility of catalysts followed by H_2-TPR

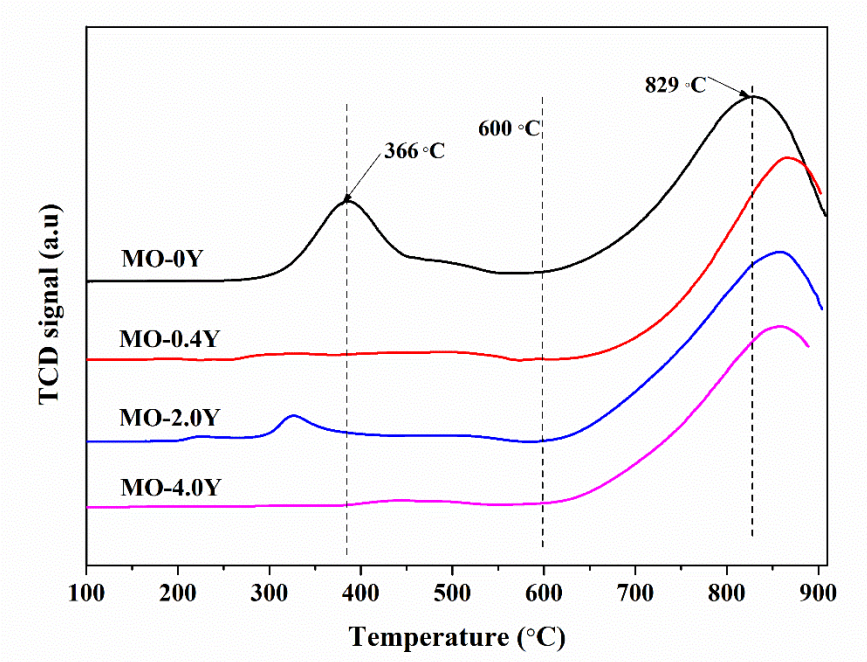

Figure. 4.5. H_2-TPR profiles for mixed oxides modified with different yttrium loadings (0.4, 2.0, or 4.0 wt.%) compared to the non-promoted catalyst (MO-0Y).

Fig.4.5 shows the H_2-TPR of calcined mixed oxides (MO). As demonstrated in other reports, the yttrium cannot be reduced under the conditions used in the measurements [64,325]. The reduction profile of MO-0Y has two main reduction bands that centered at 366 °C and 829 °C, which corresponds respectively to the reduction of nickel oxides weakly bonded with the double-layered hydroxides and nickel species that are incorporated into the structure of hydroxides [50,58,64,250,325,330]. The high-temperature peak shifts towards higher temperatures for all Y-promoted catalysts (Table 4.6, 858-866 °C), which indicates stronger interaction between nickel oxide species and the support matrix in comparison with the Y-free sample [250]. For 2.0 and 4.0 wt.% of Y, the shift of the latter peak was less pronounced, as shown in Table 4.6, indicating less strong metal-support interaction. This might be due to the segregation of yttrium or lattice

substitution of nickel species by yttrium [64]. The reduction peaks at temperatures lower than 600 °C presented low intensity for Y-modified samples in comparison to the un-promoted catalyst (MO-0Y), which means that the loading of Y results in a decreased reducibility. This phenomenon was already observed in hydrotalcite derived mixed oxides catalysts modified by Y and Zr in CO_2 dry reforming reaction, in which the adding of Y and Zr resulted in a decrease of the reducibility of nickel [58,250]. As calculated in Table 4.6, the highest H_2 consumption (1.67 mmol) was obtained for the Y-free mixed-oxide sample. After the introduction of yttrium, the H_2 consumptions (1.15-1.38 mmol) of yttrium-promoted mixed oxides decreased in contrast to the yttrium-free sample, demonstrating decreased reducibility of NiO for yttrium-promoted mixed oxides.

Table 4.6 H_2 consumption according to H_2-TPR analyses

Catalyst	Temperature (°C)		H_2 consumption (mmolH_2/g)		
	<600	>600	<600	>600	Total
MO-0Y	386	829	0.37	1.30	1.67
MO-0.4Y	320	866	0.07	1.09	1.16
MO-2.0Y	327	858	0.11	1.27	1.38
MO-4.0Y	444	858	0.05	1.10	1.15

4.2.5 Basicity of the catalysts derived from CO_2-TPD

Fig.4.6 shows the CO_2-TPD profiles of the reduced MO catalysts. Three types of CO_2 desorption peaks could be observed with a maximum temperature of 138, 203, and 364 °C for the MO-0Y sample, which refers to weak, medium (intermediate), and strong basic sites, respectively [63,138,250,307]. Similar peaks were found for yttrium-promoted mixed oxides materials, with the maximum temperature of CO_2 desorption peak shifted towards lower temperature with the

increasing yttrium content compared to the MO-0Y sample, indicating that the loading of Y changed the number and distribution of the basic sites. This phenomenon was also observed in other literature [250].

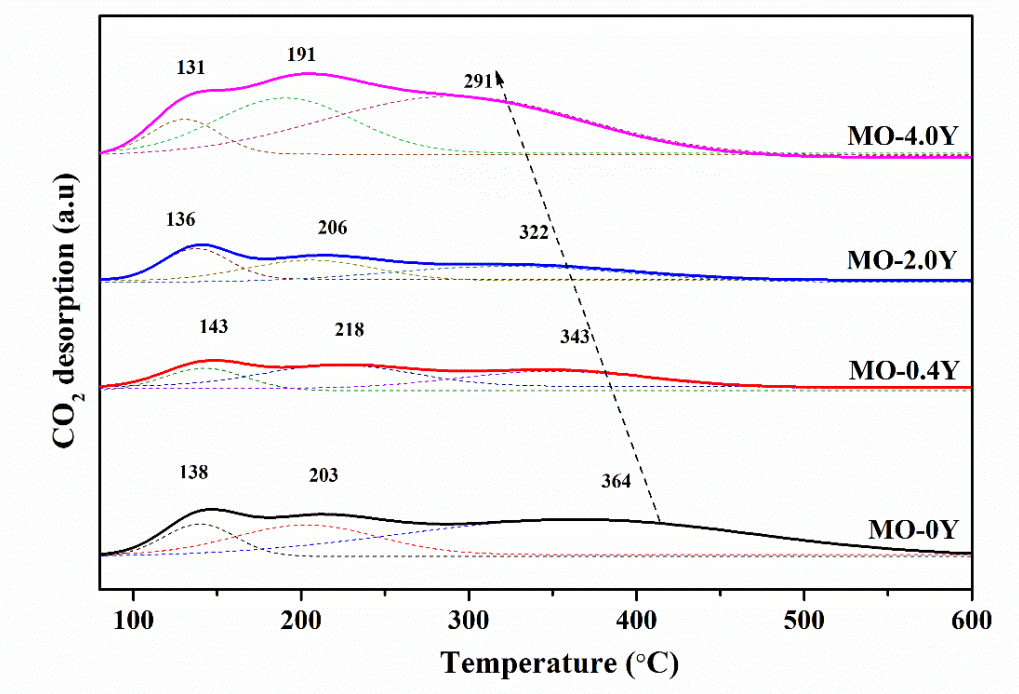

Figure. 4.6. CO_2-TPD profiles for mixed oxides catalysts

As calculated in Table 4.7, the amount of different type of basic sites for the Y-modified samples increased with the increase of yttrium loading (from 0.4 to 4.0 wt%) and the total number of basic sites also increased with the increased Y content, with MO-4.0Y having the highest number of each type of basic sites as well as the total basic sites. Compared to the basicity of the MO-0Y sample, the materials with 0.4 wt.% and 2.0 wt.% of Y showed lower content of total basic sites and individual types of basic sites (weak, medium, or strong). But compared to that of the MO-0Y, the percentage share of weak or intermediate basic sites for MO-0.4Y and MO-2.0Y was higher, with lower content of the share of strong basic sites, meaning that the doping of yttrium

significantly changed the distribution of basic sites on Y-modified samples. In conclusion, the introduction of Y with low content (0.4 wt.% and 2.0 wt.%) increases the share of medium basic sites at the expense of strong type. The highest share of medium-strength basic sites was found on the MO-0.4Y sample.

Table 4.7 Basicity of the studied catalysts, calculated from TPD-CO_2 for the reduced materials.

Catalyst	Basic sites [μmol/g]				Basic sites distribution [%]		
	Weak	Medium	Strong	Total basicity	Weak	Medium	Strong
MO-0Y	16.4	43.9	46.3	106.6	15.4	41.2	43.4
MO-0.4Y	9.4	33.7	14.6	57.7	16.2	58.5	25.3
MO-2.0Y	11.6	35.2	26.4	73.2	15.8	48.1	36.1
MO-4.0Y	41.4	91.5	91.2	224.1	18.5	40.8	40.7

4.2.6 Catalytic performance tests for CO_2 methanation

The catalytic tests of CO_2 methanation were performed in the same reactor presented above. Prior to the catalytic tests, the calcined materials were reduced in situ from room temperature to 900 °C with a heating rate of 5°C/min under reduction gas (5%H_2/Ar: 100 ml/min) and kept 1 h at 900 °C. The reduction temperature was 900 °C because the nickel species could be reduced thoroughly at 900 °C according to the TPR result, which was also used in other literature [131]. After the reduction, the reactor was cooled down to 200°C and the reaction mixture was introduced with a molar ratio of Ar/H_2/CO_2=25/60/15 and the GHSV of 12,000 h^{-1}. Subsequently, the methanation tests were performed in the temperature range from 200 to 400 °C with a temperature step of 50 °C, which are appropriate conditions for Ni-containing mixed oxides, as reported in many works

[131,322]. At each plateau of temperature, the catalyst was kept for 30 min, corresponding to a steady-state measurement. The flow rates of inlet and outlet were measured by flowmeter at each temperature when the reaction was stable (after 30-45 minutes of reaction). And the measured flow rates and the compositions obtained from GC were used to calculate the CO_2 conversion (X_{CO2}) and CH_4 selectivity (S_{CH4}) as reported in Chapter 3.

Fig. 4.7 presents the CO_2 conversion and Fig.4.8 presents the methane selectivity measured during catalytic experiments for the studied mixed oxides (MO) promoted with different amounts of Y as a function of reaction temperature.

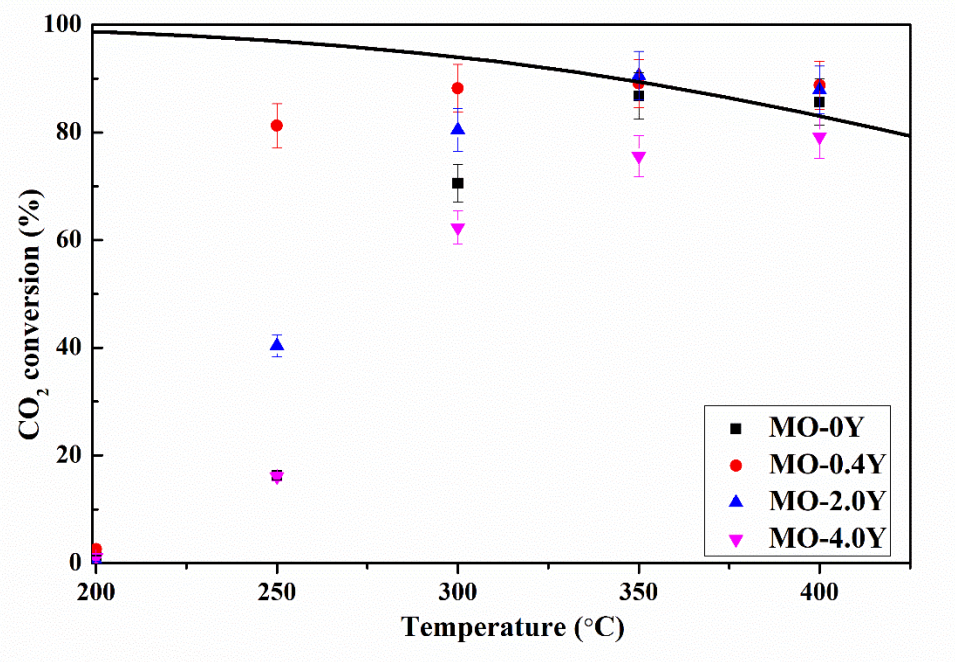

Figure. 4.7. CO_2 conversion of the studied mixed oxides catalysts (MO-0Y, MO-0.4Y, MO-2.0Y, MO-4.0Y). Experimental conditions of CO_2 methanation: GHSV=12000 h^{-1}, total flow 100 mL/min, $CO_2/H_2/Ar$ =15/60/25.

The thick continuous line shown in Fig.4.7 represents the thermodynamic equilibrium calculated for the conditions used in this work [63,138]. According to thermodynamics, CO_2 methanation is favored at low temperatures and it decreases with the increasing temperature due to the co-

existence of parallel reactions, such as reverse water-gas shift (RWGS) or reforming [63,331]. The latter results in undesired side products, among them carbon monoxide [322]. All mixed oxides were catalytically active in CO_2 methanation. The obtained conversions at 250 °C were much lower than the thermodynamic limitations, except for the MO-0.4Y catalyst. Depending on the Y-loading a change in the catalytic performance of the catalysts was observed. Nevertheless, the increase of the catalytic activity was not directly correlated to the increase of yttrium loading. For both series of results registered at 250 °C and 300 °C, the sequence for the CO_2 conversion was: MO-0.4Y > MO-2.0Y > MO-0Y > MO-4.0Y. CO_2 conversion increased at 250 °C from 16% for MO-0Y to 40% and 81% for MO-2.0Y and MO-0.4Y, respectively, and at 300°C, from 71% for MO-0Y to 80% and 88% for MO-2.0Y and MO-0.4Y, respectively. At both temperatures, 250 °C, and 300 °C, the selectivity towards methane was higher than 98.5%, with very low differences between the Y-promoted catalysts (Fig.4.8). However, in the tested temperature range, both the CO_2 conversion and CH_4 selectivity for MO-4.0Y decreased in comparison to MO-0Y. This could have been caused by the deposition of the yttrium on the external surface of the support matrix and the weaker metal-support interaction, as confirmed by XRD and TPR-H_2.

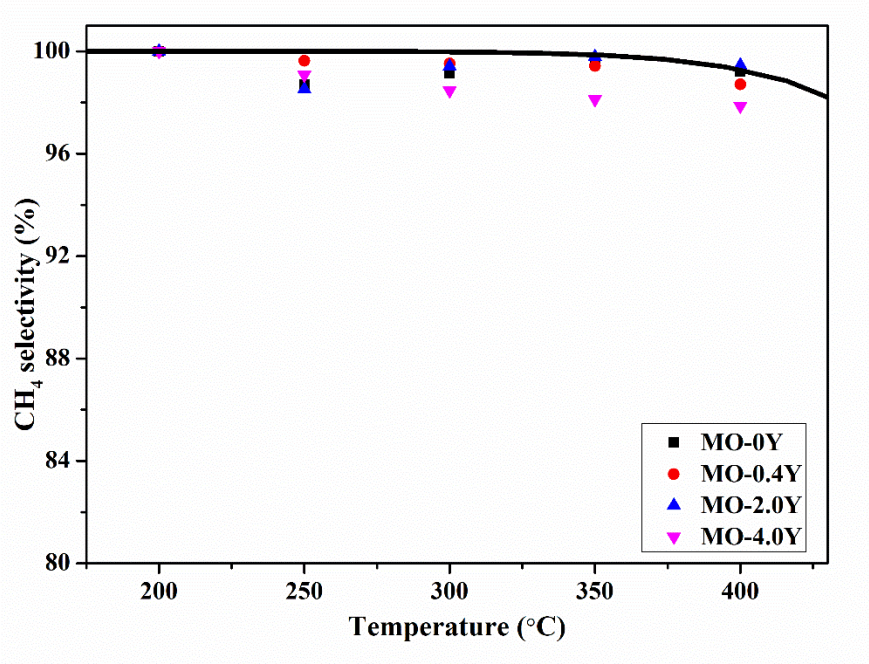

Figure. 4.8. CH_4 selectivity of the studied mixed oxides catalysts (MO-0Y, MO-0.4Y, MO-2.0Y, MO-4.0Y). Experimental conditions of CO_2 methanation: GHSV = 12000 h^{-1}, total flow 100 ml/min, $CO_2/H_2/Ar$ = 15/60/25.

The enhancement of the activity of Y-promoted catalysts except MO-4.0Y can be partially explained by the smaller Ni^0 crystallite size in comparison to the non-promoted sample, which is also found for La-promoted Ni-containing hydrotalcite-derived mixed oxides in CO_2 methanation [206].

Simultaneously, the MO-0.4Y catalyst showed the highest percentage share of intermediate-strength basic sites. Pan et al. [332] claimed that Lewis acid-base sites are involved in the CO_2 methanation mechanism and the CO_2 adsorbed on strong basic sites did not participate in the reaction and the medium-strength basic sites played an important role in the reaction. In the current study, a linear correlation between CO_2 conversion and the percentage share of medium-strength basic sites can be drawn at 250 °C and 300 °C (Fig.4.9). It shows that the CO_2 conversion increase as the increase of the percentage share of medium-strength basic sites.

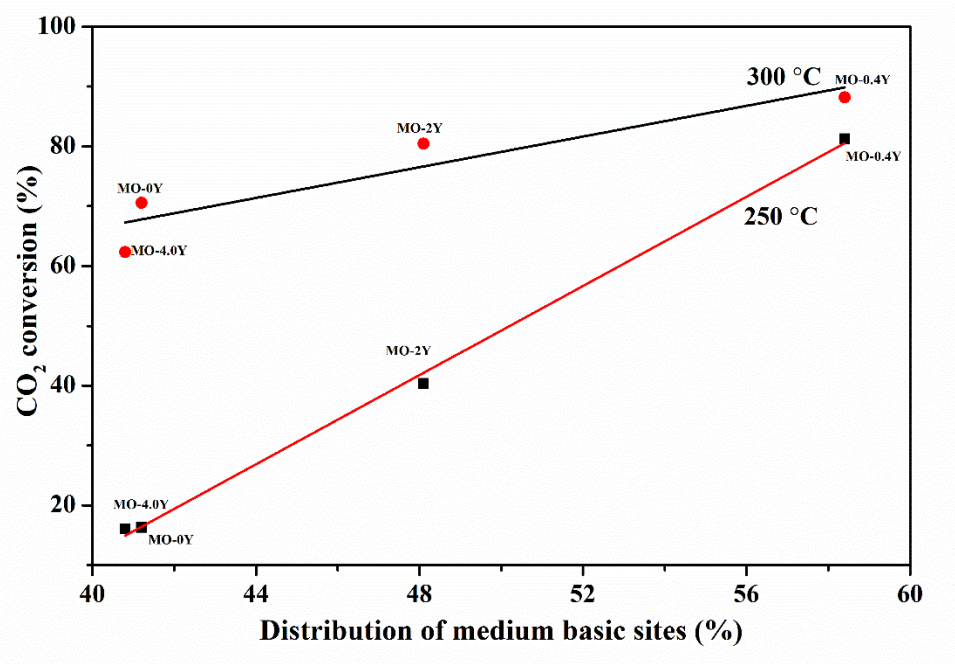

Figure. 4.9. CO_2 conversion at 250 °C and 300 °C versus percentage share of medium basic sites of tested catalysts, the black points represent CO_2 conversion at 250 °C and the red points represent CO_2 conversion at 300 °C

The medium-strength basic sites play a significant role in the methanation process. Wierzbicki et al. [131,322] found that there was a good linear correlation between the number of medium-strength basic sites and the CO_2 conversion on the unpromoted and La-promoted LDHs catalysts. This work confirms that the percentage of medium-strength basic sites has a considerable influence in the case of carbon dioxide methanation on Ni-containing Y-modified mixed oxides catalysts. Besides, the TPR results show that MO-0.4Y has the highest intensity of metal-support interaction compared to that of other samples [333]. In conclusion, the decreased nickel particle size, increased share of medium-strength basic sites, and stronger metal-support interactions found for MO-0.4Y catalyst greatly contributed to the enhanced catalytic activity in CO_2 methanation.

4.2.7 On the evolution of spent samples

4.2.7.1. Structural Evolution

Ni^0 crystallite sizes calculated for the spent catalysts are reported in Table 4.5. A decrease in the crystallite size was found for the spent catalysts compared to that of the reduced samples, in agreement with Świrk et al. [250] and Dębek et al. [58] on similar materials for other CO_2 reactions. This can be explained by the loss of crystallinity of the Ni phase due to its possible re-dispersion of nickel particles. The decreased crystallite size of Ni^0 species also indicates that no sintering happened during the reaction.

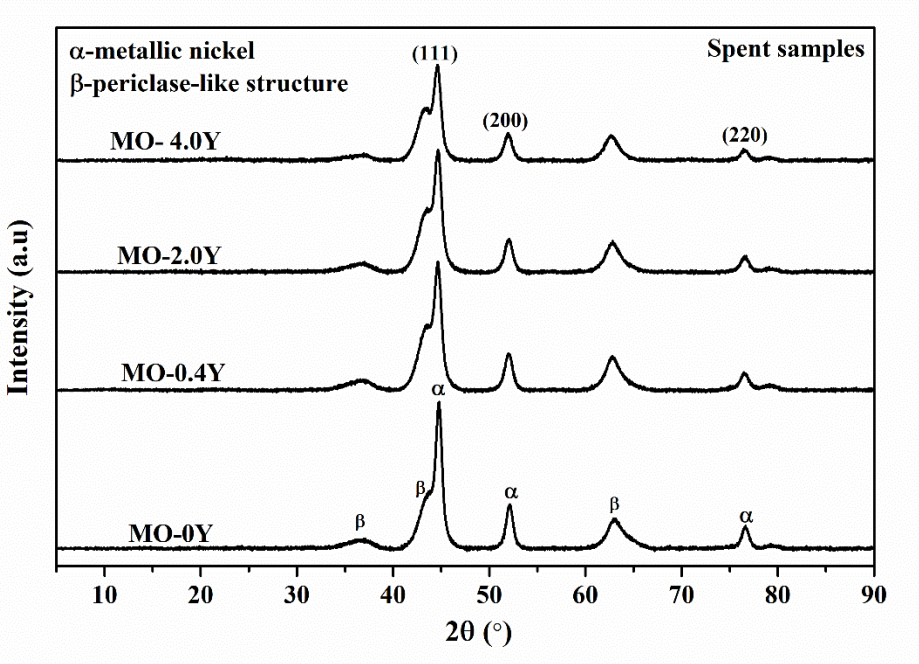

Figure. 4.10. XRD diffractograms of spent Y modified mixed oxides (0.4, 2.0, or 4.0 wt.%) as compared to the unpromoted catalyst (MO-0Y).

After the methanation tests, no reflections corresponding to graphitic carbon (at 2θ=27˚) were observed in the diffractograms of the spent catalysts (Fig.4.10). Thus, extensive coking with

graphite formation may be excluded. This is in agreement with the studies of other authors e.g. Wierzbicki et al. [131], who confirmed the absence of carbon deposition on Ni/Al LDHs-like catalysts for CO_2 methanation.

4.2.7.2. Surface evolution

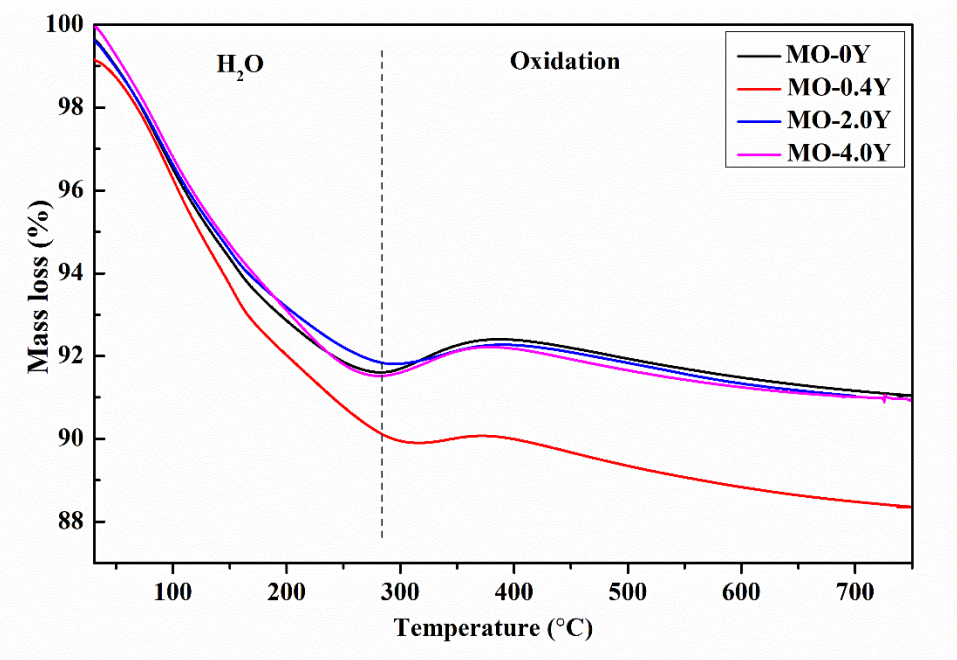

Figure. 4.11. TGA plots of the studied catalysts (MO-Y0, MO-Y0.4, MO-Y2.0, MO-Y4.0) were tested in the methanation process.

Thermogravimetric analyses were carried out for the spent catalysts to verify if other non-crystalline carbon species may have been formed (Fig.4.11). From Fig.4.11, two mass loss regions can be observed for all tested MO samples, corresponding respectively to the removal of physically adsorbed water (<250°C) and a higher temperature region (>400°C) corresponding to oxidation of metallic nickel to nickel oxide and the removal of residues. From TGA, one can conclude that no significant amount of carbonaceous species was present on the surface of the spent catalysts. To

confirm this, temperature-programmed oxidation tests were performed from RT to 650 °C on MO-0Y (Fig. 4.12a) and MO-0.4Y catalysts (Fig. 4.12b).

(a)

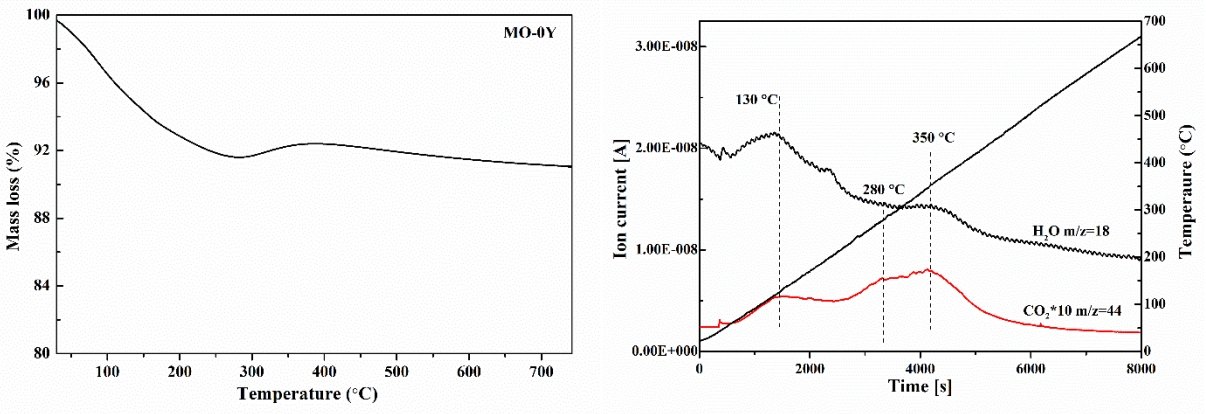

(b)

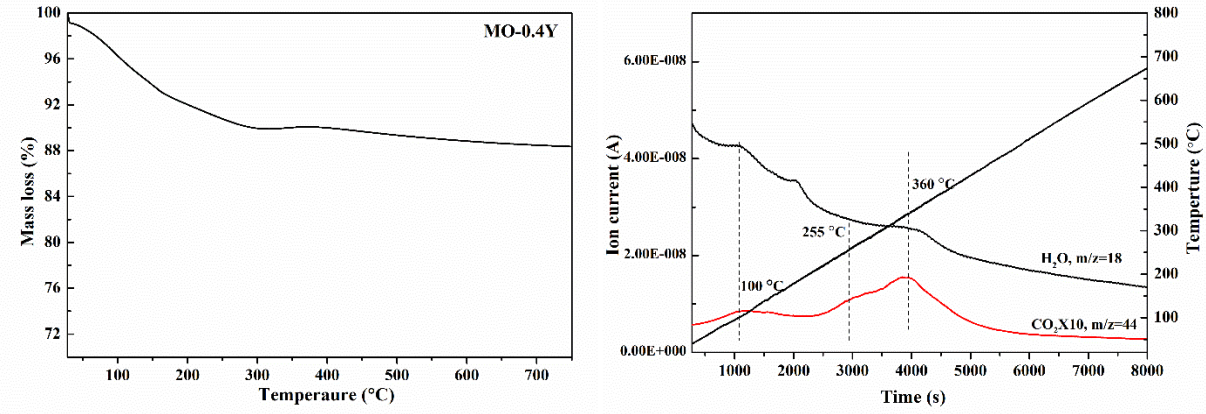

Figure. 4.12. Temperature-Programmed Oxidation results followed by mass spectroscopy (H_2O m/z=18 and CO_2 m/z=44x10) on catalysts; a) unpromoted MO catalysts, b) MO-0.4Y.

From Fig.4.12a and b, one can observe that CO_2 formation corresponding to the decomposition of carbonaceous species (250-500°C) is very low, confirming insignificant amounts of the formed

carbonaceous species during the CO_2 methanation reaction on the Y promoted catalysts. Thus, the main byproduct of the reaction is CO.

4.2.8 Conclusions of mixed oxides from LDHs

Yttrium-promoted Ni/Mg/Al hydrotalcite-derived catalysts were synthesized using the co-precipitation method at constant pH. Then, the catalysts were characterized by low-temperature N_2 sorption, X-ray diffraction, elemental analysis, and temperature-programmed reduction/desorption (H_2-TPR and CO_2-TPD), and tested as catalysts in CO_2 methanation at GHSV =12000 h^{-1} using a mixture of $CO_2/H_2/Ar$ =15/60/25.

The addition of Y affected the CO_2 adsorption capacity of the materials by changing the distribution of the basic sites, especially those of medium strength. As proven by H_2-TPR, the yttrium promotion influenced the nickel/support interaction. After the introduction of yttrium, a shift of reduction peak towards higher temperatures was observed, which was attributed to the segregation of Y on the support. The Y addition affected strongly the catalytic activity in CO_2 methanation, increasing the CO_2 conversion at 250 °C from 16% for MO-0Y to 40 and 81% for MO-2.0Y and MO-0.4Y, respectively. This could be explained by both increased distribution of medium-strength basic sites and significantly smaller metallic nickel particle size of Y-promoted catalysts. Additionally, the metallic nickel crystallite size decreased after the reaction, which points to the reorganization of Ni at the surface of the support, which could contribute to the increase of the catalytic activity in the moderate temperature region. The selectivity towards methane formation was found around 98 to 99% at 250°C. It is worth noting that the only products of the reaction registered were H_2O, CH_4, and CO. The XRD, TGA, and TPO analyses confirmed only traces of carbon in the spent catalysts.

The mixed oxides Ni catalysts derived from LDHs showed high activity and selectivity in CO_2 methanation. The yttrium promoter showed high improved performance for mixed oxides Ni catalysts.

4.3. Conclusions and perspectives

Ni catalysts based on CeO_2, ZrO_2, and MOF, etc. materials showed high activity and selectivity towards CO_2 methanation [136,212,334]. However, such materials still have a high cost for large-scale applications. The development of Ni catalysts based on low-cost materials or natural materials such as clays, ashes, and bentonite, etc. can help reduce the cost, which has received intensive attention [239,335–340].

In this chapter, the diatomite-supported Ni catalysts and yttrium-promoted Ni/Mg/Al hydrotalcite-derived catalysts were developed to catalyze the CO_2 methanation reaction. Although the diatomite-supported Ni catalysts did not show high performance, they can be improved further by other methods, which will be studied in the future. Their promotion by elements such as La, Y, and Fe would be interesting in a future study.

Ni-based hydrotalcite-derived catalysts are already known to be efficient catalysts for CO_2 methanation reaction. Promotion by Fe and La had shown interesting properties, however, the promotion by Y was never studied before. Herein, it was demonstrated that yttrium-promoted Ni/Mg/Al hydrotalcite-derived catalysts showed high performance at low temperatures during the reaction, indicating a high potential towards commercialization. Thus, the purpose of the next chapter is to use CeO_2 and Y_2O_3 as supports for methanation reaction.

Chapter V

Ni/CeO_2 nanoparticles promoted by yttrium doping as catalysts for CO_2 methanation

5. Ni/CeO_2 nanoparticles promoted by yttrium doping as catalysts for CO_2 methanation

5.1 Introduction

It is well known that noble metal-based catalysts perform good low-temperature activity and selectivity in CO_2 methanation [106]. However, the high cost and low availability make them unappropriated towards application. In such a case, Ni catalysts supported on various oxides become good alternatives for methanation reaction thanks to their benefits of relatively high catalytic activity, low cost, and high availability [187]. Supports with high surface area, appropriate basicity, and strong metal-support interaction, play important roles in enhancing CO_2 conversion and selectivity towards CH_4. Various supports have already been studied for nickel-based catalysts, such as SiO_2 [341], diatomite [143], α-Al_2O_3 [342], ZrO_2 [343], hydrotalcite derived mixed oxides [131,138,206,208], MgO [344], TiO_2 [345], mesoporous oxides [171,346–348], CeO_2, and Y_2O_3 [194,197,210,349,350]. As presented in chapter 4, low-cost materials like diatomite and hydrotalcite-derived mixed oxides were introduced.

In the meantime, CeO_2 had attracted plenty of interest because of its unique redox property. It can create oxygen vacancies during the redox process Ce (III)/Ce (IV), promoting the activation of CO_2 [351]. Tada et al. [170] reported that Ni/CeO_2 catalysts showed higher CO_2 conversion and CH_4 selectivity at low temperatures compared to Ni catalysts supported on α-Al_2O_3, TiO_2, and MgO. Such effect was attributed to the formation of oxygen vacancies on the surface of partially reduced CeO_2, promoting the activation of CO_2 and adsorption of CO_2 derivatives. Zhou et al. [192] prepared CeO_2 with different structures and used the synthesized CeO_2 as support to prepare

Ni/CeO_2 catalysts. The characterization data and CO_2 methanation results revealed that the Ni/CeO_2 catalyst with a well-ordered mesoporous structure had high specific surface area, strong metal-support interaction, smaller Ni^0 particle size, and higher dispersion of active species than Ni over other ceria oxides, thus showing the highest CO_2 conversion and the best stability at T >260°C. The study of the CO_2 methanation mechanism over Ni/CeO_2 and Ni/Al_2O_3 catalysts revealed that the high methanation activity and selectivity of Ni/CeO_2 were attributed to the presence at the nickel-ceria interface of active sites for CO_2 dissociation, while dispersed metallic Ni particles activated H_2 [159]. Thus, Ni/CeO_2 based catalysts able to chemisorb and dissociate CO_2 have been widely investigated.

Although several reports claim Ni/CeO_2 as a potential good catalyst for methanation, the catalytic stability with time on stream is still a brake to its industrialization due to the occurrence of side reactions. Many efforts have been devoted to promoting the activity and stability of Ni/CeO_2 catalysts e.g., tailoring the structure of CeO_2, promoting the dispersion of nickel species, increasing the metal-support interaction [139]. Yu et al. [350] added in the preparation of Ni/CeO_2 nanoparticles g-C_3N_4 as a sacrificial and protective template. Several characterization methods used to investigate such catalysts revealed enhanced interaction between Ni and CeO_2 and decreased Ni particle size on the modified catalyst, thus facilitating the adsorption and dissociation of the reactants with higher methanation activity and CH_4 selectivity.

Bian et al. [196] prepared Ni/CeO_2 catalysts with tunable CeO_2 structure i.e. ceria nanorods (NR) and ceria nanocubes (NC) and investigated their catalytic performance in CO_2 methanation. Among the prepared catalysts, the Ni/CeO_2 (NR) exhibited higher conversion and selectivity towards CH_4 at low temperature, which was attributed to the higher concentration of Ce (III) on the surface.

Yttrium has been reported to be an effective promoter of nickel catalysts on double-layered hydroxides for CO_2 methane reforming, because it enhances the redox properties of nickel, increases the specific surface area, and promotes weak and medium basic sites in comparison with non-modified samples [144,250].

Moreover, yttrium has been proven to stabilize ZrO_2 at high temperatures [352]. Kesavan et al. [353] reported Ni/YSZ (Yttrium stabilized ZrO_2) catalysts prepared by different methods for CO_2 methanation and found that the Ni/YSZ synthesized by wet impregnation with EDTA complex showed remarkable stability on time on stream, without deactivation under high CO_2/H_2 ratio. To the best of our knowledge, until now, almost no research concerning the effect of yttrium on Ni/CeO_2 catalysts for CO_2 methanation has been reported.

In this chapter, Ni catalysts supported on yttrium-modified CeO_2 prepared by the hydrothermal method were studied in CO_2 methanation. The present work aims to investigate the relationship between the modification induced by yttrium promotion on the physicochemical properties and catalytic performances of Ni/CeO_2 catalysts. For this purpose, the catalysts as calcined, reduced, or spent (after methanation test or steady-state test) samples were characterized by XRF, XRD, TEM/HRTEM, EDX, H_2-TPR, CO_2-TPD, N_2 adsorption-desorption, XPS, and TGA techniques. The structure-activity relation was discussed.

5.2 Catalyst preparation and physicochemical techniques

The CeO_2 nanoparticles and Ni/CeO_2 nanoparticle catalysts were prepared by the hydrothermal method and wet impregnation method, respectively. The detailed processes were listed in 3.1.3 of

Chapter 3. The names of catalysts were designed as 5Ni/CeO_2, 5Ni/Y_2O_3, and 5Ni/CeO_2-Yx (Y content, wt.%), respectively.

Elemental analysis of the catalysts was carried out using an X-ray fluorescence wave-dispersive spectrometer (XRF 1800 Shimadzu). According to XRF analyses, the real loading of Ni and Y in the prepared catalysts was equal to the nominal one ±10%.

The specific surface areas (SSA), pore-volume, and pore size of the materials were measured by N_2 adsorption-desorption isotherms using a Micromeritics ASAP2020 system (Carried out in the Italian lab, which is different from the Belsorp Mini II apparatus in 3.3.3). Before analysis, the samples were degassed in a vacuum at 250 °C for 2 h, then the measurement was performed at liquid nitrogen temperature (-196 °C). The Brunauer–Emmett–Teller (BET) method was used to calculate the SSA. The BJH method was applied to estimate the pore volume and average pore size.

The crystalline structure of calcined, reduced, and spent samples was determined by Powder X-ray diffraction patterns (XRD), performed on a Bruker D5000 diffractometer equipped with a Cu Kα anode and graphite monochromator (different from the apparatus in 3.3.5). The data were recorded in a 2θ range of 10°-80° or 20°-80° (depending on the crystalline nature of the samples) with a step size of 0.05° and time per step of 5 s. The crystalline phases of samples were analyzed according to ICSD files (Inorganic Crystal Structure Database). The mean crystallite size was calculated by the Debye-Scherrer equation shown in Eq. 13 (3.3.5).

The reducibility of the catalysts was evaluated by temperature-programmed reduction (H_2-TPR) measurements. The experiments were carried out in a Micromeritics Autochem 2950HP apparatus (different from the apparatus in 3.3.1) equipped with a thermal conductivity detector (TCD).

Before the TPR procedure, the samples (125 mg) were pretreated with the gas mixture 5% O_2/He (50 mL/min) at 350 °C for 30 minutes, then the furnace was cooled down to room temperature under pure He flows. After pretreatment, the samples were heated from ambient temperature to 1050 °C with a heating rate of 10 °C/min under the gas mixture of 5% H_2/Ar (30 mL/min). The H_2 consumption values were calculated, with a precision of ±10%, by integration of the TPR curves registered by TCD through a calibration procedure. On the basis of H_2 consumption in the α peak, the oxygen vacancy content (%), V_0 (%) was calculated according to the Eq. (5.1.1):

$$V_0(\%)=\frac{(\text{mmol O2}-/\text{gcat})}{(\text{total mmol O2}-/\text{gcat})}*100 \qquad \text{Eq. (5.1.1)}$$

where the mmol O^{2-}/g_{cat} correspond to the mmol of H_2/g_{cat} from α peak and the total mmol O^{2-}/g_{cat} where calculated on the basis of CeO_2 or CeO_2-Y content/g_{cat}).

Furthermore, the basicity of catalysts was investigated through CO_2 temperature-programmed desorption (CO_2-TPD) carried out in a BEL-M instrument as shown in 3.3.2 of Chapter 3 (BEL Japan Inc.) equipped with a thermal conductivity detector (TCD). Prior to adsorption, the samples (60 mg) were reduced under 5% H_2/Ar flow (50 mL/min) at 550 °C. Then, the furnace was cooled down to 80 °C under the same condition, following pretreatment under pure He (50 mL/min) for 15 min. Afterward, the adsorption of CO_2 was performed in a CO_2 mixture (10 % CO_2/He, 50 mL/min) for 1 h, then, pure He was then used to remove the physically adsorbed CO_2 for 30 min at 80 °C. Finally, the temperature-programmed desorption procedure was carried out from 80 °C to 550 °C with a heating rate of 10 °C/min under pure He flow of 50 mL/min.

Also, transmission electron microscopy (TEM) and Energy Dispersive X-ray spectroscopy (EDX) analyses were carried out with JEM-2010 and JEM-2100Plus (JEOL, Tokyo, Japan) transmission

electron microscopes shown in 3.3.7 of Chapter 3 for the reduced catalysts. Before measurement, the samples were reduced (reduction condition: 550 °C for 1 h in 5% H_2/Ar).

The X-ray photoelectron spectroscopy (XPS) measurements were performed with a VG Microtech ESCA 3000Multilab spectrometer, equipped with a dual Mg/Al anode, with an excitation source of unmonochromatized Al Kα radiation (1486.6 eV). See 3.3.8 of Chapter 3 for more detail.

Moreover, thermogravimetric analyses (TGA) of the CeO_2 supported catalysts, previously reduced at 550 °C for 1 h, were performed in a TGA/DSC1 STAR System (different form 3.3.9 in Chapter 3) from Mettler Toledo Inc. The sample of 15 mg was pre-treated in N_2 (30 mL/min) from 25 °C to 500 °C with a heating rate of 10 °C/min, holding time at 500 °C for 15 min, then, it was cooled down under N_2 atmosphere to 150 °C. At 150 °C, the sample was saturated with pure O_2 (30 mL/min) for 1 h and cooled to 25 °C still under O_2. Finally, the sample was heated, under N_2 (30 mL/min), from room temperature up to 600 °C (ramp rate 5°C/min), thus, the removal of physical and chemisorbed oxygen species occurred and the weight loss was taken into account in order to evaluate the surface oxygen vacancies content of the sample. The evolution of gaseous species occurring during the above four steps was monitored by online mass quadrupole (Thermostar TM, Balzers).

5.3 Elemental content, textural properties, structural parameters, and surface compositions of the catalysts

As determined by XRF analyses, the real loading of Ni and Y in the prepared catalysts was equal to the nominal one ±10%. In Table 5.2, the XRF-derived chemical composition is listed. The textural properties of the supports and calcined catalysts were measured by the N_2

adsorption/desorption technique. The SSA, pore volume, and average pore size of the supports and catalysts are displayed in Table 5.1. The results show that the SSA, pore volume, and pore diameter values of Y-modified supports increase with the increase of yttrium loading from 0.5 to 5.0 wt % of Y. The textural properties of the calcined catalysts and supports were measured by the N_2 adsorption/desorption technique. The specific surface areas (SSA), pore volume, and average pore size of such samples are displayed in Table 5.1. It results that the SSA, pore volume, and pore diameter values of Y-modified catalysts increase with the increase of yttrium loading from 0.5 to 2.0 wt.% of Y, then surface area and pore volume slightly decrease for 5 wt.% of Y compared to those of yttrium-free sample, while still higher pore diameter was observed for such sample, suggesting a change in the pore shape occurring at such high Y content. The highest values were obtained for the 5Ni/CeO_2-Y2.0% sample that is characterized by SSA of 78.9 m^2/g, pore volume equal to 0.29 cm^3/g, and pore diameter of 12.9 nm. This finding suggests that yttrium promotes the improvement of textural properties of Ni/CeO_2 based catalysts. Meanwhile, 5Ni/Y_2O_3 shows the lowest surface area and porosity.

Positive effects induced by yttrium on the textural properties of different types of supports were also reported in the literature [44,50,250]. Swirk et al. [250] studied the effect of Y on Ni-based double-layered hydroxides for dry reforming of methane and found that doping Y inside the matrix promotes the increase of BET surface area. Similar results were found for Ce and Y promoted double-layered hydroxides showing higher BET surface area as compared to the Ce-promoted material without the presence of Y [51].

Table 5.1 Textural properties of the calcined catalysts.

Catalyst	SSA (m^2/g)[a]	Pore Volume (cm^3/g)[b]	Pore diameter (nm)[c]
CeO_2	56.1	0.17	11.2
CeO_2-Y0.5%	65.3	0.22	11.9
CeO_2-Y1.0%	67.5	0.22	12.0
CeO_2-Y2.0%	90.5	0.34	13.1
CeO_2-Y5.0%	90.4	0.33	13.0
Y_2O_3	74.7	0.18	4.7
5Ni/CeO_2	45.7	0.14	10.3
5Ni/CeO_2-Y0.5%	52.7	0.18	11.5
5Ni/CeO_2-Y1.0%	55.9	0.19	11.6
5Ni/CeO_2-Y2.0%	78.9	0.29	12.9
5Ni/CeO_2-Y5.0%	69.7	0.27	12.4
5Ni/Y_2O_3	32.8	0.12	10.6

[a] The specific surface area (SSA) was calculated by the BET method.

[b] The pore volume and [c] pore diameter were calculated by the BJH method applied to the desorption curves.

In order to investigate the structural properties of the catalysts, XRD measurements were registered for calcined, reduced, and spent samples. The XRD patterns are presented in Fig. 5.1.1-5.1.2 (calcined), Fig. 5.2 (reduced) and Fig. 5.3 (spent, after methanation tests), respectively, along with the ICSD reference patterns of NiO (no. 24018), metallic Ni (no. 41508), CeO_2 (no. 28753), Y_2O_3 (no. 193377) and $Ce_{0.9}Y_{0.1}O_{1.95}$ (no. 28808) solid solution. Depending on the nature of catalysts and on the treatment, different angular ranges are displayed.

From Fig. 5.1.1a,b, distinct diffraction peaks of CeO_2 were found for all the catalysts, while signals of the Y_2O_3 crystalline phase were detected only for the Ni/Y_2O_3 sample. In Fig. 5.1.1b the

diffraction pattern of Ni/CeO_2-Y 5.0% was plotted for comparison to exclude any segregation of the yttria phase. No features at 2θ=43.25° corresponding to nickel oxide (NiO) were detected, suggesting high dispersion of nickel species. As for Y-modified CeO_2 supported Ni-based catalysts, as it can be seen in Fig. 5.1.2a, where the enlarged patterns in the angular range 27-30 ° 2θ are reported, the Y doping does not induce any important changes in the CeO_2 structure. The main peaks (111) are all centered between 28.55 ° 2θ (CeO_2 ICSD reference no. 28753, cubic, space group FM-3M) and 28.57 ° 2θ ($Ce_{0.9}Y_{0.1}O_{1.95}$ ICSD reference no. 28808, cubic, space group FM-3M)) so it cannot be excluded that at the highest Y loading (5wt%) possibly a ceria-yttria solid solution is formed. Indeed, thanks to the similar ionic radius some Ce^{4+} ions can be replaced by Y^{3+} with oxygen vacancies formation to compensate for the excess negative charge [51,327]. However, due to the relatively low crystallinity of the samples, no structural refinements were performed. Furthermore, according to ICSD files (references no. 28753 and no. 28808) the structural parameters, d_{111} values, for CeO_2 and $Ce_{0.9}Y_{0.1}O_{1.95}$ references are almost coincident, 3.122 and 3.1207 Å, respectively, so no significant differences are expected in our experimental patterns. On the other hand, if the introduction of Ni^{2+} into the ceria lattice should occur, a decrease of the lattice parameter of ceria is expected due to its smaller ionic radius (0.69 Å), however, it would generate new oxygen vacancies inducing a small expansion of the cell, so the two effects would cancel out.

Meanwhile, a broadening of the diffraction peaks of CeO_2 was also identified with the increasing dopant of yttrium, as can be seen from Fig. 5.1.2a. Accordingly, the particle sizes of CeO_2 in calcined catalysts decreased as the increased content of Y, and the smallest size was obtained for 5Ni/CeO_2-Y5% sample (see Table 5.2). This could partially interpret the increasing BET surface area and porosity values reported in Table 5.1. As for Y_2O_3 supported Ni catalyst, it can be affirmed

that no distinct diffraction peaks of NiO at 43.25° neither at 37.25° 2θ are detectable even magnifying the patterns (see Fig.5.1.2b where the NiO reference file is compared with patterns for $5Ni/Y_2O_3$ and Y_2O_3 characterized by a peak at 43.39° 2θ).

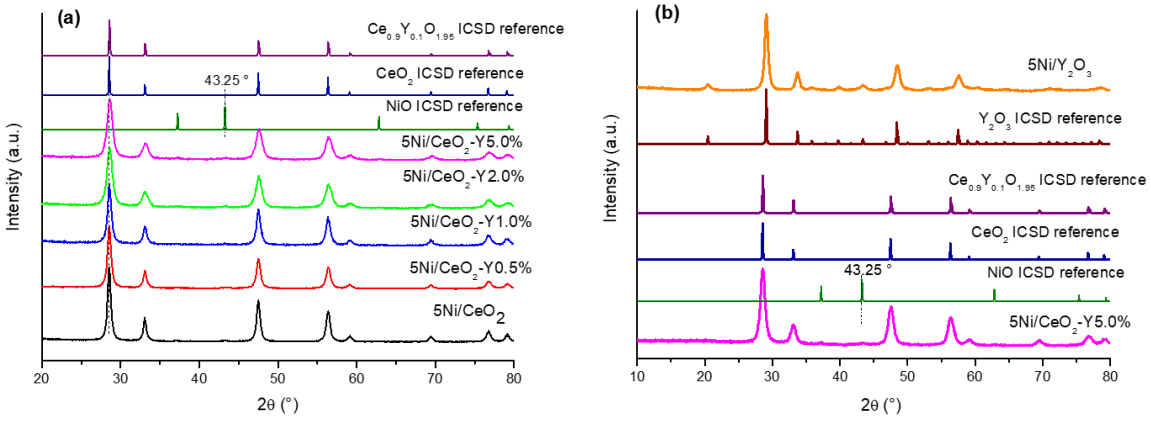

Figure. 5.1.1 XRD patterns of the catalysts calcined at 550 °C for 5 h : (a) Ni/CeO_2 and $NiCeO_2$-Y(0.5-5%) catalysts; (b) Ni/Y_2O_3 and Ni/CeO_2-Y5%. The reference ICSD files are also displayed.

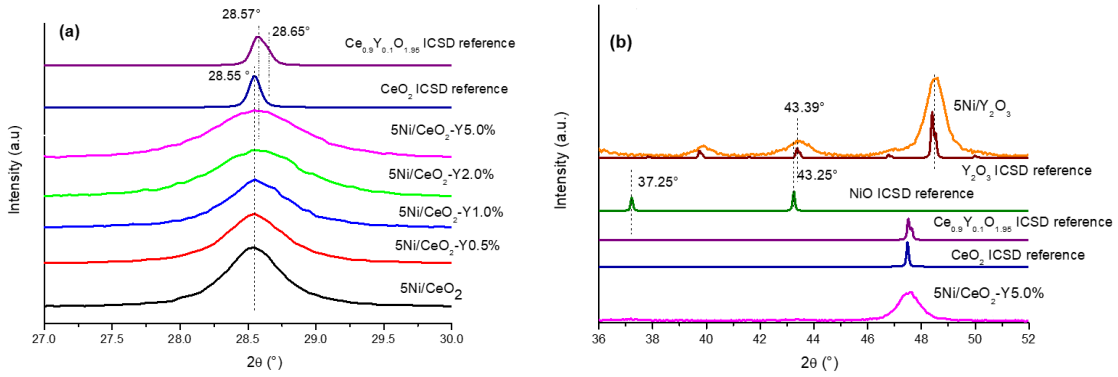

Figure. 5.1.2. XRD patterns in the enlarged range (a) 27-30 °, (b) 36-52 ° 2θ of the catalysts calcined at 550 °C for 5 h

The XRD patterns of the reduced catalysts are presented in Fig. 5.2a,b where the enlarged ranges from 42 to 52 and 20 to 52° 2θ are displayed for Ni/CeO_2, Ni/CeO_2-Y (0.5-5%), and Ni/Y_2O_3,

respectively, along with the ICSD reference files. Such angular ranges were chosen in order to detect any features ascribable to metallic Ni. No diffraction peaks of metallic nickel at 44.4 ° 2θ are detectable in any case which means that the active nickel metals keep highly dispersed on the supports after reduction.

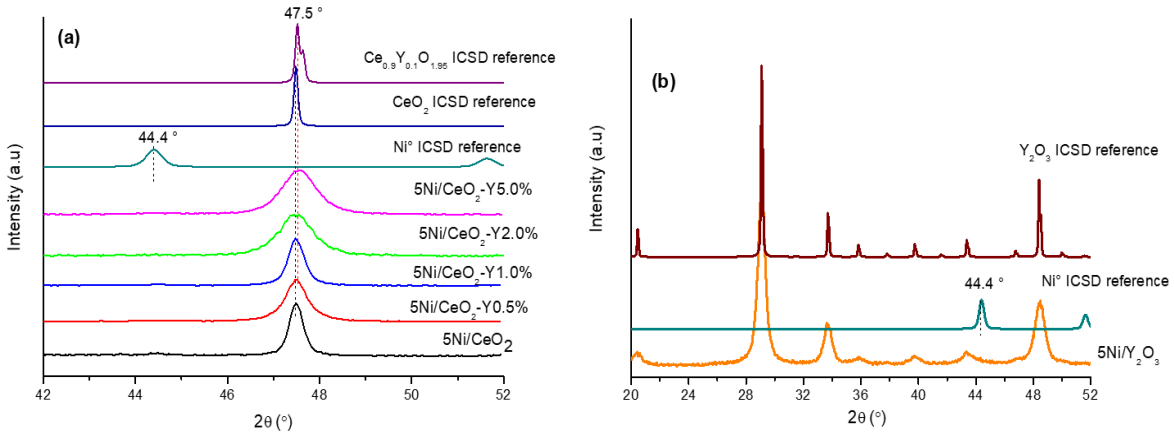

Figure. 5.2. XRD patterns of the catalysts reduced at 550 °C for 1 h in the gas mixture 5% H_2/Ar (100 mL/min). a) Ce based catalysts, b) 5Ni/Y_2O_3

For spent catalysts (after methanation reaction) similar behavior as for the reduced catalysts was confirmed, see XRD patterns shown in Fig. 5.3.

No diffraction peaks of NiO at 43.25 and 37.25° 2θ nor of Ni^0 at 44.4° 2θ were detected for Y-modified catalysts, meaning that no sintering of Ni specie (as Ni or as reoxidized NiO) occurs during the catalytic test. This finding confirms the high dispersion of nickel species and the occurrence of metal-support interaction stabilizing Ni even after reduction treatment and catalytic test.

The particle sizes of CeO_2, CeO_2-Y, and Y_2O_3 were calculated for calcined, reduced, and spent catalysts by the Debye-Scherrer equation and are listed in Table 5.2. The particle size for calcined samples decreases gradually with the increase of Y content, with the smallest size obtained on a 5 wt.% Y-modified sample. For the reduced and spent samples, similar trends were also registered by comparing Ni/CeO_2-Y samples at different Y loading, but the smallest particle size of the support was found on Ni/CeO_2-Y 2.0%.

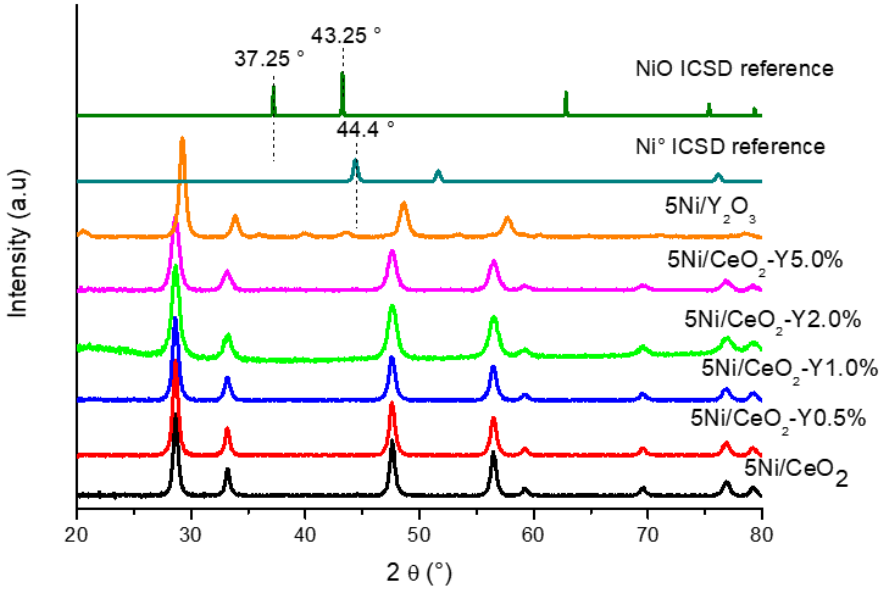

Figure. 5.3. XRD patterns of catalysts after activity test; Reactivity condition: CO_2/H_2//Ar=15/60/25(vol./vol.), flow rate=100 mL/min, WHSV=60,000 mL·g_{cat}^{-1}·h^{-1}, atmospheric pressure, temperature range from 200 to 450 °C.

By comparing the particle size of the support for each catalyst as calcined, reduced, or spent, it results that for Ni/CeO_2 the size slightly increased upon reduction or catalytic test, while for Ni/CeO_2-Y and Ni/Y_2O_3 catalysts, the particle sizes were nearly the same.

Table 5.2 Ni and Y loadings of the calcined catalysts as determined by XRF analysis and support particle size of the calcined, reduced, and spent samples

Catalyst	Ni (wt.%) [a]	Y (wt.%) [a]	Particle size of the support (nm) [b]		
			Calcined	Reduced	Spent
5Ni/CeO_2	4.95±0.5	-	17.2	18.0	18.1
5Ni/CeO_2-Y0.5%	4.95±0.5	0.5±0.05	16.1	16.0	16.3
5Ni/CeO_2-Y1.0%	4.95±0.5	1.0 ±0.1	16.0	16.2	14.8
5Ni/CeO_2-Y2.0%	4.95±0.5	2.0±0.2	11.9	11.6	11.7
5Ni/CeO_2-Y5.0%	4.95±0.5	5.0±0.5	11.4	11.6	12.1
5Ni/Y_2O_3	4.95±0.5	nd	13.3	13.7	13.6

[a] Obtained from XRF analysis

[b] Calculated by Debye-Scherrer equation fitting the 4 strongest peaks of CeO_2 or Y_2O_3 in XRD patterns

In brief, the XRD results of calcined, reduced, and spent samples indicate that the nickel species keep highly dispersed before/after reaction for all catalysts and the particle sizes of supports decreased due to Y doping. The unaffected structural properties of the catalysts after test illustrate the metal-support interaction in the catalysts, which suppress the sintering of catalyst particles [194].

The X-ray photoelectron spectroscopy (XPS) analysis performed over calcined samples was expected to identify the surface compositions and oxidation states of the catalysts. The region of Ce3d, Ni2p, Y3d, and O1s of the catalysts were recorded and analyzed by peak fitting procedure. The percentage of Ce (III)/Ce (IV), lattice oxygen (OL)/surface chemisorbed hydroxyl species (OOH), Ni/Ce or Y/Ce, the binding energy of O1s, $Ni2p_{3/2,}$ and $Y3d_{5/2}$ are listed in Table 5.3. The

survey spectrum and the Y3d, O1s, Ni2p, and Ce3d regions of 5Ni/CeO_2-Y2.0% are shown in Fig. 5.4.

As shown in Fig. 5.4, the doublet of Y3d with two peaks located at 157.4 eV ($Y3d_{5/2}$) and 159.3 eV ($Y3d_{3/2}$) represents the Y^{3+} species [354]. There is no significant difference regarding the $Y3d_{5/2}$ position (presented in Table 5.3) between Y-modified catalysts and pure Y_2O_3 supported catalysts except slight shifts (±0.2 eV), which comply with other reports [355]. The presence of cerium does not influence the position of Y3d peaks, indicating a weak interaction between the two elements. The Y/Ce atomic ratio increase is not linear with the increase of Y content. Uneven distribution of Y between bulk and surface or the presence, in the higher Y content samples, of bigger particles of Y_2O_3 may be responsible for this behavior.

The Ce3d region of 5Ni/CeO_2-Y2.0% shows the typical complex profile, consisted of 10 peaks, which is arisen by the ligand-to-metal charge transfer transitions [356]. Many different approaches deal with the fitting of the Ce3d peak [357,358], in this study, the approach reported by Burroghs et al. [358] was used, with ten components that take into account the spin-orbit splitting of $Ce3d_{5/2}$, $Ce3d_{3/2}$, and others splitting caused by a redistribution of the entire energy spectrum after a core hole is created. There are four components (labeled as v^0, u^0, v^i, u^i) attributed to Ce (III) and six components (labeled as v, u, v^{ii}, u^{ii}, v^{iii}, u^{iii}) attributed to Ce (IV). The data were fitted using the constrains between the corresponding components $3d_{5/2}$-$3d_{3/2}$ given by Preisler et al. [359] The Ce (III) percentages calculated as $(Iv^0+Iv^i)/ (Iv^0+Iv^i+Iv+Iv^{ii}+Iv^{iii})*100$, showed in Table 5.3, ranges between 9 and 19 %, and it can be concluded that the Ce (III) concentration increases with the increasing yttrium content, which was also demonstrated in other literature [360]. The dopant of Y promotes the formation of Ce^{3+}, thus, more oxygen vacancies are created [361].

The O1s region contained two contributions, one due to lattice oxygen (OL) with BE (Binding Energy) of 529.4 ±0.3 eV [355,362], the other attributed to the hydroxyl species chemisorbed on the surface (OOH) with BE of 531.5±0.4 eV[362]. As shown in Table 5.3, the relative amount of OOH increases with increasing Y up to 1-2% (within the experimental error) which could be assigned to the increase of Ce^{3+}. Because the oxygen species adsorbed on Ce^{3+} showed higher stability than that of Ce^{4+} [363].

The $Ni2p_{3/2}$ profile with a peak centered at 855.0±0.2 eV along with a shake-up peak at 862±0.5 eV is typical of Ni(II) [364]. Compared to the 5Ni/CeO_2, the binding energy of $Ni2p_{3/2}$ for the Y-modified catalyst shows a small decrease (0.2-0.5 eV) in Table 5.3, indicating a slightly increased interaction between the Ni and the support [350,365].

Such finding further confirms the occurrence of metal-support interaction in Ni/CeO_2-Y promoted catalysts as argued based on XRD data.

The Ni/Ce atomic ratio decreases with the rise of Y content of the surface of the catalysts, except for Ni/CeO_2-Y1.0%. This fact could be attributed to different factors, such as slightly bigger Ni particles, a different distribution of Ni on the surface due to changes in morphology, or the migration of Ni into the bulk likely forming Ni-Ce-O solid solution.

Table 5.3. XPS derived Ce (III) and Ce (IV) percentage, the binding energy of O1s, $Ni2p_{3/2,}$ and $Y3d_{5/2}$ in eV and Ni/Ce and Y/Ce atomic ratio of the various Ni catalysts in the calcined state. In parenthesis, the relative percentage between OL and OOH is indicated.

Catalyst	Ce(III)-Ce(IV)	O1s (eV)		$Ni2p_{3/2}$ (eV)	Ni/Ce	$Y3d_{5/2}$ (eV)	Y/Ce
		OL	OOH				
5Ni/CeO_2	11%-89%	529.5 (54%)	531,9 (46%)	855.3	0.23	-	-
5Ni/CeO_2- Y0.5%	9%- 91%	529.6 (54%)	531,4 (45%)	854.9	0.16	157.3	0.54
5Ni/CeO_2- Y1.0%	12%-88%	529.6 (40%)	531.3 (60%)	854.8	0.23	157.6	0.72
5Ni/CeO_2- Y2.0%	16% - 84%	529.1 (45%)	532.7 (54%)	855.1	0.17	157.4	0.68
5Ni/CeO_2- Y5.0%	19 %-81%	529.7 (60%)	531.5 (40%)	855.0	0.16	157.7	0.86
5Ni/Y_2O_3	-	529.4 (45%)	531.9 (54%)	855.2	-	157.4	-

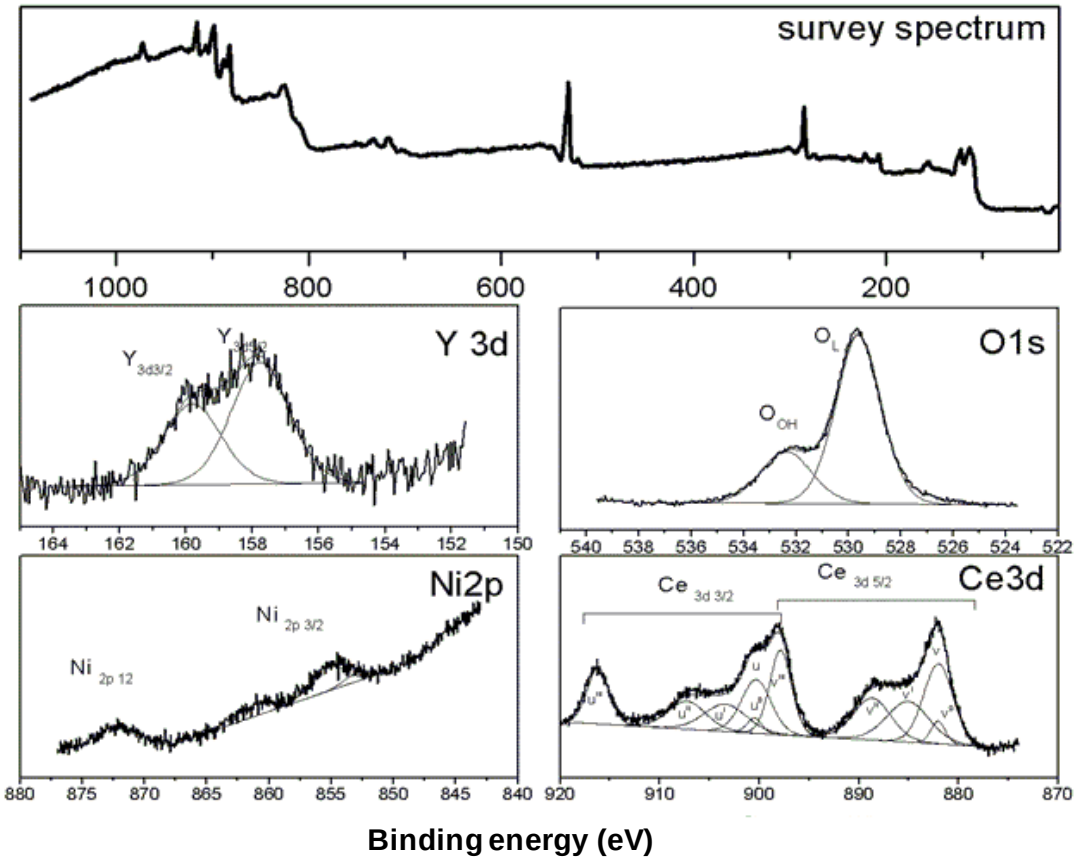

Figure. 5.4. XPS survey spectrum and XPS Y3d, O1s, Ni2p, and Ce3d profiles of the calcined 5Ni/CeO_2-Y2.0% catalyst.

5.4 On the reducibility of calcined catalysts

To study the reducibility of the calcined catalysts and determine the optimal reduction condition for CO_2 methanation, temperature-programmed reduction in H_2 (H_2-TPR) was performed on the calcined samples. The H_2-TPR profiles are displayed in Fig. 5.5, the temperatures at the maxima of reduction peaks and H_2 consumption values are listed in Table 5.4. To get more insight into the effect of Ni on the reduction properties of the supports, TPR experiments were registered also over selected supports as shown in Fig.5.5b and Table 5.4. As shown in Fig. 5.5, there are 3 main peaks

over Ni/CeO_2 and Ni/CeO_2-Y catalysts, which are labeled as α, β, and γ in the figure. The α peak, which started at a very low temperature (ca. 39 ºC) over 5Ni/CeO_2 sample, was ascribed to the reduction of oxygen species chemisorbed on the oxygen vacancies that likely are generated by the partial substitution of CeO_2 lattice by Ni^{2+} and Y^{3+} species, resulting in Ni-Ce-O solid solution or Y-Ce-O solid solution [201,350,366,367].

It is worth noting that the α peak shifts toward higher temperature with the increase of Y loading until 2 wt.% of Y, and then shift a little toward lower temperature for the sample with 5 wt.% of Y. Moreover, the H_2 consumption of the α peak (see Table 5.4) gradually increased with Y loading until 2 wt.% of Y, with the highest value. This finding could be explained by an increased concentration on the surface of the catalysts of Ce^{3+} ions able to chemisorb oxygen species reducible below 250 °C (see TGA curves and XPS analysis) and agrees with the change of the morphology of Ni/CeO_2-Y catalysts by increasing the Y loading from 0 up to 5wt % (see TEM characterization). On the other hand, the shift of the α peak toward higher temperature until 2 wt.% of Y and the highest hydrogen consumption registered for such a peak suggest that doping ceria with 2 wt % of Y produces the highest oxygen vacancy concentration with strongly chemisorbed oxygen.

It is also worth noting that no α peaks at around 200-250 °C were observed in the TPR profiles of CeO_2 and CeO_2−Y doped oxides (see Fig 5.5b), supporting the active role of Ni^{2+} in promoting the creation of oxygen vacancies in the catalysts.

On the basis of H_2 consumption in the α peak, considering that 1 mmol of H_2 is supposed to react with 1 mmol of O^{2-} species per oxygen vacancy, the V_0 content (%) was calculated based on the Eq. 5.1.1 (see 5.2) and is given in Table 5.4. A similar trend as the hydrogen consumption in the α peak was found as a function of the Y loading.

(a)

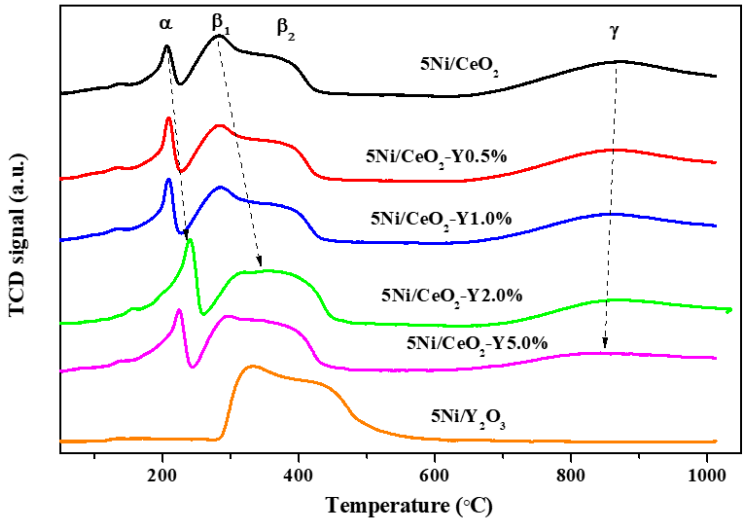

(b)

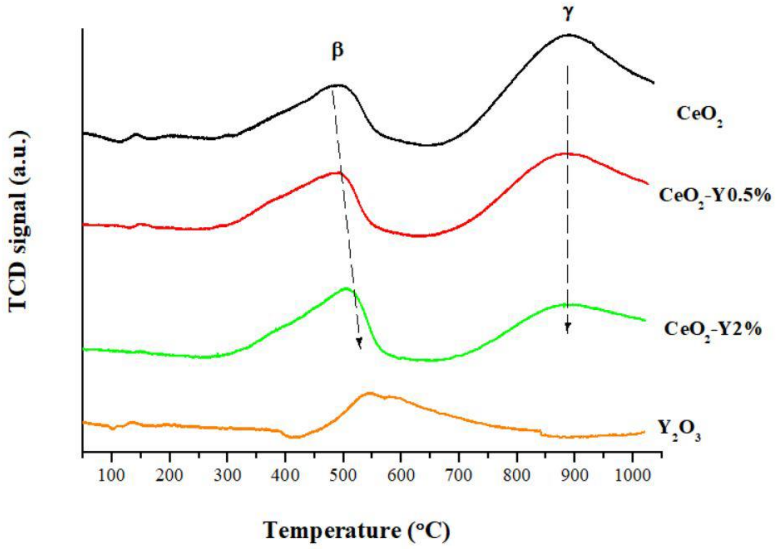

Figure. 5.5. H_2-TPR profiles of (a) catalysts and (b) selected supports; Operating condition: 5% H_2/Ar flow rate of 30 mL/min, a ramp of 10 °C/min.

The broad reduction peak, β, can be divided into 2 different features i.e. β_1 and β_2 (e.g. ca. 283 ºC and 360 ºC for 5Ni/CeO_2 sample) that can be assigned to the reduction of NiO species that have different intensity of metal-support interaction [350,368]. The β_1 peak can be attributed to the reduction of bulk NiO that has a weak interaction with the support or to un-interacted NiO crystallites [350,369]. The β_2 corresponds to the NiO nanoparticles in intimate contact with the support [170]. The β_1 and β_2 peaks shift towards higher temperature at higher Y loading, from 0.5 to 2 wt.%, confirming strong metal-support interaction with the best synergy achieved at 2 wt.% Y. Moreover, at high Y loading, the two features β1 and β2 become less defined overlapping into a single broad peak, suggesting that such a peak contains the contribution from several species that are reduced simultaneously. According to the literature and the results from Fig. 5.5b and Table 5.4 [170,350,370], the reduction of the ceria surface occurs with a maximum at ∼490−505 °C. Therefore, the β peak may correspond to the concomitant reduction of nickel species and the ceria surface, and the broader the peak, such as that detected for 5Ni/CeO2−Y2.0%, the higher the intimate contact.

At a high-temperature peak (at T > 800 °C), labeled γ in Fig. 5.5, is due to the bulk reduction of the CeO_2-based oxides, although reduction of some NiO species strongly interacting with the support cannot be excluded [350,371].

According to the H_2 consumption values reported in Table 5.4 and considering that the theoretical amount required for the overall reduction of NiO to metallic Ni is 0.85 mmol/g_{cat}, based on a real Ni loading equal to 5 wt%, the β reduction peak (ranging between 0.73-0.78 mmol/g_{cat}) may contain the contribution from some NiO in contact with ceria surface along with surface ceria reduction. The reduction of the remaining part of NiO together with some ceria bulk may occur at T > 800 °C. Similar H_2 consumptions of the β peak were registered for Ni/CeO_2 and Ni/CeO_2-Y

catalysts confirming that the catalysts contain a comparable amount of NiO particles with similar size interacting with the ceria surface. As it concerns the γ peak, the H_2 consumption decreases with the increase of Y content (0-5 wt.%), in accord with higher oxygen vacancies in the catalysts [192,350]. Such a trend was confirmed by XPS analysis (Table 5.3). and by TPR of selected supports. From the values listed in Table 5.4, it can be seen that moving from CeO_2 to CeO_2−Y0.5% and CeO_2−Y 2.0%, the hydrogen consumption of the β peak gradually increased, especially for Y 2.0%, in accordance with higher SSA. Conversely, the hydrogen consumption of the γ peak decreased and, on the whole, the β + γ uptake decreased in line with an increased oxygen vacancy concentration.

For 5Ni/Y_2O_3, only a broad peak between ~300-500 °C was registered with two maxima at 330 and 435 °C and according to the previous notation, we will continue to label such peaks as β1 and β2. For comparison, the TPR of the Y_2O_3 support was registered to show a peak centered at ~550 °Cwith H_2 consumption of 0.31 mmol/g_{cat} (see Figure 5.5b and Table 5.4). The H_2 consumption value of β peak for 5Ni/Y_2O_3 is 1.29 mmol/g_{cat}, which exceeds the theoretical value required for the total reduction of NiO to metallic Ni (0.85 mmol/g_{cat}) and 1.16 mmol/g_{cat} (corresponding to the sum 0.85 plus 0.31 mmol/g_{cat}, i.e., the H_2 consumption of the yttria oxide), suggesting that new oxygen vacancies are created in the Y_2O_3 after Ni deposition. Bellido et al. [325] studied the effect of Y_2O_3-ZrO_2 composition on Ni/Y_2O_3-ZrO_2 catalysts and they found that the reduction of pure Y_2O_3 support only accounted for a small fraction of the reduction in the H_2-TPR measurement. However, the reduction behavior of the Ni/Y_2O_3-ZrO_2 supports was significantly influenced by the interaction among the species and the introduction of Y^{3+} into ZrO_2 and likely of Ni^{2+} create new oxygen vacancies to preserve overall electroneutrality. Based on the literature [325], the relatively low temperature of the peak maximum (333 °C) registered for

5Ni/Y_2O_3 and the H_2 consumption higher than that required for NiO reduction (Table 5.4) were attributed to the presence of a high number of oxygen vacancies on the support interacting with NiO.

Table 5.4. Reduction temperatures at the peak maximum (T_{max}) and H_2 consumption values of the calcined catalysts derived from H_2-TPR.

Catalyst	T_{max} (ºC)			H_2 consumption ($mmol/g_{cat}$)			V_0 (%)[a]
	α	β	γ	α	β(β_1+β_2)	γ	
5Ni/CeO_2	207	283	873	0.26	0.76	0.73	2.36
5Ni/CeO_2- Y0.5%	209	286	861	0.29	0.73	0.67	2.62
5Ni/CeO_2- Y1.0%	209	286	861	0.30	0.73	0.62	2.70
5Ni/CeO_2- Y2.0%	240	354	872	0.44	0.75	0.59	3.95
5Ni/CeO_2- Y5.0%	225	297	843	0.33	0.78	0.43	2.92
5Ni/Y_2O_3	-	333	-	-	1.29	-	-
CeO_2	-	490	885	-	0.33	0.76	-
CeO_2-0.5%Y	-	492	882	-	0.36	0.68	-
CeO_2-2.0%Y	-	505	880	-	0.40	0.59	-
Y_2O_3	-	550	-	-	0.31	-	-

[a] Oxygen vacancies (%) calculated from α peak

5.5 Morphologies of the catalysts derived from TEM and HRTEM characterization

In order to gain more morphology information of the catalysts, the high-resolution transmission electron microscopy (HRTEM) and TEM analyses were conducted over the reduced samples using the same reduction condition as the activity test. The micrographs of reduced catalysts were shown in Fig.5.6-5.8.

It can be seen from Fig. 5.6 that all the catalysts contain well-defined crystallites and that the introduction of Y tailors the particle sizes of CeO_2 in the catalysts. In the absence of Y as shown in Fig. 5.6a, the CeO_2 particles were nanoparticles (NPs) as irregular polyhedra with some aggregated particles exceeding 50 nm. In Fig. 5.6b, the CeO_2 particles promoted with 0.5 wt.% of Y became smaller. Higher concentrations of Y nanorods (NRs) appeared (Fig.5.6c-e). It was difficult to evaluate the proportion of nanorods but we noted that on one side the NPs size decreased and on the other, the NRs became thinner. The influence of Y concentration on average grain size and the morphology is summarized in Table 5.5 where the measurements obtained from the TEM images are listed. The effect of the concentration of a doping element was already related by Saabari et al. [372]. The formation of nanorods with high exposed surface area detected from 1 to 2 wt.% of Y complies with the increased intensity of the α peak, attributed to the reduction of oxygen species chemisorbed on oxygen vacancies and is in line with the highest SSA of the Ni/CeO_2-Y2%. The aspects of the NRs are presented in Fig. 5.7. We see the decrease in the size of nanorods from 1 wt.% Y (Fig. 5.7a) to 5 wt.% Y (Fig. 5.7c). All catalysts are well crystallized as evidenced by the lattice planes. The nanorod of 5Ni/CeO_2-Y2% (Fig. 5.7d) reveals the (111) and (220) planes corresponding to the distance of 3.12 and 1.91 Å, respectively. The NPs as for them showed frequently the (111) facets. Therefore, Y addition does not produce significant modification into the CeO_2 lattice in agreement with XRD characterization.

For the pure Ni/Y_2O_3 sample, large aggregate nanoparticles of 10-15 nm were detected, see Fig. 5.6f.

From the reported data it can be concluded that the morphology of the reduced catalysts changed with the incorporation of Y. The particle size of CeO_2 decreased as increasing Y loading with the formation of nanorods and such trend is in accord with the increase of SSA shown in Table 5.1. As previously reported in the literature, CeO_2 morphology can be modulated depending on the preparation conditions, and nanorods formation is favored during the hydrothermal process [196].

By simple TEM analysis, the size distribution of Ni^0 nanoparticles cannot be distinguished according to another author's report [196]. In order to obtain more detailed information on nickel particle sizes, HRTEM images and EDX spectra were recorded and are shown in Fig.5.7-5.10, where the measured sizes of Ni^0 nanoparticles are marked, mapping was also carried out.

HRTEM images show that the Ni metallic particles are spherical and well dispersed on the support. The average size was ranging from 6-12 nm for all catalysts. The Ni metallic particles were detected by the lattice planes of 2.03 or 1.76 Å corresponding respectively to the (111) or (002) planes of the FCC (face center cubic) structure of nickel.

The EDX spectra show that the signals of Ni and Ce keep stable with the increase of Y loading, indicating again high dispersion of Ni. For the 5Ni/CeO_2-Y2.0% sample the composition homogeneity of Ni and Y was confirmed by Scanning TEM-Energy Dispersive X-ray Spectroscopy (STEM-EDX) mapping (Fig. 5.9 and Fig. 5.10).

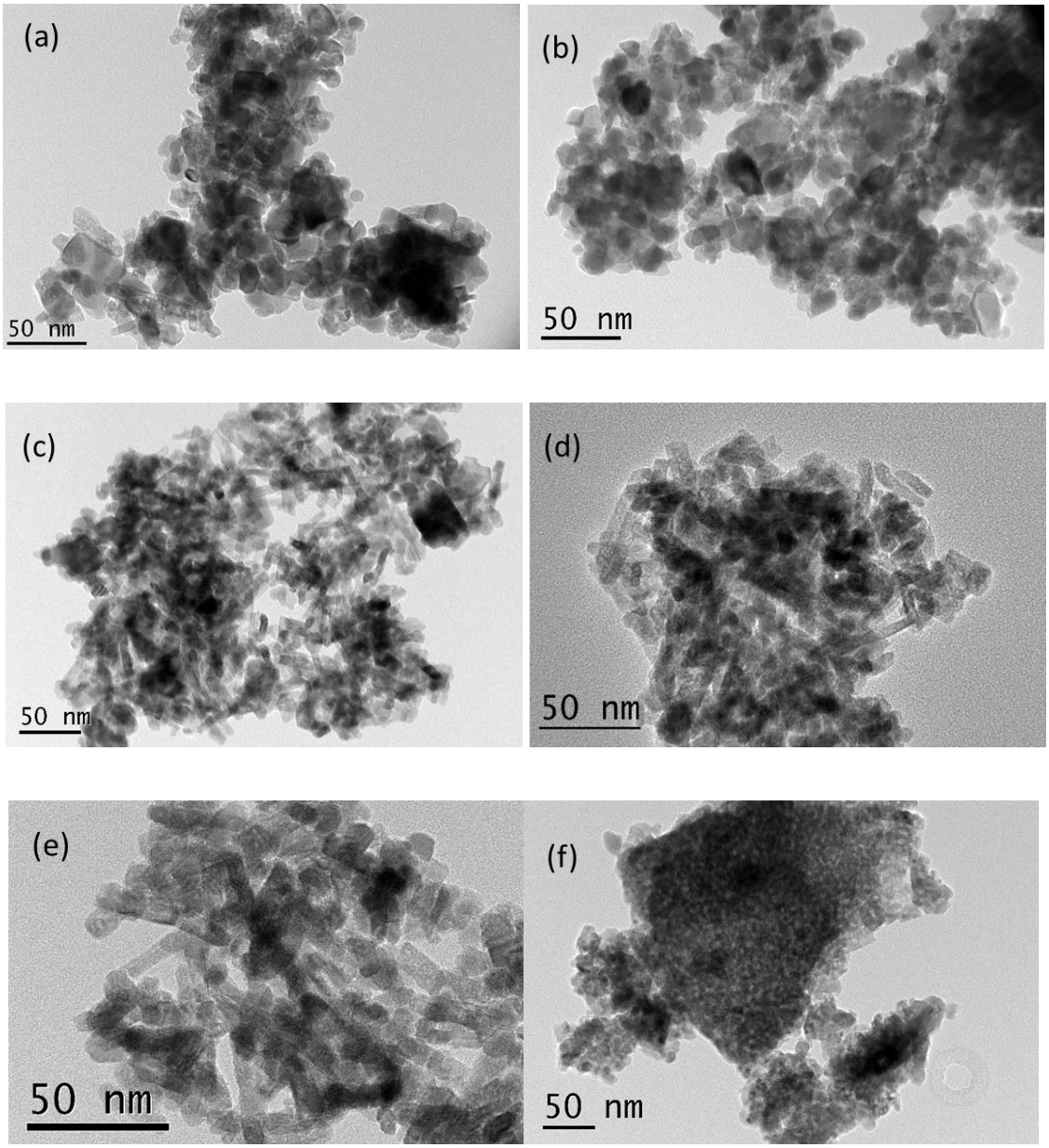

Figure. 5.6. TEM micrographs of the catalysts reduced at 550 °C for 1 h in 5% H_2/Ar (100 mL/min); (a) 5Ni/CeO_2, (b) 5Ni/CeO_2-Y0.5%, (c) 5Ni/CeO_2-Y1.0%, (d) 5Ni/CeO_2-Y2.0%, (e) 5Ni/CeO_2-Y5.0%,(f) 5Ni/Y_2O_3.

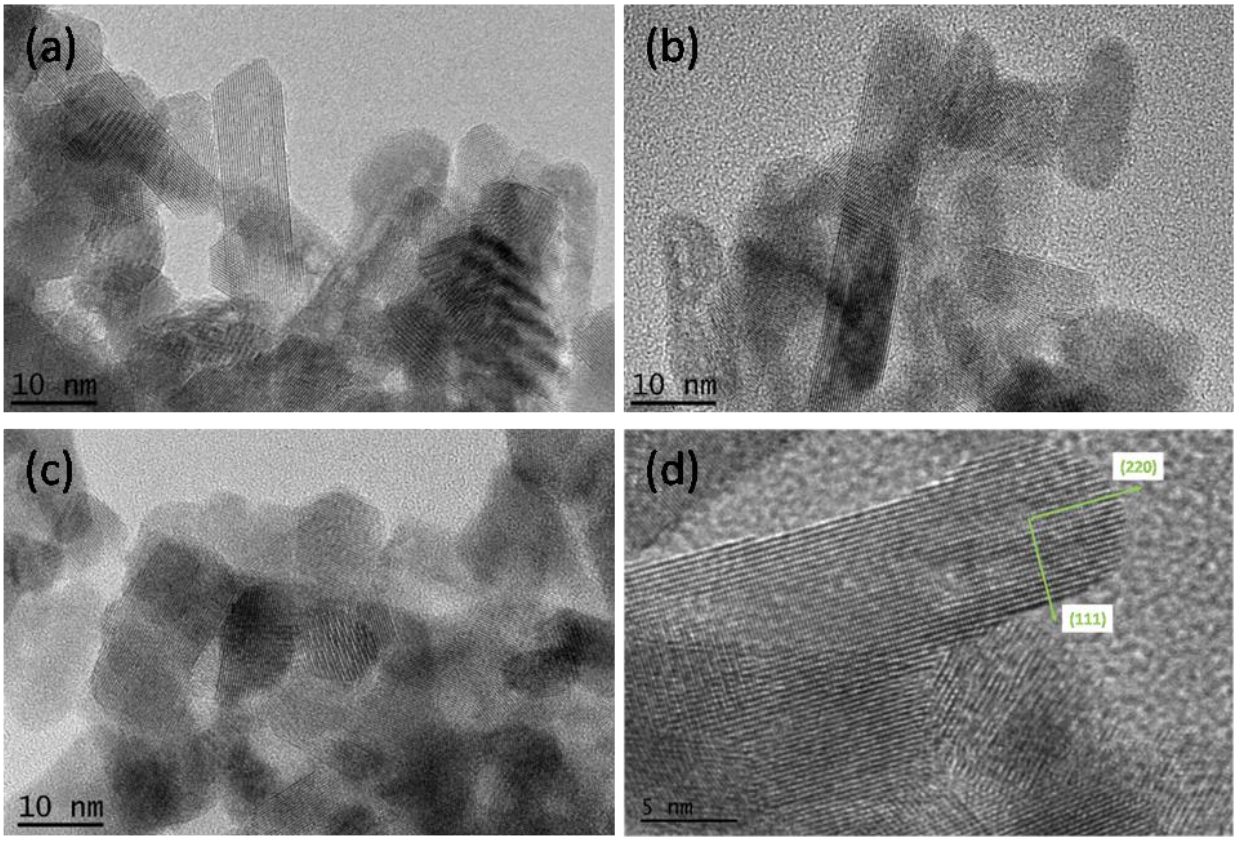

Figure. 5.7. Nano-cubes and nano-rods from HRTEM micrographs: (a) 5Ni/CeO_2-Y1.0% (b, d) 5Ni/CeO_2-Y2.0% (c) 5Ni/CeO_2-Y5.0%

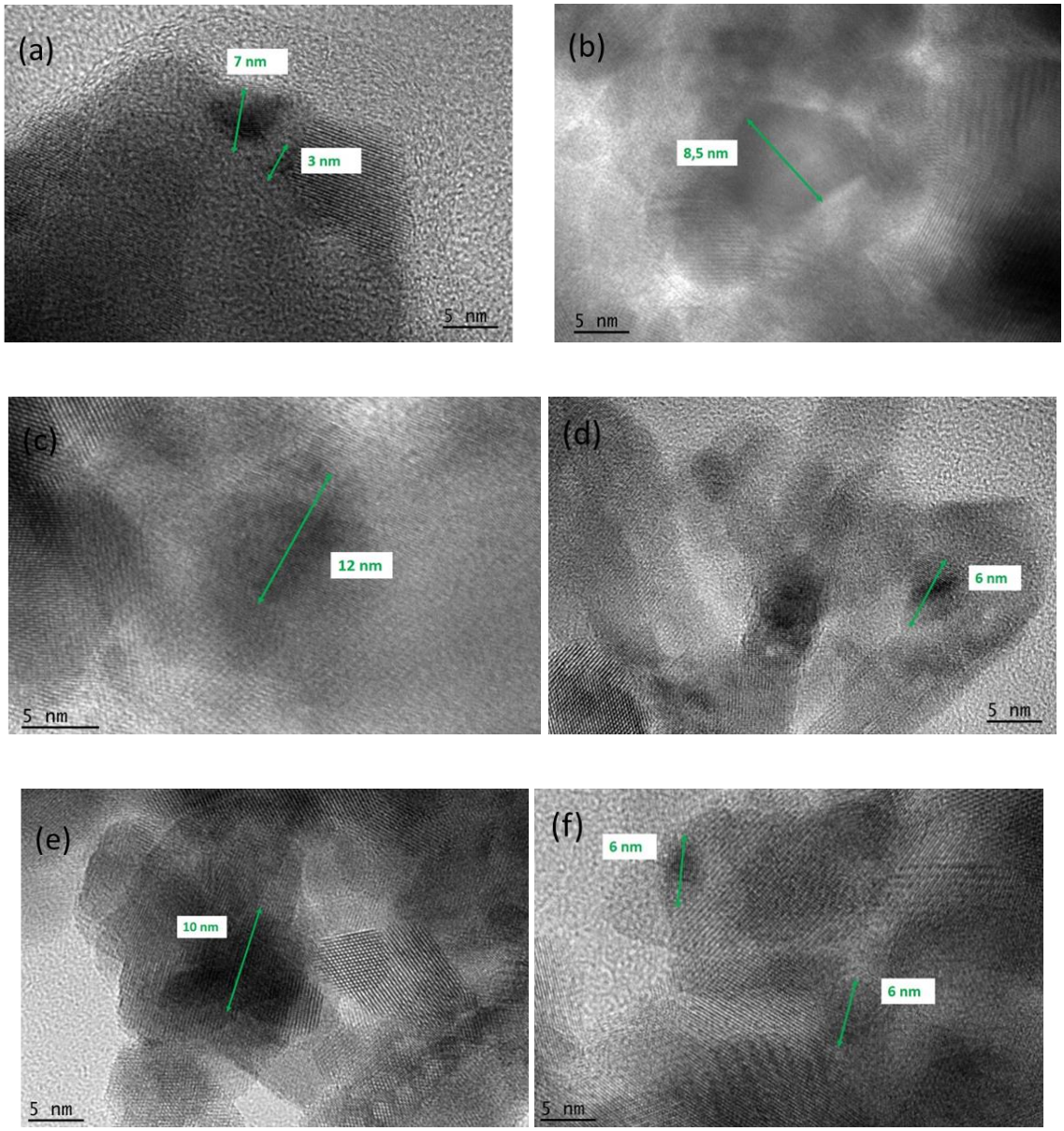

Figure. 5.8. HRTEM micrographs of the catalysts; Condition: reduced at 550 °C for 1 h in 5% H_2/Ar (100 mL/min); (a) 5Ni/CeO_2, (b) 5Ni/CeO_2-Y0.5%, (c) 5Ni/CeO_2-Y1.0%, (d) 5Ni/CeO_2-Y2.0%, (e) 5Ni/CeO_2-Y5.0%, (f) 5Ni/Y_2O_3.

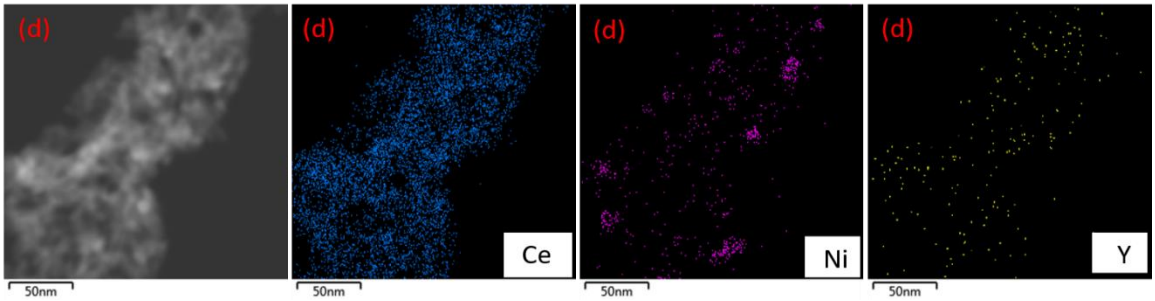

Figure. 5.9. STEM-HAADF image and STEM-EDX mapping of the catalyst, (d), 5Ni/CeO_2-Y2.0%; Condition: reduced at 550 °C for 1 h in 5% H_2/Ar (100 mL/min).

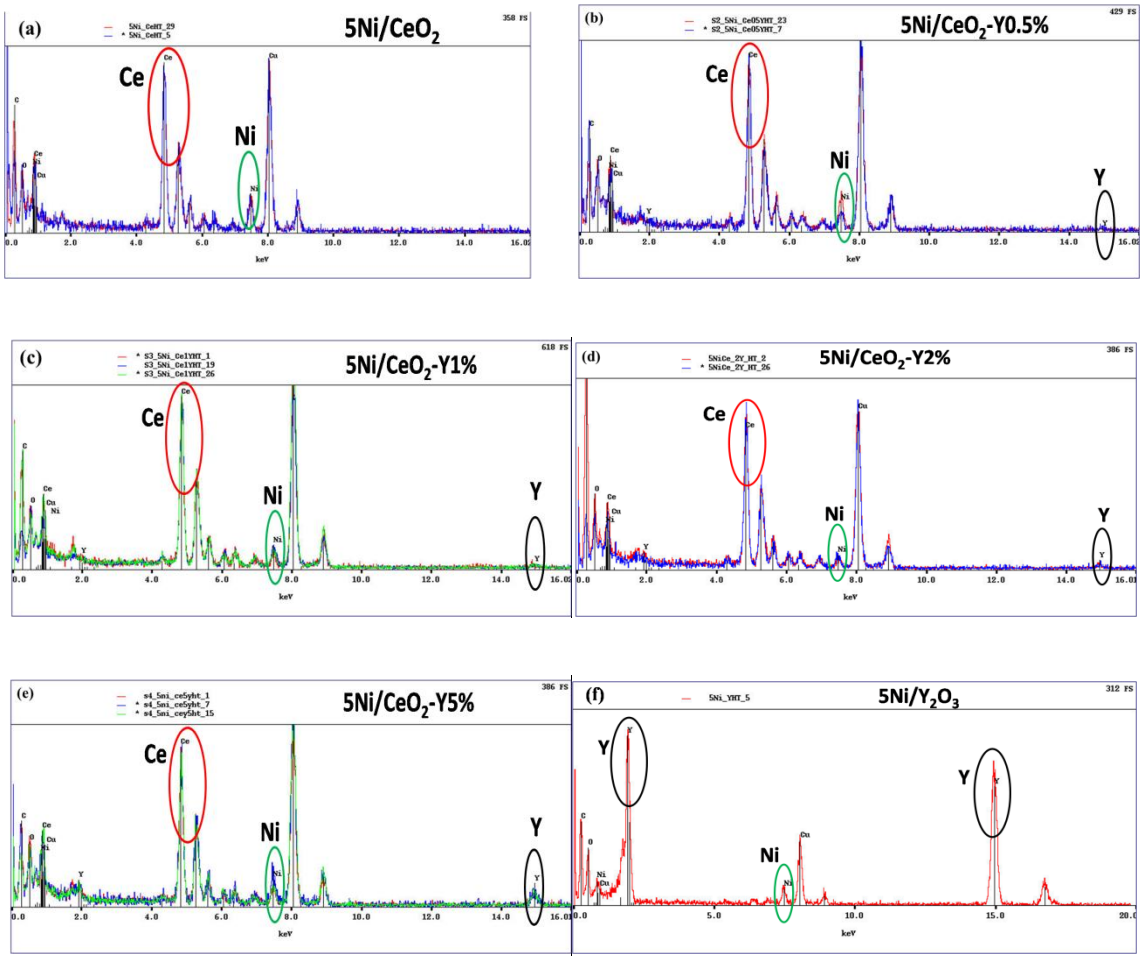

Figure. 5.10. EDX spectra of the catalysts; Condition: reduced at 550 °C for 1 h in 5% H_2/Ar (100 mL/min); (a) 5Ni/CeO_2, (b) 5Ni/CeO_2-Y0.5%, (c) 5Ni/CeO_2-Y1.0%, (d) 5Ni/CeO_2-Y2.0%, (e) 5Ni/CeO_2-Y5.0%, (f) 5Ni/Y_2O_3.

Overall, Ni^0 resulted well dispersed on CeO_2-based catalysts as confirmed by XRD results. Moreover, Y doping promotes the decrease of the CeO_2 particle size and the formation of CeO_2 nanorods.

Table 5.5. Support particle size of the reduced samples deduced from TEM image analysis.

Catalyst	Size of Nanoparticles (nm)		Size of Nanorods (nm)	
	Min-Max	Currently	Length (min-max)	Diameter (min-max)
5Ni/CeO_2	7 - 25	15	-	-
5Ni/CeO_2-Y0.5%	6 - 22	13	-	-
5Ni/CeO_2-Y1.0%	8 - 24	10	15 - 40	5 - 9
5Ni/CeO_2-Y2.0%	6 - 17	8	10 - 30	5 - 8
5Ni/CeO_2-Y5.0%	5 - 14	10	10 - 27	5.5 - 10
5Ni/Y_2O_3	8 - 15	11	-	-

5.6 Evaluation of oxygen vacancies content and oxygen mobility by TGA analysis

In order to evaluate the surface oxygen vacancies content and the oxygen mobility of the Ni/CeO_2 supported (Y-modified and Y-free) catalysts, temperature-programmed desorption curves of adsorbed oxygen (O_2-TPD) were registered over the reduced catalysts by performing thermal gravimetric analyses (TGA). The acquired TGA profiles are displayed in Fig. 5.11.

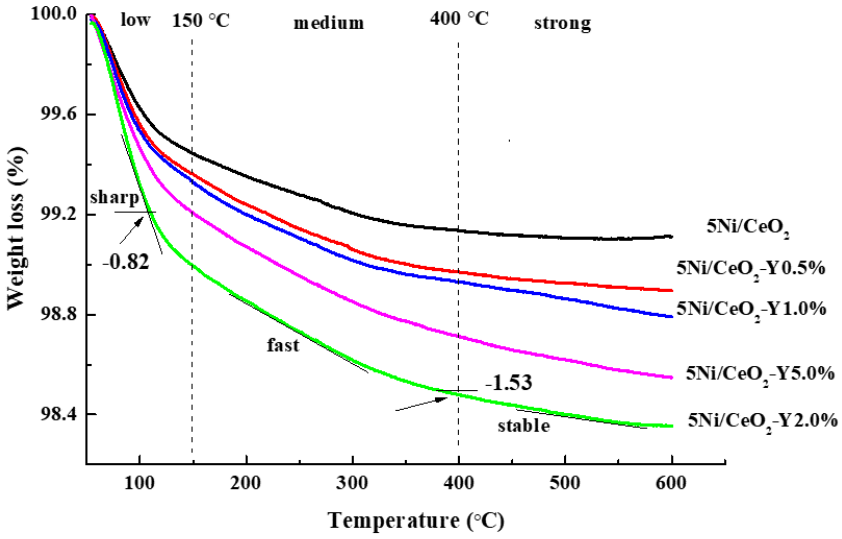

Figure. 5.11. TGA profiles under N_2 flow of reduced catalysts after saturation with pure O_2.

It can be seen from Fig. 5.11 that the reduced catalysts, after saturation with pure O_2, undergo distinct weight losses under N_2 atmosphere from room temperature until 600 °C as the desorption of adsorbed oxygen occurs. For simplicity, the curves were divided into three parts according to the weight loss slope in the different range of temperatures, i.e. sharp, fast and stable loss. So, the weight loss at the temperature below about 150 °C was ascribed to the removal of weakly adsorbed oxygen (physisorbed O_2), between ~150-400°C desorption of chemisorbed O_2 takes place, while in the range 400-600 °C or even above 600 °C the removal of bulk oxygen species should occur [373]. In our case, a stable trend was observed up to 600 °C according to the TPR curves since ceria bulk reduction occurred above 800 °C.

At low temperature and in the range 150-400 °C, the weight loss intensity increased as a function of Y loading, from Ni/CeO_2 Y-free until 2 wt.%, then, for Y 5wt.% a decrease was observed, being the TGA curve of such sample intermediate between Y 2wt.% and Y1wt.%. Looking in detail at

the profile of 5Ni/CeO_2-Y2.0%, the sharp weight loss occurring from room temperature up to ~110 °C corresponds to -0.82% while increasing the temperature up to 400 °C, an overall weight loss of -1.53% was registered. Assuming that O_2 desorbs, the mmol of oxygen removed was calculated: below 150 °C 0.25 mmol O_2/g_{cat} (physisorbed oxygen) and in the overall 0.47 mmol O_2/g_{cat} up to 400 °C are desorbed. Therefore, the amount of chemisorbed O_2 is equal to 0.22 mmol/g_{cat}. Such value is exactly the half amount of the H_2 consumption value registered for the α peak in the TPR experiment (see Table 5.4). Considering that 1 mmol of H_2 reacts with 1 mmol of O^{2-} species per oxygen vacancy, such finding confirms that the α peak is due to the reduction of oxygen species adsorbed on the vacancies.

In conclusion, TGA analyses confirmed that Y dopant promoted the formation of oxygen vacancies in our samples, the highest content being achieved for Y 2wt.%, according to other characterizations in this study and literature results [51,373–375].

5.7 Basicity distribution of the reduced catalysts derived from CO_2-TPD analyses

To investigate the basicity of the reduced catalysts, CO_2-TPD experiments were performed on the above catalysts. The CO_2-TPD profiles are plotted in Fig. 5.12, the concentration and distribution of basic sites are listed in Table 5.6. As shown in Fig. 5.12, the CO_2 desorption curves can be divided into three regions according to the temperatures, i.e. T < 150 °C, between 200-450 °C and T > 450 °C, corresponding to the weak, medium and strong basic sites, respectively.[160,307]

It is shown that the distribution of basic sites changed significantly with the increase of yttrium loading, in particular, the CO_2 desorption peaks of Y-modified catalysts shifted towards higher temperature as the increase of Y until 2 wt.%.

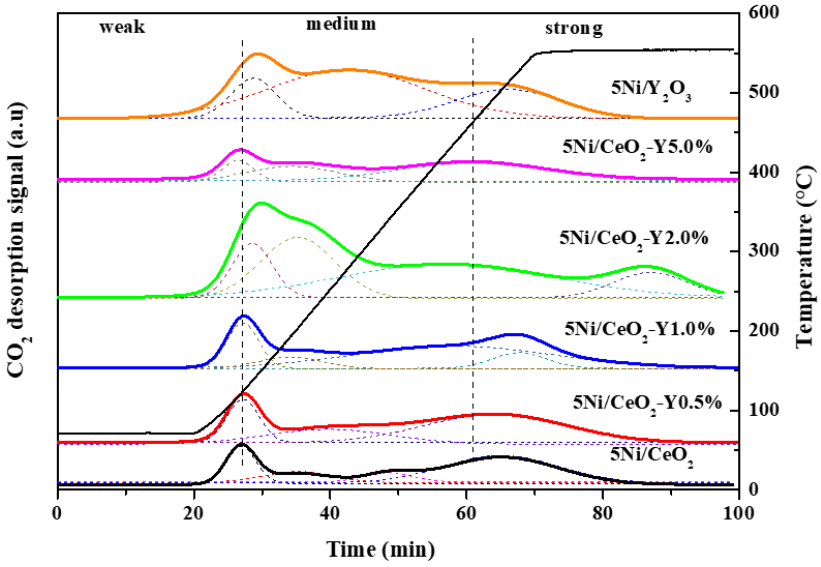

Figure. 5.12. CO_2-TPD profiles registered over reduced catalysts; Pretreatment condition: Reduction at 550 ˚C for 1 h in 5% H_2/Ar (50 mL/min), cooling down to 80 ˚C and He purging, then CO_2 adsorption under 10% CO_2/Ar for 1 h (50 mL/min).

Moreover, as reported in Table 5.6, the concentration of weak and medium + strong basic sites (as overall amount) increase as the increase of Y (up to 2.0 wt%), with slightly decreased values for Y 5.0%. The highest basicity was registered for the 5Ni/CeO_2-Y2.0% sample, while Ni/Y_2O_3 was in between Y1.0 wt% and Y 5.0 wt%.

Table 5.6. Basic sites distribution calculated from CO_2-TPD for Y-promoted catalysts after reduction at 550 ˚C

Catalyst	Basic sites [μmol/g_{cat}]				Distribution of basic sites [%]		
	Weak	Medium	Strong	Total basicity	Weak	Medium	Strong
5Ni/CeO_2	18.2	13.3	63	95	19.2	14.1	66.7
5Ni/CeO_2- Y0.5%	22.1	8.8	87.4	118	18.7	7.5	73.8
5Ni/CeO_2- Y1.0%	25.1	23.7	76.7	126	20.0	18.9	61.1
5Ni/CeO_2- Y2.0%	35.4	75.5	140.7	251	14.1	30.0	55.9
5Ni/CeO_2- Y5.0%	32.3	71.3	129.0	233	13.9	30.6	55.5
5Ni/Y_2O_3	30.9	55.9	77.8	165	18.8	34.0	47.2

5.8 Catalytic performance of Ni based catalysts in CO_2 methanation

The catalytic performances in CO_2 methanation reaction were investigated in a quartz reactor at atmospheric pressure introduced in Chapter 3. Prior to reaction, the sample (100 mg) was reduced in 5% H_2/Ar (100 mL/min) at 550 °C for 1 h with a heating rate of 5 °C/min. After cooling down to 200 °C, the reactant gas mixture, 100 mL/min, with a molar ratio of $CO_2/H_2/Ar$=15/60/25 was fed into the catalyst (WHSV=60,000 mL $h^{-1}g_{cat}^{-1}$). The CO_2 conversion and CH_4 selectivity were calculated according to equations in Chapter 3.

The catalytic performance in CO_2 methanation was investigated over the Ni catalysts supported over Y-modified CeO_2, pure CeO_2, and pure Y_2O_3, and the CO_2 conversion and CH_4 selectivity values are displayed in Fig. 5.13 along with the thermodynamic curves given for comparison. These results are in line with those presented in the literature in similar experimental conditions Table 5.7.

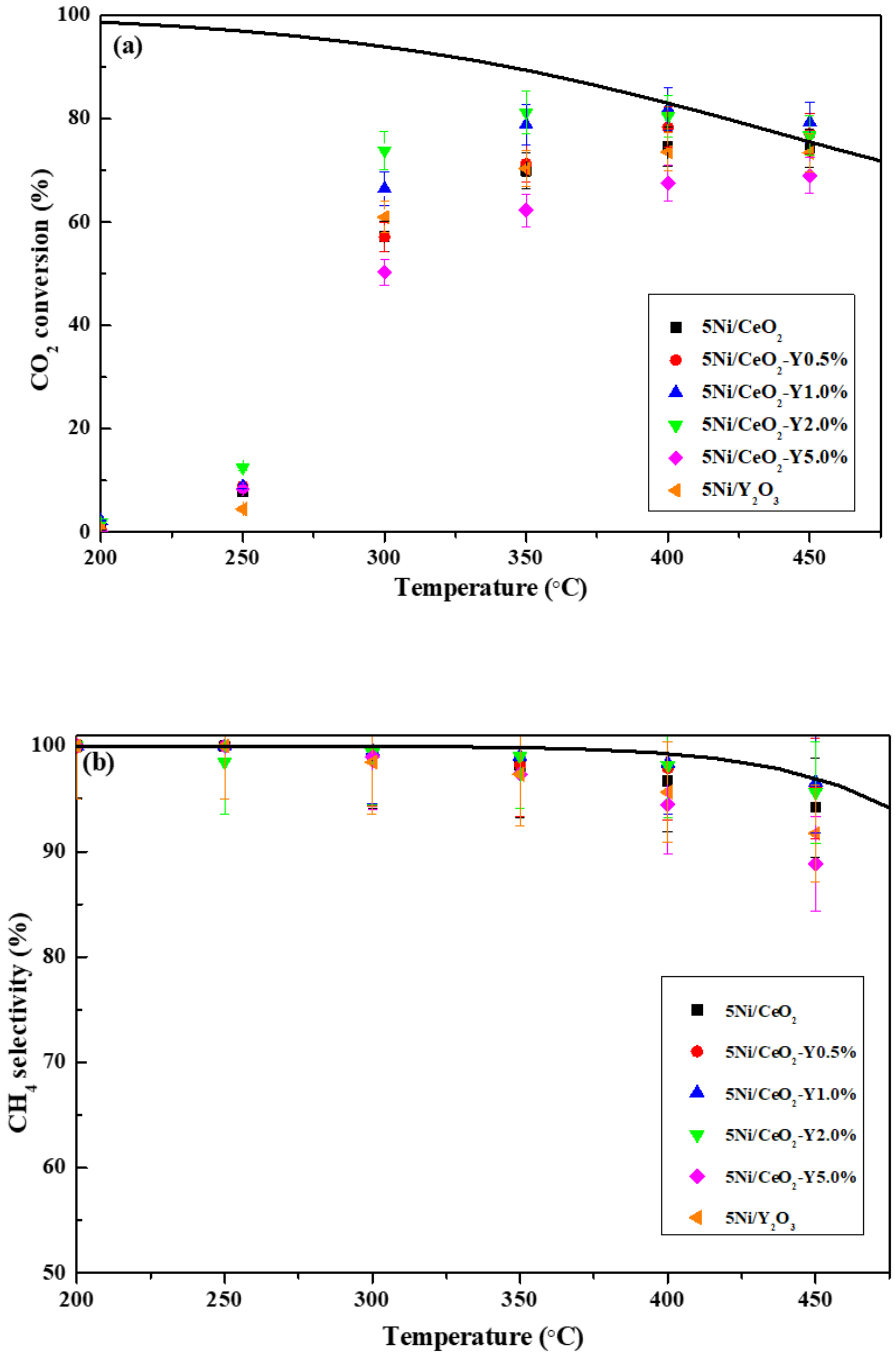

Figure. 5.13. Catalytic performances in methanation reaction as function of the temperature over the catalysts; (a) CO_2 conversion (b) CH_4 selectivity; Reaction conditions: WHSV=60,000 $h^{-1}gcat^{-1}$; $CO_2/H_2/Ar$=15/60/25; atmospheric pressure.

As shown in Fig. 5.13a, the highest CO_2 conversions for all the catalysts were obtained at 400 °C, which were close to the theoretic value, except for the sample of 5Ni/CeO_2-Y5.0%, which reached the highest conversion at 450 °C. In the temperature range of 250-350 °C, the CO_2 conversion for Y-modified catalysts gradually increased as the increase of yttrium up to 2 wt.% Y, afterward, the activity declined sharply when yttrium content reached 5 wt.%, which was less active than the 5Ni/Y_2O_3 catalyst. The 2 wt.% Y modified catalyst possessed the highest CO_2 conversion compared to the other catalysts at 250-350 °C. From Fig. 5.13b, it can be found that the CH_4 selectivity of all catalysts at low temperature (200-250 °C) appears very close to that of the theoretical value. Afterward, by further increase the temperatures up to 300-450 °C, the selectivity of all catalysts decreases gradually, and the worst value was obtained for 5Ni/CeO_2-Y5.0% and 5Ni/Y_2O_3 at a temperature higher than 400 °C.

In brief, the doping with yttrium into CeO_2 has a significant effect on the activity and selectivity of the Ni catalysts towards the Sabatier's reaction.

The Ni catalyst supported over CeO_2 modified by 2 wt.% Y possesses the best CO_2 conversion and high CH_4 selectivity at relatively low temperatures (i.e. 300-350 °C).

Table 5.7. The CO_2 methanation performance of the catalysts compared with the results reported in the references

Catalyst	GHSV/WHSV	Temperature (°C)	CO_2 conversion (%)	CH_4 selectivity	Reference
5Ni/CeO_2	60,000 $mL \cdot g^{-1}h^{-1}$	350	69.9	98.1	This work
5Ni/CeO_2-Y2%	60,000 $mL \cdot g^{-1}h^{-1}$	350	81.2	99.1	This work
10Ni/CeO_2	22,000 $mL \cdot g^{-1}h^{-1}$	340	91.1	-	[376]
5Ni/CeO_2-ZrO_2-AE	20, 000 $mL \cdot g^{-1}h^{-1}$	350	54.0	99.5	[377]
Ni/CeO_2(CT)	45,000 $mL \cdot g^{-1}h^{-1}$	340	91.1	100	[192]
Ni-CeO_2/SBA-15-V	60,000 $mL \cdot g^{-1}h^{-1}$	350	60.0	99.0	[224]
Ni-2CeO_2/Al_2O_3	15,000 $mL \cdot g^{-1}h^{-1}$	350	85.0	100	[378]
15Ni/SBA-15-Op	10,000 $mL \cdot g^{-1}h^{-1}$	350	42	81	[171]
Ni/MCM-41	2,400 h^{-1}	350	30	30	[346]
Ni/SiO_2	2,400 h^{-1}	350	58	58	[346]
Ni/Al_2O_3	2,400 h^{-1}	350	62	61	[346]
Ni/SBA-15	2,400 h^{-1}	350	65	65	[346]
Ni/ZSM-5	2,400 h^{-1}	350	70	70	[346]
Ni/ZrO_2	4,8000 $mL \cdot g^{-1}h^{-1}$	350	80	99	[168]
Ni/La_2O_3	20,000 $kg^{-1}h^{-1}$	350	53	94	[198]

Ni/Sm_2O_3	20,000 $kg^{-1}h^{-1}$	350	70	97	[198]
Ni/CeO_2	20,000 $kg^{-1}h^{-1}$	350	73	97	[198]
Ni/Al_2O_3	20,000 $kg^{-1}h^{-1}$	350	75	99	[198]
Ni/ZrO_2	20,000 $kg^{-1}h^{-1}$	350	75	99	[198]
Ni/Y_2O_3	20,000 $kg^{-1}h^{-1}$	350	86	99	[198]
Ni/ZrO_2-P(DBD)	60,000 h^{-1}	350	78	96	[136]
MO-0.4Y(hydrotalcite derived)	12,000 h^{-1}	350	89.1	99.2	[144]
Ni/Zr/CNT(carbon nanotube)	75,000 $mL \cdot g^{-1}h^{-1}$	350	40.0	96.0	[201]
$Ni_{42.5}$(hydrotalcite derived)	12,000 h^{-1}	350	81.5	99.5	[131]
$Ni_{21}La_{0.4}$(hydrotalcite derived)	12,000 h^{-1}	350	80.0	99.2	[206]
$Ni_{20}Fe_{1.5}$(hydrotalcite derived)	12,000 h^{-1}	350	82	99	[205]

5.9 Relationships between physicochemical properties and catalytic performances

The mechanism of CO_2 methanation over Ni/CeO_2 catalysts has been studied in the literature [159,160]. It was attributed to the synergistic effect of two types of active sites, i.e. the active sites at the Ni-Ce-O interface for CO_2 adsorption and dissociation as well as the Ni^0 sites for H_2 adsorption and dissociation. The H_2 dissociated to H- species on the surface of metallic nickel, and the CO_2 adsorbed on the surface of the support and then dissociated to carbonate or hydrogen carbonate species, then the carbonate or hydrogen carbonate were hydrogenated to formate species

including monodentate and bidentate formate. The monodentate formate could be hydrogenated to methane faster than the bidentate formate species. The larger is the metallic nickel surface area formed on catalyst by small Ni particles, the more favorable the adsorption and dissociation of H_2 are. The weak and medium basic sites were mainly useful for the dissociation of CO_2 in the reaction [160].

As shown in Fig. 5.14 (a, b and c), good relations were found at increasing Y loading between CO_2 conversion at 300 °C and the number of basic sites (weak + medium) ($\mu mol/g_{cat}$) (Fig. 5.14a) as well as between CO_2 conversion at 300 °C and the oxygen vacancies content, V_0 (%) (see Table 5.4) (Fig. 5.14b). A similar trend, at increasing Y loading, was observed between CO_2 conversion at 300 °C and the temperatures of β reduction peak that is related to the strength of the metal-support interaction of Ni over CeO_2-Y catalysts.

The CO_2 conversion at 300 °C was chosen for comparison because at low temperature (<300 °C) the results of CO_2 conversion were not very distinguishing. Meanwhile, the CO_2 conversion of all catalysts increases with the increase of temperature (350-450 °C, Fig. 5.13), which also makes the difference of catalytic performance unnoticeable. Thus, the 300 °C can be an appropriate temperature for comparison.

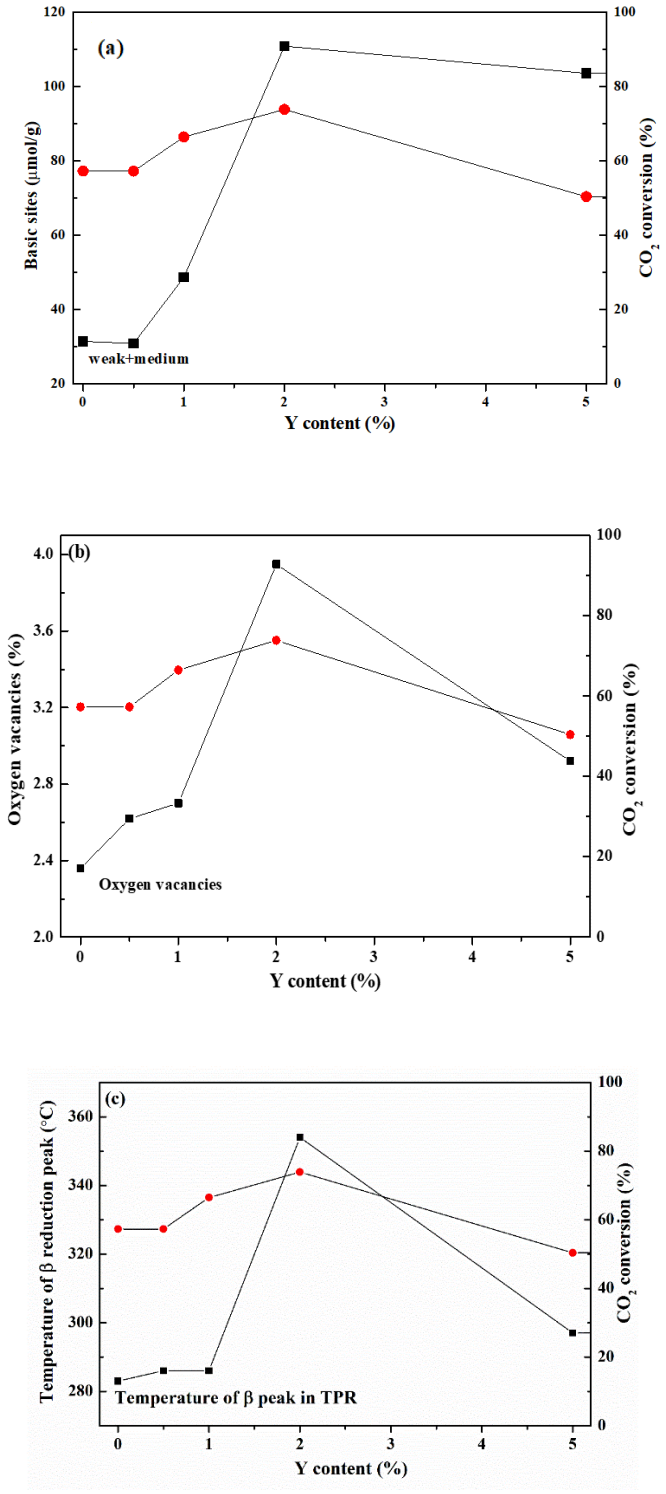

Figure. 5.14. Correlation of CO_2 conversion (at 300 °C) with (a) basic sites; (b) oxygen vacancies content, V_0 (%); (c) temperature of β reduction peak in the TPR. The Y content represents the loading of Y for Ni/CeO_2-Y catalysts, with 0% representing 5Ni/CeO_2

So, based on the reported data and in agreement with the methanation reaction mechanism previously mentioned [159,160], it can be concluded that the decrease of CeO_2 particles, the high dispersion of nickel as well as the formation of more oxygen vacancies provide more active sites for the adsorption and dissociation of hydrogen and CO_2. Moreover, the high metal-support interaction depresses the sintering of active metal. For the 5Ni/CeO_2-Y2.0% sample, highly dispersed nickel particles provide more active sites for the adsorption and dissociation of hydrogen, the highest number of oxygen vacancies favors the adsorption of CO_2 and the highest amount of medium basic sites promotes the formation of monodentate formate, which can be fast hydrogenated to methane [160]. Thus, the highest CO_2 conversion and relatively high CH_4 selectivity were obtained on the catalyst.

5.10 Steady-state test of Ni/CeO_2 based catalysts in CO_2 methanation

The steady-state tests were performed on three selected Ni catalysts, by using the same set-up previously described in Chapter 3, for evaluating the stability of CO_2 conversion and selectivity towards CH_4. In a typical process, 100 mg of calcined sample was loaded into the reactor. After reduction, the sample was cooled down to 300 °C, then the gas mixture with molar ratio $CO_2/H_2/Ar$=15/60/25 (100 mL/min) was fed into the catalyst (WHSV=60,000 mL $h^{-1}g_{cat}^{-1}$). The products were analyzed by the TCD detector in GC (490 Varian, Agilent). The experiment was maintained at 300 °C for 7 h. 5Ni/CeO_2-Y1.0% and 5Ni/CeO_2-Y2.0% were selected for steady-state tests at 300 °C for 7h. The temperature of 300 °C was selected due to the recognizable difference of CO_2 conversion values shown in Fig. 5.13. The 5Ni/CeO_2 sample was used for comparison. The selected catalysts were reduced in the same condition as for the CO_2 methanation test, then were cooled down to 300 °C and the reaction gas mixture was fed into the reactor. The

steady-state test results are displayed in Fig. 5.15. It can be seen from Fig. 5.15a that the CO_2 conversion values of all samples decrease slightly at the beginning, then keep stable on stream. Both Y-promoted catalysts performed better than Ni/CeO_2, with 5Ni/CeO_2-Y2.0% showing the best CO_2 conversion. The results of 5Ni/CeO_2 were slightly higher than those shown in Fig. 5.13a. This was attributed to possible effects, within the experimental error of 5%, during the catalytic tests. The selectivity to CH_4 is shown in Fig. 5.15b, the values maintain nearly stable during the test and both Y-modified catalysts achieved higher selectivity than Ni/CeO_2 catalyst.

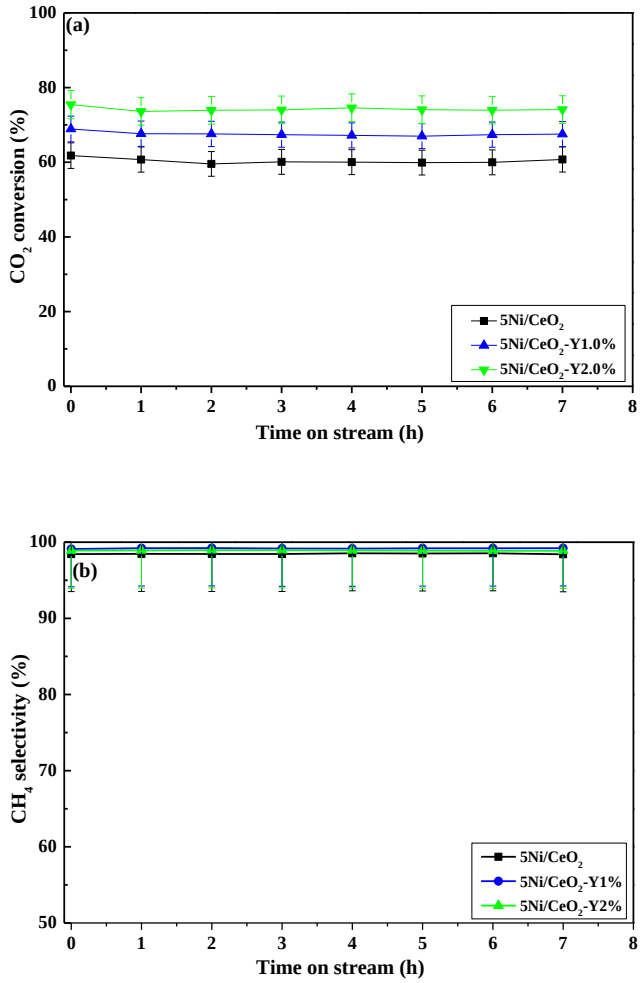

Figure. 5.15. CO_2 methanation stabilities over 5Ni/CeO_2, 5Ni/CeO_2-Y1.0% and 5Ni/CeO_2-Y2.0% catalysts (a) CO_2 conversion with error bars; (b) CH_4 selectivity; Reaction condition: temperature 300 °C, WHSV=60,000 $h^{-1}g_{cat}^{-1}$, reaction gas mixture $CO_2/H_2/Ar$=15/60/25.

The slight difference in the conversions (lower than 3%) in between catalytic tests from 200 °C to 450 °C and steady-state experiments can be explained by the fact that, in the former case, the catalysts were exposed to a lower temperature (250°C) for at least 30 min, as described in the experimental part, before reaching 300°C.

5.11 Characterization of Ni/CeO_2 based catalysts after steady-state test

5.11.1 XRD patterns of the catalysts after steady-state test

To investigate structural modifications of the catalysts after the steady-state test, XRD patterns were registered and are shown in Fig. 5.16. No diffraction peaks of metallic nickel or NiO were found, meaning that the nickel species remained highly dispersed on the support even after a steady-state test at 300 °C for 7h. This finding confirms the XRD results of the catalysts after the activity test. A perusal of Fig 5.16b (enlarged pattern in the range between 42 and 52° 2θ) shows a slight shift to higher angles of all CeO_2 and CeO_2−Y peaks in comparison with Fig 5.2a, especially in the case of 5Ni/CeO_2−Y2.0%, in which the (202) peak is centered at 47.65° 2θ. This finding would point to further inward diffusion of Y^{3+} and Ni^{2+} into the ceria lattice, as suggested by the XPS analysis (see Table 5.9). In Table 5.8 the particle sizes of CeO_2 support calculated by the Debye-Scherrer equation are listed. The values are in good agreement with those given in Table 5.2, remarking that no sintering of ceria nanoclusters takes place at 300 °C under the reaction stream. The 5Ni/CeO_2-Y2.0% maintained the smallest particle size of ceria. Such results account for the good stability in CO_2 conversion and CH_4 selectivity registered being the sintering of active metals the main reason for deactivation in Sabatier's reaction [192].

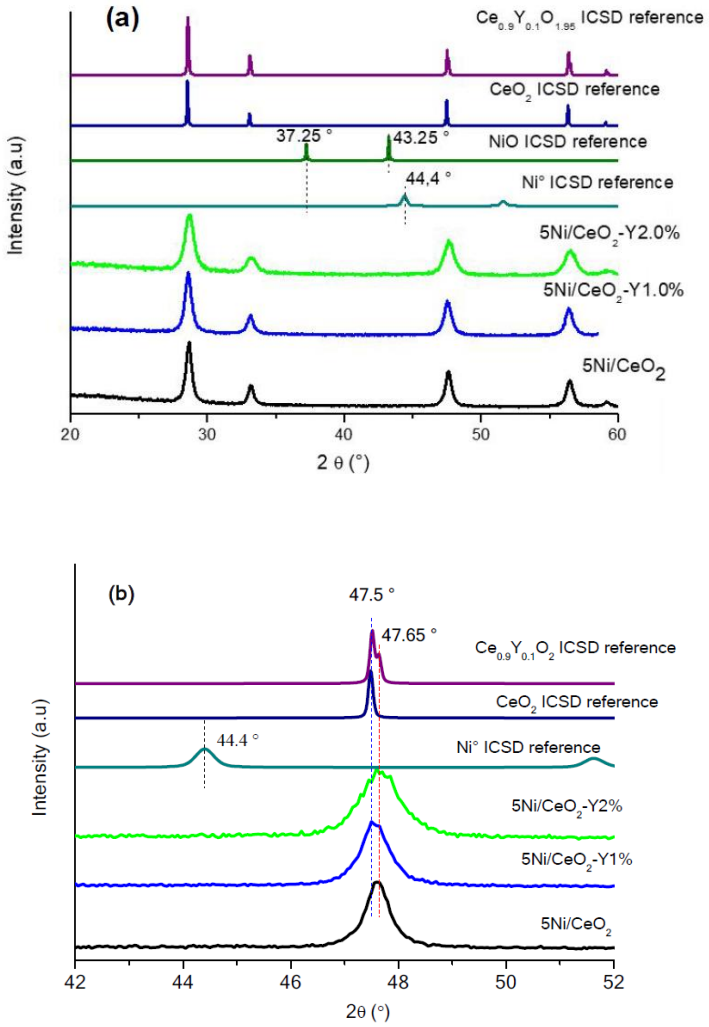

Figure. 5.16. XRD pattern of the catalysts after steady-state test; Condition: After the steady-state test, the samples were cooled down to ambient temperature under pure He flow (100 mL/min)

Table 5.8 The CeO_2 particle sizes of catalysts after steady-state test

Catalyst	Particle size of CeO_2[a] (nm)
5Ni/CeO_2	17.3
5Ni/CeO_2-Y1.0%	16.0
5Ni/CeO_2-Y2.0%	12.1

[a] Calculated by Debye-Scherrer equation fitting the 4 strongest peaks in XRD patterns.

5.11.2 XPS analysis of the catalysts after steady-state test

To obtain the surface composition and oxidation states of the catalysts after a steady test, the XPS analyses of the spent catalysts were performed. The Ce3d, Ni2p, and O1s XPS regions of the samples are displayed in Fig. 5.17, respectively. The surface oxidation state, atomic ratio, and binding energies are shown in Table 5.9. As already shown in Fig. 5.1.4, the Ce3d spectra were fitted with 10 peaks, in which four peaks are attributed to Ce (III) and six peaks are attributed to Ce (IV). Because of the small dimension of the nickel particles, surface re-oxidation occurs after catalytic reaction, likely during exposure to the atmosphere, so it was impossible to calculate the degree of nickel reduction.

Compared to the XPS results of calcined samples (Table 5.3), a small decrease in the Ni/Ce ratio was found (Table 5.9). Conversely, the Y/Ce ratio decreased by an important extent, indicating a probable migration of yttrium into the bulk during steady-state reaction.

The Ce (III) % of the samples nearly keep the same value as those of calcined samples, meaning that the surface Ce^{3+} species of the catalysts were oxidized during the test, while the values (%) of OOH decreased a little in comparison with those of the calcined samples, indicating decreased oxygen vacancies because of the occurrence of reoxidation. A decrease of the Ni/Ce ratio and a simultaneous shift of $Ni2p_{3/2}$ peak at higher energies suggest a small increase of Ni particles size after the steady-state test and different interactions with the support.

As previously stated for calcined samples, there is no significant difference regarding the binding energy of $Y3d_{5/2.}$

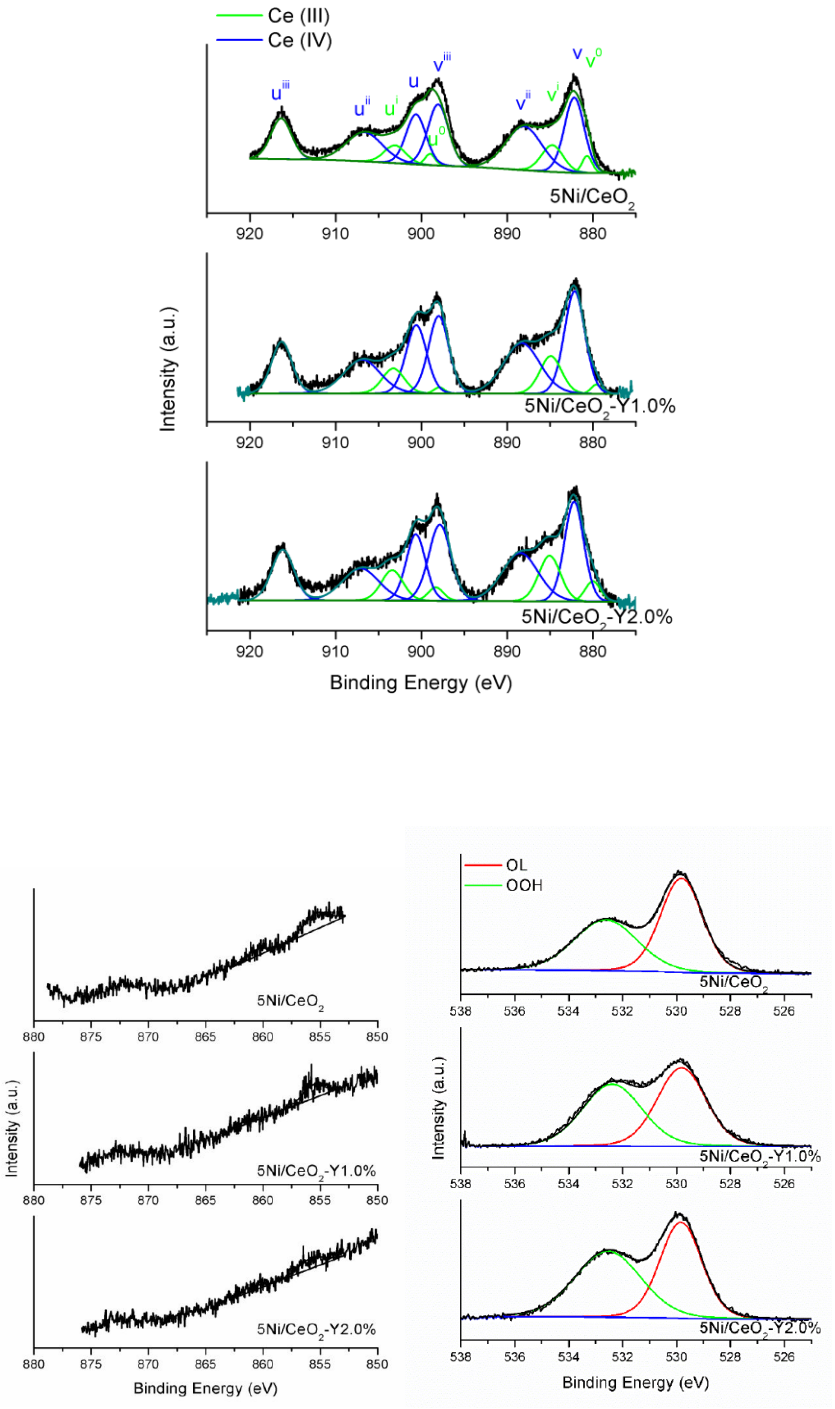

Figure. 5.17. The XPS Ce3d, Ni2p, and O1s spectra of the samples after steady-state test; Steady-state test: 300 °C for 7 h in methanation reaction

Table 5.9 XPS derived Ce (III) and Ce (IV) percentage, Binding Energy of O1s, $Ni2p_{3/2}$ and $Y3d_{5/2}$ in eV, Ni/Ce and Y/Ce atomic ratio for the samples after the steady-state test. In parenthesis, the relative percentage between OL and OOH is indicated.

Catalyst	Ce(III)-Ce(IV)	O1s (eV)		$Ni2p_{3/2}$ (eV)	Ni/Ce	$Y3d_{5/2}$ (eV)	Y/Ce
		OL	OOH				
5Ni/CeO_2	11%-89%	529.9 (53%)	532.8 (47%)	855.3	0.18	-	-
5Ni/CeO_2-Y1.0%	11%-89%	529.9 (47%)	532.6 (53%)	855.6	0.16	157.8	0.38
5Ni/CeO_2-Y2.0%	16%-84%	530.1 (49%)	532.2 (41%)	855.7	0.16	158.2	0.42

5.12. Conclusions and perspectives

Y-modified CeO_2 oxides have been successfully synthesized by the hydrothermal method and used as supports for Ni deposition by wetness impregnation. The catalytic performances were investigated in CO_2 methanation reaction and are discussed in line with Physico-chemical characterizations of calcined, reduced, and spent catalysts. It has been proven that such Ni catalysts with proper Y loadings are suitable catalysts for CO_2 methanation reaction between 250-350 °C with high selectivity towards methane formation.

The specific surface area of Ni/CeO_2-Y samples, the crystallite sizes of ceria, the oxygen vacancies content, and the interaction between NiO and CeO_2 can be tuned by different Y content as shown by N_2 adsorption/desorption, XRD, XPS, TPR, TEM, HR-TEM, TGA, CO_2 TPD. All the catalysts contain well-defined crystallites and the introduction of Y tailors the particle sizes and shapes of CeO_2 in the catalysts. Unpromoted CeO_2 particles are large nano-cubes turning to nanorods by Y promotion, with an increase of these nanorods size of up to 2 wt% of Y addition.

Highly dispersed Ni active sites in strong interaction with the ceria-based oxide and the oxygen vacancies formed by Y addition are the key factors determining high catalytic activity and stable performances of the Ni/CeO_2-Y catalysts.

The Ni/CeO_2-Y 2.0% with the highest number of oxygen vacancies able to activate CO_2 and with the strongest metal-support interaction suppressing sintering of the Ni sites for H_2 activation, was the best performing CO_2 methanation catalyst.

CeO_2 is highly active support for Ni catalysts and Y is a good promoter to improve Ni/CeO_2 catalyst in CO_2 methanation. Besides, CeO_2 and Y_2O_3 can also be good supports or promoters for Ni catalysts. Thus, the effects of such promoters in Ni catalysts supported on mesoporous materials are presented in the next chapter.

Chapter VI

Ordered mesoporous silica supported Ni catalysts for CO_2 methanation

6. Ordered mesoporous silica supported Ni catalysts for CO_2 methanation

6.1. Introduction

In this section, two types of highly ordered mesoporous silicas are presented. SBA-15 (Santa Barbara Amorphous), which was developed by Zhao et al. [379], was synthesized and used to prepare Ni catalysts for CO_2 methanation. SBA-15 has a two-dimensional *p6mm* hexagonal structure, with a well-ordered hexagonal array and one-dimensional channel structure as shown in Figure. 6.1 [379]. SBA-16, developed by the same team [379], was also synthesized and employed in Ni catalysts preparation. On the contrary, SBA16 has a three-dimensional cubic cage-like structure with an ultra-large cell parameter (Shown in Figure. 6.2) [252,380,381].

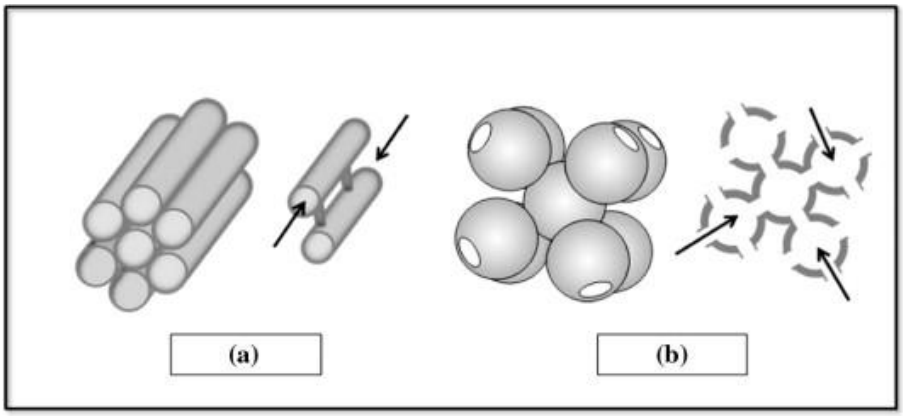

Scheme 6.1. Schematic illustration of the meso-channels of SBA-15 (a) and nano cage-like of SBA-16 (b). Adapted from [382].

As shown in Scheme 6.1, SBA-15 and SBA-16 have very distinctive structures. SBA-15 displays parallel pores and highly ordered hexagonal arrangement [382]. Meanwhile, SBA-16 possesses body-centered cage-like pores with cubic arrangement [382]. Considering the structure properties

of SBA-15 and SBA-16, they would be interesting materials in catalysis. Some reports have applied such materials in various CO_2 utilization reactions as shown in Table 6.1. Given the results above, mesoporous silica (SBA-15 and SBA-16) can be interesting to Ni catalysts in CO_2 methanation.

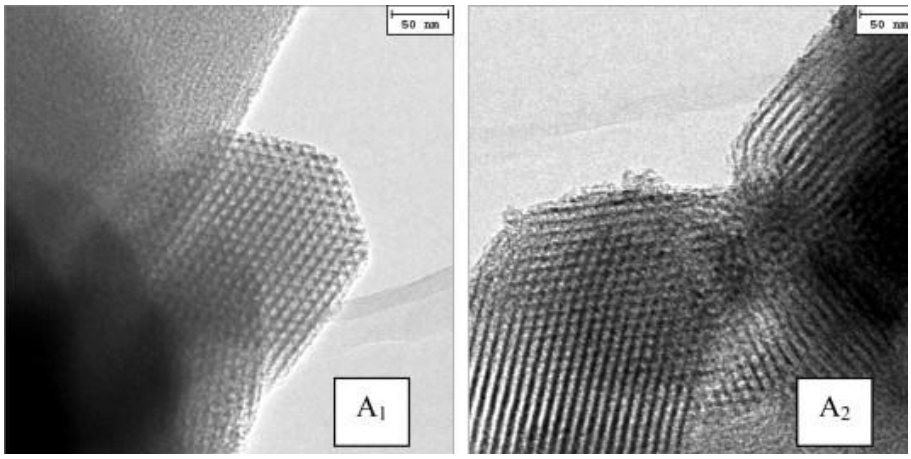

Figure. 6.1. The hexagonal structure and ordered channels of SBA-15. Adapted from [382]

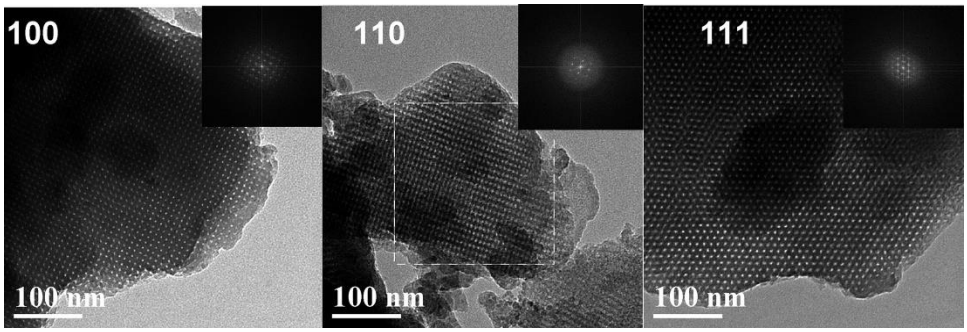

Figure. 6.2. Diffractograms along with different projections of the *Im3m* structure of SBA-16. Adapted from [380].

Table 6.1 The SBA-15 and SBA-16 utilized in various CO_2 utilization reactions

Catalyst	Reaction	Reference
Ni/SBA-15	dry reforming of methane	[383]
Ni/Ce-SBA-15	dry reforming of methane	[384]
Ni/CeZr/SBA-15	dry reforming of methane	[385]
Ni/TiN-SBA-15	dry reforming of methane	[386]
Co-Ni/Sc-SBA-15	dry reforming of methane	[387]
Ni/Ce/SBA-15	CO_2 methanation	[178]
Ni-Mg/SBA-15	CO_2 methanation	[179]
Ni-La_2O_3/SBA-15	CO_2 methanation	[169]
Ni-Y/SBA-16	Cyclic Chemical Looping Steam Methane Reforming	[388]
Ni-Ce/SBA-16	dry reforming of methane	[389]
Ni-Mg/SBA-16	dry reforming of methane	[390]
Ni/SBA-16	CO_2 methanation	[204]
Ni/SBA-16	CO_2 methanation	[182]

Thus, in this chapter, we will present first a study on SBA-15 supported catalysts doped by Ce and Y. Furthermore, Ni catalysts supported on SBA-16 are also presented.

6.2. SBA-15 supported Ni catalysts doped by Y and Ce

6.2.1 Introduction

Oxide materials such as CeO_2 [137], ZrO_2 [201], Al_2O_3 [214,275], hydrotalcite [144,391], SiO_2 [161], etc. had received intensive research interests. In chapter 4 and 5, the low-cost materials and CeO_2 were investigated. Meanwhile, the ordered mesoporous materials like SBA-15 [171,179,221,224], MCM-41 [221,392,393], KIT-6 [50], and SBA-16 [142,204], have also been used as supports for the preparation of Ni catalysts thanks to their unique properties. Among

mesoporous silicas, Santa Barbara Amorphous-15 (SBA-15) has attracted significant attention due to its high specific surface area (up to 1160 m^2/g), particular pore size distribution (50-300 Å), large pore volume (up to 2.5 cm^3/g), well-ordered pore structure, and high thermal stability [66]. The highly ordered structure can limit the sintering of Ni particles at high temperatures, whereas an enhanced specific surface area and high pore volume contribute to the high dispersion of Ni active sites. SBA-15 has been extensively used as support for the preparation of Ni/SBA-15 catalysts. Liu et al. [171] synthesized Ni/SBA-15 catalysts by one-pot hydrothermal method (Ni/SBA-15-op) and conventional impregnation method (Ni/SBA-15-Im), investigating their catalytic performance in CO_2 methanation. It was found that Ni/SBA-15-op catalyst was more active than Ni/SBA-15-Im due to higher surface area, larger pore volume, and enhanced dispersion of nickel particles in Ni/SBA-15-op. Furthermore, the addition of promoters to Ni catalysts can significantly contribute to an improvement in catalytic efficiency. Bian et al. [178] synthesized the Ni/SBA-15 and Ni/Ce/SBA-15 catalysts by the sequential impregnation method and the dried Ni/Ce/SBA-15 (nitrate nickel) samples were processed by dielectric barrier discharge (DBD) plasma and calcination in air. It was found that the Ce addition to Ni/SBA-15 significantly improved the activity and selectivity of the catalyst, regardless of the calcination or DBD plasma process. After modification with ceria, the catalyst decomposed by plasma (Ni/Ce/SBA-15-P) performed the best activity, which was attributed to the high dispersion of Ni, better reducibility, and increased number of basic sites. Apart from the process of plasma decomposition, Ni/Ce/SBA-15 catalysts calcined in air or vacuum were also reported in CO_2 methanation [224]. The study illustrated that the catalyst obtained under vacuum thermal treatment (Ni-CeO_2/SBA-15-V) showed better activity and selectivity compared to those thermally treated in the air (Ni-

CeO_2/SBA-15-air). This was attributed to the smaller particle size of Ni and CeO_2, as well as highly dispersed Ni species, being in close vicinity to Ce.

Other promoters, such as Zr [394,395], $Ce_xZr_{1-x}O_2$ [396], Y [64], Mg [179,397] were also used to enhance performance of Ni/SBA-15 catalysts in various catalytic reactions. Cerium and zirconium were commonly applied to improve nickel-based catalysts due to their redox and oxygen storage abilities. In chapter 5, the modification with Y on the catalytic performance of Ni/CeO_2 in CO_2 methanation was studied [141]. It found that the incorporation of yttrium could substantially promote the activity of Ni/CeO_2. The positive effect of yttrium was assigned to the existence of smaller CeO_2 crystal size, increased BET surface area, enhanced Ni-Ce metal-support interaction, and the increased oxygen vacancies for Y-doped Ni/CeO_2 catalysts.

Compared to the Ni catalysts promoted by one additive, the promotion with Ce-Zr or Ce-Y dual additives of Ni-based mesoporous catalysts have been studied on reactions, such as CO methanation and dry reforming of methane, which showed better performance in such reactions [385,398]. However, only a few studies focused on the Ni/SBA-15 catalyst modified by two promoters in CO_2 methanation. Considering the benefits of CeO_2 and Y_2O_3, here we investigated the effects of Ce and Y on the performances of SBA-15 supported Ni catalysts in CO_2 methanation. Ni/SBA-15 catalysts with a fixed content of Ce (10 wt.%) and different loadings of Y (2, 4, 10 wt.%) were synthesized by co-impregnation method and characterized by a variety of techniques, such as N_2 physisorption, small-angle X-ray scattering (SAXS), X-ray diffraction (XRD), transmission electron microscopy (TEM), X-ray photoelectron spectroscopy (XPS), H_2 temperature-programmed reduction (H_2-TPR), CO_2 temperature-programmed desorption (CO_2-TPD), H_2 chemisorption, and thermogravimetric analysis coupled with mass spectrometry (TGA-MS). This study aims to investigate the influence of Y on NiCe/SBA-15 catalysts in CO_2

methanation. The yttrium individually doped Ni/SBA-15 catalysts were also synthesized and tested in CO_2 methanation as a comparison.

6.2.2 Catalysts preparation and characterization

The synthesis procedures of SBA-15 and subsequent supported Ni catalysts were introduced in 3.1.4 (Chapter 3). Characterization techniques were shown in 3.3 (Chapter 3).

6.2.3 Textural properties, structural parameters, metal distribution, and chemical surface composition of the studied catalysts

The textural properties of the calcined samples were measured by N_2 physisorption. N_2 isotherms and pore size distributions are presented in Fig. 6.3. As shown in Fig. 6.3a, all samples with and without yttrium showed type IV isotherm with H1 hysteresis loop, clearly demonstrating the presence of mesoporous feature [399]. The parallel adsorption and desorption curves also indicate highly ordered cylindrical channels present in the samples. This shows that the ordered 2D structure was preserved after modification with promoters. With the increasing yttrium loading, the inflection step slightly shifts towards lower relative pressure (p/p_0), indicating a slight reduction of ordered mesopores [179]. The specific surface area (SSA), pore volume (V_p), and average pore width (D_{ap}) are presented in Table 6.2. In this study, SSA and V_p of the studied Ni/SBA-15 catalysts are similar to those described in other reports on Ni/SBA-15 catalysts [400,401]. Despite a significant decrease of SSA observed for the Ce-promoted samples, the obtained values are still high and comparable to those reported elsewhere [61,64,385]. This can be attributed to a cluster formation or deposition of promoter clogging the porous channels of the

support [385]. Moreover, this indicates that the surfactant CTAB, added in the preparation step, can be a suitable reagent used during the synthesis of Ni/SBA-15 catalysts. Furthermore, the presence of yttrium can positively influence the textural properties [141,144]. As presented in Table 6.2, SSA and V_p were higher when 4 wt.% of Y was used. Then, both SSA and V_p decreased for the sample containing 10 wt.% of Y loading. Fig. 6.3b depicts BJH pore size distribution measured for the studied catalysts. It can be seen that the pore size of all the samples mainly locates in the range of 2-8 nm. It can be seen that metal oxides (Ni and Ce) deposited onto the SBA-15 support resulted in a decrease of average pore size from 6.8 nm for SBA-15 to 6.2 nm for 15Ni10Ce/SBA-15. Moreover, the Y addition led to a slight decrease of average pore size from 6.2 nm to 5.9 nm for 15Ni10Ce/SBA-15 and 15Ni10Ce10Y/SBA-15, respectively. This can be linked with an effect of the deposition of metal oxides inside the mesopores, which was also found for La-promoted Ni/SBA-15 catalyst [169]. One can note that the appropriate loading of Y (4 wt.%) led to an increase of specific surface area and pore volume in Ce-Y-promoted Ni/SBA-15 catalysts. Similar observations were found by Świrk et al.[49] for yttrium promoted Ni/Mg/Al hydrotalcite-derived mixed oxides. Among the yttrium modified samples with 3, 4 and 8 wt.%, NiY4-DLH revealed the highest specific surface area.

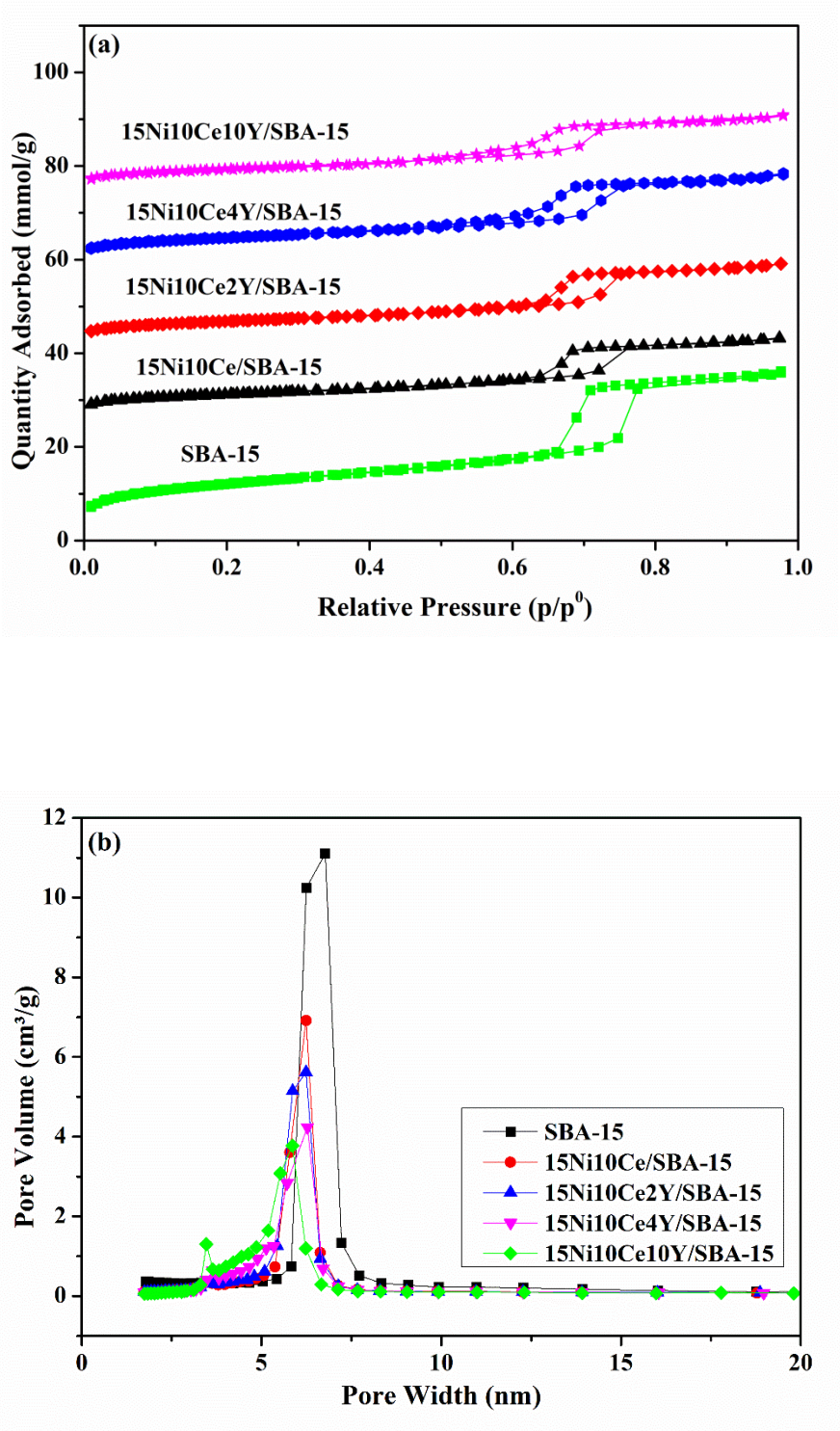

Figure. 6.3. N_2 adsorption-desorption isotherms a) and the BJH pore width distribution b) of the calcined catalysts. For clarity, the isotherms were vertically shifted.

The ordered structure of the calcined SBA-15, 15Ni10Ce/SBA-15, and 15Ni10Ce10Y/SBA-15 were studied by Small-angle X-ray diffraction. Three peaks between 2θ = 0.5-4° were registered for all samples with the most intense at 2θ = 0.9° and two well-resolved at 2θ of ca. 1.5, and 1.8° corresponding to (100) (110) and (200) crystal planes, respectively. Their presence is attributed to the highly ordered 2D hexagonal structure (*p6mm*) which is a typical structure for SBA-15 [251,402]. This shows that the co-impregnation with Ni, Ce, and Y allows maintaining the ordered mesoporous structure of SBA-15 catalysts, however, their peaks shifted toward higher angles (Fig. 6.4) as the unit cell parameter decreased after modification with metals (Table 6.2). The calculated values are in the range of 11.2-11.9 nm, being in good agreement with those estimated in other literature reports [402,403]. The recorded decrease in unit cell parameter suggests that nickel, cerium, and yttrium species were partially deposited on the outer surface of SBA-15 support [251,404]. As presented in Fig. 6.4, the intensity of the diffraction peaks gradually decreased after modifications with Ni-Ce and Ni-Ce-Y. This can be explained by partial destruction of the pore structure orderliness of 15Ni10Ce/SBA-15 and 15Ni10Ce10Y/SBA-15 catalysts [169,405].

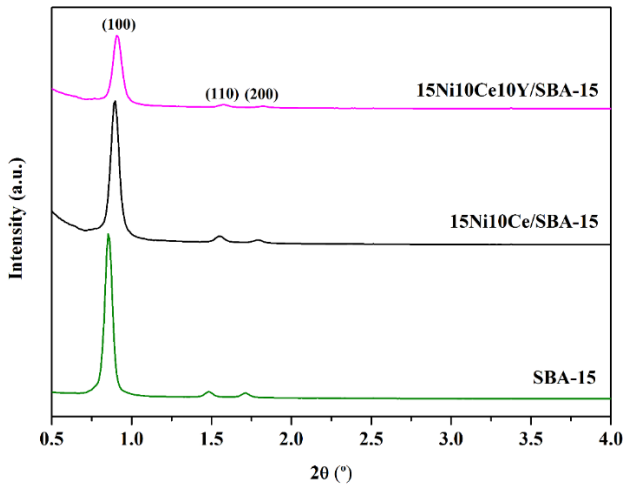

Figure. 6.4. Small-angle X-ray diffraction patterns of the calcined SBA-15, 15Ni10Ce/SBA-15 and 15Ni10Ce10Y/SBA-15.

The structural properties of the calcined and reduced catalysts were characterized by wide-angle X-ray diffraction and the recorded patterns are depicted in Fig. 6.5. As shown in Fig. 6.5a, the diffraction peaks at 2θ=37.1, 43.1, 62.7, 75.2, and 79.3° were registered for all samples, which were assigned to the presence of cubic NiO, corresponding to the (111), (200), (220), (311) and (222) planes, respectively [406,407]. For the calcined 15Ni10Ce/SBA-15 sample, only NiO was registered as a segregate phase. No separate phase of cerium species was observed which may indicate their high dispersion. By increasing the Y loading, small diffraction peaks located at 28.9° and 33.1° appeared for the 15Ni10Ce10Y/SBA-15 sample, which may suggest the existence of Y_2O_3 (ICSD reference no. 193377) and CeO_2 (ICSD reference no. 28753), respectively [141]. The modification with Y loading of 10 wt.% may lead to a slight decrease of the dispersion of yttria and ceria on the SBA-15 support due to the deposition of the metal species on the outer surface [51].

By increasing the yttrium loading, a small shift of the diffraction peak of NiO was identified for Y and Ce modified samples. The diffraction peaks located at 37.08 and 43.11° on the 15Ni10Ce/SBA-15 sample shifted to 37.27 and 43.34° for 15Ni10Ce10Y/SBA-15, indicating that the partial introduction of Ni^{2+} into CeO_2 lattice may occur [141]. For the 15Ni10Ce10Y/SBA-15 sample, apart from the possible reflection of Y_2O_3, the diffraction peaks centered at 28.56 and 28.55° possibly arising from CeO_2 (ICSD reference no. 28753) and Ce-Y solid solution (ICSD reference no. 28808, cubic, space group $Fm\bar{3}m$), respectively, cannot be excluded because of their adjacent positions. Hence, it can be speculated that the solid solution of Y-Ce can be formed on yttrium and cerium containing samples. The formation of Y-Ce solid solution can be formed by the similar ion radius of Ce^{4+} (0.97 Å) and the Y^{3+} dopant (1.02 Å), which led to the replacement of Ce by Y in the lattice [408]. This may be demonstrated by subsequent XPS results.

Table 6.2. The textural properties, the crystallite size of NiO, and metallic Ni measured for the reduced samples.

Catalyst	SSA (m^2/g)[a]	V_p (cm^3/g)[b]	Crystallite size (nm)[c]		Crystallite size of Ni° (nm)[d]	Dispersion of Ni (%)[d]	Lattice Parameter *a* (nm)[e]
			NiO	Ni^0			
SBA-15	973	1.09	n/p	n/p	n/p	n/p	11.9
15Ni10Ce/SBA-15	400	0.54	13	20	11.0	3.2	11.4
15Ni10Ce2Y/SBA-15	410	0.55	14	22	12.1	3.1	n/m
15Ni10Ce4Y/SBA-15	443	0.61	15	17	12.5	3.1	n/m
15Ni10Ce10Y/SBA-15	395	0.53	15	21	11.4	3.4	11.2

n/p: not present. n/m: not measured

[a] Calculated by a BET calculation method.

[b] Calculated by BJH desorption method.

[c] Calculated from XRD by the Scherrer equation.

[d] Calculated by H_2 chemisorption assuming spherical nickel crystallites of uniform size.

[e] Calculated from SAXS by $a=2d_{(100)}/\sqrt{3}$

Wide-angle XRD patterns of the reduced catalysts are depicted in Fig. 6.5b. The structural properties of the catalysts changed after reduction compared to the calcined samples. Only three peaks located at 2θ= 44.69, 52.03, and 76.60° were registered, which were assigned to the diffraction of metallic Ni, corresponding to (111), (200), and (220) planes, respectively [204]. The peak positioned at 2θ=28.60° was too weak to be identified, meaning the dispersion of yttria or ceria was improved after reduction. Similar to the calcined samples, a slight shift of the reflection from 2θ=44.69° for 15Ni10Ce/SBA-15 to 2θ=44.56° for 15Ni10Ce10Y/SBA-15 was found. Nevertheless, it is difficult to estimate whether the insertion of Ni into the Ce or Si structure occurred, as there was no clear diffraction peak of ceria, making the comparison of cell parameter impossible [409].

The crystallite size of NiO and Ni° were calculated by the Scherrer equation and listed in Table 6.2. It can be seen that the introduction of Y did not have a significant effect on the crystal size of NiO or Ni metal. Meanwhile, the crystallite size of metallic Ni increased compared to the NiO calculated for the calcined materials, which can be attributed to the phase change during the reduction step.

H_2 chemisorption experiments were carried out and the dispersion of Ni, as well as the estimated size of Ni° crystallites, are presented in Table 6.2. With the increasing Y loading up to 4 wt.%, the dispersion of Ni did not change significantly. Furthermore, there is no significant difference regarding the Ni° particle size, indicating that the addition of Y has only a slight effect on active sites. The difference of Ni° particle size obtained from different methods (XRD or H_2 chemisorption) can be attributed to the effect of different measurements or the not 100% reduction of nickel.

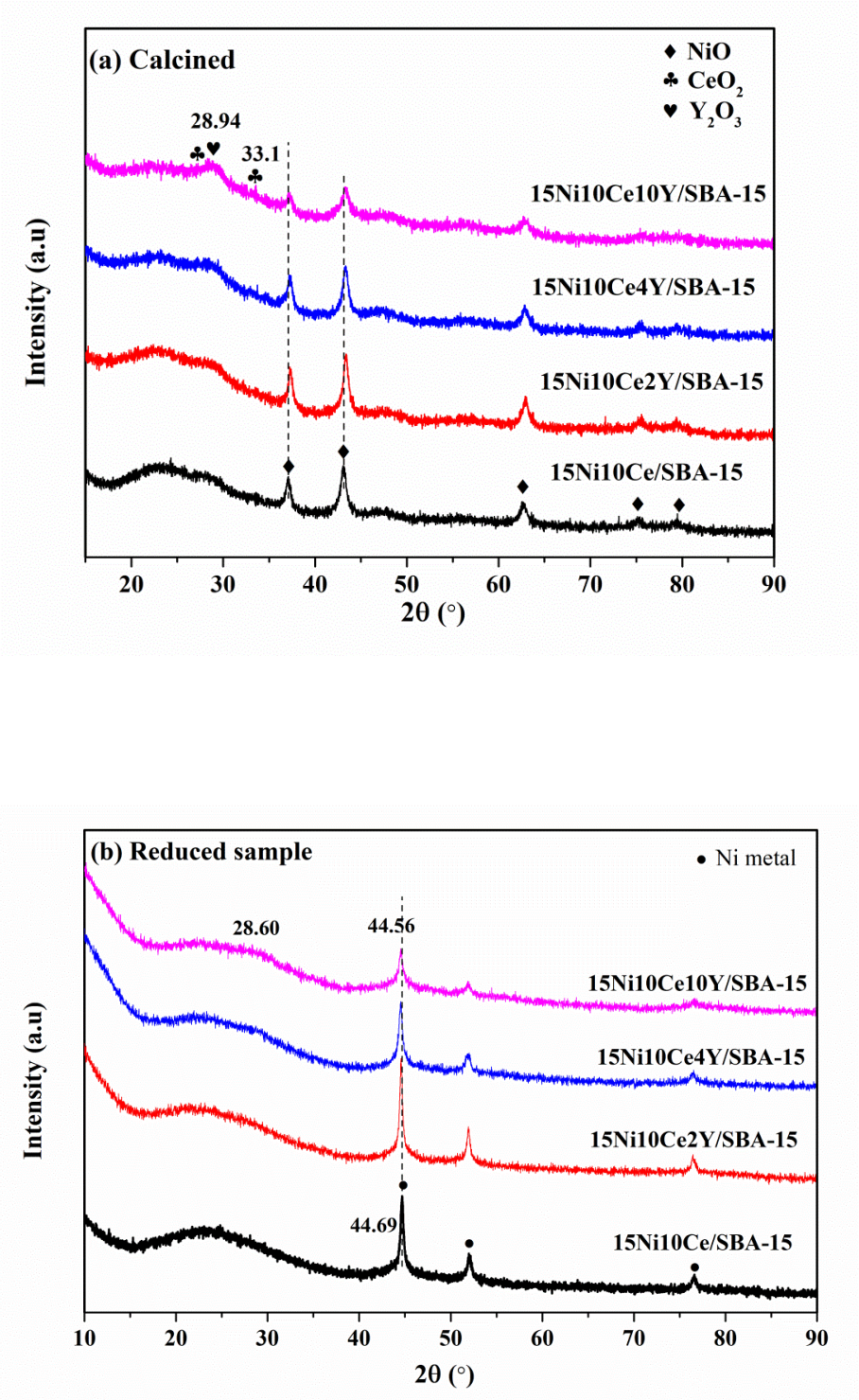

Figure. 6.5. XRD patterns of the catalysts promoted with cerium and cerium-yttrium; (a) calcined samples, (b) reduced samples

In order to confirm the unique structure of SBA-15 and to determine the dispersion of Y_2O_3, CeO_2, and Ni° on the surface, the TEM and EDS analyses were conducted for the reduced catalysts. The micrographs are presented in Fig.6.6 with the preserved well-defined two-dimensional channels and the hexagonal pore arrangement. These results demonstrated that the distinct mesostructure was maintained after impregnation with metals. This result is consistent with the SAXS. Fig.6.6a shows micrographs of 15Ni10Ce/SBA-15 catalyst with big Ni particles that were probably formed by the agglomeration of nickel outside the mesoporous channels of SBA-15. On the contrary, 15Ni10Ce10Y/SBA-15 catalyst presented well-dispersed Ni species inside the channels of the support, with only a few big particles found on the outer surface (Fig. 6.6b).

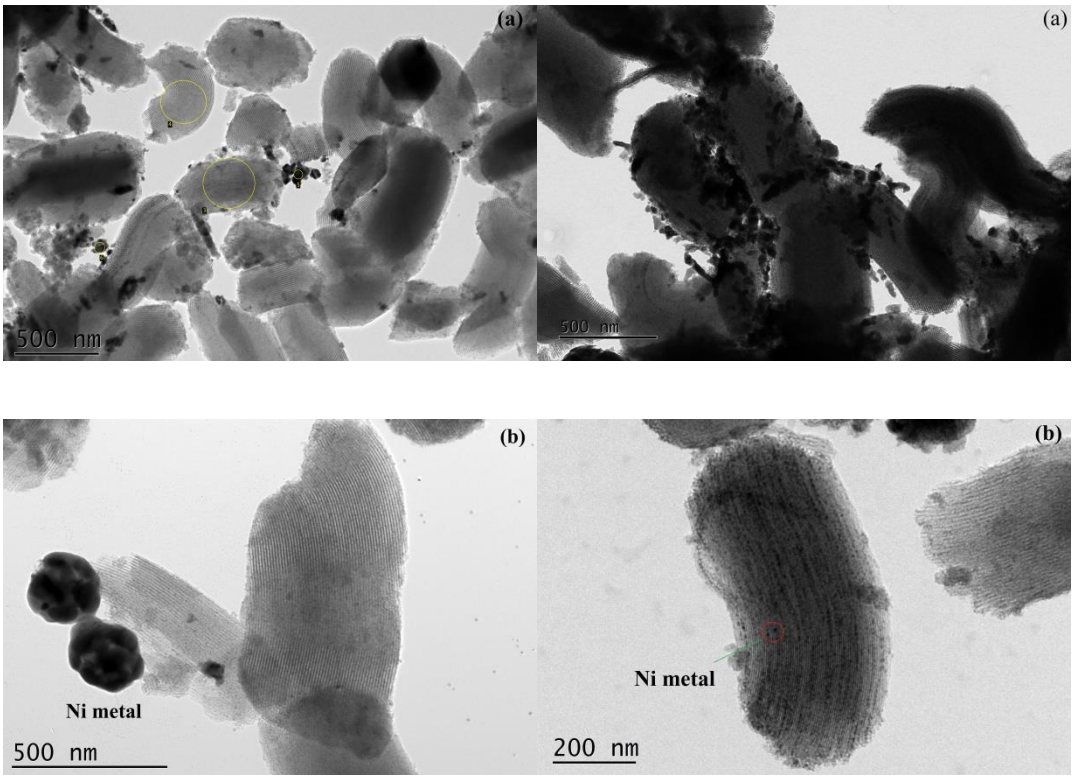

Figure. 6.6. TEM micrographs of the reduced catalysts; Conditions: 550 °C for 1.5h under 5%H_2/Ar; (a) 15Ni10Ce/SBA-15, (b) 15Ni10Ce10Y/SBA-15.

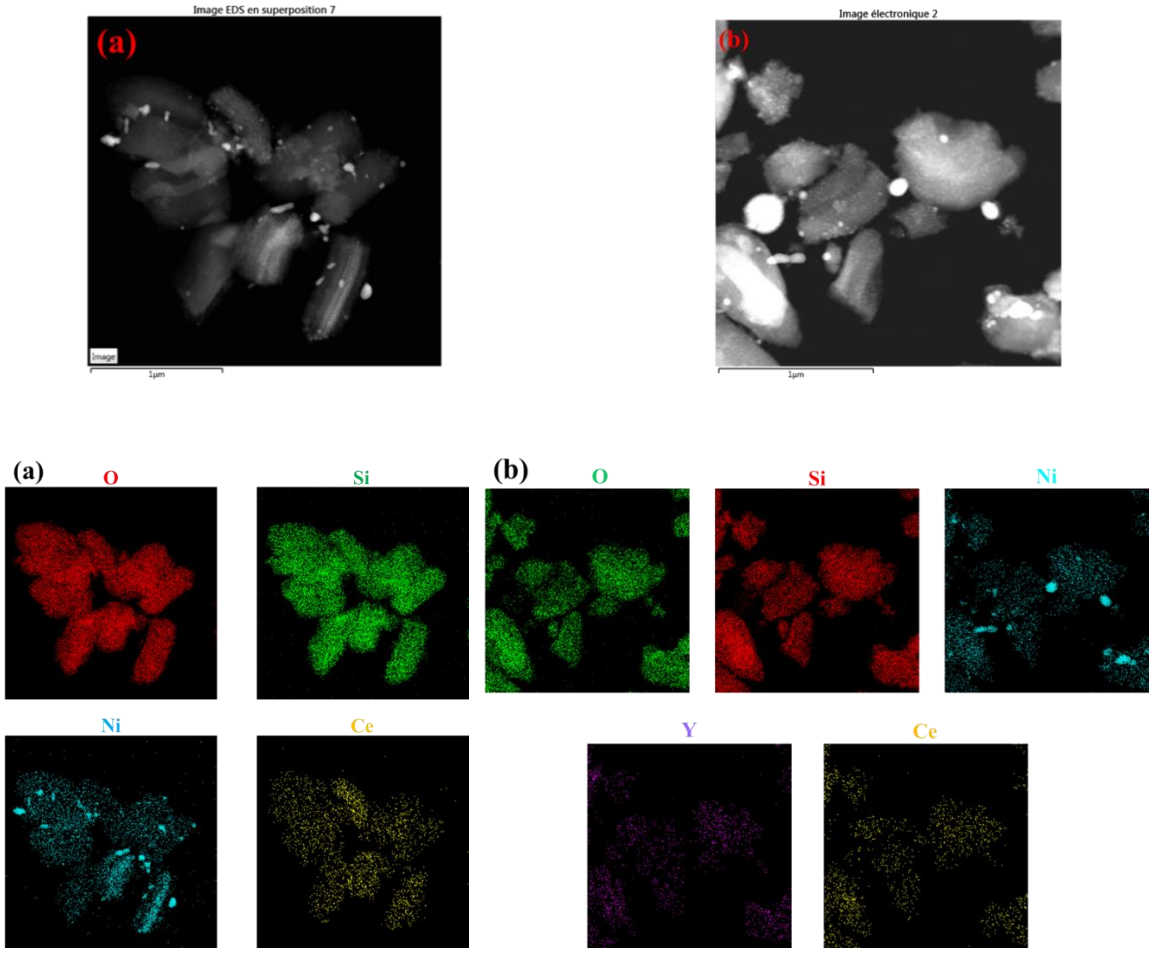

Figure. 6.7. EDS elemental mapping analysis performed for the reduced catalysts: (a) 15Ni10Ce/SBA-15, (b) 15Ni10Ce10Y/SBA-15

EDS elemental mapping analysis was carried out for 15Ni10Ce/SBA-15 and 15Ni10Ce10Y/SBA-15 and presented in Fig. 6.7a and b. In the former, cerium species were well dispersed over the support, whereas nickel was exposed in the form of big particles, as well as uniformly distributed nanoparticles. 15Ni10Ce10Y/SBA-15 revealed Y and Ce species evenly dispersed and less agglomerated particles of Ni. The reducibility of the studied catalysts will be described in detail in the next section.

To investigate the surface composition and oxidation states of the catalysts, the XPS characterization was performed for the reduced catalysts. The XPS spectra are shown in Fig. 6.8 and the atomic ratio and binding energies were calculated in Table 6.3.

As shown in Fig. 6.8a, the O1s spectrum can be deconvoluted into 3 peaks located at 530.6, 532.5, and 533.4 eV, which were attributed to the metal oxide (O_{OM}), oxygen of silica (O_{OSi}), and surface oxygen species adsorbed on oxygen defects (O_{OH}), respectively [410,411]. As shown in Table 6.3, the increase of Y loading resulted in the increase of O_{OH} species. Thus, it can be seen that the increment of Y loading leads to the increase of oxygen defects [373,375].

As shown in Fig. 6.8b, the overlapped spectra can be deconvoluted into 3 peaks. The intensive peak located at 154.0 eV was assigned to the presence of Si2s. The two weak peaks positioned at 157.5 and 159.8 eV were attributed to the presence of $Y3d_{5/2}$ and $Y3d_{3/2}$ [412]. As the increase of Y loading, the peak intensity of Y_2O_3 increases, indicating more yttria species deposited on the surface of the support. Also, no apparent peak shifts regarding $Y3d_{5/2}$ were registered (Table 6.3). From Fig. 6.8c, it can be seen that the intensity of the Si2p peak, which locates at 103.1 eV, decreases with the increase of Y loading, which can be attributed to the coverage of Ni, Ce, and Y on the surface of the SBA-15 material.

In Fig. 6.8d, the XPS spectra of $Ni2p_{3/2}$ for the for 15Ni10Ce/SBA-15 catalyst consisted of two peaks located at 852.8 and 855.5 eV, which were attributed to the Ni^0 and Ni^{2+} species, with a shake-up satellite peak at 860.7 eV [413]. As presented in Table 6.3, the $Ni2p_{3/2}$ peak shifted towards higher binding energy as the increase of Y promotion, indicating the Ni species could also be incorporated into ceria lattice [373]. It can be observed in Table 6.3 that promotion of the catalyst with Y lead to a change in the Ni^0/Ni^{2+} ratio. The addition of 2 wt.% Y resulted in the increase of surface Ni^0 concentration. However, the Y loading higher than 2 wt.% led to the

decrease of the surface ratio of Ni^0 species. Based on the XRD results, the Ni particle size over the SBA-15 support did not increase significantly with Y addition. However, the peak of Y_2O_3 may appear when the Y loading reached 10 wt.%. Thus, the decrease of Ni^0 concentration may be caused by the excess Y species on the surface of SBA-15. Also, the adsorption of oxygen species on the surface of Ni^0 species cannot be excluded. The surface ratio of Ni as shown in Table 6.3 maintains stable with the increase of Y loading until 4 wt.% and then increases when Y loading reached 10 wt.%, indicating the increased Ni species concentration on the surface of the support for 10 wt.% Y loading promoted sample.

The Ce3d XPS spectra of the catalysts were presented in Fig. 6.8e. With the increase of Y adding, the peak intensity of the Y-doped catalysts did not change largely as comparison with the peak intensity of Y-free catalysts. The Ce3d peak could be deconvoluted to 10 peaks labeled as u^{iii}, u^{ii}, u^{i}, u, u^0, v^{iii}, v^{ii}, v^{i}, v, and v^0. The components labeled as u^0, u^{i}, v^0, and v^{i} were attributed to Ce^{3+} species, and the other components labeled as u^{iii}, u^{ii}, u, v^{iii}, v^{ii}, and v were assigned to the presence of Ce^{4+} species [141]. From Table 6.3, it can be seen that the ratio of Ce^{3+}/Ce over the Y-doped catalysts increased gradually as the increase of Y loading, with the highest ratio of Ce^{3+}/Ce obtained over 10 wt.% Y promoted catalyst. Thus, it can be concluded that the dopant of Y promotes the formation of Ce^{3+}, and thus more oxygen vacancies are created [361]. The Ce3d peak position in eV for Y-doped catalysts also shows a slight shift as the increase of Y loading towards lower binding energy as the increase of Y loading, which demonstrates the incorporation of Y and Ni inside the Ce lattice over the catalysts. This is consistent with the results from XRD.

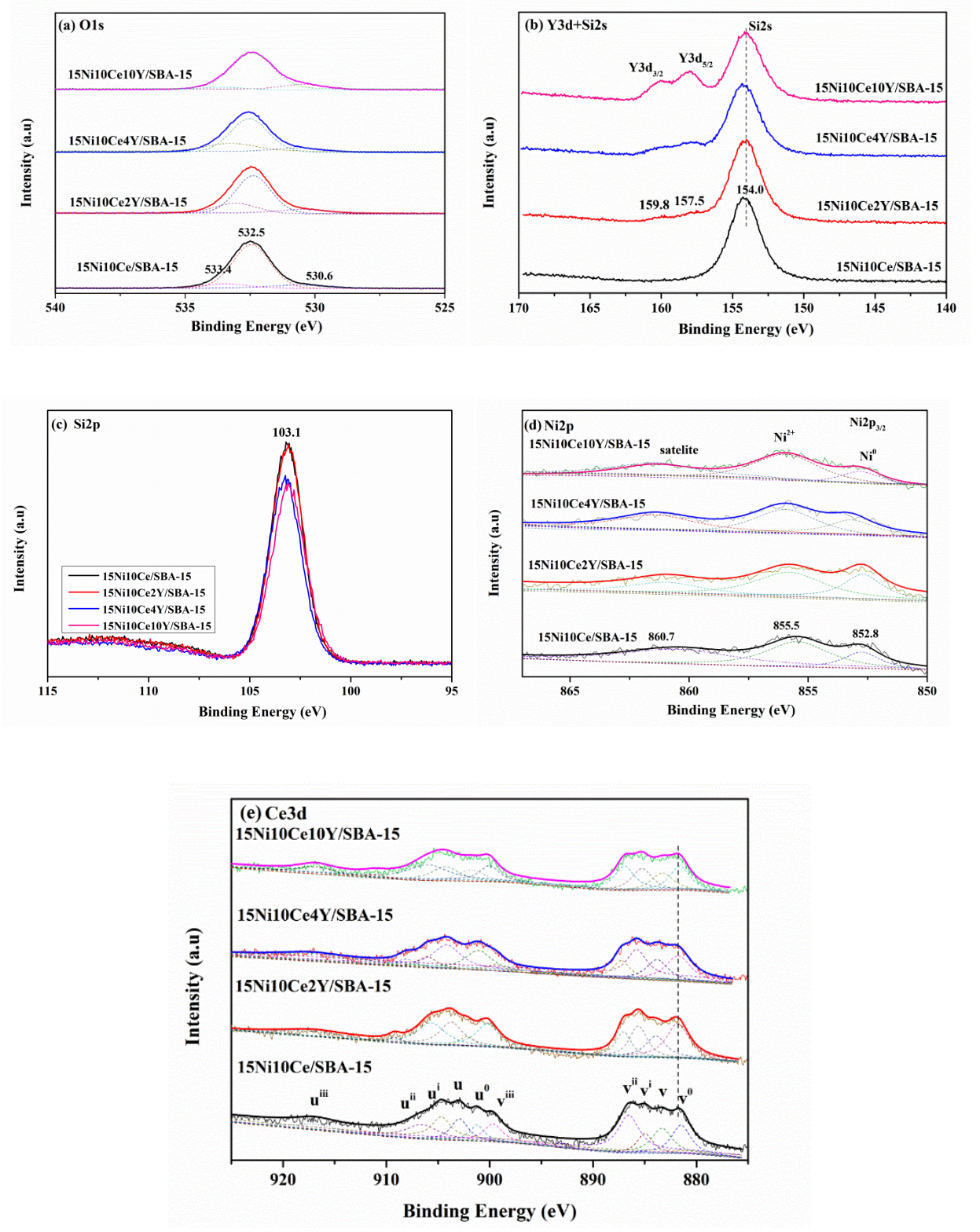

Figure. 6.8. XPS spectra for the reduced samples; Condition: 550 °C reduced under 5% (v/v) of H_2/Ar flow for 1.5h. (a) O1s, (b) Y3d, (c) Si2p, (d) Ni2p, (e) Ce3d

Table 6.3 XPS derived Ce^{3+} and Ni^0 percentage, Binding Energy of $Y3d_{5/2}$, $Ni2p_{3/2}$ and $Ce3d_{5/2}$ in eV, Ni, Ce, and Y atomic ratio for the samples after reduction.

Catalyst	Atomic ratio (%)						Binding Energy (eV)		
	Ni	Ce	Y	Ni^0/Ni^{2+}	$O_{OH}/(O_{OM}+O_{OSi}+O_{OH})$	$Ce^{3+}/(Ce^{3+}+Ce^{4+})$	$Ni2p_{3/2}$	$Ce3d_{5/2}$	$Y3d_{5/2}$
15Ni10Ce/SBA-15	1.14	0.56	-	21.8	9.0	48.2	855.5	881.8	
15Ni10Ce2Y/SBA-15	1.00	0.64	3.95	25.9	22.4	50.1	855.8	881.8	157.9
15Ni10Ce4Y/SBA-15	1.04	0.55	4.10	19.1	23.0	51.5	856.0	881.7	157.9
15Ni10Ce10Y/SBA-15	1.20	0.52	4.80	11.7	23.9	57.2	856.0	881.6	158.0

6.2.4 Reducibility of the studied catalysts

The reduction behavior was studied by the H_2-TPR method and presented in Fig.6.9. Four peaks were revealed and labeled as α, β, γ, and δ for Ni15Ce10/SBA-15 and Ni15Ce10Yx/SBA-15 catalysts (Fig.6.9a-b), and attributed to the reduction of Ni species with different degree of metal-support interactions [414,415]. The peaks centered at the temperature lower than 400 °C (α and β) were attributed to the reduction of NiO species located at the external surface of SBA-15 [415,416]. The peaks centered at 400-500 °C (γ) and 600 °C (δ) were assigned to the reduction of NiO weakly and strongly interacting with the support, respectively [417]. Fig.6.9 revealed a shift of the reduction peaks towards lower temperature with the increment of the Y content, except for the sample with 2 wt.% of Y. This indicates that the reducibility of Y-promoted catalysts has been improved with the increasing loading of yttrium. Table 6.4 presents the H_2 consumption calculated for Y-promoted NiCe/SBA-15 catalysts. The maximum of reduction peaks was lower except for

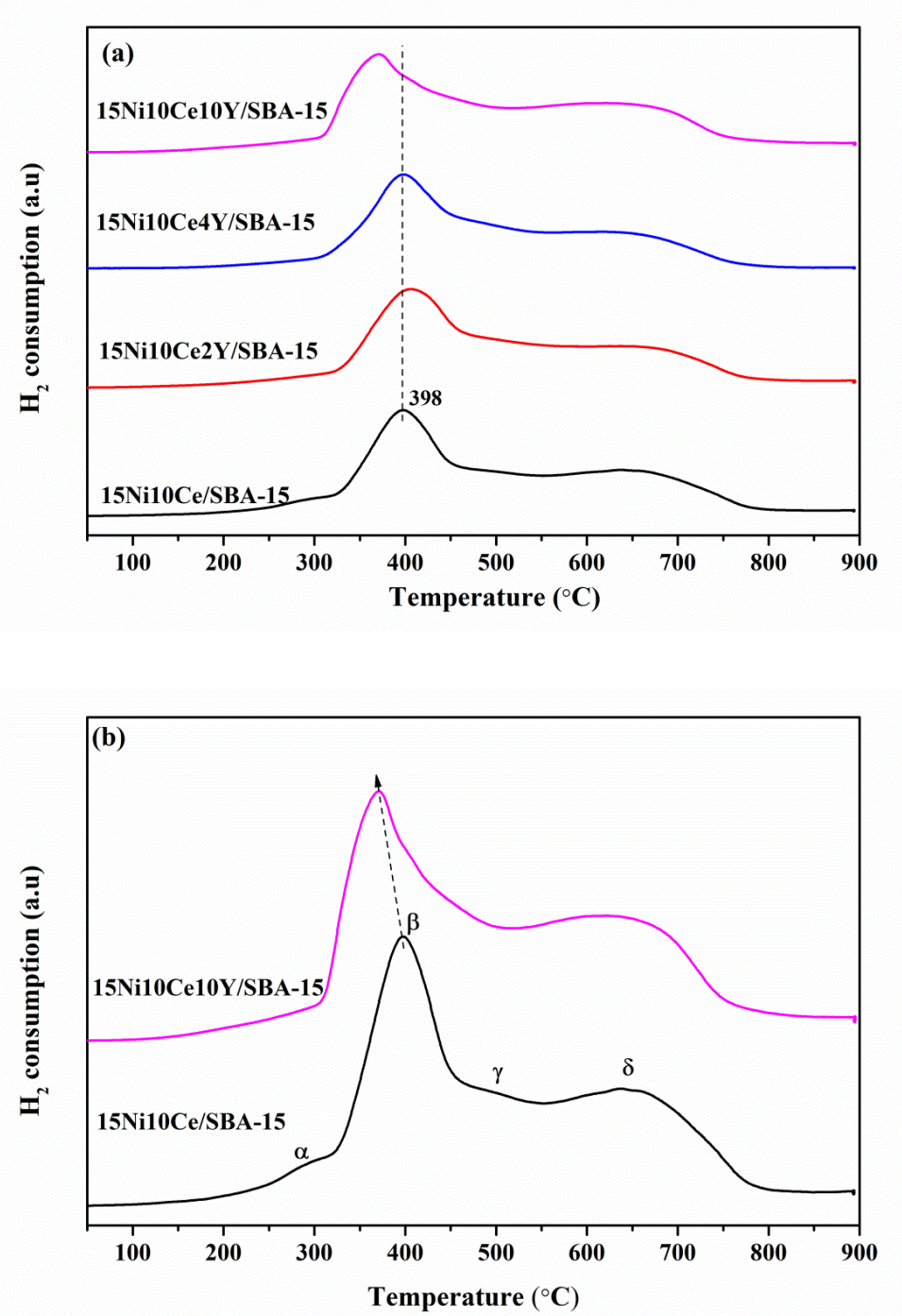

Figure. 6.9. H_2-TPR profiles of the as calcined catalysts (a) and the enlarged mapping of the profiles of 15Ni10Ce/SBA-15 and 15Ni10Ce10Y/SBA-15 (b)

those with 2 wt.% of Y-containing sample. The latter revealed maximum reduction peaks very similar to the 15Ni10Ce/SBA-15 catalyst. TEM micrographs showed an agglomeration of Ni particles in the reduced Ni15Ce10/SBA-15 sample, whereas the presence of Y facilitated the formation of small nickel particles. In this regard, the reducibility of Ni15Ce10Yx/SBA-15 catalysts has been enhanced.

Table 6.4. The reduction temperature peaks and the H_2 consumption values of the studied catalysts during H_2-TPR

Catalyst	Temperature (°C)				H_2 consumption ($mmol \cdot g^{-1}$)				
	α	β	γ	δ	α	β	γ	δ	Total
15Ni10Ce/SBA-15	299	397	483	665	0.15	0.70	1.30	0.65	2.80
15Ni10Ce2Y/SBA-15	269	401	504	673	0.09	0.84	1.27	0.49	2.70
15Ni10Ce4Y/SBA-15	223	394	455	649	0.02	0.52	1.38	0.63	2.54
15Ni10Ce10Y/SBA-15	238	363	429	622	0.08	0.56	1.07	1.18	2.89

6.2.5 Basicity of the studied catalysts

An adequate number of basic sites is known to play a crucial role in the catalytic performance of CO_2 methanation catalysts. Thus, the basicity of the studied catalysts was investigated by temperature-programmed desorption using CO_2 as a probe molecule. CO_2 desorption profiles are shown in Fig.6.10 and the basic site distribution is listed in Table 6.5. The CO_2 desorption peaks can be classified into three types based on their temperature regions: <220 °C, 220-500 °C, and >500 °C correspondings to weak, medium, and strong basic sites, respectively [141,169,391]. As shown in Table 6.5, the medium basic sites and total basic sites increased with increasing Y

loading with the expense of strong basic sites. The highest amount of medium basic sites was obtained for 15Ni10Ce10Y/SBA-15 catalyst. Pan et al. [160] investigated the reaction route of CO_2 methanation over $Ni/Ce_{0.5}Zr_{0.5}O_2$ catalyst. The authors suggested that medium basic sites can promote the formation of monodentate carbonates, enhancing activity in CO_2 methanation. Similar observations regarding the beneficial influence of medium basic sites were described elsewhere [141,179,391]. In the current study, the enhancement of moderate basicity can be attributed to the increase of the Ce^{3+} ratio shown in XPS. The incorporation of Y resulted in an increase of the Ce^{3+} ratio, thus more CO_2 species were adsorbed on the generated oxygen vacancies [141].

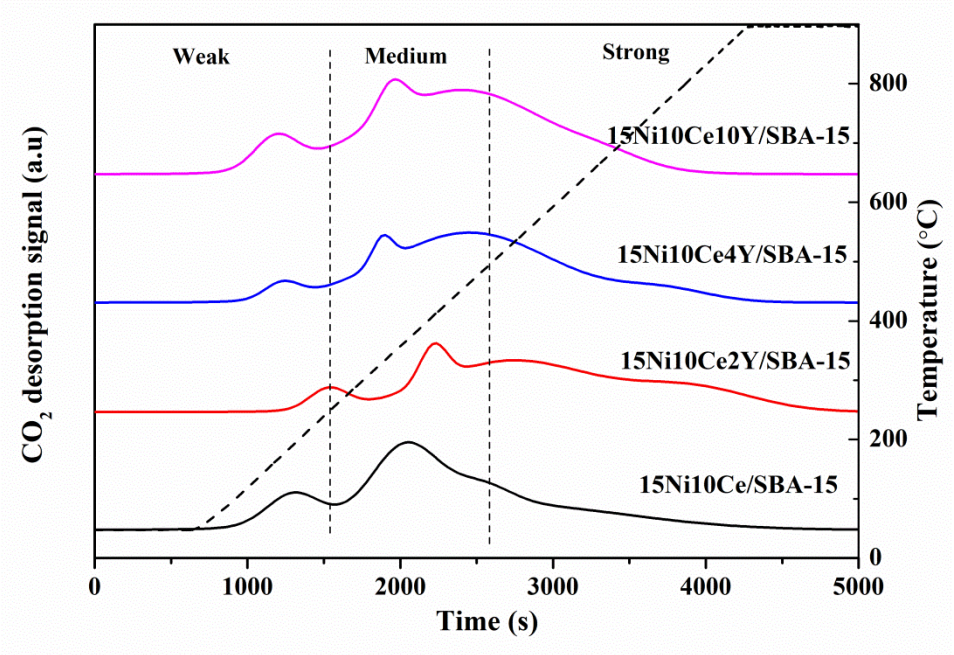

Figure. 6.10. CO_2 desorption curves of the catalysts after reduction at 550 °C for 1.5h.

Table 6.5. The basic site distribution calculated from CO_2-TPD for the reduced catalysts.

Catalyst	Basic sites [□mol/g_{cat}]			Total basic sites	Distribution of basic sites [%]		
	weak	medium	strong		weak	medium	strong
15Ni10Ce/SBA-15	6.7	23.0	24.6	54.3	12.4	42.3	45.3
15Ni102YCe/SBA-15	3.2	38.5	11.8	53.5	6.0	72.0	22.0
15Ni10Ce4Y/SBA-15	2.2	50.5	4.6	57.4	3.9	88.1	8.0
15Ni10Ce10Y/SBA-15	5.4	64.4	2.6	72.5	7.5	88.9	3.6

6.2.6 Catalytic performance in CO_2 methanation

The catalytic activity and CH_4 selectivity of NiCe/SBA-15 catalysts promoted with Y are presented in Fig.6.11a and Fig.6.11b. The blue dash lines in both figures represent the thermodynamic equilibrium of CO_2 conversion and CH_4 selectivity in CO_2 methanation for the assumed experimental conditions. CO_2 conversion, obtained for the studied catalysts, increased with the increasing reaction temperature and reached nearly equilibrium at 450 °C. In the temperature range of 300-350 °C, in which the conversion values of the catalysts are distinguished, it can be seen that yttrium promoted catalysts showed higher CO_2 conversion compared to that of Ni15Ce10/SBA-15. Depending on the loading of yttrium, the following activity order was observed at 350°C: 10Ce (40.0%) < 2Y (44.0%) < 4Y (54.5%) < 10Y (61.2%), in which 10Ce refers to the 15Ni10Ce/SBA-15 sample.

Fig.6.11b shows selectivity to CH_4, revealing a gradual decrease with the temperature rise. At temperatures lower than 300 °C, there is no difference in the CH_4 selectivity for all catalysts as the CO_2 conversion is negligible in this temperature region. In the temperature window between 300 and 400 °C, the Y-free catalyst showed the lowest CH_4 selectivity. Meanwhile, the series of Y-

promoted catalysts showed equally high CH_4 selectivity. It is worth noting that only carbon monoxide (CO) was registered as a side product in the studied reaction conditions. The formation of CO is mainly caused by the reverse water-gas shift reaction ($CO_2 + H_2 = CO + H_2O$) [418]. According to the thermodynamics of the CO_2 methanation reaction, the CO selectivity increases with the increasing temperature, consequently decreasing selectivity towards CH_4 production [418,419]. It has been reported that the Ce promotion of Ni/SBA-15 catalyst can increase the activity and CH_4 selectivity in CO_2 methanation [178,224]. The presence of cerium can enhance the activation of CO_2 at low temperatures, hence improve the activity and CH_4 selectivity [221]. Herein, the promotive effect of Y on NiCeY/SBA-15 catalysts was observed.

The catalytic performance of yttrium individually doped Ni/SBA-15 catalysts were also displayed in Fig.6.11c and d. It can be seen that the Ni/SBA-15 catalysts doped by yttrium show worse activities compared to those catalysts doped by Ce and Y.

It has been reported that the methanation mechanism over Ni-containing SBA-15 and MCM-41 mesoporous silicas undergoes the route of CO-free and without the participation of intermediates, such as carbonate and formate [221]. In the study of Bacariza et al. [221], FTIR analysis carried out for Ni/SBA-15 catalyst showed the adsorbed CO_2 species on the surface of Ni metal transformed to carbonate species, following the formation of formate species, then led to the formation of methane. However, many carbonyl species could be formed over the catalysts, which accounted for the formation of CO and the feasible poisoning of metallic nickel. In the CO_2 adsorption experiment carried out with the assistance of FTIR, only CO species (probably originating from the CO_2 disproportionation/dissociation reaction) were found over the bare SBA-15 support, which suggests that the methanation reaction could not occur in the presence of Ni metal [221]. When Ce was loaded onto the Ni/SBA-15 catalyst, the carbonyl species that led to

the formation of CO decreased, consequently promoted the activation of CO_2 and enhanced the formation of CH_4. The promotion effect of Ce for Ni/SBA-15 catalyst in CO_2 methanation was undisputed [178]. Moreover, the promoting effect of Y on Ni/CeO_2 catalysts has been reported in CO_2 methanation, in which the addition of Y can lead to an increase of weak and medium basicity, more oxygen vacancies, and enhanced metal-support interaction [141].

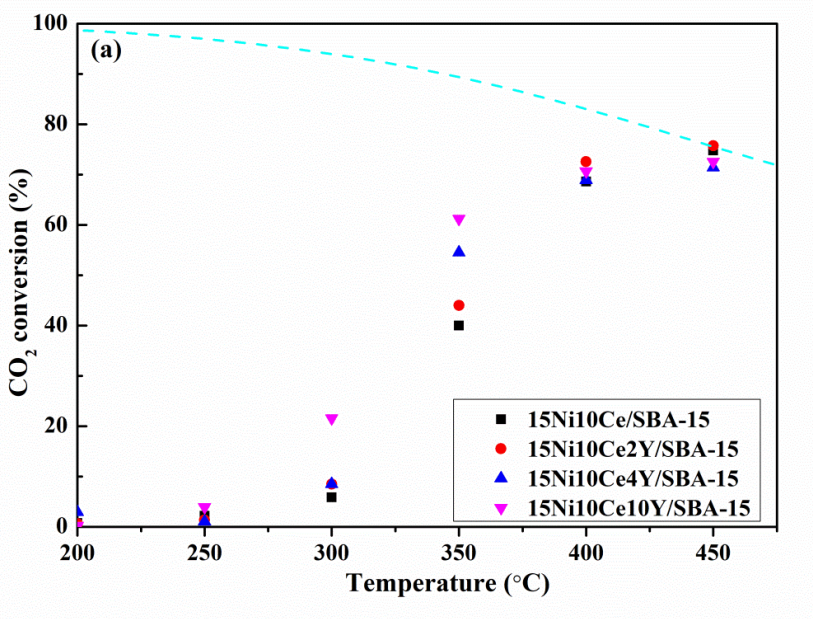

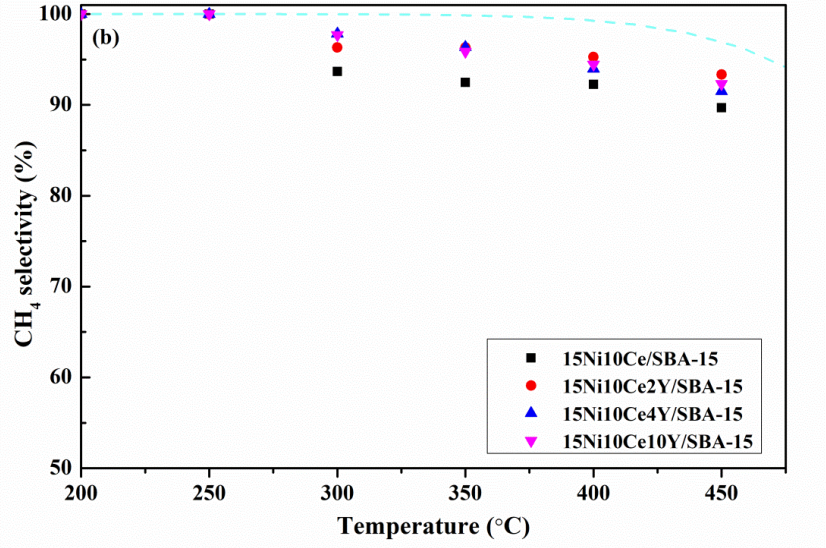

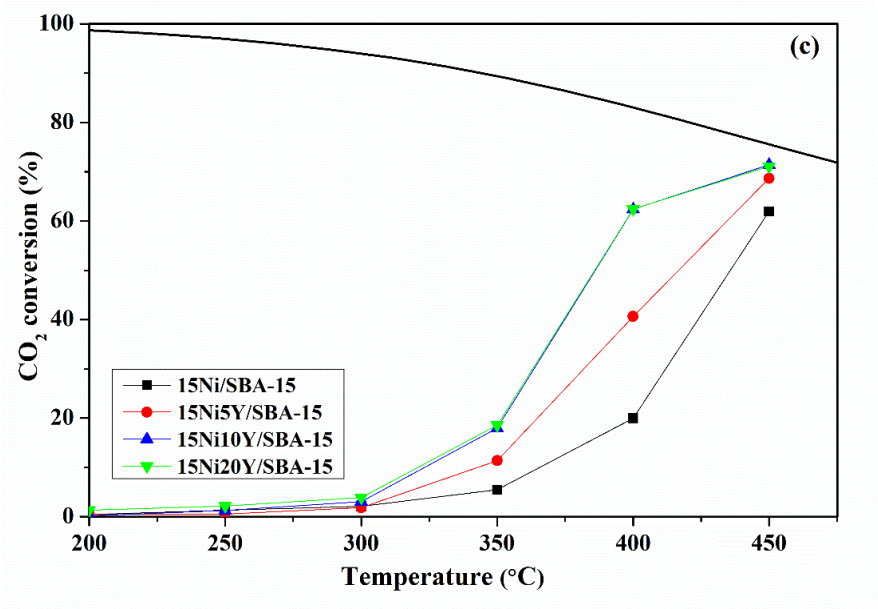

Figure. 6.11. The CO_2 conversion (a) and CH_4 selectivity (b) of NiCe/SBA-15 catalysts with and without yttrium in CO_2 methanation; CO_2 conversion (c) and CH_4 selectivity (d) of yttrium promoted Ni/SBA-15 catalysts.

In the current study, the presence of Y promoted the reduction of Ni species of 15Ni10CexY/SBA-15 catalysts, as proven by the H_2-TPR experiment. Meanwhile, the formation of solid solution of Y-Ce was demonstrated by XPS. Also, the addition of Y could lead to the increased ratio of

$Ce^{3+}/(Ce^{3+}+Ce^{4+})$, with 10 wt.% Y-modified catalysts having the highest ratio of $Ce^{3+}/(Ce^{3+}+Ce^{4+})$, and favoring an increase of oxygen vacancies. The latter is believed to promote the activation of CO_2 [141]. Moreover, CO_2-TPD results show that the presence of yttrium oxide can contribute to the increase of medium-strength basic sites, which are advantageous in CO_2 methanation [160]. In our study, the 10 wt.% Y-modified catalysts presented the highest number of medium basic sites, which can explain the increased CO_2 conversion and CH_4 selectivity.

By correlating the CO_2 conversion at 350 °C with the ratio of $Ce^{3+}/(Ce^{3+}+Ce^{4+})$ (Fig.6.12a), a linear correlation can be found between $Ce^{3+}/(Ce^{3+}+Ce^{4+})$ ratio and the increasing Y loading. With increasing Y loading up to 10 wt.%, the ratio of $Ce^{3+}/(Ce^{3+}+Ce^{4+})$ and CO_2 conversion increase linearly. Furthermore, CO_2 conversion at 350 °C can be also correlated with the amount of medium basic sites as shown in Fig.6.12b. With the increasing Y content, both CO_2 conversion and number of medium basic sites increased until 10 wt.% of Y. Promotion of 15Ni10Ce/SBA-15 catalysts with the appropriate loading of yttrium can improve the Ni dispersion and its reducibility, increase the ratio of $Ce^{3+}/(Ce^{3+}+Ce^{4+})$, and enhance the moderate basicity. All these factors can positively influence CO_2 conversion and CH_4 selectivity in CO_2 methanation reaction.

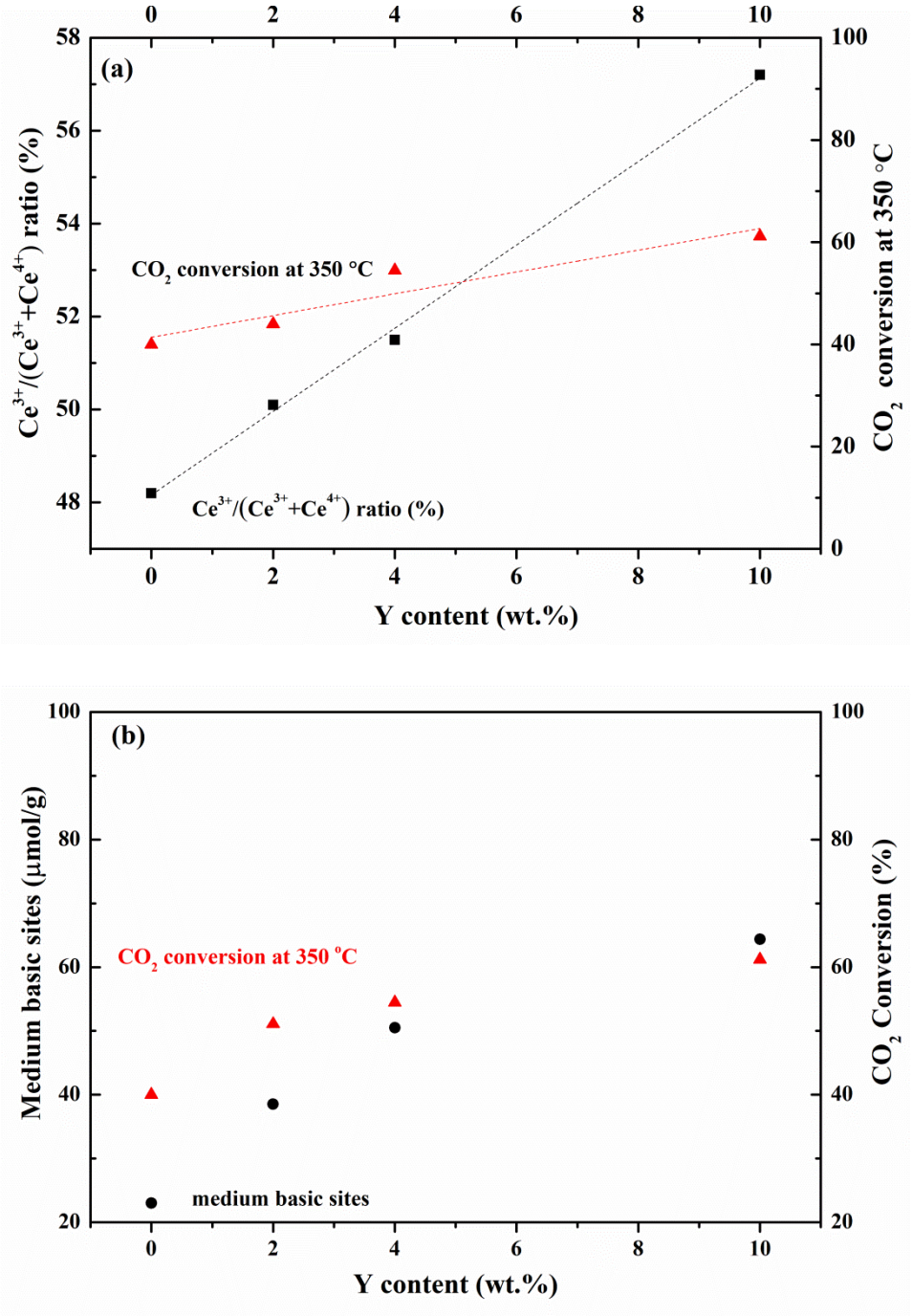

Figure. 6.12. Correlation between the CO_2 conversion at 350 °C with the ratio of $Ce^{3+}/(Ce^{3+}+ Ce^{4+})$ (a) and medium basic sites (b) with the 0 wt.% Y representing the NiCe/SBA-15 sample.

6.2.7 Stability tests of NiCe/SBA-15 and NiCeY/SBA-15 catalysts at 350 °C

The stability tests were performed at 350°C for 15Ni10Ce/SBA-15, 15Ni10Ce4Y/SBA-15, and 15Ni10Ce10Y/SBA-15 catalysts. Fig. 6.13a shows stable CO_2 conversion values during 7 h of time-on-stream (TOS) experiments. The highest CO_2 conversion was measured for 15Ni10Ce10Y/SBA-15, in good agreement with previously conducted experiments (Fig. 6.11a). In Fig. 6.13b, the catalysts modified with 4 and 10 wt.% of Y showed nearly the same CH_4 selectivity values during the stability test. Nevertheless, the 15Ni10Ce/SBA-15 catalyst showed a slight loss in CH_4 selectivity after the 2 h test, which may be caused by the formation of Ni carbonyls, leading to the possible sintering of Ni metal and formation of CO species [221]. Carbon monoxide is a side product of parallelly occurring reactions during CO_2 hydrogenation, i.e. reverse-water gas shift [420]. On the other hand, carbon monoxide production can be associated with a deactivation of metallic nickel nanoparticles. Zurrer et al. [421] studied differently modified NiMg-MOF-74 mixed metals catalysts in CO_2 methanation. The authors reported that the selectivity tends toward CO production rather than CH_4 for the catalysts containing the most content of nickel (80Ni20Mg and 100Ni). Once the nickel particles are encapsulated by graphitic carbon, a reduction of the adsorbed CO intermediate is diminished due to a hydrogen deficient environment. Another explanation can be a change in the nickel-metal electronic state caused by the carbon shell formation. In the latter case, the resulting product can be carbon monoxide. Both hypotheses imply the importance of the usage of a carbon-resistant catalyst in CO_2 methanation.

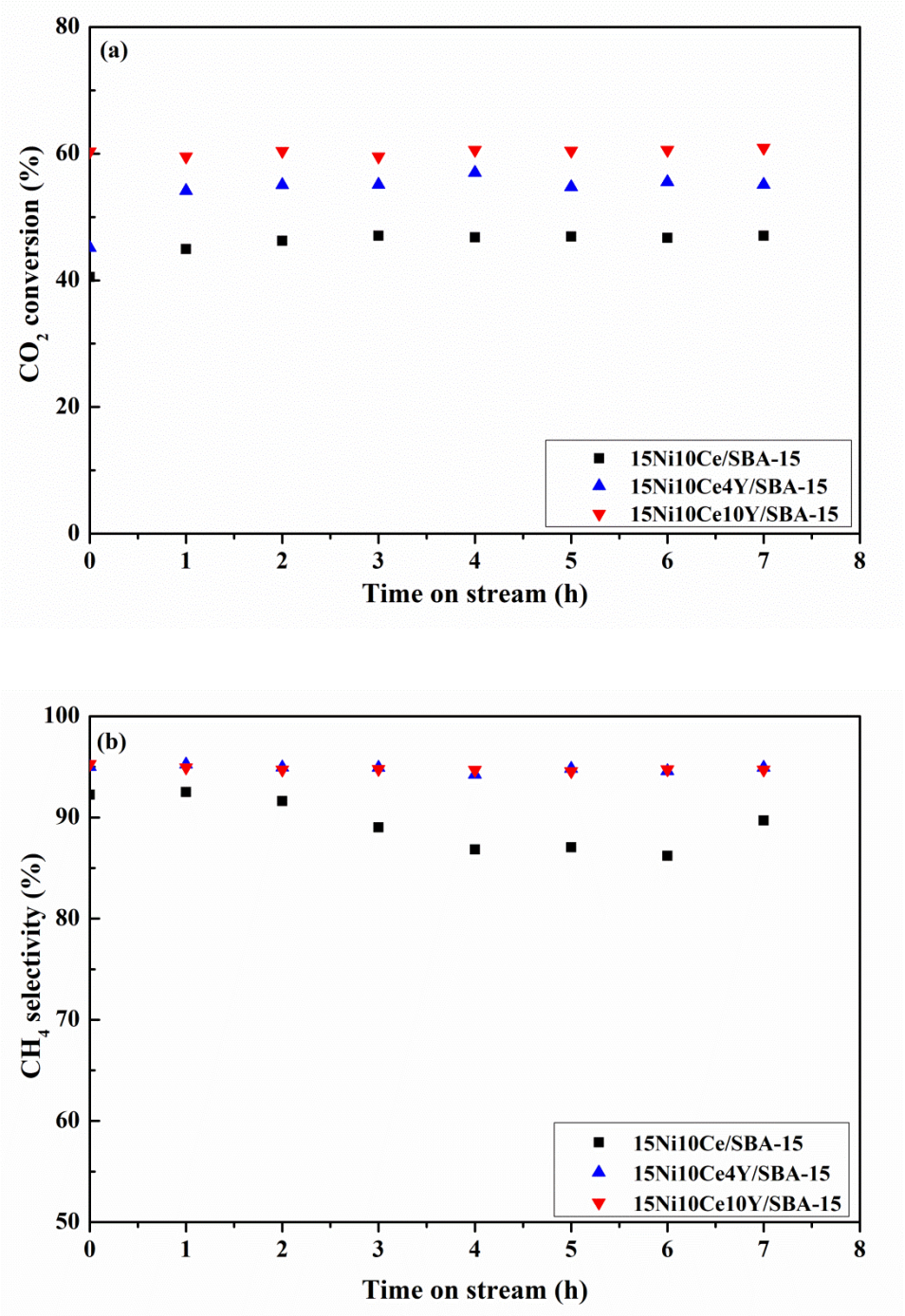

Figure. 6.13. The stability tests of CO_2 methanation over selected NiCe/SBA-15 and NiCeY/SBA-15 catalysts; (a) CO_2 conversion versus time; (b) CH_4 selectivity versus time. Experimental conditions: 350 °C, $H_2/CO_2/Ar$=60/15/25, GHSV=12,000h^{-1}.

6.2.8 Characterization of catalysts after CO_2 methanation reaction

6.2.8.1 XRD patterns of the catalysts after test

Wide-angle XRD measurements were carried out to investigate the structural features of the catalysts after CO_2 methanation. Fig.6.14 presents that nearly no changes of the diffraction peaks were registered, compared to the XRD results recorded for the reduced catalysts (Fig.6.5b). No reflection peak arising from graphitic carbon was observed. These observations can be ascribed to the good confinement of the SBA-15 structure which suppressed the sintering of nickel [179]. Nevertheless, the crystal size of metallic Ni metal was rearranged after the reaction (Table 6.6), which can be attributed to the formation of carbonyl species formed on the surface of Ni metal, leading to a partial deactivation of the catalyst [144,221].

6.2.8.2 TGA-MS tests of catalysts after test

Thermogravimetric analysis was performed to examine the existence of carbon deposits formed during CO_2 methanation. The registered curves are shown in Fig. 6.15. Spent 15Ni10Ce10Y/SBA-15 catalyst was decomposed in air, revealing the formation of products with mass signals of m/z= 18 (H_2O) and m/z= 44 (CO_2). The first weight loss registered in the temperature range from 35 to 200°C can be attributed to the removal of water molecules from the SBA-15 supported catalyst. The second mass change occurred between 200 and 400°C and can be related to desorption of the adsorbed molecules during the reaction, e.g. CO_2 (m/z = 44). The mass gain is a result of Ni° oxidation into NiO crystallites [217]. The third mass change was recorded between ca. 400 and 900°C which can be linked with possible oxidation of deposited carbon, however, that was not the case for our spent catalyst as no change of the m/z=44 signal was registered ($C+O_2=CO_2$).

Moreover, no mass difference was recorded above 800°C, excluding the existence of graphitic carbon.

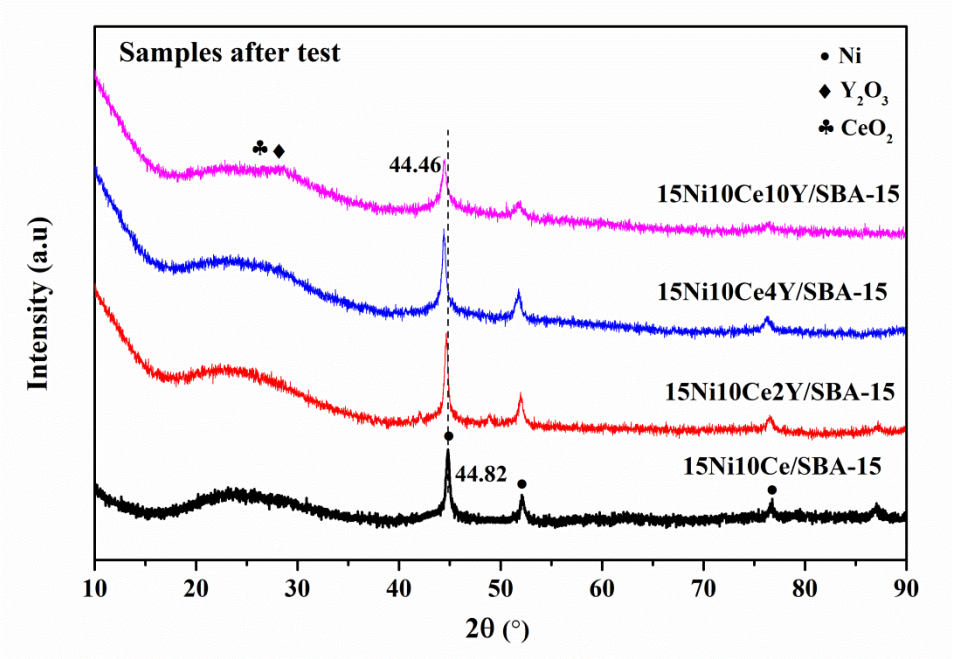

Figure. 6.14. XRD patterns of the catalysts after CO_2 methanation tests.

Table 6.6. Ni metal crystallite size calculated from XRD by Scherrer equation for the catalysts after methanation reaction.

Catalyst	Ni metal crystallite size (nm)
15Ni10Ce/SBA-15	18.8
15Ni10Ce2Y/SBA-15	17.6
15Ni10Ce4Y/SBA-15	16.8
15Ni10Ce10Y/SBA-15	16.4

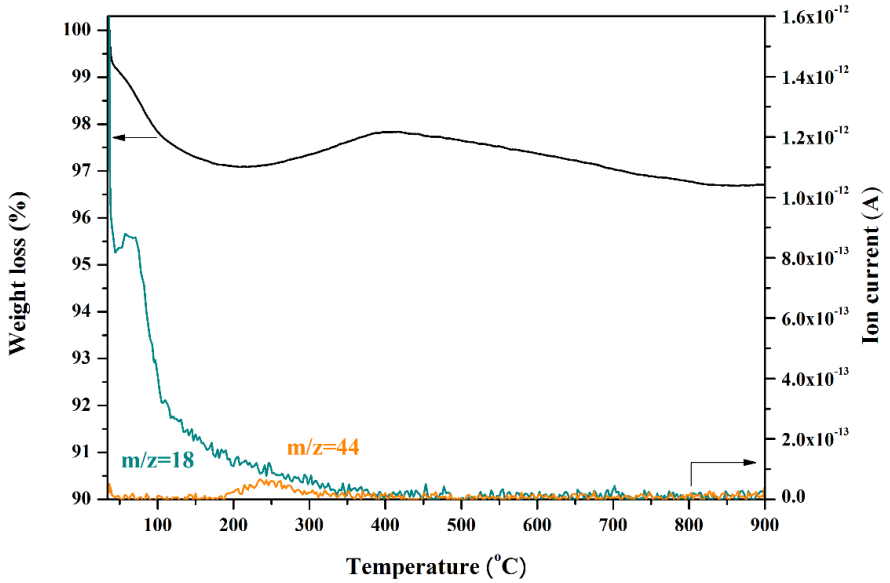

Figure. 6.15. Thermogravimetric analysis coupled with mass spectrometry carried out for 15Ni10Ce10Y/SBA-15 catalyst used in CO_2 methanation for 7 h at 350 °C.

6.2.9 Conclusions of Ce and Y promoted Ni/SBA-15 catalysts

A series of NiCeY/SBA-15 catalysts were characterized and tested in CO_2 methanation. The effect of yttrium promotion on SBA-15-supported Ni-Ce catalysts was investigated in CO_2 methanation. The microscopy analyses revealed that modification with Y positively affects the distribution of Ni particles, being extensively dispersed inside the mesoporous channels of SBA-15 silica support. Moreover, yttrium as a promoter contributed to an increase of $Ce^{3+}/(Ce^{3+}+Ce^{4+})$ ratio and the number of medium basic sites, enhanced the reducibility of nickel species, and led to the formation of a Y-Ce solid solution. NiCeY/SBA-15 catalysts showed better catalytic performance in CO_2 methanation than Y-free catalyst, with the highest CO_2 conversion and CH_4 selectivity measured for 10 wt.% Y loading. Both 15Ni10Ce/SBA-15 and 15Ni10Ce10Y/SBA-15 catalysts revealed

stable CO_2 conversion without an activity loss during 7 h of time-on-stream (TOS) experiment at 350°C. In addition, the modification with yttrium favors selective CO_2 hydrogenation towards CH_4 production. 15Ni10Ce10Y/SBA-15 showed excellent coking resistance and anti-sintering ability, which can be attributed to the confinement of the SBA-15 structure. Meanwhile, although increases of activity and selectivity of Ni/SBA-15 catalysts doped by yttrium were found, they were lower compared with Ce and Ce-Y doped NiCexY/SBA-15 catalysts.

In conclusion, both Y and Ce show improved effects on the performance of Ni/SBA-15 catalysts in CO_2 methanation. Ce is more superior than Y in individually promoting the activity of Ni/SBA-15 catalyst. The Y-Ce doped Ni/SBA-15 shows the best activities compared to Ni/SBA-15 doped by one promoter.

6.3 SBA-16 supported Ni catalysts for CO_2 methanation: on the effects of Ce or Y promoter

6.3.1 Ce promoted Ni/SBA-16 catalysts for CO_2 methanation

6.3.1.1 Introduction

Mesoporous silica materials have unique mesoporous structure and textural properties such as a high specific surface area (SSA), a large porous volume, and high thermal stability, which could confine the particle of Ni [389]. The mesoporous silica like SBA-15, KIT-6, MCM-41, and SBA-16 had been widely used as supports in various catalytic reactions [50,389,422,423]. It was found that the mesoporous structure of the support could facilitate the formation of smaller Ni particles and suppress the mobility of Ni particles at high temperatures, thus promote the activity and stability of catalyst [422]. MCM-41, SBA-15, and USY zeolite had been employed as support in the preparation of Ni catalysts for CO_2 methanation and it was found that the Ni species were highly dispersed in the mesoporous framework of the support [171,221,347,423]. However, the two-dimensional mesoporous materials like SBA-15 and KIT-6 still encounter insufficiently suppressing the sintering of Ni particles at high temperature as the movement of Ni particles in the channels or on the external surface, which is caused by the weak interaction between nickel and the support [424]. Thus, three-dimensional mesoporous material e.g., SBA-16 could be an alternative for the stabilization of Ni metal particles.

The SBA-16 supported Ni catalysts have been already used in CO_2 methanation reaction and other CO_2 utilization reaction [182,204,389,425]. It was found that smaller particles were formed within the mesopores of SBA-16 material as the confinement effect of cubic cage-like mesopores and thick pore walls [204]. In addition, the Ce promoter had a remarkable effect on the structural

stability of the Ni particles and SBA-16 framework [389]. Moreover, it has also been reported that Ni catalysts supported on Ce-incorporated-SBA-16 showed a good activity toward the chemical looping steam methane reforming (CL-SMR) process and DRM reaction as the smaller Ni metal particles in the presence of Ce, which prevented the coke formation [389,425]. The undoped Ni/SBA-16 catalysts reported in the literature did not show satisfactory activities in CO2 methanation. Thus, it is important to try to improve the performance of Ni/SBA-16 catalysts via doping various additives. Considering the advantages of the Ce promoter, it could be a promising additive for Ni/SBA-16 catalysts in CO_2 methanation.

In this chapter, the Ni/SBA-16 catalysts doped with different loading of Ce were synthesized and the effect of Ce loading on the catalytic performance of Ni/SBA-16 catalyst for CO_2 methanation reaction was investigated. XRD, N_2 physisorption, TEM/HRTEM, XPS, H_2-TPR, and CO_2-TPD technologies were used to characterize the physicochemical properties of the supports and catalysts to drive a correlation between the physicochemical properties of the catalysts and their activities in CO_2 methanation.

6.3.1.2 Materials preparation and characterization

The SBA-16 material was synthesized by the hydrothermal method and the detailed process was depicted in 3.1.4.2 of chapter 3.

The Ni/SBA-16 and Ce-promoted Ni/Ce/SBA-16 catalysts with different Ce content were synthesized by the wet impregnation method described in 3.1.4.2 of chapter 3. The catalysts were denoted as 10Ni/xCe/SBA-16 (x represents the weight percent relative to support).

The textural properties i.e. SSA, pore volume (V_p), and average pore size (r_p) of the calcined materials (supports and catalysts) were measured by N_2 adsorption-desorption technology described in chapter 3.

The XRD and TEM/HRTEM experiments followed the process in chapter 3.

The X-ray photoelectron spectra (XPS) were recorded for reduced samples on a Thermo Scientific ESCALAB 250Xi spectrometer (Thermo Fisher Scientific Inc.) (different from the apparatus shown in chapter 3)with an Al anode for Ka (1486.6 eV) radiation. The sample was reduced to 500 °C for 1 h in a 5% H_2/Ar mixture (100 mL/min) and then used for the XPS experiment. The charging effects were corrected by adjusting the binding energy of the C1s peak to 284.6 eV and the data was processed by the Thermo Avantage software attaching to the equipment. The Ce3d peak was split into ten components that considered the spin orbit splitting of $Ce3d_{5/2}$ and $Ce3d_{3/2}$. Four peaks labeled as v^0 u^0, v^i, u^i were attributed to Ce^{3+} species, and six peaks labeled as v, u, v^{ii}, u^{ii}, v^{iii}, u^{iii} were attributed to Ce^{4+} species [332,426,427].

The reducibility and basicity of the catalysts were evaluated by H_2-TPR and CO_2- TPD shown in chapter 3. The pre-treatment condition for CO_2- TPD was different from chapter 3 and described as below. Before CO_2 adsorption, the sample (60 mg) was reduced in 5% H_2/Ar flow (50 mL/min) at 500 °C for 1 h. Then, the adsorption and desorption process was carried out following the process in chapter 3.

6.3.1.3 Catalytic activity test and stability test

The catalytic activity of catalysts was evaluated by the same process shown in chapter 3. The reduction condition was from ambient temperature to 500 °C and then kept for 1 h with a ramp of

10 °C/min. The reduction temperature was deployed based on the methanation results under different pre-treatment temperatures in which 500 °C showed the best performance

The stability test was performed in the same apparatus as the activity test. The sample (0.5 mL) was reduced at 500 °C for 1 h following cooled down to 350 °C for stability test, with the GHSV of 12,000 h^{-1}. Then, it was maintained at 350 °C for 7 h. The CO_2 conversion and CH_4 selectivity were also calculated following the equations of Eq.1 and Eq.2 in chapter 3.

6.3.1.4 Textural properties, structural properties, morphology, and surface states of elements

The N_2 sorption curves and pore distribution curves of the samples obtained from N_2 adsorption-desorption isotherms were displayed in Fig.6.16. The textural properties were displayed in Table 6.7. As shown in Fig.6.16a, all samples have a type-IV N_2 adsorption-desorption curve with a hysteresis loop located at a relative pressure of 0.40-0.75, suggesting that all samples have ink-bottle mesopores [428]. After loading Ce onto the SBA-16 matrix, there is a decreasing trend regarding the hysteresis loop as the increasing Ce loading, indicating that the Ce was incorporated into the mesopores of SBA-16. A further slight decrease of the hysteresis loop is registered when Ni was loaded. The isotherms of pore size distribution, shown in Fig.6.16b, display that the diameter of primary mesopores of the samples is in the range of 2.6-4.0 nm. It can be seen from Table 6.7 that the fresh SBA-16 material had significantly high SSA and porosity (V_p and r_p). After impregnating the Ce onto the SBA-16 matrix, the SSA and porosity of Ce-doped SBA-16 materials decreased apparently with the introduction of Ce. This can be attributed to the deposition and incorporation of Ce into the pores and onto the surface of SBA-16 [389]. Meanwhile, it was reported that the high calcination temperature could result in the decreases of SSA and mesopores

for ordered mesoporous silicas with spherical mesopores, which could partly account for the decrease of SSA and pore volume for the studied samples [389,429]. After nickel introduction into the SBA-16 and x/SBA-16, further decreases of SSA and V_p (Table 6.7) of catalysts compared with supports were observed for all Ni catalysts, suggesting that the incorporation of Ni into the pores resulted in the blockage of pores of the SBA-16 matrix as already mentioned elsewhere [389]. Moreover, the further shrinkage of the SBA-16 framework also partially happened during the calcination procedure of Ni catalyst, which also accounts for the decreased SSA and the V_p [389]. The pore size of catalysts, however, remained similar or slightly increased when compared to supports, which was also observed in different types of mesoporous silica-supported catalysts [64,189]. Also, the porous structures of SBA-16 for the catalysts remained after Ni and Ce introduction as demonstrated in TEM. In Fig.6.16, it was testified that the ordered structure with cubic cage-like pores of SBA-16 was formed for all catalysts.

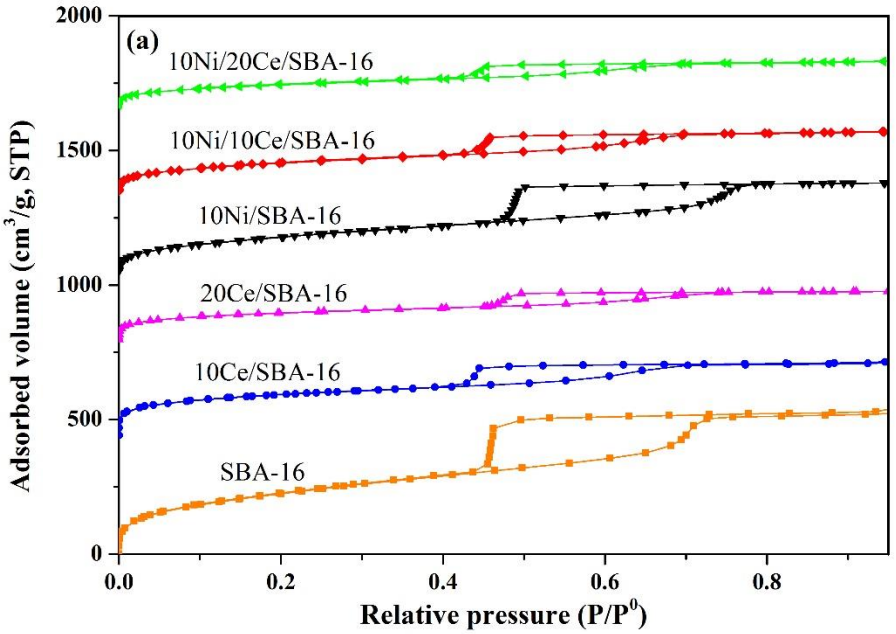

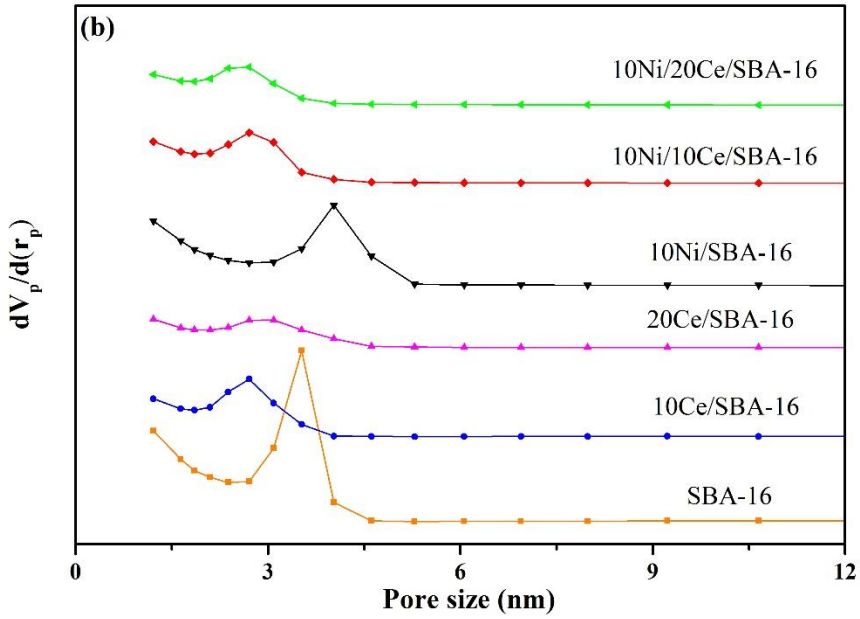

Figure. 6.16. N_2 adsorption-desorption isotherms of samples (a) and pore size distribution of samples (b).

In conclusion, compared to Ni/SBA-16 catalyst, the SSA and V_p of Ce-promoted Ni/SBA-16 catalysts decreased with the increase of Ce loading. The 10Ni/SBA-16 catalyst presented the highest SSA and pore volume, meanwhile, the 10Ni/20Ce/SBA-16 catalyst showed the lowest SSA and V_p.

The SAXRD was performed for the SBA-16 material and displayed in Fig.6.17. As shown in Fig. 6.17, two small peaks at 2θ=1.25 and 1.56 were observed for SBA-16 support, representing (200) and (211) reflection, respectively, indicating the existence of ordered mesopores in SBA-16 with body-centered cubic symmetry (*Im3m*) [430].

Table 6.7 BET surface area, pore volume, mean pore diameter from N_2 adsorption-desorption, and the particle size of nickel species calculated from XRD-on calcined samples.

Sample	[a]S_{BET} (m_2/g)	[b]V_p(cm^3/g)	[b]r_p (nm)	Particle size (nm)	
				[c]NiO	[d]CeO_2
SBA-16	934	4.2	3.5	NA	NA
10Ce/SBA-16	536	2.0	2.7	NA	NA
20Ce/SBA-16	402	0.5	1.2	NA	NA
10Ni/SBA-16	630	0.8	4.0	4.3	NA
10Ni/10Ce/SBA-16	484	0.7	2.7	7.7	10.8
10Ni/20Ce/SBA-16	383	0.5	2.7	10.3	10.8

NA: not applicable.

[a] The specific surface area was calculated for the calcined sample by the BET method.

[b] The pore volume and mean pore size was obtained for calcined samples from the BJH method.

[c] The particle size of NiO was calculated based on the three strong diffraction peaks of the calcined sample by Scherrer Equation.

[d] The particle size of CeO_2 was calculated based on the four strong diffraction peaks of the calcined sample by Scherrer Equation.

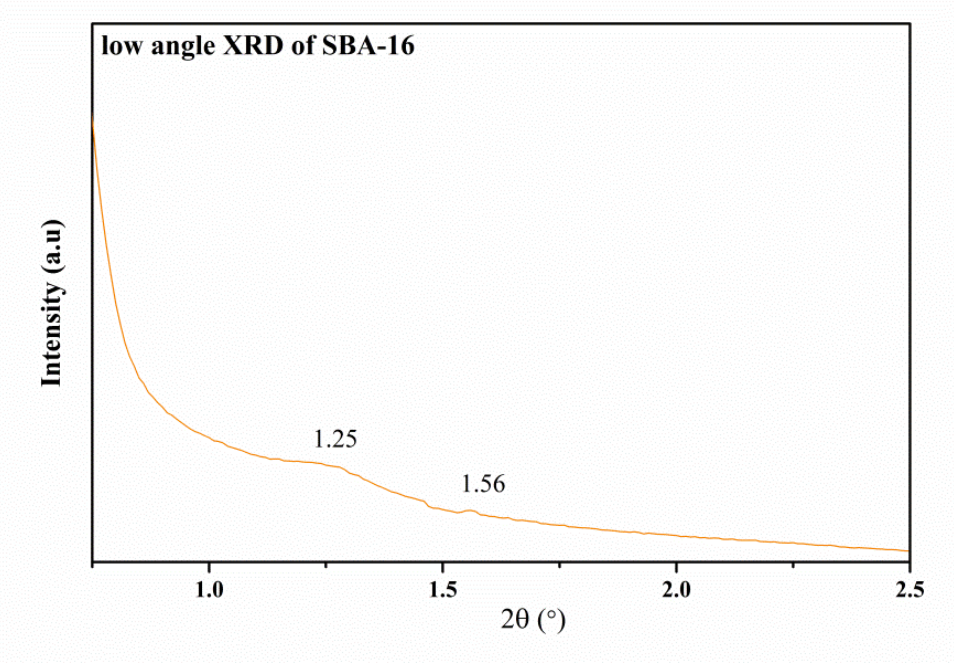

Figure. 6.17. Small-angle XRD (SAXRD) of the synthesized SBA-16 material

The structural properties of calcined and reduced catalysts were characterized by XRD measurements and the patterns were displayed in Fig.6.18. As shown in Fig.6.18a, the XRD patterns showed the existence of an amorphous silica peak at 2θ=23.2 ° for the SBA-16 support and all the calcined catalysts. Moreover, the intensity of the patterns corresponding to amorphous silica weakens for Ce-promoted catalysts due to the introduction of Ce, which can be caused by the highly dispersed Ce particles on the SBA-16. The diffraction peak of CeO_2 at 2θ = 28.5 ° affects the diffraction intensity of SiO_2 [415]. A similar effect was also shown over Ce or La-promoted Ni/SBA-15 catalysts [431]. The diffraction peaks of NiO were registered for all the Ni/SBA-16 based catalysts, which are characterized by peaks at 2θ=37.2, 43.2, and 62.8 °. They were attributed to the diffraction of the (111), (200), and (220) plane of NiO, respectively [64]. Simultaneously, the diffraction peaks at 2θ=28.8°, 33.5°, 47.8°, 56.7°, and 70.1° were assigned to the diffraction of face-centered CeO_2 cubic lattice [414,432]. The incorporation of Ce into the mesoporous structure of the SBA-16 matrix significantly affected the structure and distribution of Ni species. The diffraction peaks of NiO showed a narrowed trend as the increase of Ce loading in Fig.6.18a. The particle sizes of NiO and CeO_2 nanoparticles were calculated in Table 6.7 using the Scherrer equation. It can be noted that the particle size of NiO increases with the increase of Ce loading. A similar phenomenon was also found by other authors. It had been reported for Ni-Ce/SBA-15 (Ce-promoted Ni/SBA-15, with 6 wt.% Ce and 5 wt.% Ni) catalysts that the particle size of Ni for Ni-Ce/SBA-15 (impregnating Ce first following Ni) could be larger than that of Ni/SBA-15 catalyst but smaller than that of Ce-Ni/SBA-15(impregnating Ni first following Ce) catalyst [432]. Moreover, concerning the diffraction peaks of Ce, there is no significant difference when the Ce loading increases from 10 to 20 wt.%. The particle sizes of Ce were calculated in Table 6.6, with the same particle size (10.8 nm) of Ce for Ce-promoted catalysts. For reduced

catalysts, presented from Fig.6.18b, the broad diffraction peaks of Ni metal and NiO were registered for all catalysts, indicating that the Ni species cannot be reduced completely at 500 °C. There are no significant differences for the diffraction peaks of Ni species after reduction, meaning the Ni species keep stable after reduction. Furthermore, the peak intensity Ce for reduced catalysts remains stable after reduction, indicating the crystallinity and particle size of Ce keep stable.

From XRD measurements, it can be concluded that the Ni species keep highly dispersed over Ni/SBA-16 catalyst. After the incorporation of Ce, the particle size of Ni species increases as the increase of Ce loading for Ni/Ce/SBA-16 catalysts, but the crystallinity and particle size of Ce keep stable. The co-existence of NiO and Ni metal was confirmed over reduced catalysts, with broad peaks of Ni species over catalysts, indicating the Ni species keep dispersed after reduction. And the crystallinity Ce also remains stable after reduction.

In order to obtain the morphology information of the catalysts, TEM and HRTEM analyses were performed over the reduced samples and the images were displayed in Fig.6.19 and Fig.6.20. The TEM micrographs demonstrated that the ordered cage-like mesopores were well-formed in Ni/SBA-16 catalysts with or without Ce (Fig.6.19), although other organization along other directions may be observed depending on the deposition of the samples under the grid [389,433]. In Fig.6.19 (A2, B2, and C2), these images presented a cubic array of uniform channels when the incident electron beam was parallel to the main axis of the mesopores) and also unidirectional or cubic channels when the electron beam took different orientations concerning the sample (Fig.6.19, B2), which demonstrates that the order structure of SBA-16 was preserved despite the incorporation of Ce and Ni into the pores.

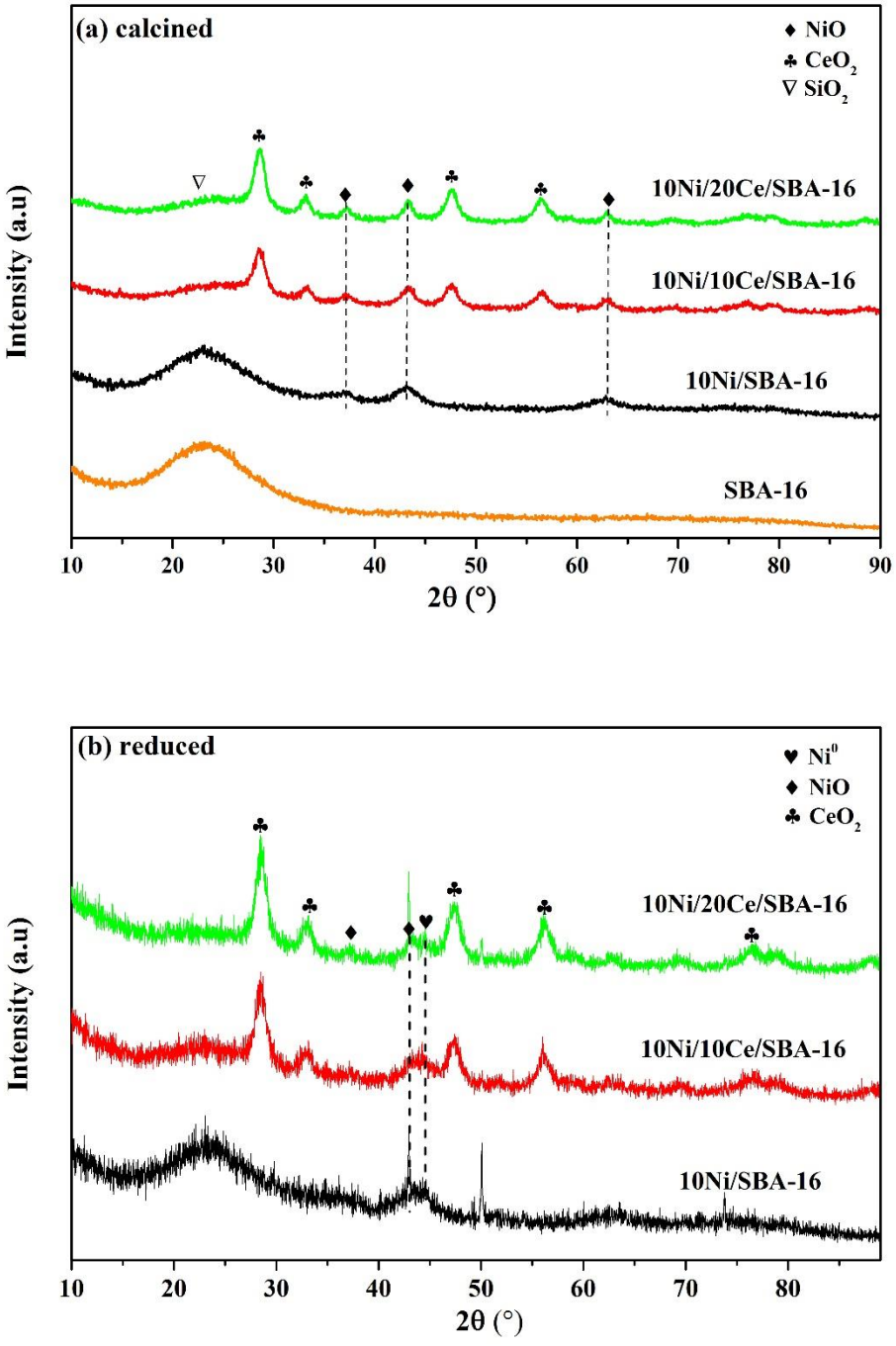

Figure. 6.18. XRD patterns of the Ni/SBA-16 based catalysts by varying Ce loading with SBA-16 as comparison; a) calcined samples at 550 °C in flowing air; b) reduced samples at 500 °C for 1.0 h under H_2/Ar=5/95, flow rate: 100 mL/min

The mesopore size measured by the HRTEM (Fig.6.20b) was about 6.6 nm with a wall thickness of 3.4 nm, which was different from the pore size measured by the BJH method. This can be assigned to the effect of different measurement methods. Fig.6.19B1 and Fig.6.19C1 confirmed also the cubic organization of the porosity of the Ce-promoted Ni/SBA-16 catalyst.

For the 10Ni/SBA-16 sample (Fig.6.19A1), the nickel species were highly dispersed on the SBA-16 matrix, with the measured Ni particle size of 3-5 nm. In Fig.6.20a, dark spots were assigned to the smaller Ni particles observed. On the other hand, the particle size of Ni species for 10 wt.% Ce-doped samples increased when compared to the unpromoted 10Ni/SBA-16 sample, with both NiO (7.7 nm) and Ni particles (6.0-7.5 nm) (Fig.6.20b) identified by the typical reticular distances of 2.4 and 2.03 Å, respectively. The presence of CeO_2 particles was confirmed by the lattice fringes of 3.12 and 1.91 Å corresponding, respectively, to the (111) or (220) planes. They were well dispersed within the support. Their average size is from 5 to 9 nm, which is in line with the result of XRD analyses. Moreover, it should be noticed that by increasing the Ce loading to 20 wt.%, the quality of the dispersion of CeO_2 decreased and aggregates of Ce were observed (Fig.6.19A1). The Ce species were not homogeneous on the SBA-16. Inside the porosity, by HRTEM (Fig.6.20c), larger Ni particles of around 8.2 nm and NiO particles of 9.2 nm, and CeO_2 particles of ca.7-9 nm can also be identified. There are differences regarding the particle size of Ni measured by XRD, which can be assigned to differences of techniques [250]. The XRD measurement only shows the particles with high crystallinity, but the TEM technique can measure the aggregated Ni particles without regard to whether the Ni particles are highly crystalline or not.

In both cases, the nickel species were found to be in contact with CeO_2 particles (Fig.6.20b and c). And, it can be concluded that the increase of the Ce loading led to the increase of Ni particles and the aggregates of Ce (20 wt.%).

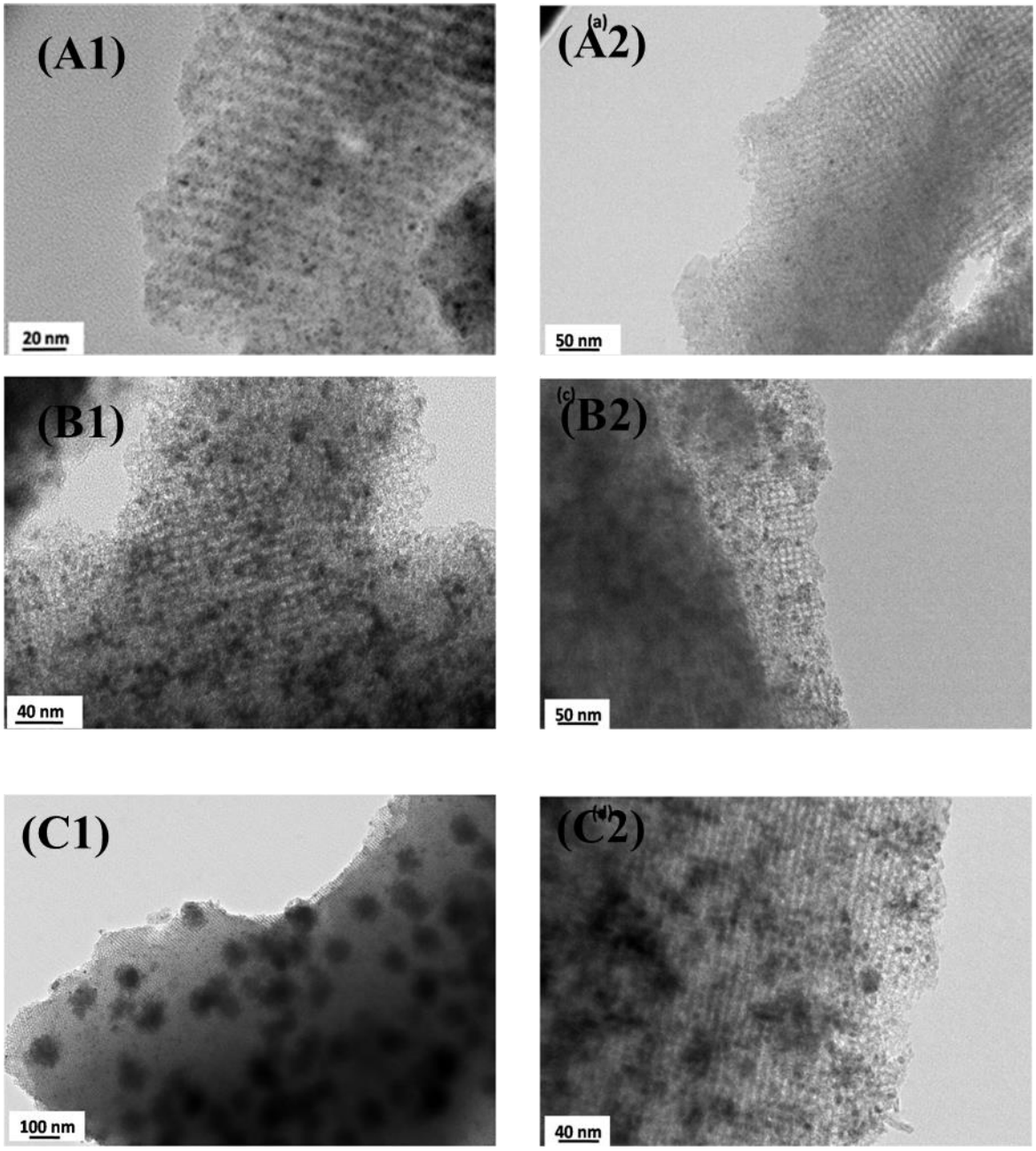

Figure. 6.19. TEM micrographs of the reduced catalysts; Condition: 500 °C for 1 h (H_2/Ar=5/95, 100 mL/min); 10Ni/SBA-16 (A), 10Ni/10Ce/SBA-16 (B), 10Ni/20Ce/SBA-16 (C).

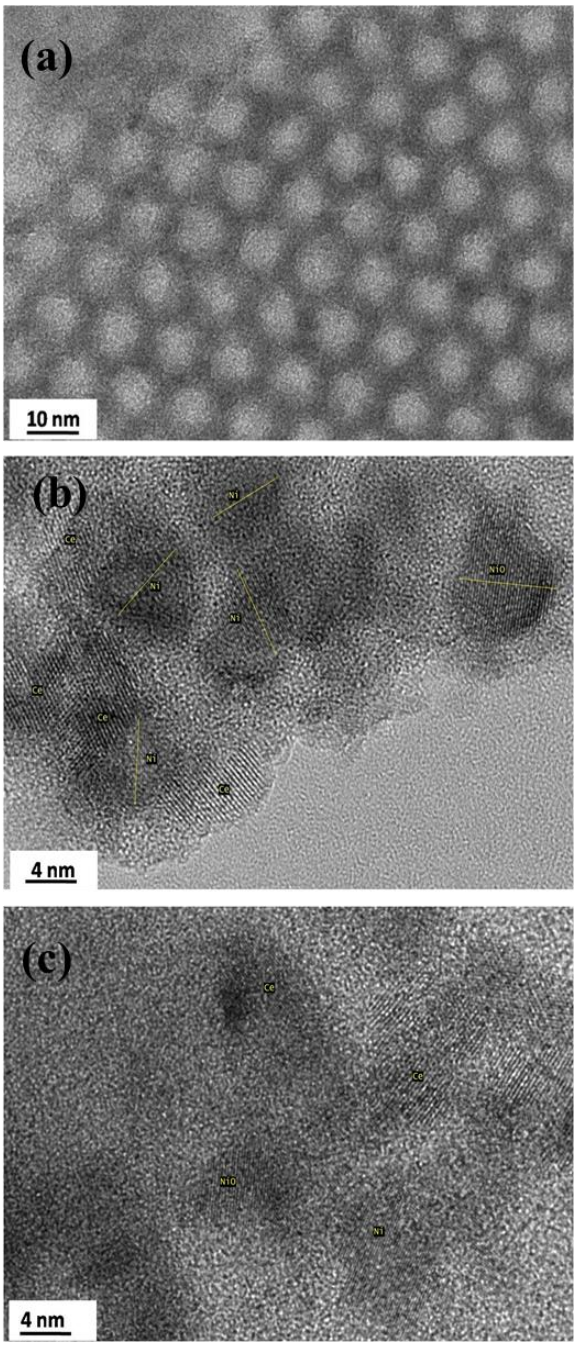

Figure. 6.20. HR-TEM micrographs of the reduced catalysts; Condition: 500 °C for 1 h (H_2/Ar=5/95, 100 mL/min); 10Ni/SBA-16 (a), 10Ni/10Ce/SBA-16 (b), 10Ni/20Ce/SBA-16 (c).

In order to study the surface composition and chemical states of Ni and Ce on the reduced catalysts, XPS measurements were carried out over reduced catalysts. The XPS spectra of O1s, Ni2p, Ce3d,

and Si2p have been displayed in Fig. 6.21 and the surface atomic ratios of Ni, O, and Ce species, as well as the binding energies of Ni2p and Ce3d, were presented in Table 6.7. In Fig. 6.21a, it can be seen that the peak located at 533.2 eV, which can be attributed to the superimposed O1s peaks from SiO_2, NiO, and CeO_2 (for Ce-doped samples), corresponding to the lattice oxygen (O_β) [64]. The small peak that appeared at 530.3 eV corresponds to the adsorbed oxygen species (O_α) [64]. As shown in Table 6.8, the percentage of O_α increased with the increase of Ce loading which was agreed with that the presence of ceria promoting the oxygen mobility of catalysts [365]. In Fig. 6.21b, the peak located at 103.9 eV was assigned to the presence of $Si2p_{3/2}$ [64]. The intensity of the $Si2p_{3/2}$ peak decreased with the increase of Ce, which can be attributed to the effect of impregnated Ce on the surface. This is in line with the XRD results. In Fig. 6.21c, the $Ni2p_{3/2}$ binding energy located at 852.8 eV and 856±0.7 eV with a shake-up satellite at 862 eV were attributed to the existence of Ni metal and Ni^{2+} species, respectively [434]. The $Ni2p_{3/2}$ binding energies of Ce-doped samples (Table 6.8) were lower than that of the Ce-free sample, indicating stronger metal-support interaction (MSI) on Ce-doped samples. And the percentage of metallic Ni increases from 4.5% for 10Ni/SBA-16 catalyst to 36.0% for 10Ni/20Ce/SBA-16 catalyst as the incorporation of Ce (Table 6.8), respectively, indicating that the doping of Ce promoted the presence of metallic Ni species on the surface of the catalysts. The XRD results in Fig.6.18b revealed the existence of metallic Ni over 10Ni/SBA-16. However, the XPS result shows nearly complete Ni^{2+} species, which can be attributed to the effect of adsorbed oxygen species on the surface of metallic Ni when exposed to oxygen. The adsorbed oxygen on the surface of Ni metal can promote the formation of a nickel oxide layer [435,436]. The Ni species over 10Ni/SBA-16 catalyst were highly dispersed on the SBA-16 support, resulting in the small nanoparticles of Ni

species (4.3 nm Table 6.7), thus the surface of metallic Ni could be covered by abundant oxygen, forming nickel oxide layers [435,436].

From XPS spectra, The Ce/Si atomic ratio increased with the increase of Ce loading, implying the higher dispersion of Ce species over 10Ni/10Ce/SBA-16 catalyst. The Ni/Si atomic ratio of 10Ni/10Ce/SBA-16 was smaller than that of other catalysts, which could be assigned to the combined effects of small Ni nanoparticles over SBA-16 and coverage of Ni and Ce on the support. As confirmed in BET and XRD measurements, the loading of Ce and Ni resulted in a decrease of SSA, which could give rise to the decrease of Ni/Si ratio on the surface as the covered surface. In TEM, the smaller Ni particles over 10 wt.% Ce-doped catalysts relative to 20 wt.% Ce-doped catalyst was registered and homogeneous distribution of Ce was found on 20 wt.% Ce-doped catalyst. The combined effects led to the lowest Ni/Si ratio obtained on the 10Ni/10Ce/SBA-16 catalyst. In Fig.6.21d, the Ce3d peaks were divided into 10 peaks using the deconvolution method labeled as u and v, and the molar ratio of Ce^{3+} species was calculated [332,426,427,437]. As shown in Table 6.8, the binding energy of Ce3d on 10Ni/20Ce/SBA-16 slightly shifted to a higher energy than those for 10Ni/10Ce/SBA-16. And for Ni species, one could see that the binding energy of $Ni2p_{3/2}$ was higher on 10Ni/10Ce/SBA-16 than on 10Ni/20Ce/SBA-16, showing that the interaction between Ni and Ce is stronger on 10Ni/10Ce/SBA-16 sample. Furthermore, at the surface, the Ce content increased with the Ce loading. However, the $Ce^{3+}/(Ce^{3+}+Ce^{4+})$ ratio is higher on10Ni/10Ce/SBA-16 than on 10Ni/20Ce/SBA-16, which could be caused by the better dispersion of Ce on the surface and the substitution of Ce by Ni inside the lattice, leading then to more oxygen vacancies as suggested elsewhere [211,332,361,438].

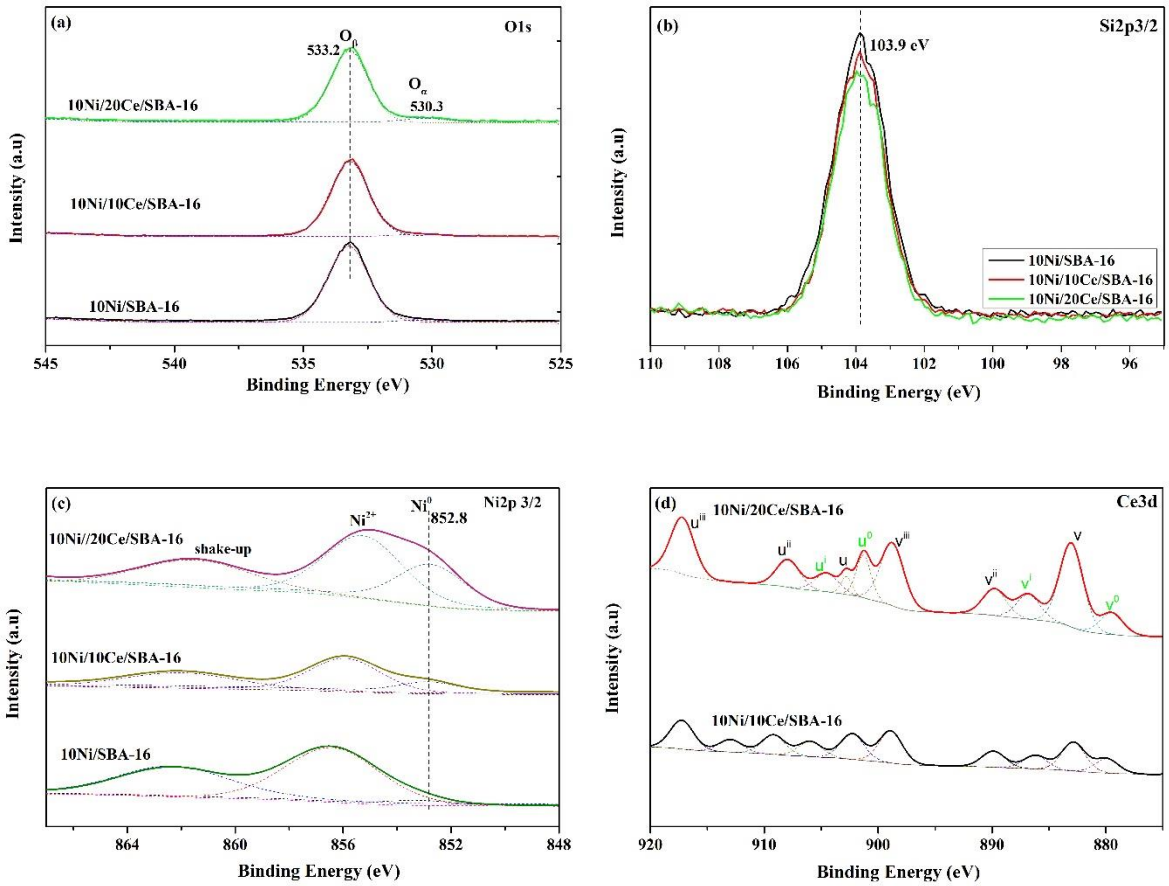

Figure. 6.21. The XPS spectra over the reduced catalysts; Reduction condition: the same as TEM measurement; a) O1s, b) Si2p, c) Ni2p, d) Ce3d

Thus, the promotion of Ni/SBA-16 catalysts by Ce induced the creation of oxygen vacancies, higher dispersion of Ni and Ce on the surface, and stronger metal-support interaction between Ni and Ce formed on 10 wt.% Ce-promoted catalysts compared to 20 wt.% Ce one.

Table 6.8 The binding energies of $Ni2p_{3/2}$ and $Ce3d_{5/2}$ and atomic ratios of Ni (Ni^0 and Ni^{2+}) on the catalysts.

Catalyst	Atomic ratio (%)					Binding Energy (eV)	
	Ce/Si	Ni/Si	$Ni^0/(Ni^{2+}+Ni^0)$	$O_\alpha/(O_\alpha+O_\beta)$	$Ce^{3+}/(Ce^{3+}+Ce^{4+})$	$Ni2p_{3/2}$	$Ce3d_{5/2}$
10Ni/SBA-16	-	4.5	4.5	3.3	-	856.4	-
10Ni/10Ce/SBA-16	1.1	3.2	19.7	4.3	35.3	856.0	882.9
10Ni/20Ce/SBA-16	1.4	6.2	36.0	6.3	25.7	855.3	883.1

6.3.1.5 Reducibility of the catalysts originated from H_2-TPR

In order to study the reducibility of supports and catalysts, the temperature-programmed reduction of H_2 was carried out. The plots are displayed in Fig.6.22. The maxima of reduction peak and H_2 consumption of the samples were calculated and presented in Table 6.9. As shown in Fig.6.22a, three reduction peaks of Ce-modified SBA-16 supports can be observed for the xCe/SBA-16 samples. The silica could not be reduced during the employed condition. Thus, the reduction of the supports was attributed to the reduction of Ce species. According to the literature [375,439,440], reduction peaks of 10Ce/SBA-16 at 360-496°C and 757°C in Fig.6.22a were assigned to the reduction of surface and bulk Ce, respectively. As shown in Fig.6.22a, the β and γ peaks of 20Ce/SBA-16 shifted to higher temperature compared to those of 10Ce/SBA-16, indicating that the surface ceria species were more difficult to be reduced over 20Ce/SBA-16, which was in line with the XPS result that more Ce^{3+} formed on 10Ni/10Ce/SBA-16. The total H_2 consumption of 20Ce/SBA-16, as shown in Table 6.9, was also higher than 10Ce/SBA-16. This could be attributed to the more reducible Ce species over 20Ce/SBA-16.

After Ni impregnation, the reducibility of Ni/xCe/SBA-16 catalysts was modified as the incorporation of Ce. As shown in Fig.6.22b, there are three reduction peaks centered at 332, 439, and 584 °C labeled as α, β, and γ, respectively for 10Ni/SBA-16 catalyst. Those reduction peaks located at 332 and 439 °C corresponded to the reduction of NiO crystallites weakly interacted with the SBA-16 support, meanwhile, the reduction peak positioned at 584 °C was attributed to the reduction of Ni phyllosilicate or Ni hydrosilicate species highly dispersed on the surface [389,415,441].

For the Ce-doped Ni/SBA-16 catalysts, H_2 consumption peaks consisted of 5 peaks i.e. δ, α, β, γ and ε (Table 6.9), with two new peaks of δ and ε. Similarly, the peaks of α and β were attributed to the reduction of Ni-Ce biphasic oxides, and the peak of γ corresponded to the reduction of highly dispersed Ni crystallites [389]. The δ peak was attributed to the reduction of adsorbed oxygen species, while the ε peak is attributed to the reduction of Ce^{4+} to Ce^{3+} [256,414].

The Ni species can be incorporated into the CeO_2 lattice because of its smaller ion radius, thus the charge unbalances and lattice distortion results in the formation of oxygen vacancies, which are easier for the adsorption of oxygen species [256]. From Fig.6.22b, the peaks of α, β, and γ for Ni/xCe/SBA-16 catalysts showed shifts towards higher temperatures with the increase of Ce loading, indicating the increase of the interaction between metal and support. As shown in Table 6.9, the total H_2 consumption excluding the effect of Ce reduction of the catalysts also increased with the increase of Ce loading, which demonstrates the Ni species are more difficult to be reduced over 20 wt.% Ce-promoted catalysts.

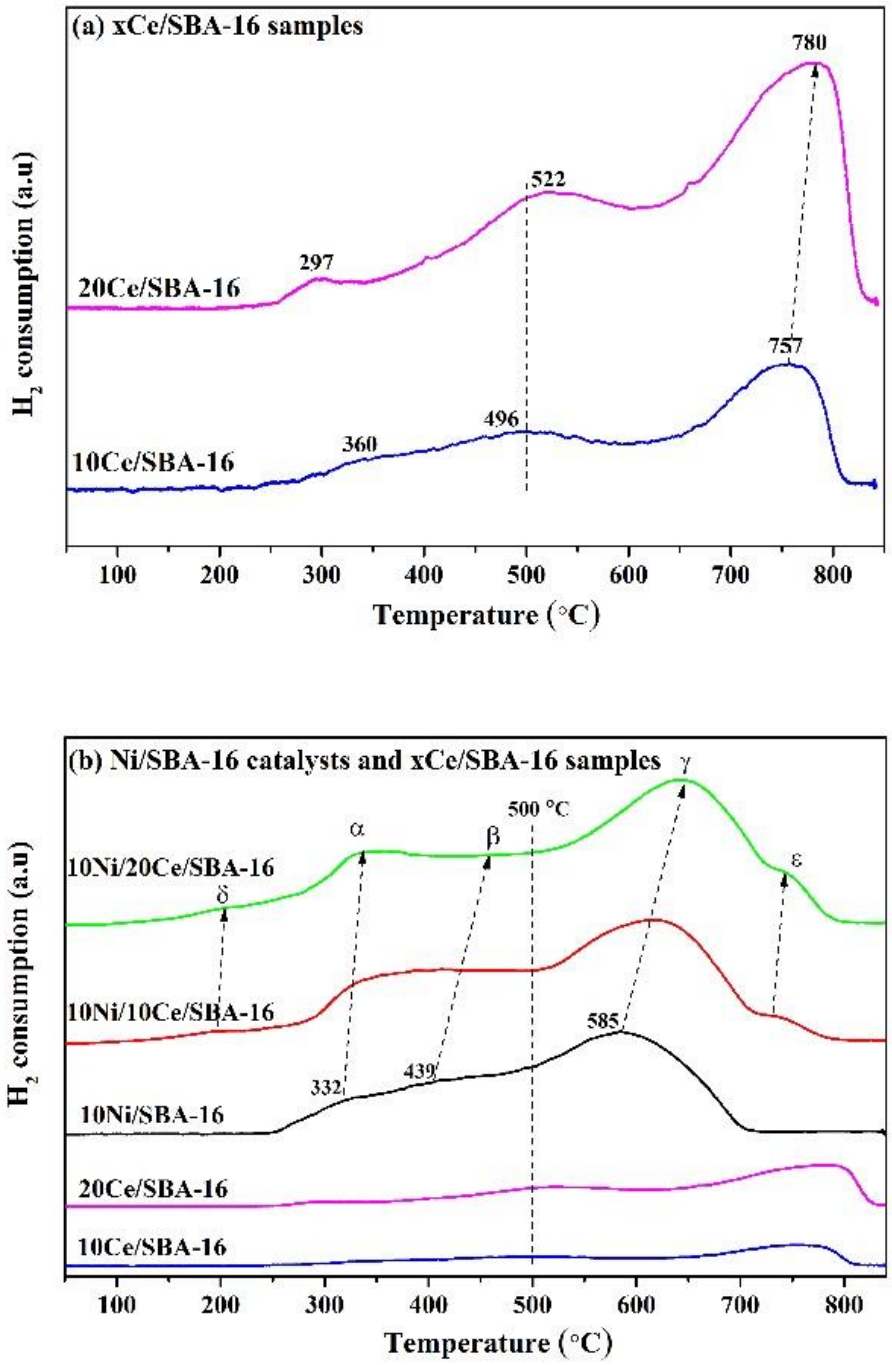

Figure. 6.22. a) H_2-TPR plots of the Ce doped SBA-16 supports; b) H_2-TPR plots of catalysts with xCe/SBA-16 as a comparison.

Table 6.9 H_2 consumption and reduction peaks of the supports and catalysts.

Catalyst	Temperature (°C)					H_2 consumption (mmol/g)					
	δ	α	β	γ	ε	δ	α	β	γ	ε	total
10Ce/SBA-16	-	359	494	756	-	-	0.01	0.17	0.12	-	0.30
20Ce/SBA-16	-	297	522	781	-	-	0.01	0.29	0.25	-	0.55
10Ni/SBA-16	-	332	439	584	-	-	0.17	0.66	0.63	-	1.46
10Ni/10Ce/SBA-16	206	346	457	617	727	0.05	0.10	0.86	0.99	0.02	2.03
10Ni/20Ce/SBA-16	210	350	474	642	737	0.05	0.16	1.17	1.01	0.03	2.42

6.3.1.6 Basicity of the catalysts originated from CO_2-TPD

The CO_2-TPD profiles were displayed in Fig.6.23. Four different desorption peaks of CO_2 can be identified for the 10Ni/SBA-16 catalysts centered at 100, 170, 289, and 650 °C, respectively. The desorption peaks centered at 100 °C, 170-289 °C, and 650 °C were attributed to the weak basic sites, medium basic sites, and strong basic sites, respectively [442]. Since the silica does not adsorb significant amounts of CO_2, it is reasonable to conclude that this activated adsorption occurs only on Ni species of 10Ni/SBA-16 catalyst [165,443].

As displayed in Table 6.10, the total basicity of the catalysts seemed not significantly different, with the highest total basicity obtained over the Ce-free catalyst. This can be attributed to the highly dispersed small Ni metal nanoparticles over the SBA-16 support, as confirmed in TEM, which adsorbed large amounts of CO_2 [443]. For Ce-doped catalysts, the adsorbed CO_2 could be assigned to the adsorption of Ni metal and the active sites of Ce. The introduction of Ce affected

the distribution of basic sites. The number of medium basic sites of Ce-doped catalysts was higher than that of the Ce-free sample. The highest amount of medium basic sites was obtained on the 10Ni/10Ce/SBA-16 catalyst. As reported in the literature [160,206], medium basic sites played a more important role in the CO_2 methanation process and the strong basic sites did not participate in the reaction. The number of medium basic sites was as follows: 10Ni/10Ce/SBA-16>10Ni/20Ce/SBA-16>10Ni/SBA-16, which can also explain the differences in catalytic activity for CO_2 conversion.

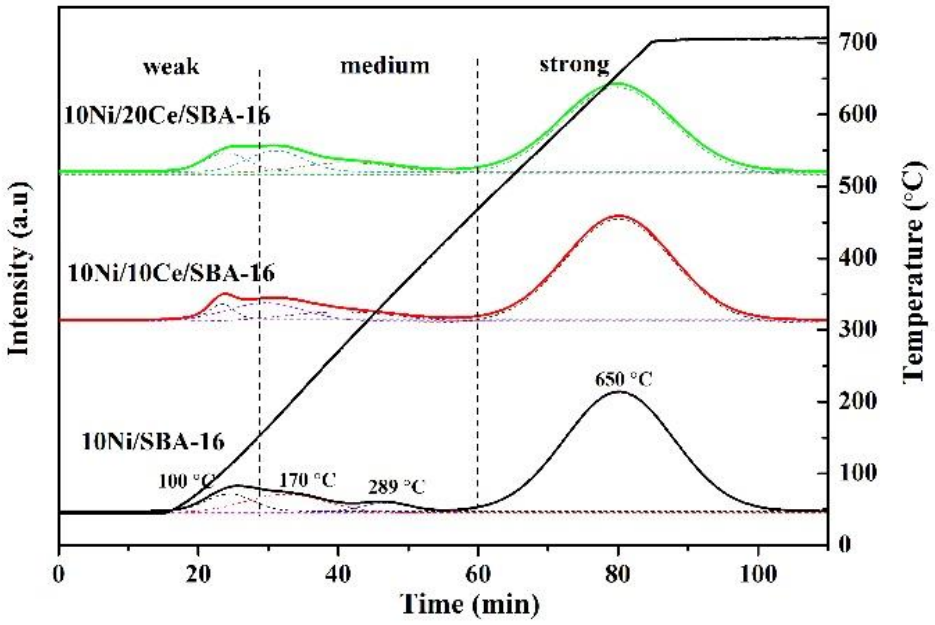

Figure. 6.23. CO_2-TPD curves of Ni/SBA-16 catalysts with or without Ce.

Table 6.10 Basic sites distribution calculated from CO_2-TPD for Ni/SBA-16 based catalysts after reduction at 500°C

Catalyst	Basic sites [μmol/g]				Distribution of basic sites [%]		
	Weak	Medium	Strong	Total basicity	Weak	Medium	Strong
10Ni/SBA-16	14.1	33.5	245.0	292.6	4.8	11.5	83.7
10Ni/10Ce/SBA-16	6.3	43.4	210.0	259.7	2.4	16.7	80.9
10Ni/20Ce/SBA-16	14.6	40.8	181.9	237.3	6.2	17.1	76.7

6.3.1.7 Catalytic tests of the catalysts in CO_2 methanation reaction

The catalytic performances of the catalysts in CO_2 methanation were investigated as a function of temperature. The results are displayed in Fig.6.24. The thick lines without a symbol on the top of the graphs represented the theoretical thermodynamic CO_2 conversion and CH_4 selectivity. From Fig.6.24a, it can be seen that the CO_2 conversions of the catalysts followed the order: 10Ni/SBA-16<10Ni/20Ce/SBA-16<10Ni/10Ce/SBA-16 at the range of 250-350 °C. At higher temperatures (400 °C), for all samples, CO_2 conversions reached nearly the same value. Then at 450 °C, CO_2 conversions of all catalysts were nearing the theoretical values. From Fig.6.24b, the CH_4 selectivity of all the catalysts increases with the increase of temperature and reaches the highest value at 400 °C, which is nearly the theoretical value, then slightly decreases at 450 °C. The CH_4 selectivity on Ce-modified catalysts is significantly higher than that of Ce-free catalyst at the range of 200-350 °C, but they are similar from 400 to 450 °C. The selectivity of 10Ni/10Ce/SBA-16 was also slightly higher than those obtained on 10Ni/20Ce/SBA-16 at all temperatures except 250 °C. At

350 °C, the best CO_2 conversion and highest CH_4 selectivity are obtained over 10Ni/10Ce/SBA-16. Thus, one can conclude that the 10 wt.% of Ce loading is appropriate content for Ce-doped Ni/SBA-16 catalysts for CO_2 methanation.

According to the literature [161,443], the Ni particle size significantly affected the CH_4 selectivity of silica-supported Ni catalysts in CO_2 methanation reaction. The small Ni particles could favor the formation of CO and the turnover frequency of CO formation. As for Ni/SBA-16 catalyst, in the current study, the active sites are mainly Ni metal sites, thus, the smaller Ni particle sizes favor the formation of CO, thus resulting in the poor CH_4 selectivity at a low-temperature range (<350 °C). But the CH_4 selectivity increases with the increase of temperature and reaches as high as Ce-promoted catalysts at 400 °C, which is attributed to the hydrogenation of CO to CH_4, in which CO played as an important intermediate [161].

However, in the presence of Ce for the Ni/xCe/SBA-16 catalysts, the methanation reaction pathway changes as the Ce actively participates in the reaction [159,224]. In such case, the SBA-16 support plays only as a skeleton to stabilize and disperse the Ni and Ce species, and the catalytic performance is determined by the combined effects of Ni and Ce species, which had also been demonstrated in other catalytic conversions of CO_2 reactions over SBA-16, SBA-15 or KIT-6 mesoporous silica materials supported catalysts [50,171,224,389]. The high dispersion of Ni and Ce species was obtained over 10Ni/10Ce/SBA-16 catalyst, resulting in easily reducible Ni and Ce species as confirmed by TPR characterization. Moreover, more molar ratio of $Ce^{3+}/(Ce^{3+}+Ce^{4+})$ obtained over 10Ni/10Ce/SBA-16, indicating more created oxygen vacancies over the catalyst, which can effectively activate CO_2 in the reaction [160,196,211,332,350]. In this CO_2 methanation pathway, the CO was only a main by-product that originated from the decomposition of formate intermediates over Ce^{3+} sites [211,350]. The CO_2 species adsorbed over Ce^{3+} sites showed different

desorption behaviors over catalysts as revealed in CO_2-TPD, forming different basic sites, in which the weak and moderate basic sites played a significant effect in the reaction [144,160,206,444].

The Ni metal active sites were contributed to the activation and decomposition of H_2, thus, the small Ni particles could provide more sites for the activation of H_2 [211,445]. Compared to 20 wt.% Ce-doped catalyst, the smaller Ni particles of 10 wt.% Ce doped catalyst, as shown in HRTEM, could be more favorable in H_2 activation.

The synergistic effect between Ce and Ni promotes the formation of CH_4. The interaction between Ce and Ni was higher over 10Ni/10Ce/SBA-16 than over 10Ni/20Ce/SBA-16, resulting in the better CO_2 conversion over 10Ni/10Ce/SBA-16.

In Fig.6.25 and Fig.6.26, correlating the catalytic performance with $Ce^{3+}/(Ce^{3+}+Ce^{4+})$ and medium basic sites, it was found that 10Ni/10Ce/SBA-16 showed the best CO_2 conversion at 350 °C with the highest ratio of $Ce^{3+}/(Ce^{3+}+Ce^{4+})$ and the amount of medium basic sites.

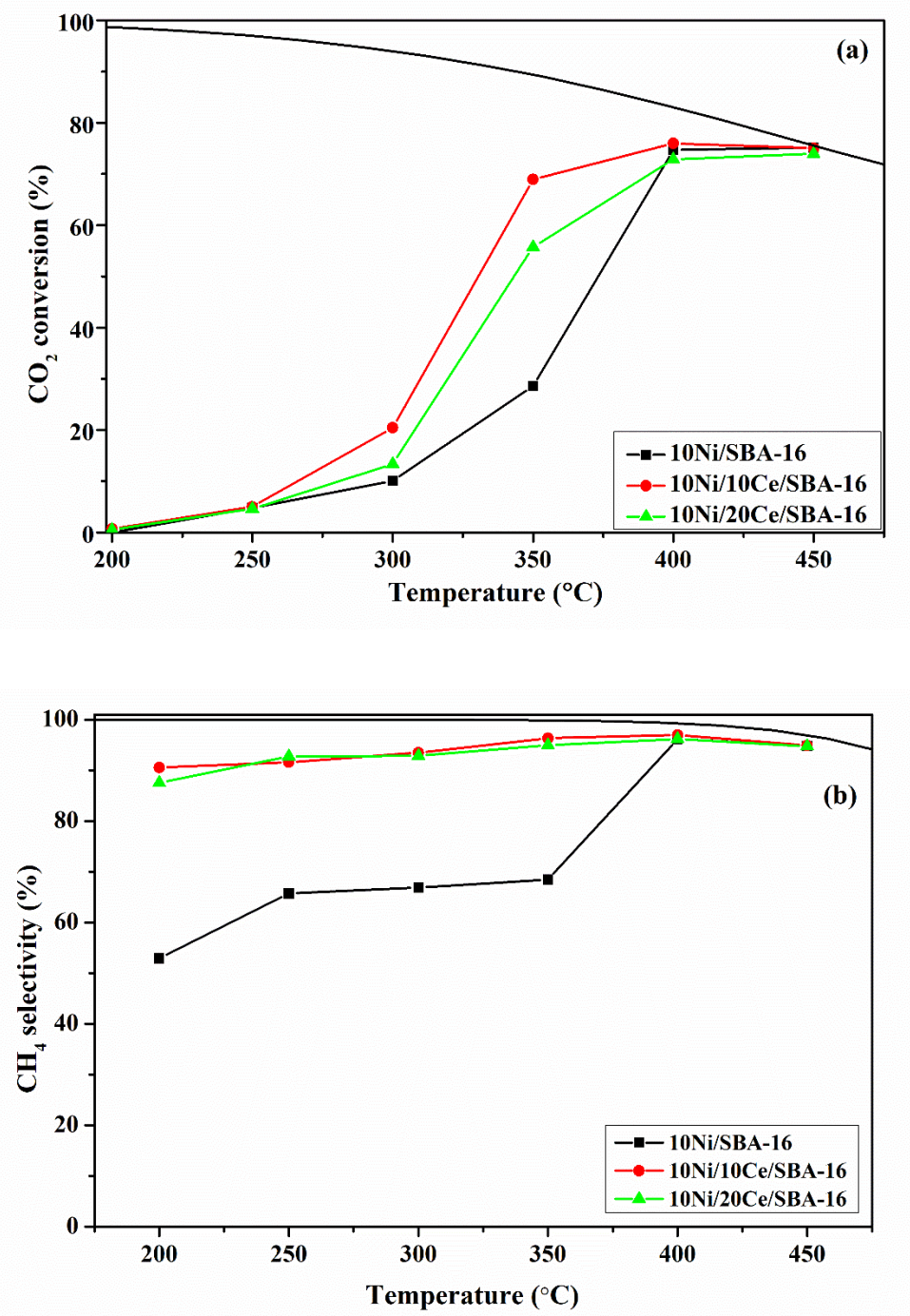

Figure. 6.24. The catalytic performances of Ni/SBA-16 catalysts with or without Ce in CO_2 methanation; a) CO_2 conversion, b) CH_4 selectivity

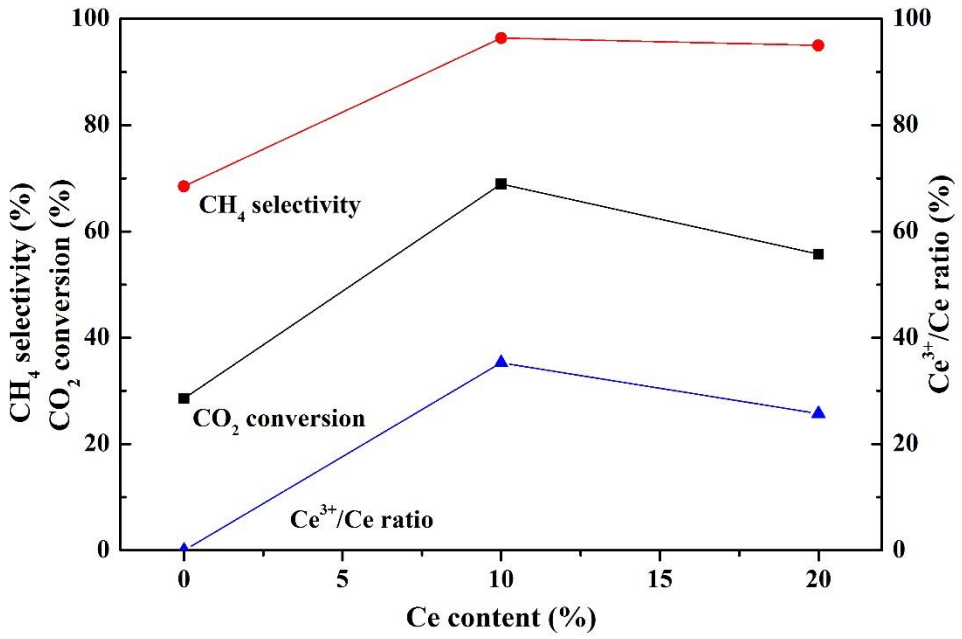

Figure. 6.25. The correlation of CO_2 conversion and CH_4 selectivity at 350 °C with regard to the surface $Ce^{3+}/(Ce^{3+}+Ce^{4+})$ ratio calculated from XPS; The sample of 0 wt.% Ce loading represents the 10Ni/SBA-16 sample.

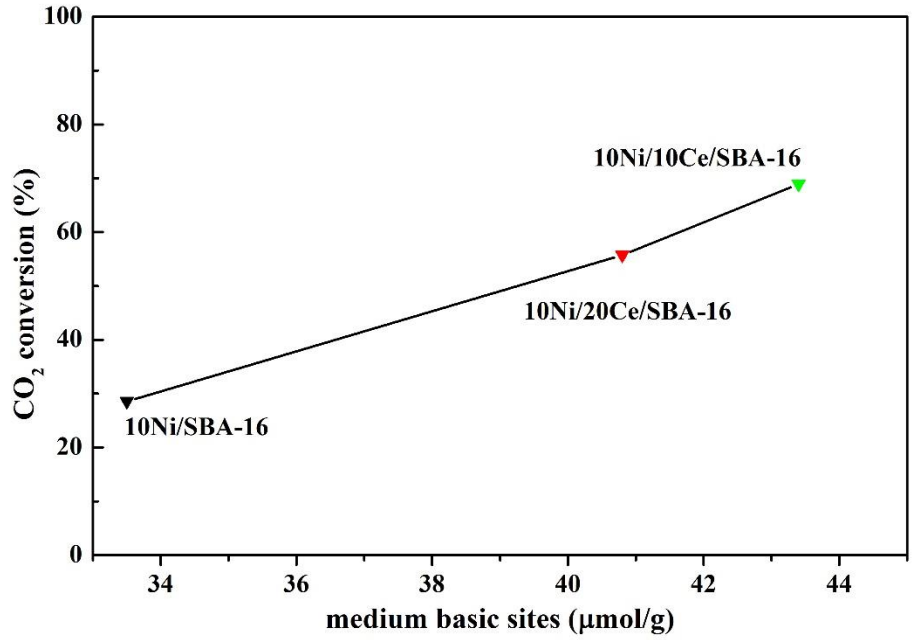

Figure. 6.26. The correlation of CO_2 conversion at 350 °C with medium basic sites.

6.3.1.8 Stability tests of the catalysts in CO_2 methanation reaction

The stability tests of the catalysts in CO_2 methanation reaction were performed and the results were displayed in Fig.6.27. As shown in Fig.6.27, the 10Ni/SBA-16 and 10Ni/10Ce/SBA-16 catalysts all show good stability regarding CO_2 conversion and CH_4 selectivity in the time on stream process. The good stability of Ni/SBA-16 catalysts could be attributed to the confinement of the SBA-16 structure, which can suppress the sintering of active sites [389].

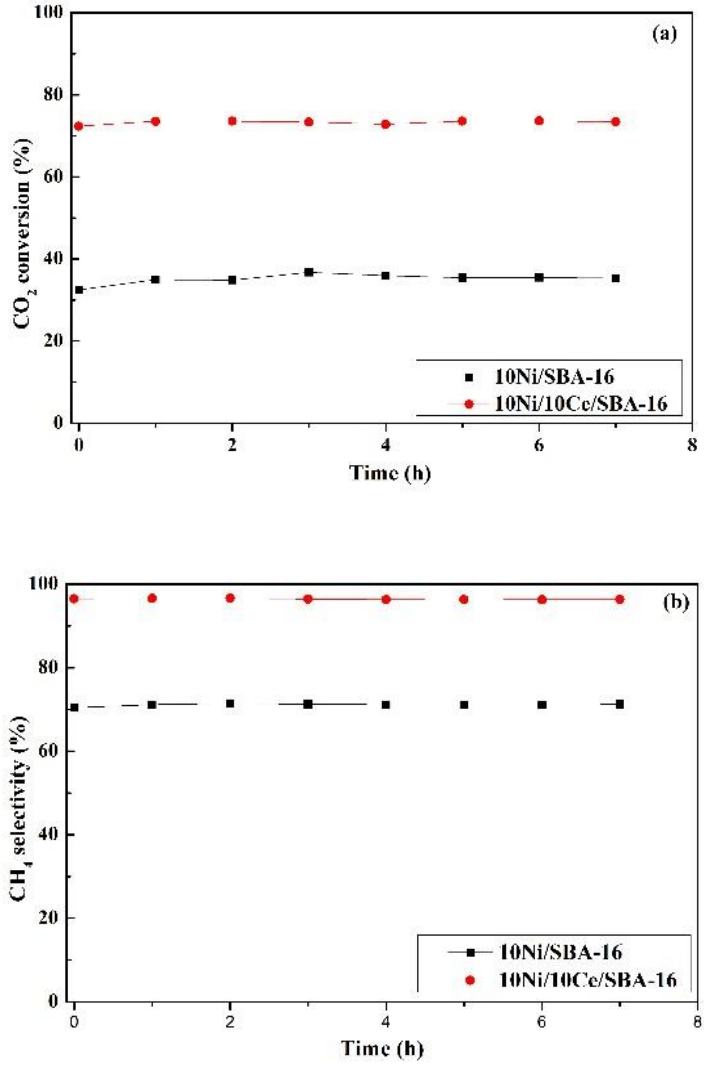

Figure. 6.27. The stability tests of 10Ni/SBA-16 and 10Ni/10Ce/SBA-16 catalysts in CO_2 methanation; Condition: 350 °C, GHSV=12,000 h^{-1}; a) CO_2 conversion, b) CH_4 selectivity.

6.3.1.9 XRD patterns of the catalysts after methanation test

As shown in Fig.6.28, the diffraction peaks of Ni or Ce on spent catalysts remained stable as compared to those on reduced catalysts, indicating that no sintering occurs after time on stream of 7 h.

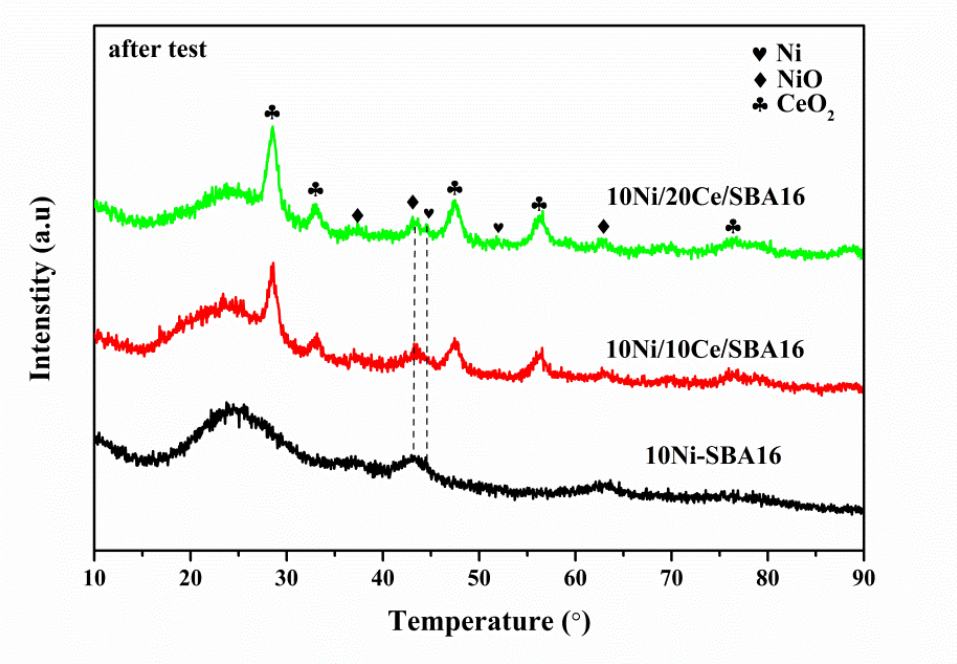

Figure.6.28. XRD patterns of the spent Ni/SBA-16 based catalysts with varying Ce loading.

6.3.1.10 The selection of pre-treatment temperature and Ce loading based on activity test

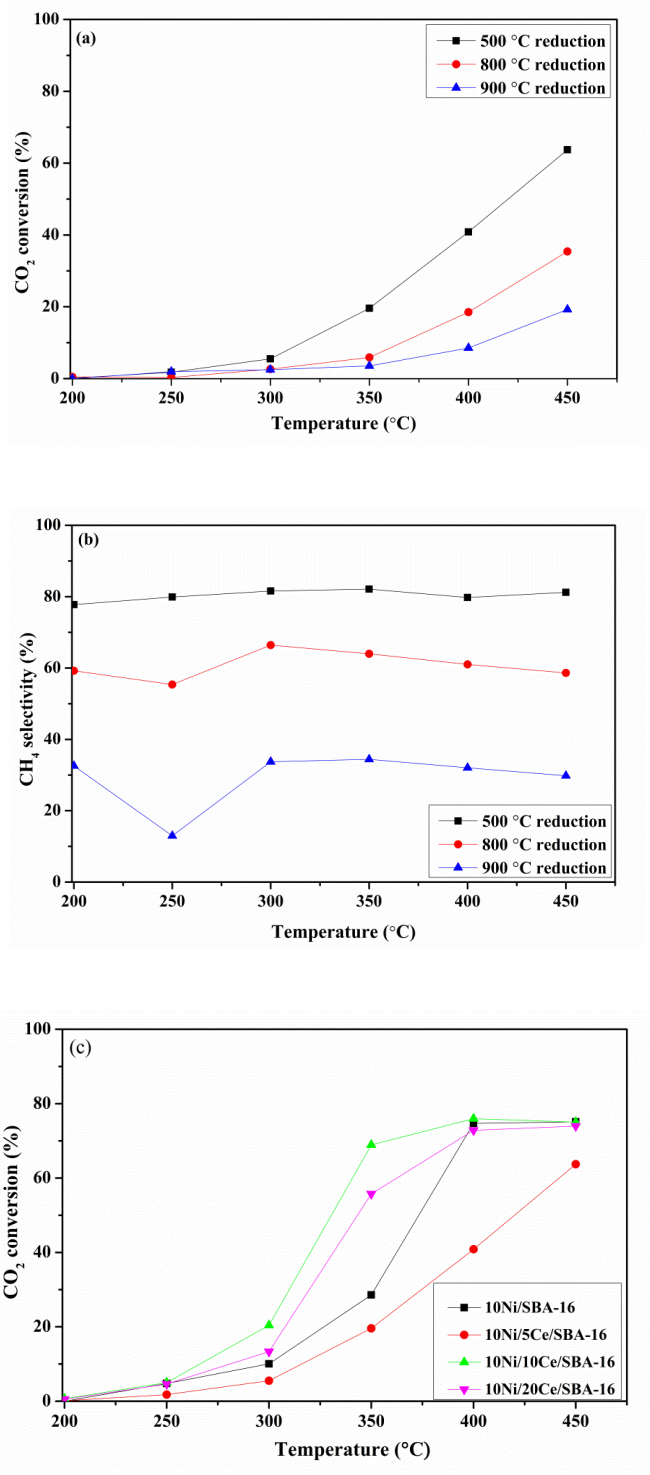

Figure. 6.29. The CO_2 methanation test of 10Ni/5Ce/SBA-16 catalyst reduced at different temperatures; a) CO_2 conversion (%), b) CH_4 selectivity (%)

As shown in Fig.6.29c, the 5 wt.% Ce modified Ni/SBA-16 catalyst shows a worse activity compared to other catalysts at the testing temperature range. In Fig.6.29a and b, it also can be seen that the activity and CH_4 selectivity decrease with the increase of reduction temperature until 900 °C. Thus, it can be concluded that 10 wt.% Ce is appropriate content for Ce-promoted Ni/SBA-16 catalyst in CO_2 methanation and 500 °C is the best condition for the reduction process.

6.3.1.11. Comparison of the Ni/Ce/SBA-16 and Ni/CeY/SBA-16 catalysts in CO_2 methanation.

A series of Ni/CeY/SBA-16 catalysts prepared by citric acid-assisted impregnation method as depicted in 3.1.4.5 of chapter 3. The catalysts were pretreated at 650 ℃ under 5% H_2/Ar flow for 1 h. The catalytic performance of catalysts was displayed in **Fig.6.30**.

As shown in **Fig.6.30**, the CO_2 conversion and CH_4 selectivity of Ni/Ce/SBA-16 catalyst were improved after doping Y in which 5 wt.% of Y showed the best promotion effect.

However, the Ni/Y/SBA-16 catalyst performs comparative activity as compared to Ni/CeY/SBA-16 catalyst. In such a case, it is interesting to study the effect of Y on Ni/SBA-16 catalyst, which will be discussed in the next sub-chapter.

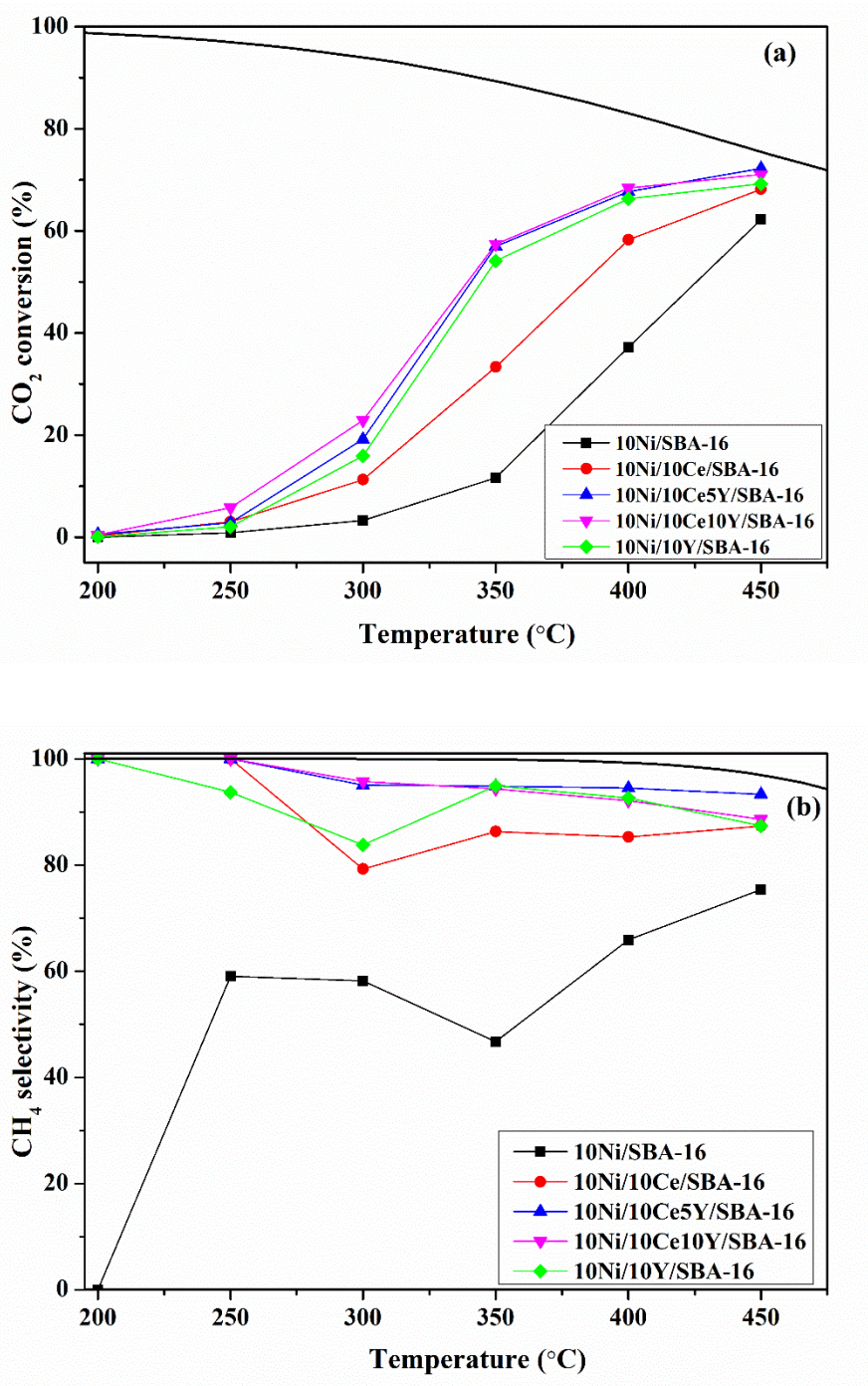

Figure. 6.30. The catalytic performance of Ni/CexY/SBA-16 catalysts in CO_2 methanation; Condition: 650 ℃ reduced for 1 h, GHSV=12,000; (a) CO_2 methanation, (b) CH_4 selectivity.

6.3.1.12 Conclusions

In this study, the SBA-16 material with cage-type mesopores was successfully synthesized and used to prepare Ni/SBA-16 based catalysts for CO_2 methanation. The effects of Ce promoter on the physic-chemical properties and catalytic performance of the catalysts were studied. It was found that the cage-type mesopores of the SBA-16 matrix, which could suppress the moving and sintering of active metals, leading to good dispersions of active metals. The smallest Ni particles were obtained over the Ce-free Ni/SBA-16 catalyst. Meanwhile, the increase of Ce loading led to larger Ni particles inside/outside the matrix. The Ni and Ce particles of catalyst were found to be smaller over 10 wt.% Ce-doped Ni/SBA-16 catalyst than over 20 wt.% Ce-doped catalyst. Besides, the dispersion degree of Ce decreased over 20 wt.% Ce-doped catalyst and aggregates of Ce were also registered. Moreover, a higher $Ce^{3+}/(Ce^{3+}+Ce^{4+})$ ratio formed on the surface of 10 wt.% Ce-doped Ni/SBA-16 catalyst, favoring the activation and hydrogenation of CO_2 species adsorbed Ce^{3+} active sites. Furthermore, the highest number of medium basic sites was obtained over 10 wt.% Ce-doped Ni/SBA-16 catalyst, which was favorable for the formation of CH_4. Besides, the stronger Ni-Ce interaction was also formed over 10 wt.% Ce-doped Ni/SBA-16 catalyst.

In the CO_2 methanation, the CO_2 conversion and CH_4 selectivity of Ni/SBA-16 catalyst were lower than Ni/xCe/SBA-16 catalysts at low temperatures, which could be assigned to the lack of active sites for CO_2 activation, which resulted in the CO_2 species adsorbed on Ni/SBA-16 catalyst were easily converted to CO, leading to poor conversion and selectivity. The highest CO_2 conversion and CH_4 selectivity were obtained over 10 wt.% Ce-doped Ni/SBA-16 catalyst due to several advantages relative to 20 wt.% Ce-doped catalysts, such as the smaller particles of Ni and Ce, stronger Ni-Ce interaction, higher molar ratio of $Ce^{3+}/(Ce^{3+}+Ce^{4+})$, more oxygen vacancies, and more medium basic sites.

In brief, the SBA-16 is appropriate support for Ni catalysts dedicated to CO_2 methanation. Also, Cerium is a good additive to improve Ni/SBA-16 catalyst. Besides, other promoters e.g., Y can also be interesting to modify Ni/SBA-16 catalyst, which will be discussed in the next chapter.

6.4 SBA-15 versus SBA-16: a comparison of the catalytic properties

6.4.1 Comparation of SBA-15 and SBA-16 supported catalysts in CO_2 hydrogenation

Table 6.11 presents the activity in methanation on the different supported materials, performed at 350°C and 400°C after steady-state.

Table 6.11 A summary of SBA-15 and SBA-16 supported catalysts in the presence of promoter.

Catalyst	CO_2 conversion (%)		CH_4 selectivity (%)	
	350 °C	400 °C	350 °C	400 °C
15Ni/SBA-15	5.5	20.0	35.4	48.3
15Ni10Y/SBA-15	18.0	62.4	87.7	88.0
15Ni10Ce/SBA-15	40.0	68.6	92.5	92.3
15Ni10Ce10Y/SBA-15	**61.2**	**70.6**	95.9	94.5
10Ni/SBA-16-WI[b]	28.6	74.7	68.5	96.2
10Ni/10Ce/SBA-16-WI	68.9	76.0	96.4	97.0
10Ni/10Y/SBA-16-CA[a]	54.1	66.3	94.9	92.6
10Ni/10Ce/SBA-16-CA	33.4	58.3	86.3	85.3
10Ni/10Ce10Y/SBA-16-CA	**57.4**	**68.4**	94.3	92.1

[a] Wet impregnation (ethanol)

[b] Citric acid assisted impregnation.

In **Table 6.11**, the activity and selectivity of Ni/SBA-15 and Ni/SBA-16 catalysts were listed. It can be concluded that Ni/SBA-16 shows better activity compared with that of Ni/SBA-15. Also, the performance of Ni/SBA-15 can be improved by doping Ce and/or Y in which the Ce-Y doped Ni/SBA-15 shows the best performance.

Both Ce and Y have shown a positive effect on the performance of Ni/SBA-16 catalyst in which Ce promoted Ni/SBA-16 catalyst prepared by wet impregnation shows the best performance. However, for citric acid-assisted impregnation prepared catalysts, the Y-doped Ni/SBA-16 catalyst performs comparative activity compared to the Ce-Y doped Ni/SBA-16 catalyst. The different activities can be linked with surface properties, basicity, the particle size of the catalysts as presented below.

6.4.2 On the basicity properties: SBA-15 versus SBA-16 supported catalysts

Table 6.12 presents the basic properties measured by CO_2 TPD on the different supporting materials.

As reported in **Table 6.12**, the basicity distribution of SBA-15 and SBA-16 supported catalysts were listed. The promotion with Ce and Y can change the basic site distribution of Ni/SBA-15 catalysts. As observed, Y can promote the increase of medium basic sites with a subsequent decrease of strong basic sites. Cerium can significantly promote the increase of total basic sites of Ni/SBA-15. Finally, Ce-Y can promote the formation of even more medium basic sites.

As for Ni/SBA-16 catalysts, Ni/SBA-16 shows more basic sites compared to Ni/SBA-15 and the presence of Ce promotes the increase of medium basic sites.

Table 6.12 Basicity comparison of SBA-15 and SBA-16 supported catalysts

Catalyst	Basic sites (μmol/mg)			
	weak	medium	strong	Total
15Ni/SBA-15	15.8	10.2	8.3	34.3
15Ni10Y/SBA-15	15.2	16.0	3.3	34.4
15Ni10Ce/SBA-15	2.61	47.47	174.45	224.53
15Ni10Ce10Y/SBA-15	4.87	65.94	150	220.81
10Ni/SBA-16-WI	14.1	33.5	245.0	292.6
10Ni/10Ce/SBA-16-WI	6.3	43.4	210.0	259.7

To conclude, the Ni/SBA-16 presents more basic sites compared to that of the Ni/SBA-15 catalyst. Doping with a promoter such as Ce, Y, and Ce-Y can thus promote the basicity of the SBA-15 supported Ni catalysts.

6.4.3 Ni particle size comparison between SBA-15 and SBA-16 supported catalysts

Table 6.13 reports the particle size calculated from the Scherrer equation from XRD on the different supported calcined materials.

Table 6.13 shows the particle size of NiO of SBA-15 and SBA-16 supported catalysts. It can be seen that the promotion by Ce, Y, and Ce-Y lead to the decrease of NiO particle size of Ni/SBA-15. For SBA-16 supported catalysts, the presence of Ce leads to a slight increase in NiO particle size. The media NiO particle size of Ni/SBA-16 with/without Ce is smaller than that of Ni/SBA-15 catalysts.

Table 6.13 Particle size of the calcined samples from XRD

Catalyst	Ni particle size (nm)[a]
15Ni/SBA-15	18.0
15Ni10Y/SBA-15	14.5
15Ni10Ce/SBA-15	13.4
15Ni10Ce10Y/SBA-15	15.3
10Ni/SBA-16-WI	4.3
10Ni/10Ce/SBA-16-WI	7.7

Table 6.14 presents the particle size calculated from the Scherrer equation from XRD on the different supported reduced materials.

Table 6.14 Particle size of the reduced samples from XRD

Catalyst	Ni metal particle size (nm)[a]
15Ni/SBA-15	24.1
15Ni10Y/SBA-15	16.0
15Ni10Ce/SBA-15	19.5
15Ni10Ce10Y/SBA-15	21.0
10Ni/SBA-16-WI	6.4
10Ni/10Ce/SBA-16-WI	7.2

As shown in Table 6.14, the largest Ni metal particle was found on 15Ni/SBA-15 catalyst. The Ni metal particle size was smaller when Y, Ce, or Ce-Y was added. Compared to 15Ni10Ce/SBA-15, the particle size of Ni metal increased slightly.

As for SBA-16 supported catalysts, the particle size of Ni metal is much smaller than that of SBA-15 supported catalysts. Doping Ce leads to a slight increase of Ni metal particle size over 10Ni/10Ce/SBA-16-WI catalyst.

6.4.4 Surface atom ratio comparison from XPS between SBA-15 and SBA-16 supported catalysts

By XPS, the surface comparison of both Ni supported SBA-15. And SBA-16 catalysts were evaluated. The results are presented in Table 6.15.

Table 6.15 Surface composition of the reduced catalysts from XPS

Catalyst	Atomic ratio (%)					
	Ni	Ce	Y	Ni^0/Ni^{2+}	O_{OH}/O	$Ce^{3+}/(Ce^{3+}+ Ce^{4+})$
15Ni10Ce/SBA-15	1.1	0.6	-	21.8	9.0	48.2
15Ni10Ce10Y/SBA-15	1.2	0.5	4.8	11.7	23.9	57.2
10Ni/SBA-16-WI	0.8	-	-	4.7	3.3	-
10Ni/10Ce/SBA-16-WI	0.08	0.01	-	24.5	4.3	35.3

Table 6.15 shows the surface composition of reduced catalysts. It can be noted that the surface atom ratio of Ni and Ce on SBA-15 support is higher than on SBA-16 support.

The highest Ni^0/Ni^{2+} ratio was found on the 10Ni/10Ce/SBA-16 catalyst. Thus, this can explain that such catalysts are active in methanation since the Ni° species are well known to be the active site in the methanation reaction [232].

On the contrary, the highest surface adsorbed oxygen species and highest Ce^{3+} ratio was found on 15Ni10Ce10Y/SBA-15 catalyst. Thus, on this support, the importance of the oxygen vacancies led to high activity in methanation [366].

Thus, it is worth noting that depending on the support 2D or 3D structure, the surface properties have changed.

6.5 Conclusion

Ni catalysts supported on SBA-15 and SBA-16 are promising catalysts due to their high SSA, pore volume, and unique ordered mesostructure. It was shown here, that the presence of Ce or Y can promote the activity of Ni/SBA-15 catalysts in CO_2 methanation. Meanwhile, the Ce-Y promoted Ni/SBA-15 catalyst showed the best activity.

Compared to SBA-15, SBA-16 can be better alternative support for Ni catalysts due to its three-dimension mesoporous structure. Ni/SBA-16 showed the smallest Ni particle size and high dispersion of Ni. In the presence of Ce, the medium basic sites and Ce^{3+} ratio increased over Ni/SBA-16-Ce, which resulted in higher activity.

Although the Ce-Y promoters can promote the activity of the Ni/SBA-16 catalyst, the Y doped Ni/SBA-16 catalyst shows comparative activity. Thus, it can be interesting to study the effect of the only Y on the catalytic performance of the Ni/SBA-16 catalyst.

Chapter VII

Conclusion and perspectives of this work

VII Conclusion and perspective of this work

7. Conclusion and perspectives of this work

7.1 Conclusion

In the first part of this work, low-cost materials such as diatomite and LDHs were employed to synthesize Ni catalysts. The effect of nickel salts on the performance of Ni catalysts in CO_2 methanation was investigated by H_2-TPR, CO_2-TPD, N_2 physisorption, and XRD technologies. It was found that Ni-Mg catalyst derived from nickel nitrate presented the best activity and selectivity, which could be ascribed to the small Ni^0 particle, good reducibility, and the highest medium basic sites. However, the activity of diatomite-based Ni catalysts seems not satisfactory. Thus, the diatomite-supported catalysts still need more research to improve the activity in CO_2 methanation.

As for LDHs derived Ni catalysts, the effect of Y on the performance of Ni catalysts was studied. It was found that the addition of Y affected the CO_2 adsorption capacity of the materials by changing the distribution of the basic sites, especially those of medium strength. The yttrium promotion influenced the nickel/support interaction. The Y addition affected strongly the catalytic activity in CO_2 methanation, increasing the CO_2 conversion at 250 °C from 16% for MO-0Y to 40 and 81% for MO-2.0Y and MO-0.4Y, respectively. This could be explained by both increased distribution of medium-strength basic sites and significantly smaller metallic nickel particle size of Y-promoted catalysts.

The mixed oxides Ni catalysts derived from LDHs showed high activity and selectivity in CO_2 methanation. The yttrium promoter showed highly improved performance for mixed oxides Ni catalysts.

In the second part, the CeO_2 nanoparticles doped by Y were synthesized by the hydrothermal method and employed to prepared Ni catalysts. The catalysts were studied in CO_2 methanation and

characterized by a series of physicochemical technologies. The catalytic test showed that doping Y could significantly improve the activity of the Ni/CeO_2 catalyst. In the range of 250-350 °C, the Ni/CeO_2-Y catalysts showed high activity and CH_4 selectivity. By characterization, it was found that the specific surface area of Ni/CeO_2-Y samples, the crystallite sizes of ceria, the oxygen vacancies content, and the interaction between NiO and CeO_2 can be tuned by different Y content.

All the catalysts contain well-defined Ni crystallites and the introduction of Y tailors the particle sizes and shapes of CeO_2 in the catalysts. Unpromoted CeO_2 particles are large nano-cubes turning to nanorods by Y promotion, with an increase of these nanorods size of up to 2 wt% of Y addition.

Highly dispersed Ni active sites in strong interaction with the ceria-based oxide and the oxygen vacancies formed by Y addition are the key factors determining high catalytic activity and stable performances of the Ni/CeO_2-Y catalysts.

The Ni/CeO_2-Y 2.0% with the highest number of oxygen vacancies able to activate CO_2 and with the strongest metal-support interaction suppressing sintering of the Ni sites for H_2 activation, was the best performing CO_2 methanation catalyst.

In the third part, two different mesoporous silica SBA-15 and SBA-16 were synthesized and used to prepare Ni catalysts. The effect of yttrium promotion on SBA-15-supported Ni-Ce catalysts was also investigated on these catalysts for CO_2 methanation. The microscopy analyses (TEM, HRTEM, EDS) revealed that modification with Y positively affects the distribution of Ni particles, being extensively dispersed inside the mesoporous channels of SBA-15 silica support. Moreover, as shown by XPS, yttrium as a promoter contributed to an increase of $Ce^{3+}/(Ce^{3+}+Ce^{4+})$ ratio and the number of medium basic sites, enhanced the reducibility of nickel species, and led to the formation of a Y-Ce solid solution. NiCeY/SBA-15 catalysts showed better catalytic performance

in CO_2 methanation than Y-free catalyst, with the highest CO_2 conversion and CH_4 selectivity measured for 10 wt.% Y loading. Meanwhile, 15Ni10Ce10Y/SBA-15 showed excellent coking resistance and anti-sintering ability, which can be attributed to the confinement of the SBA-15 structure. However, although increases of activity and selectivity of Ni/SBA-15 catalysts doped by yttrium were found, they were lower compared with Ce and Ce-Y doped NiCexY/SBA-15 catalysts.

The effects of Ce promoter on the physical-chemical properties and catalytic performance of the Ni/SBA-16 catalysts were investigated. It was found that the cage-type mesopores of the SBA-16 matrix, which could suppress the moving and sintering of active metals, leading to good dispersions of active metals. The smallest Ni particles were obtained over the Ce-free Ni/SBA-16 catalyst. Meanwhile, the increase of Ce loading led to larger Ni particles inside/outside the matrix. The Ni and Ce particles of catalyst were found to be smaller over 10 wt.% Ce-doped Ni/SBA-16 catalyst than over 20 wt.% Ce-doped catalyst. Besides, the dispersion degree of Ce decreased over 20 wt.% Ce-doped catalyst and aggregates of Ce were also registered. Moreover, a higher $Ce^{3+}/(Ce^{3+}+Ce^{4+})$ ratio formed on the surface of 10 wt.% Ce-doped Ni/SBA-16 catalyst, favoring the activation and hydrogenation of CO_2 species adsorbed Ce^{3+} active sites. Furthermore, the highest number of medium basic sites was obtained over 10 wt.% Ce-doped Ni/SBA-16 catalyst, which was favorable for the formation of CH_4. Besides, the stronger Ni-Ce interaction was also formed over 10 wt.% Ce-doped Ni/SBA-16 catalyst.

In the CO_2 methanation, the CO_2 conversion and CH_4 selectivity of Ni/SBA-16 catalysts were found lower than for Ni/xCe/SBA-16 catalysts at low temperatures. This latter result could be assigned to the lack of active sites for CO_2 activation, which resulted in the CO_2 species adsorbed on Ni/SBA-16 catalyst were easily converted to CO, leading to poor conversion and selectivity.

The higher CO_2 conversion and CH_4 selectivity (<350 ℃) were obtained over 10 wt.% Ce-doped Ni/SBA-16 catalyst due to several advantages relative to 20 wt.% Ce-doped catalysts, such as the smaller particles of Ni and Ce, stronger Ni-Ce interaction, higher molar ratio of $Ce^{3+}/(Ce^{3+}+Ce^{4+})$, more oxygen vacancies, and more medium basic sites.

7.2 Perspectives

In CO_2 methanation reaction, Ni particle size, high surface area, high pore volume, good basicity, enhanced Ni-support interaction, and high oxygen vacancies, etc. can significantly affect the activity and CH_4 selectivity of Ni catalysts. The support and promoter have an important influence on such aspects. Based on the results of this work, several perspectives can be listed as follows:

- The low-cost materials can be competitive in future industrialization. Diatomite-supported Ni catalysts need further improvement. LDHs derived Ni catalysts showed high activity and selectivity making them promising alternatives toward large-scale application.
- Yttrium is an interesting promoter to modify the properties of Ni/CeO_2 catalysts. The solid solution of Y-Ce can be interesting in the study of Y-doped Ni/CeO_2 catalysts.
- SBA-15 supported Ni catalysts showed good stability. However, further improvement researches should be carried out by doping other promoters, changing the preparation method, or modifying the support by ammonia, etc.
- SBA-16 can be good support due to its three-dimension structure and good textural properties. Y-doped Ni/SBA-16 catalysts can be interesting in the next study.

References

[1] V.A. Kuuskraa, M.L. Godec, P. Dipietro, CO2 utilization from “next generation” CO2 enhanced oil recovery technology, Energy Procedia. 37 (2013) 6854–6866. https://doi.org/10.1016/j.egypro.2013.06.618.

[2] C. Ampelli, S. Perathoner, G. Centi, CO2 utilization: An enabling element to move to a resource-and energy-efficient chemical and fuel production, Philos. Trans. R. Soc. A Math. Phys. Eng. Sci. 373 (2015) 20140177. https://doi.org/10.1098/rsta.2014.0177.

[3] J. Artz, T.E. Müller, K. Thenert, J. Kleinekorte, R. Meys, A. Sternberg, A. Bardow, W. Leitner, Sustainable Conversion of Carbon Dioxide: An Integrated Review of Catalysis and Life Cycle Assessment, Chem. Rev. 118 (2018) 434–504. https://doi.org/10.1021/acs.chemrev.7b00435.

[4] A. Mustafa, B.G. Lougou, Y. Shuai, Z. Wang, H. Tan, Current technology development for CO2 utilization into solar fuels and chemicals: A review, J. Energy Chem. 49 (2020) 96–123. https://doi.org/10.1016/j.jechem.2020.01.023.

[5] A.J.S. and J.M.S. Eric E. Benson, Clifford P. Kubiak, E.E. Benson, C.P. Kubiak, A.J. Sathrum, J.M. Smieja, Electrocatalytic and homogeneous approaches to conversion of CO2 to liquid fuels, Chem. Soc. Rev. 38 (2009) 89–99. https://doi.org/10.1039/b804323j.

[6] S. Kar, R. Sen, A. Goeppert, G.K.S. Prakash, Integrative CO2 Capture and hydrogenation to methanol with reusable catalyst and amine: Toward a carbon neutral methanol economy, J. Am. Chem. Soc. 140 (2018) 1580–1583. https://doi.org/10.1021/jacs.7b12183.

[7] T. Schaaf, J. Grünig, M.R. Schuster, T. Rothenfluh, A. Orth, Methanation of CO2 - storage of renewable energy in a gas distribution system, Energy. Sustain. Soc. 4 (2014) 1–14. https://doi.org/10.1186/s13705-014-0029-1.

[8] T. Schaub, R.A. Paciello, A process for the synthesis of formic acid by CO2 hydrogenation: Thermodynamic aspects and the role of CO, Angew. Chemie - Int. Ed. 50 (2011) 7278–7282. https://doi.org/10.1002/anie.201101292.

[9] B. Ouyang, S. Xiong, Y. Zhang, B. Liu, J. Li, The study of morphology effect of Pt/Co3O4 catalysts for higher alcohol synthesis from CO2 hydrogenation, Appl. Catal. A Gen. 543 (2017) 189–195. https://doi.org/10.1016/j.apcata.2017.06.031.

[10] A. Nakhaei Pour, M.R. Housaindokht, A new kinetic model for direct CO2 hydrogenation to higher hydrocarbons on a precipitated iron catalyst: Effect of catalyst particle size, J. Energy Chem. 26 (2017) 359–367. https://doi.org/10.1016/j.jechem.2016.12.006.

[11] Y. Wang, L. Yao, Y. Wang, S. Wang, Q. Zhao, D. Mao, C. Hu, Low-Temperature Catalytic CO2 Dry Reforming of Methane on Ni-Si/ZrO2 Catalyst, ACS Catal. 8 (2018) 6495–6506. https://doi.org/10.1021/acscatal.8b00584.

[12] F. Massa, A. Coppola, F. Scala, A thermodynamic study of sorption-enhanced CO2 methanation at low pressure, J. CO2 Util. 35 (2020) 176–184. https://doi.org/10.1016/j.jcou.2019.09.014.

[13] K. Stangeland, D. Kalai, H. Li, Z. Yu, CO2 methanation: The effect of catalysts and reaction conditions, Energy Procedia. 105 (2017) 2022–2027. https://doi.org/10.1016/j.egypro.2017.03.577.

[14] WMO Greenhouse Gas Bulletin The State of Greenhouse Gases in the Atmosphere Based on Global Observations through 2019, 2020. https://reliefweb.int/report/world/wmo-greenhouse-gas-bulletin-state-greenhouse-gases-atmosphere-based-global-0.

[15] P. Nema, S. Nema, P. Roy, An overview of global climate changing in current scenario and mitigation action, Renew. Sustain. Energy Rev. 16 (2012) 2329–2336. https://doi.org/10.1016/j.rser.2012.01.044.

[16] Paris Agreement, (2015). https://unfccc.int/process-and-meetings/the-paris-agreement/the-paris-agreement.

[17] World Energy Balances: Overview, IEA, Paris. (2020). https://www.iea.org/reports/world-energy-balances-overview.

[18] H. Ritchie, M. Roser, CO_2 and Greenhouse Gas Emissions, Our World Data. (2020). https://doi.org/10.18160/gcp-2020.

[19] Niklas von der Assen, Johannes Jung, André Bardow, Life-Cycle Assessment of Carbon Dioxide Capture and Utilization: Avoiding the Pitfalls, Energy Environ. Sci. 6 (2013) 2721–2734. https://doi.org/10.1039/b000000x.

[20] N. Von Der Assen, L.J. Müller, A. Steingrube, P. Voll, A. Bardow, Selecting CO2 Sources for CO2 Utilization by Environmental-Merit-Order Curves, Environ. Sci. Technol. 50 (2016) 1093–1101. https://doi.org/10.1021/acs.est.5b03474.

[21] P. Bains, P. Psarras, J. Wilcox, CO2 capture from the industry sector, Prog. Energy Combust. Sci. 63 (2017) 146–172. https://doi.org/10.1016/j.pecs.2017.07.001.

[22] A. Goeppert, M. Czaun, G.K. Surya Prakash, G.A. Olah, Air as the renewable carbon source of the future: An overview of CO2 capture from the atmosphere, Energy Environ. Sci. 5 (2012) 7833–7853. https://doi.org/10.1039/c2ee21586a.

[23] R. Sathre, M. Chester, J. Cain, E. Masanet, A framework for environmental assessment of CO2 capture and storage systems, Energy. 37 (2012) 540–548. https://doi.org/10.1016/j.energy.2011.10.050.

[24] Y. Ye, H. Zhang, L. Chen, S. Chen, Q. Lin, F. Wei, Z. Zhang, S. Xiang, Metal-Organic Framework with Rich Accessible Nitrogen Sites for Highly Efficient CO2 Capture and Separation, Inorg. Chem. 58 (2019) 7754–7759. https://doi.org/10.1021/acs.inorgchem.9b00182.

[25] M. Frondel, C.M. Schmidt, C. Vance, A regression on climate policy: The European

Commission's legislation to reduce CO2 emissions from automobiles, Transp. Res. Part A Policy Pract. 45 (2011) 1043–1051. https://doi.org/10.1016/j.tra.2009.12.001.

[26] F. Zeman, Energy and material balance of CO2 capture from ambient air, Environ. Sci. Technol. 41 (2007) 7558–7563. https://doi.org/10.1021/es070874m.

[27] L. Zhang, Y. Wang, X. Miao, M. Gan, X. Li, Advances in Geochemistry in geologic CO_2 utilization and storage : A brief review, Adv. Geo-Energy Res. 3 (2019) 304–313. https://doi.org/10.26804/ager.2019.03.08.Corresponding.

[28] A. Kumar, D.G. Madden, M. Lusi, K.J. Chen, E.A. Daniels, T. Curtin, J.J. Perry, M.J. Zaworotko, Direct Air Capture of CO2 by Physisorbent Materials, Angew. Chemie - Int. Ed. 54 (2015) 14372–14377. https://doi.org/10.1002/anie.201506952.

[29] H.H. Wang, L. Hou, Y.Z. Li, C.Y. Jiang, Y.Y. Wang, Z. Zhu, Porous MOF with Highly Efficient Selectivity and Chemical Conversion for CO2, ACS Appl. Mater. Interfaces. 9 (2017) 17969–17976. https://doi.org/10.1021/acsami.7b03835.

[30] S. Park, M.G. Lee, J. Park, CO2 (carbon dioxide) fixation by applying new chemical absorption-precipitation methods, Energy. 59 (2013) 737–742. https://doi.org/10.1016/j.energy.2013.07.057.

[31] E.S. Rubin, J.E. Davison, H.J. Herzog, The cost of CO2 capture and storage, Int. J. Greenh. Gas Control. 40 (2015) 378–400. https://doi.org/10.1016/j.ijggc.2015.05.018.

[32] R. Chauvy, G. De Weireld, CO2 Utilization Technologies in Europe: A Short Review, Energy Technol. 8 (2020) 1–17. https://doi.org/10.1002/ente.202000627.

[33] M. Aresta, A. Dibenedetto, A. Angelini, Catalysis for the valorization of exhaust carbon: From CO2 to chemicals, materials, and fuels. technological use of CO2, Chem. Rev. 114 (2014) 1709–1742. https://doi.org/10.1021/cr4002758.

[34] World captured CO2 by source in the Sustainable Development Scenario, 2020-2070, IEA, Paris. (2021). https://www.iea.org/data-and-statistics/charts/world-captured-co2-by-source-in-the-sustainable-development-scenario-2020-2070.

[35] Y. Zeng, X. Tu, Plasma-Catalytic CO2 Hydrogenation at Low Temperatures, IEEE Trans. Plasma Sci. 44 (2016) 405–411. https://doi.org/10.1109/TPS.2015.2504549.

[36] D.T. Whipple, P.J.A. Kenis, Prospects of CO2 utilization via direct heterogeneous electrochemical reduction, J. Phys. Chem. Lett. 1 (2010) 3451–3458. https://doi.org/10.1021/jz1012627.

[37] U. Ulmer, T. Dingle, P.N. Duchesne, R.H. Morris, A. Tavasoli, T. Wood, G.A. Ozin, Fundamentals and applications of photocatalytic CO2 methanation, Nat. Commun. 10 (2019) 1–12. https://doi.org/10.1038/s41467-019-10996-2.

[38] C.H. Huang, C.S. Tan, A review: CO2 utilization, Aerosol Air Qual. Res. 14 (2014) 480–499. https://doi.org/10.4209/aaqr.2013.10.0326.

[39] N. Thybaud, D. Lebain, Panorama des voies de valorisation du CO2, 2010. www.ademe.fr.

[40] D. Mignard, M. Sahibzada, J.M. Duthie, H.W. Whittington, Methanol synthesis from flue-gas CO2 and renewable electricity: A feasibility study, Int. J. Hydrogen Energy. 28 (2003) 455–464. https://doi.org/10.1016/S0360-3199(02)00082-4.

[41] L.K. Rihko-Struckmann, A. Peschel, R. Hanke-Rauschenbach, K. Sundmacher, Assessment of methanol synthesis utilizing exhaust CO2 for chemical storage of electrical energy, Ind. Eng. Chem. Res. 49 (2010) 11073–11078. https://doi.org/10.1021/ie100508w.

[42] C. Steinlechner, H. Junge, Renewable Methane Generation from Carbon Dioxide and Sunlight, Angew. Chemie - Int. Ed. 57 (2018) 44–45. https://doi.org/10.1002/anie.201709032.

[43] D. Pakhare, J. Spivey, A review of dry (CO2) reforming of methane over noble metal catalysts, Chem. Soc. Rev. 43 (2014) 7813–7837. https://doi.org/10.1039/c3cs60395d.

[44] K. Świrk, M.E. Gálvez, M. Motak, T. Grzybek, M. Rønning, P. Da Costa, Dry reforming of methane over Zr- and Y-modified Ni/Mg/Al double-layered hydroxides, Catal. Commun. 117 (2018) 26–32. https://doi.org/10.1016/j.catcom.2018.08.024.

[45] M. García-diéguez, E. Finocchio, M. Ángeles, L.J. Alemany, G. Busca, Characterization of alumina-supported Pt , Ni and PtNi alloy catalysts for the dry reforming of methane, J. Catal. 274 (2010) 11–20. https://doi.org/10.1016/j.jcat.2010.05.020.

[46] B. Faroldi, J. Múnera, J.M. Falivene, I.R. Ramos, Á.G. García, L.T. Fernández, S.G. Carrazán, L. Cornaglia, Well-dispersed Rh nanoparticles with high activity for the dry reforming of methane, Int. J. Hydrogen Energy. 42 (2017) 16127–16138. https://doi.org/10.1016/j.ijhydene.2017.04.070.

[47] H.S. Whang, M.S. Choi, J. Lim, C. Kim, I. Heo, T.S. Chang, H. Lee, Enhanced activity and durability of Ru catalyst dispersed on zirconia for dry reforming of methane, Catal. Today. 293–294 (2017) 122–128. https://doi.org/10.1016/j.cattod.2016.12.034.

[48] Y. Wang, Q. Zhao, Y. Wang, C. Hu, P. Da Costa, One-Step Synthesis of Highly Active and Stable Ni-ZrOx for Dry Reforming of Methane, Ind. Eng. Chem. Res. 59 (2020) 11441–11452. https://doi.org/10.1021/acs.iecr.0c01416.

[49] K. Świrk, H. Zhang, S. Li, Y. Chen, M. Rønning, M. Motak, T. Grzybek, P. Da Costa, Carbon-resistant NiO-Y2O3-nanostructured catalysts derived from double-layered hydroxides for dry reforming of methane, Catal. Today. 366 (2021) 103–113. https://doi.org/10.1016/j.cattod.2020.03.032.

[50] K. Świrk, M.E. Gálvez, M. Motak, T. Grzybek, M. Rønning, P. Da Costa, Syngas production from dry methane reforming over yttrium-promoted nickel-KIT-6 catalysts, Int. J. Hydrogen Energy. 44 (2019) 274–286. https://doi.org/10.1016/j.ijhydene.2018.02.164.

[51] K. Świrk, M. Rønning, M. Motak, P. Beaunier, P. Da Costa, T. Grzybek, Ce- and Y-Modified Double-Layered Hydroxides as Catalysts for Dry Reforming of Methane: On the Effect of Yttrium Promotion, Catalysts. 9 (2019) 56. https://doi.org/10.3390/catal9010056.

[52] N.A.K. Aramouni, J.G. Touma, B.A. Tarboush, J. Zeaiter, M.N. Ahmad, Catalyst design for dry reforming of methane: Analysis review, Renew. Sustain. Energy Rev. 82 (2018) 2570–2585. https://doi.org/10.1016/j.rser.2017.09.076.

[53] Y. Wang, L. Li, Y. Wang, P. Da Costa, C. Hu, Highly carbon-resistant Y doped NiO–ZrOm catalysts for dry reforming of methane, Catalysts. 9 (2019) 1055. https://doi.org/10.3390/catal9121055.

[54] H. Wu, G. Pantaleo, V. La Parola, A.M. Venezia, X. Collard, C. Aprile, L.F. Liotta, Bi- and trimetallic Ni catalysts over Al2O3 and Al2O3-MOx (M=Ce or Mg) oxides for methane dry reforming: Au and Pt additive effects, Appl. Catal. B Environ. 156–157 (2014) 350–361. https://doi.org/10.1016/j.apcatb.2014.03.018.

[55] V.M. Gonzalez-Delacruz, F. Ternero, R. Pereñíguez, A. Caballero, J.P. Holgado, Study of nanostructured Ni/CeO2 catalysts prepared by combustion synthesis in dry reforming of methane, Appl. Catal. A Gen. 384 (2010) 1–9. https://doi.org/10.1016/j.apcata.2010.05.027.

[56] M.S. Lanre, A.S. Al-Fatesh, A.H. Fakeeha, S.O. Kasim, A.A. Ibrahim, A.S. Al-Awadi, A.A. Al-Zahrani, A.E. Abasaeed, Catalytic performance of lanthanum promoted Ni/ZrO2 for carbon dioxide reforming of methane, Processes. 8 (2020) 1502. https://doi.org/10.3390/pr8111502.

[57] S. Singh, T.D. Nguyen, T.J. Siang, P.T.T. Phuong, N.H. Huy Phuc, Q.D. Truong, S.S. Lam, D.V.N. Vo, Boron-doped Ni/SBA-15 catalysts with enhanced coke resistance and catalytic performance for dry reforming of methane, J. Energy Inst. 93 (2020) 31–42. https://doi.org/10.1016/j.joei.2019.04.011.

[58] R. Dębek, M. Motak, M.E. Galvez, T. Grzybek, P. Da Costa, Promotion effect of zirconia on Mg(Ni,Al)O mixed oxides derived from hydrotalcites in CO2 methane reforming, Appl. Catal. B Environ. 223 (2018) 36–46. https://doi.org/10.1016/j.apcatb.2017.06.024.

[59] K. Świrk, M.E. Gálvez, M. Motak, T. Grzybek, M. Rønning, P. Da Costa, Syngas production from dry methane reforming over yttrium-promoted nickel-KIT-6 catalysts, Int. J. Hydrogen Energy. 4 (2019) 274–286. https://doi.org/10.1016/j.ijhydene.2018.02.164.

[60] S. Zhang, S. Muratsugu, N. Ishiguro, M. Tada, Ceria-doped Ni/SBA-16 catalysts for dry reforming of methane, ACS Catal. 3 (2013) 1855–1864. https://doi.org/10.1021/cs400159w.

[61] Z. Taherian, M. Yousefpour, M. Tajally, B. Khoshandam, A comparative study of ZrO2, Y2O3 and Sm2O3 promoted Ni/SBA-15 catalysts for evaluation of CO2/methane reforming performance, Int. J. Hydrogen Energy. 42 (2017) 16408–16420. https://doi.org/10.1016/j.ijhydene.2017.05.095.

[62] R. Dębek, M.E. Galvez, F. Launay, M. Motak, T. Grzybek, P. Da Costa, Low temperature dry methane reforming over Ce, Zr and CeZr promoted Ni–Mg–Al hydrotalcite-derived catalysts, Int. J. Hydrogen Energy. 41 (2016) 11616–11623. https://doi.org/10.1016/j.ijhydene.2016.02.074.

[63] H. Liu, D. Wierzbicki, R. Debek, M. Motak, T. Grzybek, P. Da Costa, M.E. Gálvez, La-promoted Ni-hydrotalcite-derived catalysts for dry reforming of methane at low temperatures, Fuel. 182 (2016) 8–16. https://doi.org/10.1016/j.fuel.2016.05.073.

[64] J.F. Li, C. Xia, C.T. Au, B.S. Liu, Y2O3-promoted NiO/SBA-15 catalysts highly active for CO2/CH4 reforming, Int. J. Hydrogen Energy. 39 (2014) 10927–10940. https://doi.org/10.1016/j.ijhydene.2014.05.021.

[65] A. Kambolis, H. Matralis, A. Trovarelli, C. Papadopoulou, Ni/CeO2 -ZrO2 catalysts for the dry reforming of methane, Appl. Catal. A Gen. 377 (2010) 16–26. https://doi.org/10.1016/j.apcata.2010.01.013.

[66] B. Li, S. Zhang, Methane reforming with CO2 using nickel catalysts supported on yttria-doped SBA-15 mesoporous materials via sol-gel process, Int. J. Hydrogen Energy. 38 (2013) 14250–14260. https://doi.org/10.1016/j.ijhydene.2013.08.105.

[67] H.W. Kim, K.M. Kang, H.Y. Kwak, J.H. Kim, Preparation of supported Ni catalysts on various metal oxides with core/shell structures and their tests for the steam reforming of methane, Chem. Eng. J. 168 (2011) 775–783. https://doi.org/10.1016/j.cej.2010.11.045.

[68] P.T. Krenzke, J.R. Fosheim, J.H. Davidson, Solar fuels via chemical-looping reforming, Sol. Energy. 156 (2017) 48–72. https://doi.org/10.1016/j.solener.2017.05.095.

[69] A. Sternberg, A. Bardow, Life Cycle Assessment of Power-to-Gas: Syngas vs Methane, ACS Sustain. Chem. Eng. 4 (2016) 4156–4165. https://doi.org/10.1021/acssuschemeng.6b00644.

[70] S. Chiuta, N. Engelbrecht, G. Human, D.G. Bessarabov, Techno-economic assessment of power-to-methane and power-to-syngas business models for sustainable carbon dioxide utilization in coal-to-liquid facilities, J. CO2 Util. 16 (2016) 399–411. https://doi.org/10.1016/j.jcou.2016.10.001.

[71] S. Natalia, M. Martin, Catalytic hydrogenation of CO2 to methane over supported Pd, Rh and Ni catalysts, Catal. Sci. Technol. 7 (2017) 1086. https://doi.org/10.1039/c6cy02536f.

[72] T. Schaub, CO2-based hydrogen storage: CO2 hydrogenation to formic acid, formaldehyde and methanol, Phys. Sci. Rev. 3 (2018). https://doi.org/10.1515/psr-2017-0015.

[73] L. Torrente-Murciano, D. Mattia, M.D. Jones, P.K. Plucinski, Formation of hydrocarbons via CO2 hydrogenation - A thermodynamic study, J. CO2 Util. 6 (2014) 34–39. https://doi.org/10.1016/j.jcou.2014.03.002.

[74] X. Jiang, X. Nie, X. Guo, C. Song, J.G. Chen, Recent Advances in Carbon Dioxide Hydrogenation to Methanol via Heterogeneous Catalysis, Chem. Rev. 120 (2020) 7984–

8034. https://doi.org/10.1021/acs.chemrev.9b00723.

[75] T. Liu, X. Hong, G. Liu, In Situ Generation of the Cu@3D-ZrOx Framework Catalyst for Selective Methanol Synthesis from CO2/H2, ACS Catal. 10 (2020) 93–102. https://doi.org/10.1021/acscatal.9b03738.

[76] S. Kattel, J.G. Chen, P. Liu, Active sites for CO2 hydrogenation to methanol on Cu/ZnO catalysts, Science (80-.). 355 (2017) 1296–1299. https://doi.org/10.1126/science.aal3573.

[77] Y. Matsumura, W. Shen, Y. Ichihashi, M. Okumura, Low-Temperature Methanol Synthesis Catalyzed over Ultrafine Palladium Particles Supported on Cerium Oxide, J. Catal. 197 (2001) 267–272. https://doi.org/10.1006/jcat.2000.3094.

[78] Y. Men, Y. Liu, Q. Wang, Z. Luo, S. Shao, Y. Li, Y. Pan, Highly dispersed Pt-based catalysts for selective CO2 hydrogenation to methanol at atmospheric pressure, Chem. Eng. Sci. 200 (2019) 167–175. https://doi.org/10.1016/j.ces.2019.02.004.

[79] A. Tsoukalou, P.M. Abdala, D. Stoian, X. Huang, M. Willinger, A. Fedorov, C.R. Muller, Structural Evolution and Dynamics of an In2O3 Catalyst for CO2 Hydrogenation to Methanol: An Operando XAS-XRD and In Situ TEM Study, J. Am. Chem. Soc. 141 (2019) 13497–13505. https://doi.org/10.1021/jacs.9b04873.

[80] J. Wang, C. Tang, G. Li, Z. Han, Z. Li, H. Liu, F. Cheng, C. Li, High-Performance MaZrOx (Ma = Cd, Ga) Solid-Solution Catalysts for CO2 Hydrogenation to Methanol, ACS Catal. 9 (2019) 10253–10259. https://doi.org/10.1021/acscatal.9b03449.

[81] S. Natesakhawat, J.W. Lekse, J.P. Baltrus, P.R. Ohodnicki, B.H. Howard, X. Deng, C. Matranga, Active Sites and Structure − Activity Relationships of Copper-Based Catalysts for Carbon Dioxide Hydrogenation to Methanol, ACS Catal. 2 (2012) 1667–1676. https://doi.org/https://doi.org/10.1021/cs300008g.

[82] J. Yoshihara, C.T. Campbell, Methanol synthesis and reverse water-gas shift kinetics over Cu(110) model catalysts: Structural sensitivity, J. Catal. 161 (1996) 776–782. https://doi.org/10.1006/jcat.1996.0240.

[83] B. Liang, J. Ma, X. Su, C. Yang, H. Duan, H. Zhou, S. Deng, L. Li, Y. Huang, Investigation on Deactivation of Cu/ZnO/Al2O3 Catalyst for CO2 Hydrogenation to Methanol, Ind. Eng. Chem. Res. 58 (2019) 9030−9037. https://doi.org/10.1021/acs.iecr.9b01546.

[84] A. Bansode, B. Tidona, P.R. Von Rohr, A. Urakawa, Impact of K and Ba promoters on CO2 hydrogenation over Cu/Al2O3 catalysts at high pressure, Catal. Sci. Technol. 3 (2013) 767–778. https://doi.org/10.1039/c2cy20604h.

[85] M. Saito, T. Fujitani, M. Takeuchi, T. Watanabe, Development of copper/zinc oxide-based multicomponent catalysts for methanol synthesis from carbon dioxide and hydrogen, Appl. Catal. A Gen. 138 (1996) 311–318. https://doi.org/10.1016/0926-860X(95)00305-3.

[86] H. Ban, C. Li, K. Asami, K. Fujimoto, Influence of rare-earth elements (La, Ce, Nd and

Pr) on the performance of Cu/Zn/Zr catalyst for CH3OH synthesis from CO2, Catal. Commun. 54 (2014) 50–54. https://doi.org/10.1016/j.catcom.2014.05.014.

[87] N. Nomura, T. Tagawa, S. Goto, Effect of acid-base properties on copper catalysts for hydrogenation of carbon dioxide, React. Kinet. Catal. Lett. 63 (1998) 21–25. https://doi.org/10.1007/BF02475425.

[88] N. Pasupulety, H. Driss, Y.A. Alhamed, A.A. Alzahrani, M.A. Daous, L. Petrov, Studies on Au/Cu-Zn-Al catalyst for methanol synthesis from CO2, Appl. Catal. A Gen. 504 (2015) 308–318. https://doi.org/10.1016/j.apcata.2015.01.036.

[89] S. Tada, F. Watanabe, K. Kiyota, N. Shimoda, R. Hayashi, M. Takahashi, A. Nariyuki, A. Igarashi, S. Satokawa, Ag addition to CuO-ZrO2 catalysts promotes methanol synthesis via CO2 hydrogenation, J. Catal. 351 (2017) 107–118. https://doi.org/10.1016/j.jcat.2017.04.021.

[90] E. Samei, M. Taghizadeh, M. Bahmani, Enhancement of stability and activity of Cu/ZnO/Al 2O 3 catalysts by colloidal silica and metal oxides additives for methanol synthesis from a CO 2-rich feed, Fuel Process. Technol. 96 (2012) 128–133. https://doi.org/10.1016/j.fuproc.2011.12.028.

[91] K. Deng, B. Hu, Q. Lu, X. Hong, Cu/g-C3N4 modified ZnO/Al2O3 catalyst: methanol yield improvement of CO2 hydrogenation, Catal. Commun. 100 (2017) 81–84. https://doi.org/10.1016/j.catcom.2017.06.041.

[92] G. Prieto, M. Shakeri, K.P. De Jong, P.E. De Jongh, Quantitative relationship between support porosity and the stability of pore-confined metal nanoparticles studied on CuZnO/SiO2 methanol synthesis catalysts, ACS Nano. 8 (2014) 2522–2531. https://doi.org/10.1021/nn406119j.

[93] M.Z. Ramli, S.S.A. Syed-Hassan, A. Hadi, Performance of Cu-Zn-Al-Zr catalyst prepared by ultrasonic spray precipitation technique in the synthesis of methanol via CO2 hydrogenation, Fuel Process. Technol. 169 (2018) 191–198. https://doi.org/10.1016/j.fuproc.2017.10.004.

[94] X. Dong, F. Li, N. Zhao, Y. Tan, J. Wang, F. Xiao, CO2 hydrogenation to methanol over Cu/Zn/Al/Zr catalysts prepared by liquid reduction, Cuihua Xuebao/Chinese J. Catal. 38 (2017) 717–725. https://doi.org/10.1016/S1872-2067(17)62793-1.

[95] Q. Chen, Y. Gu, Z. Tang, Y. Sun, Comparative environmental and economic performance of solar energy integrated methanol production systems in China, Energy Convers. Manag. 187 (2019) 63–75. https://doi.org/10.1016/j.enconman.2019.03.013.

[96] C.F. Shih, T. Zhang, J. Li, C. Bai, Powering the Future with Liquid Sunshine, Joule. 2 (2018) 1925–1949. https://doi.org/10.1016/j.joule.2018.08.016.

[97] C. Li, M. Negnevitsky, X. Wang, Prospective assessment of methanol vehicles in China using FANP-SWOT analysis, Transp. Policy. 96 (2020) 60–75. https://doi.org/10.1016/j.tranpol.2020.06.010.

[98] P. Sabatier, Nouvelles synthèses du méthane, Comptes Rendus Acad. Sci. 82 (1902) 514–516.

[99] W.J. Lee, C. Li, H. Prajitno, J. Yoo, J. Patel, Y. Yang, S. Lim, Recent trend in thermal catalytic low temperature CO2 methanation: A critical review, Catal. Today. (2020). https://doi.org/10.1016/j.cattod.2020.02.017.

[100] M. Götz, J. Lefebvre, F. Mörs, A. McDaniel Koch, F. Graf, S. Bajohr, R. Reimert, T. Kolb, Renewable Power-to-Gas: A technological and economic review, Renew. Energy. 85 (2016) 1371–1390. https://doi.org/10.1016/j.renene.2015.07.066.

[101] S.C. Peter, Reduction of CO2 to Chemicals and Fuels: A Solution to Global Warming and Energy Crisis, ACS Energy Lett. 3 (2018) 1557–1561. https://doi.org/10.1021/acsenergylett.8b00878.

[102] A. Karelovic, P. Ruiz, Improving the hydrogenation function of Pd/γ-Al2O 3 catalyst by Rh/γ-Al2O3 Addition in CO2 methanation at low temperature, ACS Catal. 3 (2013) 2799–2812. https://doi.org/10.1021/cs400576w.

[103] J.N. Park, E.W. McFarland, A highly dispersed Pd-Mg/SiO2 catalyst active for methanation of CO2, J. Catal. 266 (2009) 92–97. https://doi.org/10.1016/j.jcat.2009.05.018.

[104] H.Y. Kim, H.M. Lee, J. Park, Bifunctional Mechanism of CO2 Methanation on Pd-MgO/SiO2 Catalyst: Independent Roles of MgO and Pd on CO2 Methanation, J. Phys. Chem. C. 114 (2010) 7128–7131. https://doi.org/10.1021/jp100938v.

[105] F. Hemmingsson, A. Schaefer, CO2 Methanation over Rh/CeO2 Studied with Infrared Modulation Excitation Spectroscopy and Phase Sensitive Detection, Catalysts. 10 (2020) 601. https://doi.org/10.3390/catal10060601.

[106] A. Beuls, C. Swalus, M. Jacquemin, G. Heyen, A. Karelovic, P. Ruiz, Methanation of CO2: Further insight into the mechanism over Rh/γ-Al2O3 catalyst, Appl. Catal. B Environ. 113–114 (2012) 2–10. https://doi.org/10.1016/j.apcatb.2011.02.033.

[107] A. Karelovic, P. Ruiz, CO2 hydrogenation at low temperature over Rh/γ-Al2O3 catalysts: Effect of the metal particle size on catalytic performances and reaction mechanism, Appl. Catal. B Environ. 113–114 (2012) 237–249. https://doi.org/10.1016/j.apcatb.2011.11.043.

[108] F. Solymosi, A. Erdöhelyi, Methanation of CO2 on supported rhodium catalysts, J. Catal. 68 (1981) 371–382.

[109] M.A.A. Aziz, A.A. Jalil, S. Triwahyono, S.M. Sidik, Methanation of carbon dioxide on metal-promoted mesostructured silica nanoparticles, Appl. Catal. A Gen. 486 (2014) 115–122. https://doi.org/10.1016/j.apcata.2014.08.022.

[110] A. Karelovic, P. Ruiz, Mechanistic study of low temperature CO2 methanation over Rh/TiO2 catalysts, J. Catal. 301 (2013) 141–153. https://doi.org/http://dx.doi.org/10.1016/j.jcat.2013.02.009.

[111] A. Kim, C. Sanchez, B. Haye, C. Boissière, C. Sassoye, D.P. Debecker, Mesoporous TiO2 Support Materials for Ru-Based CO2 Methanation Catalysts, ACS Appl. Nano Mater. 2 (2019) 3220–3230. https://doi.org/10.1021/acsanm.9b00518.

[112] S. Tada, O.J. Ochieng, R. Kikuchi, T. Haneda, H. Kameyama, Promotion of CO2 methanation activity and CH4 selectivity at low temperatures over Ru/CeO2/Al2O3 catalysts, Int. J. Hydrogen Energy. 39 (2014) 10090–10100. https://doi.org/10.1016/j.ijhydene.2014.04.133.

[113] E.M. Petersen, R.G. Rao, B.C. Vance, J.-P. Tessonnier, SiO2/SiC supports with tailored thermal conductivity to reveal the effect of surface temperature on Ru-catalyzed CO2 methanation, Appl. Catal. B Environ. 286 (2021) 119904. https://doi.org/10.1016/j.apcatb.2021.119904.

[114] A. Petala, P. Panagiotopoulou, Methanation of CO2 over alkali-promoted Ru/TiO2 catalysts: I. Effect of alkali additives on catalytic activity and selectivity, Appl. Catal. B Environ. 224 (2018) 919–927. https://doi.org/10.1016/j.apcatb.2017.11.048.

[115] S. Toemen, W.A.W. Abu Bakar, R. Ali, Effect of ceria and strontia over Ru/Mn/Al2O3 catalyst: Catalytic methanation, physicochemical and mechanistic studies, J. CO2 Util. 13 (2016) 38–49. https://doi.org/10.1016/j.jcou.2015.11.005.

[116] G. Garbarino, D. Bellotti, E. Finocchio, L. Magistri, G. Busca, Methanation of carbon dioxide on Ru/Al2O3: Catalytic activity and infrared study, Catal. Today. 277 (2016) 21–28. https://doi.org/10.1016/j.cattod.2015.12.010.

[117] F. Wang, C. Li, X. Zhang, M. Wei, D.G. Evans, X. Duan, Catalytic behavior of supported Ru nanoparticles on the {100}, {110}, and {111} facet of CeO2, J. Catal. 329 (2015) 177–186. https://doi.org/10.1016/j.jcat.2015.05.014.

[118] Y. Guo, S. Mei, K. Yuan, D.J. Wang, H.C. Liu, C.H. Yan, Y.W. Zhang, Low-Temperature CO2 Methanation over CeO2-Supported Ru Single Atoms, Nanoclusters, and Nanoparticles Competitively Tuned by Strong Metal-Support Interactions and H-Spillover Effect, ACS Catal. 8 (2018) 6203–6215. https://doi.org/10.1021/acscatal.7b04469.

[119] S.K. Beaumont, S. Alayoglu, C. Specht, W.D. Michalak, V. V. Pushkarev, J. Guo, N. Kruse, G.A. Somorjai, Combining in situ NEXAFS spectroscopy and CO2 methanation kinetics to study Pt and Co nanoparticle catalysts reveals key insights into the role of platinum in promoted cobalt catalysis, J. Am. Chem. Soc. 136 (2014) 9898–9901. https://doi.org/10.1021/ja505286j.

[120] M. Mihet, G. Blanita, M. Dan, L. Barbu-Tudoran, M.D. Lazar, Pt/UiO-66 Nanocomposites as Catalysts for CO2 Methanation Process, J. Nanosci. Nanotechnol. 19 (2019) 3187–3196. https://doi.org/10.1166/jnn.2019.16607.

[121] Z. Baysal, S. Kureti, CO2 methanation on Mg-promoted Fe catalysts, Appl. Catal. B Environ. 262 (2020) 118300. https://doi.org/10.1016/j.apcatb.2019.118300.

[122] J. Kruatim, S. Jantasee, B. Jongsomjit, Improvement of cobalt dispersion on Co/SBA-15

and Co/SBA-16 catalysts by ultrasound and vacuum treatments during Post-impregnation step, Eng. J. 21 (2017) 17–28. https://doi.org/10.4186/ej.2017.21.1.17.

[123] C. Liang, H. Tian, G. Gao, S. Zhang, Q. Liu, D. Dong, X. Hu, Methanation of CO2 over alumina supported nickel or cobalt catalysts: Effects of the coordination between metal and support on formation of the reaction intermediates, Int. J. Hydrogen Energy. 45 (2020) 531–543. https://doi.org/10.1016/j.ijhydene.2019.10.195.

[124] H. Ho Shin, L. Lu, Z. Yang, C. J. Kiely, S. McIntosh, Cobalt Catalysts Decorated with Platinum Atoms Supported on Barium Zirconate Provide Enhanced Activity and Selectivity for CO2 Methanation, ACS Catal. 6 (2016) 2811–2818. https://doi.org/10.1021/acscatal.6b00005.

[125] X. Nie, H. Wang, W. Li, Y. Chen, X. Guo, C. Song, DFT insight into the support effect on the adsorption and activation of key species over Co catalysts for CO2 methanation, J. CO2 Util. 24 (2018) 99–111. https://doi.org/10.1016/j.jcou.2017.12.005.

[126] J. Tu, H. Wu, Q. Qian, S. Han, M. Chu, S. Jia, R. Feng, J. Zhai, M. He, B. Han, Low temperature methanation of CO2 over an amorphous cobalt-based catalyst, Chem. Sci. (2021). https://doi.org/10.1039/d0sc06414a.

[127] W. Li, Y. Liu, M. Mu, F. Ding, Z. Liu, X. Guo, C. Song, Organic acid-assisted preparation of highly dispersed Co/ZrO2 catalysts with superior activity for CO2 methanation, Appl. Catal. B Environ. 254 (2019) 531–540. https://doi.org/10.1016/j.apcatb.2019.05.028.

[128] C. Jia, Y. Dai, Y. Yang, J.W. Chew, Nickel-cobalt catalyst supported on TiO2-coated SiO2 spheres for CO2 methanation in a fluidized bed, Int. J. Hydrogen Energy. 44 (2019) 13443–13455. https://doi.org/10.1016/j.ijhydene.2019.04.009.

[129] W. Li, X. Nie, X. Jiang, A. Zhang, F. Ding, M. Liu, Z. Liu, X. Guo, C. Song, ZrO2 support imparts superior activity and stability of Co catalysts for CO2 methanation, Appl. Catal. B Environ. 220 (2018) 397–408. https://doi.org/10.1016/j.apcatb.2017.08.048.

[130] W. Gac, W. Zawadzki, S. Grzegorz, A. Sienkiewicz, A. Kierys, Nickel catalysts supported on silica microspheres for CO2 methanation, Microporous Mesoporous Mater. 272 (2018) 79–91. https://doi.org/10.1016/j.micromeso.2018.06.022.

[131] D. Wierzbicki, R. Baran, R. Dębek, M. Motak, T. Grzybek, M.E. Gálvez, P. Da Costa, The influence of nickel content on the performance of hydrotalcite-derived catalysts in CO2 methanation reaction, Int. J. Hydrogen Energy. 42 (2017) 23548–23555. https://doi.org/10.1016/j.ijhydene.2017.02.148.

[132] G.I. Siakavelas, N.D. Charisiou, S. AlKhoori, A.A. AlKhoori, V. Sebastian, S.J. Hinder, M.A. Baker, I. V. Yentekakis, K. Polychronopoulou, M.A. Goula, Highly selective and stable nickel catalysts supported on ceria promoted with Sm2O3, Pr2O3 and MgO for the CO2 methanation reaction, Appl. Catal. B Environ. 282 (2021) 119562. https://doi.org/10.1016/j.apcatb.2020.119562.

[133] C. Mebrahtu, S. Abate, S. Perathoner, S. Chen, G. Centi, CO2 methanation over Ni

catalysts based on ternary and quaternary mixed oxide: A comparison and analysis of the structure-activity relationships, Catal. Today. 304 (2018) 181–189. https://doi.org/10.1016/j.cattod.2017.08.060.

[134] C. Fukuhara, K. Hayakawa, Y. Suzuki, W. Kawasaki, R. Watanabe, A novel nickel-based structured catalyst for CO2 methanation: A honeycomb-type Ni/CeO2 catalyst to transform greenhouse gas into useful resources, Appl. Catal. A Gen. 532 (2017) 12–18. https://doi.org/10.1016/j.apcata.2016.11.036.

[135] X. Yan, Y. Liu, B. Zhao, Z. Wang, Y. Wang, C.J. Liu, Methanation over Ni/SiO2: Effect of the catalyst preparation methodologies, Int. J. Hydrogen Energy. 38 (2013) 2283–2291. https://doi.org/10.1016/j.ijhydene.2012.12.024.

[136] X. Jia, X. Zhang, N. Rui, X. Hu, C. jun Liu, Structural effect of Ni/ZrO2 catalyst on CO2 methanation with enhanced activity, Appl. Catal. B Environ. 244 (2019) 159–169. https://doi.org/10.1016/j.apcatb.2018.11.024.

[137] M. Li, H. Amari, A.C. van Veen, Metal-oxide interaction enhanced CO2 activation in methanation over ceria supported nickel nanocrystallites, Appl. Catal. B Environ. 239 (2018) 27–35. https://doi.org/10.1016/j.apcatb.2018.07.074.

[138] D. Wierzbicki, R. Baran, R. Dębek, M. Motak, M.E. Gálvez, T. Grzybek, P. Da Costa, P. Glatzel, Examination of the influence of La promotion on Ni state in hydrotalcite-derived catalysts under CO2 methanation reaction conditions: Operando X-ray absorption and emission spectroscopy investigation, Appl. Catal. B Environ. 232 (2018) 409–419. https://doi.org/10.1016/j.apcatb.2018.03.089.

[139] R.P. Ye, Q. Li, W. Gong, T. Wang, J.J. Razink, L. Lin, Y.Y. Qin, Z. Zhou, H. Adidharma, J. Tang, A.G. Russell, M. Fan, Y.G. Yao, High-performance of nanostructured Ni/CeO2 catalyst on CO2 methanation, Appl. Catal. B Environ. 268 (2019) 118474. https://doi.org/10.1016/j.apcatb.2019.118474.

[140] X. Jia, X. Zhang, N. Rui, X. Hu, C. jun Liu, Structural effect of Ni/ZrO2 catalyst on CO2 methanation with enhanced activity, Appl. Catal. B Environ. 244 (2019) 159–169. https://doi.org/10.1016/j.apcatb.2018.11.024.

[141] C. Sun, P. Beaunier, V. La Parola, L. F. Liotta, P. Da Costa, Ni/CeO2 Nanoparticles Promoted by Yttrium Doping as Catalysts for CO2 Methanation, ACS Appl. Nano Mater. 3 (2020) 12355–12368. https://doi.org/10.1021/acsanm.0c02841.

[142] C. Sun, P. Beaunier, P. Da Costa, Effect of ceria promotion on the catalytic performance of Ni/SBA-16 catalysts for CO2 methanation, Catal. Sci. Technol. 10 (2020) 6330–6341. https://doi.org/10.1039/d0cy00922a.

[143] C. Sun, J. Krstic, V. Radonjic, M. Stankovic, P. Da Costa, The effect of Ni precursor salts on diatomite supported Ni-Mg catalysts in methanation of CO2, Mater. Sci. Forum. 1016 (2021) 1417–1422. https://doi.org/https://doi.org/10.4028/www.scientific.net/MSF.1016.1417.

[144] C. Sun, K. Świrk, D. Wierzbicki, M. Motak, T. Grzybek, P. Da Costa, On the effect of yttrium promotion on Ni-layered double hydroxides-derived catalysts for hydrogenation of CO2 to methane, Int. J. Hydrogen Energy. 46 (2021) 12169–12179. https://doi.org/10.1016/j.ijhydene.2020.03.202.

[145] P. Panagiotopoulou, Hydrogenation of CO2 over supported noble metal catalysts, Appl. Catal. A Gen. 542 (2017) 63–70. http://dx.doi.org/10.1016/j.apcata.2017.05.026.

[146] A. Karelovic, P. Ruiz, Mechanistic study of low temperature CO2 methanation over Rh/TiO2 catalysts, J. Catal. 301 (2013) 141–153. https://doi.org/10.1016/j.jcat.2013.02.009.

[147] J. Li, Y. Lin, X. Pan, D. Miao, D. Ding, Y. Cui, J. Dong, X. Bao, Enhanced CO2 Methanation Activity of Ni/Anatase Catalyst by Tuning Strong Metal-Support Interactions, ACS Catal. 9 (2019) 6342–6348. https://doi.org/10.1021/acscatal.9b00401.

[148] J. Gao, Y. Wang, Y. Ping, D. Hu, G. Xu, F. Gu, F. Su, A thermodynamic analysis of methanation reactions of carbon oxides for the production of synthetic natural gas, RSC Adv. 2 (2012) 2358–2368. https://doi.org/10.1039/c2ra00632d.

[149] K.R. Thampi, J. Kiwi, M. Grätzel, Methanation and photo-methanation of carbon dioxide at room temperature and atmospheric pressure, Nature. 327 (1987) 506–508. https://doi.org/10.1038/327506a0.

[150] F. Ocampo, B. Louis, A.C. Roger, Methanation of carbon dioxide over nickel-based Ce0.72Zr0.28O2 mixed oxide catalysts prepared by sol-gel method, Appl. Catal. A Gen. 369 (2009) 90–96. https://doi.org/10.1016/j.apcata.2009.09.005.

[151] W. Wang, S. Wang, X. Ma, J. Gong, Recent advances in catalytic hydrogenation of carbon dioxide, Chem. Soc. Rev. 40 (2011) 3703–3727. https://doi.org/10.1039/c1cs15008a.

[152] Y.A. Agafonov, T.N. Myshenkova, The Mechanism of Carbon Dioxide Hydrogenation on Copper and Nickel Catalysts, Pet. Chem. 47 (2007) 75–82. https://doi.org/10.1134/S0965544107020028.

[153] J. Ren, H. Guo, J. Yang, Z. Qin, J. Lin, Z. Li, Insights into the mechanisms of CO2 methanation on Ni(111) surfaces by density functional theory, Appl. Surf. Sci. 351 (2015) 504–516. https://doi.org/10.1016/j.apsusc.2015.05.173.

[154] A.R. Michel Marwood, Ralf Doepper, In-situ surface and gas phase analysis for kinetic studies under transient conditions The catalytic hydrogenation of CO2, Appl. Catal. A Gen. 151 (1997) 223–246.

[155] R. Zhou, N. Rui, Z. Fan, C. Liu, Effect of the structure of Ni /TiO2 catalyst on CO2 methanation, Int. J. Hydrogen Energy. 41 (2016) 22017–22025. https://doi.org/10.1016/j.ijhydene.2016.08.093.

[156] M. Jacquemin, A. Beuls, P. Ruiz, Catalytic production of methane from CO2 and H2 at low temperature: Insight on the reaction mechanism, Catal. Today. 157 (2010) 462–466.

https://doi.org/10.1016/j.cattod.2010.06.016.

[157] A. Beuls, C. Swalus, M. Jacquemin, G. Heyen, A. Karelovic, P. Ruiz, Methanation of CO2 : Further insight into the mechanism over Rh/□-Al2O3 catalyst, Appl. Catal. B Environ. 113–114 (2012) 2–10. https://doi.org/10.1016/j.apcatb.2011.02.033.

[158] S.M. Lee, Y.H. Lee, D.H. Moon, J.Y. Ahn, D.D. Nguyen, S.W. Chang, S.S. Kim, Reaction Mechanism and Catalytic Impact of Ni/CeO2-x Catalyst for Low-Temperature CO2 Methanation, Ind. Eng. Chem. Res. 58 (2019) 8656–8662. https://doi.org/10.1021/acs.iecr.9b00983.

[159] A. Cárdenas-Arenas, A. Quindimil, A. Davó-Quiñonero, E. Bailón-García, D. Lozano-Castelló, U. De-La-Torre, B. Pereda-Ayo, J.A. González-Marcos, J.R. González-Velasco, A. Bueno-López, Isotopic and in situ DRIFTS study of the CO2 methanation mechanism using Ni/CeO2 and Ni/Al2O3 catalysts, Appl. Catal. B Environ. 265 (2020) 118538. https://doi.org/10.1016/j.apcatb.2019.118538.

[160] Q. Pan, J. Peng, T. Sun, S.S. Wang, S.S. Wang, P. Qiushi, J. Peng, T. Sun, S.S. Wang, S.S. Wang, J. Peng, Q. Pan, Insight into the reaction route of CO2 methanation: Promotion effect of medium basic sites, Catal. Commun. 45 (2014) 74–78. https://doi.org/10.1016/j.catcom.2013.10.034.

[161] H.C. Wu, Y.C. Chang, J.H. Wu, J.H. Lin, I.K. Lin, C.S. Chen, Methanation of CO2 and reverse water gas shift reactions on Ni/SiO2 catalysts: the influence of particle size on selectivity and reaction pathway, Catal. Sci. Technol. 5 (2015) 4154–4163. https://doi.org/10.1039/C5CY00667H.

[162] Y. Chen, B. Qiu, Y. Liu, Y. Zhang, An active and stable nickel-based catalyst with embedment structure for CO2 methanation, Appl. Catal. B Environ. 269 (2020) 118801. https://doi.org/10.1016/j.apcatb.2020.118801.

[163] C. Mebrahtu, S. Perathoner, G. Giorgianni, S. Chen, G. Centi, F. Krebs, R. Palkovits, S. Abate, Deactivation mechanism of hydrotalcite-derived Ni-AlOX catalysts during low-temperature CO2 methanation via Ni-hydroxide formation and the role of Fe in limiting this effect, Catal. Sci. Technol. 9 (2019) 4023–4035. https://doi.org/10.1039/c9cy00744j.

[164] S. Sharma, Z. Hu, P. Zhang, E.W. McFarland, H. Metiu, CO2 methanation on Ru-doped ceria, J. Catal. 278 (2011) 297–309. https://doi.org/doi:10.1016/j.jcat.2010.12.015.

[165] E. Zağli, J.L. Falconer, Carbon dioxide adsorption and methanation on Ruthenium, J. Catal. 69 (1981) 1–8.

[166] A. Karelovic, P. Ruiz, c, ACS Catal. 3 (2013) 2799–2812. https://doi.org/10.1021/cs400576w.

[167] M.A.A. Aziz, A.A. Jalil, S. Triwahyono, A. Ahmad, CO2 methanation over heterogeneous catalysts: Recent progress and future prospects, Green Chem. 17 (2015) 2647–2663. https://doi.org/10.1039/c5gc00119f.

[168] K. Zhao, W. Wang, Z. Li, Highly efficient Ni/ZrO2 catalysts prepared via combustion

method for CO2 methanation, J. CO2 Util. 16 (2016) 236–244. https://doi.org/10.1016/j.jcou.2016.07.010.

[169] X. Wang, L. Zhu, Y. Zhuo, Y. Zhu, S. Wang, Enhancement of CO2 Methanation over La-Modified Ni/SBA-15 Catalysts Prepared by Different Doping Methods, ACS Sustain. Chem. Eng. 7 (2019) 14647–14660. https://doi.org/10.1021/acssuschemeng.9b02563.

[170] S. Tada, T. Shimizu, H. Kameyama, T. Haneda, R. Kikuchi, Ni/CeO2 catalysts with high CO2 methanation activity and high CH4 selectivity at low temperatures, Int. J. Hydrogen Energy. 37 (2012) 5527–5531. https://doi.org/10.1016/j.ijhydene.2011.12.122.

[171] Q. Liu, Y. Tian, One-pot synthesis of NiO/SBA-15 monolith catalyst with a three-dimensional framework for CO2 methanation, Int. J. Hydrogen Energy. 42 (2017) 12295–12300. https://doi.org/10.1016/j.ijhydene.2017.02.070.

[172] S. Ewald, M. Kolbeck, T. Kratky, M. Wolf, O. Hinrichsen, On the deactivation of Ni-Al catalysts in CO2 methanation, Appl. Catal. A Gen. 570 (2019) 376–386. https://doi.org/10.1016/j.apcata.2018.10.033.

[173] R.P. Ye, W. Gong, Z. Sun, Q. Sheng, X. Shi, T. Wang, Y. Yao, J.J. Razink, L. Lin, Z. Zhou, H. Adidharma, J. Tang, M. Fan, Y.G. Yao, Enhanced stability of Ni/SiO2 catalyst for CO2 methanation: Derived from nickel phyllosilicate with strong metal-support interactions, Energy. 188 (2019) 116059. https://doi.org/10.1016/j.energy.2019.116059.

[174] L. Falbo, M. Martinelli, C.G. Visconti, L. Lietti, C. Bassano, P. Deiana, Kinetics of CO2 methanation on a Ru-based catalyst at process conditions relevant for Power-to-Gas applications, Appl. Catal. B Environ. 225 (2018) 354–363. https://doi.org/10.1016/j.apcatb.2017.11.066.

[175] M. Agnelli, M. Kolb, C. Mirodatos, CO hydrogenation on a Nickel Catalyst: Kinetics and Modeling of a low temperature sintering process, J. Catal. 148 (1994) 9–21. https://doi.org/https://doi.org/10.1006/jcat.1994.1180.

[176] M. Agnelli, M. Kolb, C. Nicot, C. Mirodatos, Sintering of a Ni-based Catalyst During CO Hydrogenation: Kinetics and Modeling, Stud. Surf. Sci. Catal. 68 (1991) 605–612. https://doi.org/https://doi.org/10.1016/S0167-2991(08)62690-7.

[177] J. Ren, X. Qin, J.Z. Yang, Z.F. Qin, H.L. Guo, J.Y. Lin, Z. Li, Methanation of carbon dioxide over Ni-M/ZrO2 (M = Fe, Co, Cu) catalysts: Effect of addition of a second metal, Fuel Process. Technol. 137 (2015) 204–211. https://doi.org/10.1016/j.fuproc.2015.04.022.

[178] L. Bian, L. Zhang, Z. Zhu, Z. Li, Methanation of carbon oxides on Ni/Ce/SBA-15 pretreated with dielectric barrier discharge plasma, Mol. Catal. 446 (2018) 131–139. https://doi.org/10.1016/j.mcat.2017.12.027.

[179] P. Hongmanorom, J. Ashok, G. Zhang, Z. Bian, M.H. Wai, Y. Zeng, S. Xi, A. Borgna, S. Kawi, Enhanced performance and selectivity of CO2 methanation over phyllosilicate structure derived Ni-Mg/SBA-15 catalysts, Appl. Catal. B Environ. 282 (2021) 119564. https://doi.org/10.1016/j.apcatb.2020.119564.

[180] H.S. Lim, G. Kim, Y. Kim, M. Lee, D. Kang, H. Lee, J.W. Lee, Ni-exsolved La1-xCaxNiO3 perovskites for improving CO2 methanation, Chem. Eng. J. 412 (2021) 127557. https://doi.org/10.1016/j.cej.2020.127557.

[181] S.N. Bukhari, C.C. Chong, H.D. Setiabudi, N. Ainirazali, M.A.A. Aziz, A.A. Jalil, S.Y. Chin, Optimal Ni loading towards efficient CH4 production from H2 and CO2 over Ni supported onto fibrous SBA-15, Int. J. Hydrogen Energy. 44 (2019) 7228–7240. https://doi.org/10.1016/j.ijhydene.2019.01.259.

[182] C.S. Chen, C.S. Budi, H.C. Wu, D. Saikia, H.M. Kao, Size-Tunable Ni Nanoparticles Supported on Surface-Modified, Cage-Type Mesoporous Silica as Highly Active Catalysts for CO2 Hydrogenation, ACS Catal. 7 (2017) 8367–8381. https://doi.org/10.1021/acscatal.7b02310.

[183] P. Burattin, M. Che, C. Louis, Metal particle size in Ni/SiO2 materials prepared by deposition-precipitation: Influence of the nature of the Ni(II) phase and of its interaction with the support, J. Phys. Chem. B. 103 (1999) 6171–6178. https://doi.org/10.1021/jp990115t.

[184] M.A.A. Aziz, A.A. Jalil, S. Triwahyono, M.W.A. Saad, CO2 methanation over Ni-promoted mesostructured silica nanoparticles: Influence of Ni loading and water vapor on activity and response surface methodology studies, Chem. Eng. J. 260 (2015) 757–764. https://doi.org/10.1016/j.cej.2014.09.031.

[185] S. Rahmani, M. Rezaei, F. Meshkani, Preparation of highly active nickel catalysts supported on mesoporous nanocrystalline γ-Al2O3 for CO2 methanation, J. Ind. Eng. Chem. 20 (2014) 1346–1352. https://doi.org/10.1016/j.jiec.2013.07.017.

[186] G. Li, L. Hu, J.M. Hill, Comparison of reducibility and stability of alumina-supported Ni catalysts prepared by impregnation and co-precipitation, Appl. Catal. A Gen. 301 (2006) 16–24. https://doi.org/10.1016/j.apcata.2005.11.013.

[187] Y. Yan, Y. Dai, Y. Yang, A.A. Lapkin, Improved stability of Y2O3 supported Ni catalysts for CO2 methanation by precursor-determined metal-support interaction, Appl. Catal. B Environ. 237 (2018) 504–512. https://doi.org/10.1016/j.apcatb.2018.06.021.

[188] Y. Lv, Z. Xin, X. Meng, M. Tao, Z. Bian, Ni based catalyst supported on KIT-6 silica for CO methanation: Confinement effect of three dimensional channel on NiO and Ni particles, Microporous Mesoporous Mater. 262 (2018) 89–97. https://doi.org/10.1016/j.micromeso.2017.06.022.

[189] B. Lu, Y. Ju, T. Abe, K. Kawamoto, Grafting Ni particles onto SBA-15 , and their enhanced performance for CO2 methanation, RSC Adv. 5 (2015) 56444–56454. https://doi.org/10.1039/c5ra07461d.

[190] Y. Park, T. Kang, J. Lee, P. Kim, H. Kim, J. Yi, Single-step preparation of Ni catalysts supported on mesoporous silicas (SBA-15 and SBA-16) and the effect of pore structure on the selective hydrodechlorination of 1,1,2-trichloroethane to VCM, Catal. Today. 97 (2004) 195–203. https://doi.org/10.1016/j.cattod.2004.03.070.

[191] S. Tada, T. Shimizu, H. Kameyama, T. Haneda, R. Kikuchi, Ni/CeO2 catalysts with high CO2 methanation activity and high CH4 selectivity at low temperatures, Int. J. Hydrogen Energy. 37 (2012) 5527–5531. https://doi.org/10.1016/j.ijhydene.2011.12.122.

[192] G. Zhou, H. Liu, K. Cui, H. Xie, Z. Jiao, G. Zhang, K. Xiong, X. Zheng, Methanation of carbon dioxide over Ni/CeO2 catalysts: Effects of support CeO2 structure, Int. J. Hydrogen Energy. 42 (2017) 16108–16117. https://doi.org/10.1016/j.ijhydene.2017.05.154.

[193] R.K. Singha, A. Yadav, A. Agrawal, A. Shukla, S. Adak, T. Sasaki, R. Bal, Synthesis of highly coke resistant Ni nanoparticles supported MgO/ZnO catalyst for reforming of methane with carbon dioxide, Appl. Catal. B Environ. 191 (2016) 165–178. https://doi.org/10.1016/j.apcatb.2016.03.029.

[194] R.K. Singha, A. Shukla, A. Yadav, L.N. Sivakumar Konathala, R. Bal, Effect of metal-support interaction on activity and stability of Ni-CeO2 catalyst for partial oxidation of methane, Appl. Catal. B Environ. 202 (2017) 473–488. https://doi.org/10.1016/j.apcatb.2016.09.060.

[195] S. Lin, Z. Hao, J. Shen, X. Chang, S. Huang, M. Li, X. Ma, Enhancing the CO2 methanation activity of Ni/CeO2 via activation treatment-determined metal-support interaction, J. Energy Chem. 59 (2021) 334–342. https://doi.org/10.1016/j.jechem.2020.11.011.

[196] Z. Bian, Y.M. Chan, Y. Yu, S. Kawi, Morphology dependence of catalytic properties of Ni/CeO2 for CO2 methanation: A kinetic and mechanism study, Catal. Today. 347 (2018) 31–38. https://doi.org/10.1016/j.cattod.2018.04.067.

[197] T.A. Le, M.S. Kim, S.H. Lee, T.W. Kim, E.D. Park, CO and CO2 methanation over supported Ni catalysts, Catal. Today. 293–294 (2017) 89–96. https://doi.org/10.1016/j.cattod.2016.12.036.

[198] H. Muroyama, Y. Tsuda, T. Asakoshi, H. Masitah, T. Okanishi, T. Matsui, Carbon dioxide methanation over Ni catalysts supported on various metal oxides, J. Catal. 343 (2016) 178–184. https://doi.org/10.1016/j.jcat.2016.07.018.

[199] A. Loder, M. Siebenhofer, S. Lux, The reaction kinetics of CO2 methanation on a bifunctional Ni/MgO catalyst, J. Ind. Eng. Chem. 85 (2020) 196–207. https://doi.org/10.1016/j.jiec.2020.02.001.

[200] Q. Pan, J. Peng, S.S. Wang, S.S. Wang, In situ FTIR spectroscopic study of the CO2 methanation mechanism on Ni/Ce0.5Zr0.5O2, Catal. Sci. Technol. 4 (2014) 502–509. https://doi.org/10.1039/c3cy00868a.

[201] M. Romero-Sáez, A.B. Dongil, N. Benito, R. Espinoza-González, N. Escalona, F. Gracia, CO2 methanation over nickel-ZrO2 catalyst supported on carbon nanotubes: A comparison between two impregnation strategies, Appl. Catal. B Environ. 237 (2018) 817–825. https://doi.org/10.1016/j.apcatb.2018.06.045.

[202] M.C. Bacariza, S. Amjad, P. Teixeira, J.M. Lopes, C. Henriques, Boosting Ni Dispersion on Zeolite-Supported Catalysts for CO2 Methanation: The Influence of the Impregnation Solvent, Energy and Fuels. 34 (2020) 14656–14666. https://doi.org/10.1021/acs.energyfuels.0c02561.

[203] H. Lu, X. Yang, G. Gao, J. Wang, C. Han, X. Liang, C. Li, Y. Li, W. Zhang, X. Chen, Metal (Fe, Co, Ce or La) doped nickel catalyst supported on ZrO2 modified mesoporous clays for CO and CO2 methanation, Fuel. 183 (2016) 335–344. https://doi.org/10.1016/j.fuel.2016.06.084.

[204] C.S. Budi, H.C. Wu, C.S. Chen, D. Saikia, H.M. Kao, Ni Nanoparticles Supported on Cage-Type Mesoporous Silica for CO2 Hydrogenation with High CH4 Selectivity, ChemSusChem. 9 (2016) 2326–2331. https://doi.org/10.1002/cssc.201600710.

[205] D. Wierzbicki, M.V. Moreno, S. Ognier, M. Motak, T. Grzybek, P. Da Costa, M.E. Gálvez, Ni-Fe layered double hydroxide derived catalysts for non-plasma and DBD plasma-assisted CO2 methanation, Int. J. Hydrogen Energy. 45 (2020) 10423–10432. https://doi.org/10.1016/j.ijhydene.2019.06.095.

[206] D. Wierzbicki, M. Motak, T. Grzybek, M.E. Gálvez, P. Da Costa, The influence of lanthanum incorporation method on the performance of nickel-containing hydrotalcite-derived catalysts in CO2 methanation reaction, Catal. Today. 307 (2018) 205–211. https://doi.org/10.1016/j.cattod.2017.04.020.

[207] P. Marocco, E.A. Morosanu, E. Giglio, D. Ferrero, C. Mebrahtu, A. Lanzini, S. Abate, S. Bensaid, S. Perathoner, M. Santarelli, R. Pirone, G. Centi, CO2 methanation over Ni/Al hydrotalcite-derived catalyst: Experimental characterization and kinetic study, Fuel. 225 (2018) 230–242. https://doi.org/10.1016/j.fuel.2018.03.137.

[208] D. Wierzbicki, R. Debek, M. Motak, T. Grzybek, M.E. Gálvez, P. Da Costa, Novel Ni-La-hydrotalcite derived catalysts for CO2 methanation, Catal. Commun. 83 (2016) 5–8. https://doi.org/10.1016/j.catcom.2016.04.021.

[209] L. Atzori, E. Rombi, D. Meloni, R. Monaci, M.F. Sini, M.G. Cutrufello, Nanostructured Ni/CeO2 –ZrO2 Catalysts for CO2 Conversion into Synthetic Natural Gas, J. Nanosci. Nanotechnol. 19 (2019) 3269–3276. https://doi.org/10.1166/jnn.2019.16612.

[210] C. Italiano, J. Llorca, L. Pino, M. Ferraro, V. Antonucci, A. Vita, CO and CO2 methanation over Ni catalysts supported on CeO2, Al2O3 and Y2O3 oxides, Appl. Catal. B Environ. 264 (2020) 118494. https://doi.org/10.1016/j.apcatb.2019.118494.

[211] Q. Pan, J. Peng, S. Wang, S. Wang, In situ FTIR spectroscopic study of the CO2 methanation mechanism on Ni/Ce0.5Zr0.5O2, Catal. Sci. Technol. 4 (2014) 502–509. https://doi.org/10.1039/c3cy00868a.

[212] X. Lin, S. Wang, MOF-derived hierarchical hollow spheres composed of carbon-confined Ni nanoparticles for efficient CO2 methanation, Catal. Sci. Technol. 9 (2019) 731–738. https://doi.org/10.1039/c8cy02329h.

[213] M. Mihet, M.D. Lazar, Methanation of CO2 on Ni/γ-Al2O3: Influence of Pt, Pd or Rh promotion, Catal. Today. 306 (2018) 294–299. https://doi.org/10.1016/j.cattod.2016.12.001.

[214] Garbarino Gabriella, Riani Paola, M. Loredana, Busca Guido, A study of the methanation of carbon dioxide on Ni/Al2O3 catalysts at atmospheric pressure, Int. J. Hydrogen Energy. 39 (2014) 11557–11565. https://doi.org/http://dx.doi.org/10.1016/j.ijhydene.2014.05.111.

[215] Y. Varun, I. Sreedhar, S.A. Singh, Highly stable M/NiO–MgO (M = Co, Cu and Fe) catalysts towards CO2 methanation, Int. J. Hydrogen Energy. 45 (2020) 28716–28731. https://doi.org/10.1016/j.ijhydene.2020.07.212.

[216] R. Zhou, N. Rui, Z. Fan, C. Liu, Effect of the structure of Ni/TiO2 catalyst on CO2 methanation, Int. J. Hydrogen Energy. 41 (2016) 22017–22025. https://doi.org/10.1016/j.ijhydene.2016.08.093.

[217] Y.R. Dias, O.W. Perez-Lopez, Carbon dioxide methanation over Ni-Cu/SiO2 catalysts, Energy Convers. Manag. 203 (2020) 112214. https://doi.org/10.1016/j.enconman.2019.112214.

[218] G. Tang, D. Gong, H. Liu, L. Wang, Highly Loaded Mesoporous Ni–La2O3 Catalyst Prepared by Colloidal Solution Combustion Method for CO2 Methanation, Catalysts. 9 (2019) 442. https://doi.org/doi:10.3390/catal9050442.

[219] J. Ashok, M.L. Ang, S. Kawi, Enhanced activity of CO2 methanation over Ni/CeO2-ZrO2 catalysts: Influence of preparation methods, Catal. Today. 281 (2017) 304–311. https://doi.org/10.1016/j.cattod.2016.07.020.

[220] X. Wang, L. Zhu, Y. Liu, S. Wang, CO2 methanation on the catalyst of Ni/MCM-41 promoted with CeO2, Sci. Total Environ. 625 (2018) 686–695. https://doi.org/10.1016/j.scitotenv.2017.12.308.

[221] M.C. Bacariza, I. Graça, S.S. Bebiano, J.M. Lopes, C. Henriques, Micro- and mesoporous supports for CO2 methanation catalysts: A comparison between SBA-15, MCM-41 and USY zeolite, Chem. Eng. Sci. 175 (2018) 72–83. https://doi.org/10.1016/j.ces.2017.09.027.

[222] F. Ocampo, B. Louis, L. Kiwi-Minsker, A.C. Roger, Effect of Ce/Zr composition and noble metal promotion on nickel based CexZr1-xO2 catalysts for carbon dioxide methanation, Appl. Catal. A Gen. 392 (2011) 36–44. https://doi.org/10.1016/j.apcata.2010.10.025.

[223] T. Zhang, Q. Liu, Lanthanum-Modified MCF-Derived Nickel Phyllosilicate Catalyst for Enhanced CO2 Methanation: A Comprehensive Study, ACS Appl. Mater. Interfaces. 12 (2020) 19587–19600. https://doi.org/10.1021/acsami.0c03243.

[224] L. Wang, H. Liu, H. Ye, R. Hu, S. Yang, G. Tang, K. Li, Y. Yang, Vacuum thermal treated Ni-CeO2/SBA-15 catalyst for CO2 methanation, Nanomaterials. 8 (2018) 1–10. https://doi.org/10.3390/nano8100759.

[225] A. Westermann, B. Azambre, M.C. Bacariza, I. Graça, M.F. Ribeiro, J.M. Lopes, C. Henriques, The promoting effect of Ce in the CO2 methanation performances on NiUSY zeolite: A FTIR In Situ/Operando study, Catal. Today. 283 (2017) 74–81. https://doi.org/10.1016/j.cattod.2016.02.031.

[226] I. Iglesias, A. Quindimil, F. Mariño, U. De-La-Torre, J.R. González-Velasco, Zr promotion effect in CO2 methanation over ceria supported nickel catalysts, Int. J. Hydrogen Energy. 44 (2019) 1710–1719. https://doi.org/10.1016/j.ijhydene.2018.11.059.

[227] H. Takano, Y. Kirihata, K. Izumiya, N. Kumagai, H. Habazaki, K. Hashimoto, Highly active Ni/Y-doped ZrO2 catalysts for CO2 methanation, Appl. Surf. Sci. 388 (2016) 653–663. https://doi.org/10.1016/j.apsusc.2015.11.187.

[228] Q. Liu, B. Bian, J. Fan, J. Yang, Cobalt doped Ni based ordered mesoporous catalysts for CO2 methanation with enhanced catalytic performance, Int. J. Hydrogen Energy. 43 (2018) 4893–4901. https://doi.org/10.1016/j.ijhydene.2018.01.132.

[229] J. Ren, X. Qin, J.Z. Yang, Z.F. Qin, H.L. Guo, J.Y. Lin, Z. Li, Methanation of carbon dioxide over Ni-M/ZrO<inf>2</inf> (M = Fe, Co, Cu) catalysts: Effect of addition of a second metal, Fuel Process. Technol. 137 (2015) 204–211. https://doi.org/10.1016/j.fuproc.2015.04.022.

[230] J. Guilera, J. Del Valle, A. Alarcón, J.A. Díaz, T. Andreu, Metal-oxide promoted Ni/Al2O3 as CO2 methanation micro-size catalysts, J. CO2 Util. 30 (2019) 11–17. https://doi.org/10.1016/j.jcou.2019.01.003.

[231] G. Garbarino, C. Wang, T. Cavattoni, E. Finocchio, P. Riani, M. Flytzani-Stephanopoulos, G. Busca, A study of Ni/La-Al2O3 catalysts: A competitive system for CO2 methanation, Appl. Catal. B Environ. 248 (2019) 286–297. https://doi.org/10.1016/j.apcatb.2018.12.063.

[232] M.J. Kim, J.R. Youn, H.J. Kim, M.W. Seo, D. Lee, K.S. Go, K.B. Lee, S.G. Jeon, Effect of surface properties controlled by Ce addition on CO2 methanation over Ni/Ce/Al2O3 catalyst, Int. J. Hydrogen Energy. 45 (2020) 24595–24603. https://doi.org/10.1016/j.ijhydene.2020.06.144.

[233] M. Yang, Z. Lingjun, Z. Xiaonan, R. Prasert, W. Shurong, CO2 methanation over nickel-based catalysts supported on MCM-41 with in situ doping of zirconium, J. CO2 Util. 42 (2020) 101304. https://doi.org/10.1016/j.jcou.2020.101304.

[234] T.A. Le, J. Kim, J.K. Kang, E.D. Park, CO and CO2 methanation over M (M=Mn, Ce, Zr, Mg, K, Zn, or V)-promoted Ni/Al@Al2O3 catalysts, Catal. Today. 348 (2020) 80–88. https://doi.org/10.1016/j.cattod.2019.08.058.

[235] L. Xu, H. Yang, M. Chen, F. Wang, D. Nie, L. Qi, X. Lian, H. Chen, M. Wu, CO2 methanation over Ca doped ordered mesoporous Ni-Al composite oxide catalysts: The promoting effect of basic modifier, J. CO2 Util. 21 (2017) 200–210. https://doi.org/10.1016/j.jcou.2017.07.014.

[236] O. La, M. Mihet, M. Dan, L. Barbu-tudoran, M.D. Lazar, CO2 Methanation Using Multimodal Ni/SiO2 Catalysts: Effect of Support Modification by MgO, CeO2, and La2O3, Catalysts. 11 (2021) 443. https://doi.org/https://doi.org/10.3390/catal11040443.

[237] C. Mebrahtu, F. Krebs, S. Perathoner, S. Abate, G. Centi, R. Palkovits, Hydrotalcite based Ni-Fe/(Mg, Al)OX catalysts for CO2 methanation-tailoring Fe content for improved CO dissociation, basicity, and particle size, Catal. Sci. Technol. 8 (2018) 1016–1027.

[238] T. Burger, F. Koschany, O. Thomys, K. Köhler, O. Hinrichsen, CO2 methanation over Fe- and Mn-promoted co-precipitated Ni-Al catalysts: Synthesis, characterization and catalysis study, Appl. Catal. A Gen. 558 (2018) 44–54. https://doi.org/10.1016/j.apcata.2018.03.021.

[239] X. Lu, F. Gu, Q. Liu, J. Gao, Y. Liu, H. Li, L. Jia, G. Xu, Z. Zhong, F. Su, VOx promoted Ni catalysts supported on the modified bentonite for CO and CO2 methanation, Fuel Process. Technol. 135 (2015) 34–46. https://doi.org/10.1016/j.fuproc.2014.10.009.

[240] K. Liu, X. Xu, J. Xu, X. Fang, L. Liu, X. Wang, The distributions of alkaline earth metal oxides and their promotional effects on Ni/CeO2 for CO2 methanation, J. CO2 Util. 38 (2020) 113–124. https://doi.org/10.1016/j.jcou.2020.01.016.

[241] M.C. Le, K. Le Van, T.H.T. Nguyen, N.H. Nguyen, The Impact of Ce-Zr Addition on Nickel Dispersion and Catalytic Behavior for CO2 Methanation of Ni/AC Catalyst at Low Temperature, Hindawi J. Chem. (2017) 4361056. https://doi.org/10.1155/2017/4361056.

[242] S. Li, G. Liu, S. Zhang, K. An, Z. Ma, L. Wang, Y. Liu, Cerium-modified Ni-La2O3/ZrO2 for CO2 methanation, J. Energy Chem. 43 (2020) 155–164. https://doi.org/10.1016/j.jechem.2019.08.024.

[243] S. Abate, C. Mebrahtu, E. Giglio, F. Deorsola, S. Bensaid, S. Perathoner, R. Pirone, G. Centi, Catalytic Performance of γ-Al2O3-ZrO2-TiO2-CeO2 Composite Oxide Supported Ni-Based Catalysts for CO2 Methanation, Ind. Eng. Chem. Res. 55 (2016) 4451–4460. https://doi.org/10.1021/acs.iecr.6b00134.

[244] G. Zhou, T. Wu, H. Zhang, H. Xie, Y. Feng, Carbon Dioxide Methanation on Ordered Mesoporous Co/Kit-6 Catalyst, Chem. Eng. Commun. 201 (2014) 233–240. https://doi.org/10.1080/00986445.2013.766881.

[245] D. Jampaiah, D. Damma, A. Chalkidis, P. Venkataswamy, S.K. Bhargava, B.M. Reddy, MOF-derived ceria-zirconia supported Co3O4 catalysts with enhanced activity in CO2 methanation, Catal. Today. 356 (2020) 519–526. https://doi.org/10.1016/j.cattod.2020.05.047.

[246] R. Razzaq, H. Zhu, L. Jiang, U. Muhammad, C. Li, S. Zhang, Catalytic methanation of CO and CO2 in coke oven gas over Ni-Co/ZrO2-CeO2, Ind. Eng. Chem. Res. 52 (2013) 2247–2256. https://doi.org/10.1021/ie301399z.

[247] J. Ma, Q. Li, M. Kühn, N. Nakaten, Power-to-gas based subsurface energy storage: A review, Renew. Sustain. Energy Rev. 97 (2018) 478–496.

https://doi.org/10.1016/j.rser.2018.08.056.

[248] M. Thema, F. Bauer, M. Sterner, Power-to-Gas: Electrolysis and methanation status review, Renew. Sustain. Energy Rev. 112 (2019) 775–787. https://doi.org/10.1016/j.rser.2019.06.030.

[249] D. Jovanovic, R. Radovic, L. Mares, M. Stankovic, B. Markovic, Nickel hydrogenation catalyst for tallow hydrogenation and for the selective hydrogenation of sunflower seed oil and soybean oil, Catal. Today. 43 (1998) 21–28. https://doi.org/10.1016/S0920-5861(98)00133-3.

[250] K. Świrk, M.E. Gálvez, M. Motak, T. Grzybek, M. Rønning, P. Da Costa, Yttrium promoted Ni-based double-layered hydroxides for dry methane reforming, J. CO2 Util. 27 (2018) 247–258. https://doi.org/10.1016/j.jcou.2018.08.004.

[251] Y.F. Han, F. Chen, Z. Zhong, K. Ramesh, L. Chen, E. Widjaja, Controlled synthesis, characterization, and catalytic properties of Mn2O3 and Mn3O4 nanoparticles supported on mesoporous silica SBA-15, J. Phys. Chem. B. 110 (2006) 24450–24456. https://doi.org/10.1021/jp064941v.

[252] T.W. Kim, R. Ryoo, M. Kruk, K.P. Gierszal, M. Jaroniec, S. Kamiya, O. Terasaki, Tailoring the pore structure of SBA-16 silica molecular sieve through the use of copolymer blends and control of synthesis temperature and time, J. Phys. Chem. B. 108 (2004) 11480–11489. https://doi.org/10.1021/jp048582k.

[253] A. Albarazi, M.E. Gálvez, P. Da Costa, Synthesis strategies of ceria-zirconia doped Ni/SBA-15 catalysts for methane dry reforming, Catal. Commun. 59 (2015) 108–112. https://doi.org/10.1016/j.catcom.2014.09.050.

[254] M.N. Kaydouh, N. El, A. Davidson, S. Casale, H. El, P. Massiani, N. El Hassan, A. Davidson, S. Casale, H. El Zakhem, P. Massiani, Effect of the order of Ni and Ce addition in SBA-15 on the activity in dry reforming of methane, Comptes Rendus - Chim. 18 (2015) 293–301. https://doi.org/10.1016/j.crci.2015.01.004.

[255] M. Tao, X. Meng, Y. Lv, Z. Bian, Z. Xin, Effect of impregnation solvent on Ni dispersion and catalytic properties of Ni/SBA-15 for CO methanation reaction, Fuel. 165 (2016) 289–297. https://doi.org/10.1016/j.fuel.2015.10.023.

[256] W. Shan, M. Luo, P. Ying, W. Shen, C. Li, Reduction property and catalytic activity of Ce1-XNiXO2 mixed oxide catalysts for CH4 oxidation, Appl. Catal. A Gen. 246 (2003) 1–9. https://doi.org/10.1016/S0926-860X(02)00659-2.

[257] J.A.H. Dreyer, P. Li, L. Zhang, G.K. Beh, R. Zhang, P.H.L. Sit, W.Y. Teoh, Influence of the oxide support reducibility on the CO2 methanation over Ru-based catalysts, Appl. Catal. B Environ. 219 (2017) 715–726. https://doi.org/10.1016/j.apcatb.2017.08.011.

[258] A. Quindimil, U. De-La-Torre, B. Pereda-Ayo, J.A. González-Marcos, J.R. González-Velasco, Ni catalysts with La as promoter supported over Y- and BETA- zeolites for CO2 methanation, Appl. Catal. B Environ. 238 (2018) 393–403.

https://doi.org/10.1016/j.apcatb.2018.07.034.

[259] A.S. Al-Fatesh, M.A. Naeem, A.H. Fakeeha, A.E. Abasaeed, Role of La2O3 as promoter and support in Ni/γ-Al2O3 catalysts for dry reforming of methane, Chinese J. Chem. Eng. 22 (2014) 28–37. https://doi.org/10.1016/S1004-9541(14)60029-X.

[260] L.J.I. Coleman, W. Epling, R.R. Hudgins, E. Croiset, Ni/Mg-Al mixed oxide catalyst for the steam reforming of ethanol, Appl. Catal. A Gen. 363 (2009) 52–63. https://doi.org/10.1016/j.apcata.2009.04.032.

[261] S. Brunauer, P.H. Emmett, The Use of Low Temperature van der Waals Adsorption Isotherms in Determining the Surface Areas of Various Adsorbents, J. Am. Chem. Soc. 59 (1937) 2682–2689. https://doi.org/10.1021/ja01291a060.

[262] M. Wei, L. Zhang, Y. Xiong, J. Li, P. Peng, Nanopore structure characterization for organic-rich shale using the non-local-density functional theory by a combination of N2 and CO2 adsorption, Microporous Mesoporous Mater. 227 (2016) 88–94. https://doi.org/10.1016/j.micromeso.2016.02.050.

[263] R. Bardestani, G.S. Patience, S. Kaliaguine, Experimental methods in chemical engineering: specific surface area and pore size distribution measurements—BET, BJH, and DFT, Can. J. Chem. Eng. 97 (2019) 2781–2791. https://doi.org/10.1002/cjce.23632.

[264] L.D. Gelb, K.E. Gubbins, Pore Size Distributions in Porous Glasses: A Computer Simulation Study, Langmuir. 15 (1999) 305–308. https://doi.org/10.1021/la9808418.

[265] M.M. Labani, R. Rezaee, A. Saeedi, A. Al Hinai, Evaluation of pore size spectrum of gas shale reservoirs using low pressure nitrogen adsorption, gas expansion and mercury porosimetry: A case study from the Perth and Canning Basins, Western Australia, J. Pet. Sci. Eng. 112 (2013) 7–16. https://doi.org/10.1016/j.petrol.2013.11.022.

[266] D.G. Mustard, C.H. Bartholomew, Determination of metal crystallite size and morphology in supported nickel catalysts, J. Catal. 67 (1981) 186–206. https://doi.org/10.1016/0021-9517(81)90271-2.

[267] T.A. Le, T.W. Kim, S.H. Lee, E.D. Park, Effects of Na content in Na/Ni/SiO2 and Na/Ni/CeO2 catalysts for CO and CO2 methanation, Catal. Today. 303 (2018) 159–167. https://doi.org/10.1016/j.cattod.2017.09.031.

[268] M.A. Moram, M.E. Vickers, X-ray diffraction of III-nitrides, Reports Prog. Phys. 72 (2009) 036502. https://doi.org/10.1088/0034-4885/72/3/036502.

[269] C. Song, Global challenges and strategies for control, conversion and utilization of CO2 for sustainable development involving energy, catalysis, adsorption and chemical processing, Catal. Today. 115 (2006) 2–32. https://doi.org/10.1016/j.cattod.2006.02.029.

[270] Q. Zhu, Developments on CO2-utilization technologies, Clean Energy. 3 (2019) 85–100. https://doi.org/10.1093/ce/zkz008.

[271] W. Wang, J. Gong, Methanation of carbon dioxide: An overview, Front. Chem. Sci. Eng.

5 (2011) 2–10. https://doi.org/10.1007/s11705-010-0528-3.

[272] D. Chery, V. Lair, M. Cassir, Overview on CO2 Valorization: Challenge of Molten Carbonates, Front. Energy Res. 3 (2015) 1–10. https://doi.org/10.3389/fenrg.2015.00043.

[273] W. Zhang, S. Yang, J. Li, W. Gao, Y. Deng, W. Dong, C. Zhao, G. Lu, Visible-to-ultraviolet Upconvertion: Energy transfer, material matrix, and synthesis strategies, Appl. Catal. B Environ. 206 (2017) 89–103. https://doi.org/10.1016/j.apcatb.2017.01.023.

[274] W. Zhen, F. Gao, B. Tian, P. Ding, Y. Deng, Z. Li, H. Gao, G. Lu, Enhancing activity for carbon dioxide methanation by encapsulating (1 1 1) facet Ni particle in metal–organic frameworks at low temperature, J. Catal. 348 (2017) 200–211. https://doi.org/10.1016/j.jcat.2017.02.031.

[275] C. Liang, X. Hu, T. Wei, P. Jia, Z. Zhang, Methanation of CO2 over Ni/Al2O3 modified with alkaline earth metals : Impacts of oxygen vacancies on catalytic activity, Int. J. Hydrogen Energy. 44 (2019) 8197–8213. https://doi.org/10.1016/j.ijhydene.2019.02.014.

[276] F. Solymosi, A. Erdöhelyi, T. Bánsági, Methanation of CO2 on Supported Rhodium Catalyst, J. Catal. 68 (1981) 371–382. https://doi.org/https://doi.org/10.1016/0021-9517(81)90106-8.

[277] S. Tada, O.J. Ochieng, R. Kikuchi, T. Haneda, H. Kameyama, Promotion of CO2methanation activity and CH4selectivity at low temperatures over Ru/CeO2/Al2O3catalysts, Int. J. Hydrogen Energy. 39 (2014) 10090–10100. https://doi.org/10.1016/j.ijhydene.2014.04.133.

[278] N.A.A. Fatah, A.A. Jalil, A.F.A. Rahman, H.U. Hambali, I. Hussain, CO2 Methanation over Mesoporous Silica Based Catalyst : A Comprehensive Study, J. Energy Saf. Technol. 02 (2019) 49–53.

[279] A. Beuls, C. Swalus, M. Jacquemin, G. Heyen, A. Karelovic, P. Ruiz, Methanation of CO2 : Further insight into the mechanism over Rh/Al2O3 catalyst, Appl. Catal. B, Environ. Environ. 113–114 (2012) 2–10. https://doi.org/10.1016/j.apcatb.2011.02.033.

[280] P. Panagiotopoulou, D.I. Kondarides, X.E. Verykios, Selective methanation of CO over supported noble metal catalysts: Effects of the nature of the metallic phase on catalytic performance, Appl. Catal. A Gen. 344 (2008) 45–54.

[281] K. Yaccato, R. Carhart, A. Hagemeyer, A. Lesik, P. Strasser, A.F. Volpe, H. Turner, H. Weinberg, R.K. Grasselli, C. Brooks, Competitive CO and CO2 methanation over supported noble metal catalysts in high throughput scanning mass spectrometer, Appl. Catal. A Gen. 296 (2005) 30–48. https://doi.org/10.1016/j.apcata.2005.07.052.

[282] P. Frontera, A. Macario, M. Ferraro, P. Antonucci, Supported Catalysts for CO2 Methanation: A Review, Catalysts. 7 (2017) 59. https://doi.org/10.3390/catal7020059.

[283] N. Czuma, K. Zarębska, M. Motak, M.E. Gálvez, P. Da Costa, Ni/zeolite X derived from fly ash as catalysts for CO2 methanation, Fuel. 267 (2020). https://doi.org/10.1016/j.fuel.2020.117139.

[284] I. Sreedhar, Y. Varun, S.A. Singh, A. Venugopal, B.M. Reddy, Developmental trends in CO2 methanation using various catalysts, Catal. Sci. Technol. 9 (2019) 4478–4504. https://doi.org/10.1039/c9cy01234f.

[285] J.R.G.-V. Ignacio Iglesias, Adrian Quindimil, Fernando Marino, Unai De-La-Torre, Zr promotion effect in CO2 methanation over ceria supported nickel catalysts, Int. J. Hydrogen Energy. 44 (2019) 1710–1719. https://doi.org/10.1016/j.ijhydene.2018.11.059.

[286] W.L. Vrijburg, G. Garbarino, W. Chen, A. Parastaev, A. Longo, E.A. Pidko, E.J.M. Hensen, Ni-Mn catalysts on silica-modified alumina for CO2 methanation, J. Catal. 382 (2020) 358–371. https://doi.org/10.1016/j.jcat.2019.12.026.

[287] K. Yatagai, Y. Shishido, R. Gemma, T. Boll, H.H. Uchida, K. Oguri, Mechanochemical CO2 methanation over LaNi-based alloys, Int. J. Hydrogen Energy. 45 (2020) 5264–5275. https://doi.org/10.1016/j.ijhydene.2019.07.055.

[288] O.E. Everett, P.C. Zonetti, O.C. Alves, R.R. de Avillez, L.G. Appel, The role of oxygen vacancies in the CO2 methanation employing Ni/ZrO2 doped with Ca, Int. J. Hydrogen Energy. 45 (2020) 6352–6359. https://doi.org/10.1016/j.ijhydene.2019.12.140.

[289] T. Zhang, Q. Liu, Mesostructured cellular foam silica supported bimetallic LaNi1-xCoxO3 catalyst for CO2 methanation, Int. J. Hydrogen Energy. 45 (2020) 4417–4426. https://doi.org/10.1016/j.ijhydene.2019.12.006.

[290] B. Mutz, M. Belimov, W. Wang, P. Sprenger, M.A. Serrer, D. Wang, P. Pfeifer, W. Kleist, J.D. Grunwaldt, Potential of an alumina-supported Ni3Fe catalyst in the methanation of CO2: Impact of alloy formation on activity and stability, ACS Catal. 7 (2017) 6802–6814. https://doi.org/10.1021/acscatal.7b01896.

[291] M. Guo, G. Lu, The effect of impregnation strategy on structural characters and CO2 methanation properties over MgO modified Ni/SiO2 catalysts, Catal. Commun. 54 (2014) 55–60. https://doi.org/10.1016/j.catcom.2014.05.022.

[292] M.M. Nair, S. Kaliaguine, F. Kleitz, Nanocast LaNiO3 perovskites as precursors for the preparation of coke-resistant dry reforming catalysts, ACS Catal. 4 (2014) 3837–3846. https://doi.org/10.1021/cs500918c.

[293] K. Jabbour, N. El Hassan, A. Davidson, P. Massiani, S. Casale, Characterizations and performances of Ni/diatomite catalysts for dry reforming of methane, Chem. Eng. J. 264 (2015) 351–358. https://doi.org/10.1016/j.cej.2014.11.109.

[294] S. Dehestaniathar, M. Khajelakzay, M. Ramezani-Farani, H. Ijadpanah-Saravi, Modified diatomite-supported CuO-TiO2 composite: Preparation, characterization and catalytic CO oxidation, J. Taiwan Inst. Chem. Eng. 58 (2016) 252–258. https://doi.org/10.1016/j.jtice.2015.05.030.

[295] H. Liang, S. Zhou, Y. Chen, F. Zhou, C. Yan, Diatomite coated with Fe2O3 as an efficient heterogeneous catalyst for degradation of organic pollutant, J. Taiwan Inst. Chem. Eng. 49 (2015) 105–112. https://doi.org/10.1016/j.jtice.2014.11.002.

[296] R. Shan, C. Zhao, H. Yuan, S. Wang, Y. Wang, Transesterification of vegetable oil using stable natural diatomite-supported catalyst, Energy Convers. Manag. 138 (2017) 547–555. https://doi.org/10.1016/j.enconman.2017.02.028.

[297] M. Stanković, M. Gabrovska, J. Krstić, P. Tzvetkov, M. Shopska, T. Tsacheva, P. Banković, R. Edreva-Kardjieva, D. Jovanović, Effect of silver modification on structure and catalytic performance of Ni-Mg/diatomite catalysts for edible oil hydrogenation, J. Mol. Catal. A Chem. 297 (2009) 54–62. https://doi.org/10.1016/j.molcata.2008.09.004.

[298] Y. Chen, K. Liu, Fabrication of Ce/N co-doped TiO2/diatomite granule catalyst and its improved visible-light-driven photoactivity, J. Hazard. Mater. 324 (2017) 139–150. https://doi.org/10.1016/j.jhazmat.2016.10.043.

[299] Y. Chen, Q. Wu, L. Liu, J. Wang, Y. Song, The fabrication of self-floating Ti3+/N co-doped TiO2 /diatomite granule catalyst with enhanced photocatalytic performance under visible light irradiation, Appl. Surf. Sci. 467–468 (2019) 514–525. https://doi.org/10.1016/j.apsusc.2018.10.146.

[300] Z. Zhang, Z. Wang, Diatomite-Supported Pd Nanoparticles : An Efficient Catalyst for Heck and Suzuki Reactions, J. Org. Chem. 71 (2006) 7485–7487. https://doi.org/https://doi.org/10.1021/jo061179k.

[301] J. Zhang, Z. Xin, X. Meng, Y. Lv, M. Tao, Effect of MoO3 on structures and properties of Ni-SiO2 methanation catalysts prepared by the hydrothermal synthesis method, Ind. Eng. Chem. Res. 52 (2013) 14533–14544. https://doi.org/10.1021/ie401708h.

[302] X. Du, D. Zhang, L. Shi, R. Gao, J. Zhang, Morphology dependence of catalytic properties of Ni/CeO 2 nanostructures for carbon dioxide reforming of methane, J. Phys. Chem. C. 116 (2012) 10009–10016. https://doi.org/10.1021/jp300543r.

[303] B. Mile, D. Stirling, M.A. Zammitt, A. Lovell, M. Webb, The location of nickel oxide and nickel in silica-supported catalysts: Two forms of "NiO" and the assignment of temperature-programmed reduction profiles, J. Catal. 114 (1988) 217–229. https://doi.org/10.1016/0021-9517(88)90026-7.

[304] A.V. F. Cavani, F. Trifirò, F. Cavani, F. Trifirò, A. Vaccari, Hydrotalcite-type anionic clays: Preparation, properties and applications, Catal. Today. 11 (1991) 173–301. https://doi.org/10.1016/0920-5861(91)80068-K.

[305] J. Liu, W. Bing, X. Xue, F. Wang, B. Wang, S. He, Y. Zhang, M. Wei, Alkaline-assisted Ni nanocatalysts with largely enhanced low-temperature activity toward CO2 methanation, Catal. Sci. Technol. 6 (2016) 3976–3983. https://doi.org/10.1039/c5cy02026c.

[306] R. Dębek, M. Motak, M.E. Galvez, T. Grzybek, P. Da Costa, Influence of Ce/Zr molar ratio on catalytic performance of hydrotalcite-derived catalysts at low temperature CO2 methane reforming, Int. J. Hydrogen Energy. 42 (2017) 23556–23567. https://doi.org/10.1016/j.ijhydene.2016.12.121.

[307] R. Dębek, M. Radlik, M. Motak, M.E. Galvez, W. Turek, P. Da Costa, T. Grzybek, Ni-containing Ce-promoted hydrotalcite derived materials as catalysts for methane reforming with carbon dioxide at low temperature - On the effect of basicity, Catal. Today. 257 (2015) 59–65. https://doi.org/10.1016/j.cattod.2015.03.017.

[308] D. Wierzbicki, R. Dębek, J. Szczurowski, S. Basąg, M. Włodarczyk, M. Motak, R. Baran, Copper, cobalt and manganese: Modified hydrotalcite materials as catalysts for the selective catalytic reduction of NO with ammonia. the influence of manganese concentration, Comptes Rendus Chim. 18 (2015) 1074–1083.

[309] L. Chmielarz, P. Kuśtrowski, A. Rafalska-Łasocha, D. Majda, R. Dziembaj, Catalytic activity of Co-Mg-Al, Cu-Mg-Al and Cu-Co-Mg-Al mixed oxides derived from hydrotalcites in SCR of NO with ammonia, Appl. Catal. B Environ. 35 (2002) 195–210. https://doi.org/10.1016/S0926-3373(01)00254-5.

[310] G. Carja, G. Delahay, Mesoporous mixed oxides derived from pillared oxovanadates layered double hydroxides as new catalysts for the selective catalytic reduction of NO by NH3, Appl. Catal. B Environ. 47 (2004) 59–66. https://doi.org/10.1016/j.apcatb.2003.07.004.

[311] X. Wu, Y. Feng, Y. Du, X. Liu, C. Zou, Z. Li, Enhancing DeNOx performance of CoMnAl mixed metal oxides in low-temperature NH3-SCR by optimizing layered double hydroxides (LDHs) precursor template, Appl. Surf. Sci. 467–468 (2019) 802–810. https://doi.org/10.1016/j.apsusc.2018.10.191.

[312] T.T. Quoc, S.L. Du, D.P. Van, N.N. Khac, L.T. Dinh, Temporary overvoltages in the Vietnam 500 kV transmission line, Proc. IEEE Int. Conf. Transm. Distrib. Constr. Live Line Maintenance, ESMO. (1998) 225–230. https://doi.org/10.1109/tdcllm.1998.668378.

[313] R. Chai, S. Fan, Z. Zhang, P. Chen, G. Zhao, Y. Liu, Y. Lu, Free-Standing NiO-MgO-Al2O3 Nanosheets Derived from Layered Double Hydroxides Grown onto FeCrAl-Fiber as Structured Catalysts for Dry Reforming of Methane, ACS Sustain. Chem. Eng. 5 (2017) 4517–4522. https://doi.org/10.1021/acssuschemeng.7b00717.

[314] X. Zhang, C. Yang, Y. Zhang, Y. Xu, S. Shang, Y. Yin, Ni-Co catalyst derived from layered double hydroxides for dry reforming of methane, Int. J. Hydrogen Energy. 40 (2015) 16115–16126. https://doi.org/10.1016/j.ijhydene.2015.09.150.

[315] A.I. Tsyganok, T. Tsunoda, S. Hamakawa, K. Suzuki, K. Takehira, T. Hayakawa, Dry reforming of methane over catalysts derived from nickel-containing Mg-Al layered double hydroxides, J. Catal. 213 (2003) 191–203. https://doi.org/10.1016/S0021-9517(02)00047-7.

[316] K. Świrk, M. Motak, T. Grzybek, M. Rønning, P. Da Costa, Effect of low loading of yttrium on Ni-based layered double hydroxides in CO2 reforming of CH4, React. Kinet. Mech. Catal. (2018). https://doi.org/10.1007/s11144-018-1515-9.

[317] Z. Zhang, Y. Tian, L. Zhang, S. Hu, J. Xiang, Y. Wang, L. Xu, Q. Liu, S. Zhang, X. Hu, Impacts of nickel loading on properties, catalytic behaviors of Ni/Al2O3 catalysts and the

reaction intermediates formed in methanation of CO2, Int. J. Hydrogen Energy. 44 (2019) 9291–9306. https://doi.org/10.1016/j.ijhydene.2019.02.129.

[318] J. Zhou, H. Ma, C. Liu, H. Zhang, W. Ying, High temperature methanation over Ni catalysts supported on high surface area ZnxMg1-xAl2O4: Influence on Zn loading, Int. J. Hydrogen Energy. 44 (2019) 13253–13261. https://doi.org/10.1016/j.ijhydene.2019.03.197.

[319] X. Wang, T. Zhen, C. Yu, Application of Ni–Al-hydrotalcite-derived catalyst modified with Fe or Mg in CO2 methanation, Appl. Petrochemical Res. 6 (2016) 217–223.

[320] Z. Fan, K. Sun, N. Rui, B. Zhao, C.J. Liu, Improved activity of Ni/MgAl 2 O 4 for CO 2 methanation by the plasma decomposition, J. Energy Chem. 24 (2015) 655–659. http://dx.doi.org/10.1016/j.jechem.2015.09.004.

[321] Z. Fan, K. Sun, N. Rui, B. Zhao, C.J. Liu, Improved activity of Ni/MgAl 2 O 4 for CO 2 methanation by the plasma decomposition, J. Energy Chem. 24 (2015) 655–659. https://doi.org/10.1016/j.jechem.2015.09.004.

[322] D. Wierzbicki, M. Motak, T. Grzybek, M.E. Gálvez, P. Da Costa, The influence of lanthanum incorporation method on the performance of nickel-containing hydrotalcite-derived catalysts in CO2 methanation reaction, Catal. Today. 307 (2018) 205–211. https://doi.org/10.1016/j.cattod.2017.04.020.

[323] ‡ and V. Rives‡ J. M. Ferna´ndez,† C. Barriga,† M. A. Ulibarri,*,† F. M. Labajos, New Hydrotalcite-like Compounds Containing Yttrium, Chem Mater. 9 (1997) 312–318.

[324] H.R. Liu, K. Świrk, M.E. Galvez, P. da Costa, Nickel Supported Modified Ceria Zirconia Lanthanum/ Praseodymium/Yttrium Oxides Catalysts for Syngas Production through Dry Methane Reforming, Mater. Sci. Forum. 941 (2018) 2214–2219. https://doi.org/10.4028/www.scientific.net/msf.941.2214.

[325] J.D.A. Bellido, E.M. Assaf, Effect of the Y2O3-ZrO2 support composition on nickel catalyst evaluated in dry reforming of methane, Appl. Catal. A Gen. 352 (2009) 179–187.

[326] J.M. García-García, M.E. Pérez-Bernal, R.J. Ruano-Casero, V. Rives, Chromium and yttrium-doped magnesium aluminum oxides prepared from layered double hydroxides, Solid State Sci. 9 (2007) 1115–1125. https://doi.org/10.1016/j.solidstatesciences.2007.07.029.

[327] J.M. Fernández, C. Barriga, M.A. Ulibarri, F.M. Labajos, V. Rives, New Hydrotalcite-like Compounds Containing Yttrium, Chem. Mater. 9 (1997) 312–318. https://doi.org/10.1021/cm9603720.

[328] F. Kovanda, D. Koloušek, Z. Cílová, V. Hulínský, Crystallization of synthetic hydrotalcite under hydrothermal conditions, Appl. Clay Sci. 28 (2005) 101–109. https://doi.org/10.1016/j.clay.2004.01.009.

[329] J.T. Kloprogge, J. Kristóf, R.L. Frost, Thermogravimetric analysis-mass spectrometry (TGA-MS) of hydrotalcites containing CO32−, NO3−, Cl−, SO42− or ClO4−, 2003.

[330] E.A. Sánchez, M.A. D'Angelo, R.A. Comelli, Hydrogen production from glycerol on Ni/Al2O3 catalyst, Int. J. Hydrogen Energy. 35 (2010) 5902–5907. https://doi.org/10.1016/j.ijhydene.2009.12.115.

[331] L. Wang, H. Liu, Y. Liu, Y. Chen, S. Yang, Effect of precipitants on Ni-CeO2 catalysts prepared by a co-precipitation method for the reverse water-gas shift reaction, J. Rare Earths. 31 (2013) 969–974. https://doi.org/10.1016/S1002-0721(13)60014-9.

[332] S.S.S.S.S. Wang, Q. Pan, J. Peng, T. Sun, D. Gao, S.S.S.S.S. Wang, S.S.S.S.S. Wang, Q. Pan, J. Peng, T. Sun, D. Gao, S.S.S.S.S. Wang, CO2 methanation on Ni/Ce0.5Zr0.5O2 catalysts for the production of synthetic natural gas, Fuel Process. Technol. 123 (2014) 166–171. https://doi.org/10.1016/j.fuproc.2014.01.004.

[333] R. Kumar, K. Kumar, K.K. Pant, N. V. Choudary, Tuning the metal-support interaction of methane tri-reforming catalysts for industrial flue gas utilization, Int. J. Hydrogen Energy. 45 (2019) 1911–1929. https://doi.org/10.1016/j.ijhydene.2019.11.111.

[334] S. Ratchahat, M. Sudoh, Y. Suzuki, W. Kawasaki, R. Watanabe, C. Fukuhara, Development of a powerful CO2 methanation process using a structured Ni/CeO2 catalyst, J. CO2 Util. 24 (2018) 210–219. https://doi.org/10.1016/j.jcou.2018.01.004.

[335] H. Lu, X. Yang, G. Gao, K. Wang, Q. Shi, J. Wang, C. Han, J. Liu, M. Tong, X. Liang, C. Li, Mesoporous zirconia-modified clays supported nickel catalysts for CO and CO2methanation, Int. J. Hydrogen Energy. 39 (2014) 18894–18907. https://doi.org/10.1016/j.ijhydene.2014.09.076.

[336] H. Lu, X. Yang, G. Gao, J. Wang, C. Han, X. Liang, C. Li, Y. Li, W. Zhang, X. Chen, Metal (Fe, Co, Ce or La) doped nickel catalyst supported on ZrO2 modified mesoporous clays for CO and CO2 methanation, Fuel. 183 (2016) 335–344. https://doi.org/10.1016/j.fuel.2016.06.084.

[337] M.A. Paviotti, L.A. Salazar Hoyos, V. Busilacchio, B.M. Faroldi, L.M. Cornaglia, Ni mesostructured catalysts obtained from rice husk ashes by microwave-Assisted synthesis for CO2methanation, J. CO2 Util. 42 (2020) 101328. https://doi.org/10.1016/j.jcou.2020.101328.

[338] N. Czuma, K. Zarębska, M. Motak, M.E. Gálvez, P. Da Costa, Ni/zeolite X derived from fly ash as catalysts for CO2 methanation, Fuel. 267 (2020) 117139. https://doi.org/10.1016/j.fuel.2020.117139.

[339] X. Dong, B. Jin, S. Cao, F. Meng, T. Chen, Q. Ding, C. Tong, Facile use of coal combustion fly ash (CCFA) as Ni-Re bimetallic catalyst support for high-performance CO2 methanation, Waste Manag. 107 (2020) 244–251. https://doi.org/10.1016/j.wasman.2020.04.014.

[340] C. Liang, Z. Gao, H. Lian, X. Li, S. Zhang, Q. Liu, D. Dong, X. Hu, Impacts of metal loading in Ni/attapulgite on distribution of the alkalinity sites and reaction intermediates in CO2 methanation reaction, Int. J. Hydrogen Energy. 45 (2020) 16153–16160. https://doi.org/10.1016/j.ijhydene.2020.04.070.

[341] X. Zhang, W.J. Sun, W. Chu, Effect of glow discharge plasma treatment on the performance of Ni/SiO2 catalyst in CO2 methanation, Ranliao Huaxue Xuebao/Journal Fuel Chem. Technol. 41 (2013) 96–101. https://doi.org/10.1016/S1872-5813(13)60012-2.

[342] S. He, C. Li, H. Chen, D. Su, B. Zhang, X. Cao, B. Wang, M. Wei, D.G. Evans, X. Duan, A surface defect-promoted Ni nanocatalyst with simultaneously enhanced activity and stability, Chem. Mater. 25 (2013) 1040–1046. https://doi.org/10.1021/cm303517z.

[343] M. Romero-Sáez, A.B. Dongil, N. Benito, R. Espinoza-González, N. Escalona, F. Gracia, CO2 methanation over nickel-ZrO2 catalyst supported on carbon nanotubes: A comparison between two impregnation strategies, Appl. Catal. B Environ. 237 (2018) 817–825. https://doi.org/10.1016/j.apcatb.2018.06.045.

[344] C. Fukuhara, K. Hayakawa, Y. Suzuki, W. Kawasaki, R. Watanabe, A novel nickel-based structured catalyst for CO2methanation: A honeycomb-type Ni/CeO2catalyst to transform greenhouse gas into useful resources, Appl. Catal. A Gen. 532 (2017) 12–18. https://doi.org/10.1016/j.apcata.2016.11.036.

[345] R. Zhou, N. Rui, Z. Fan, C. jun Liu, Effect of the structure of Ni/TiO2 catalyst on CO2 methanation, Int. J. Hydrogen Energy. 41 (2016) 22017–22025. https://doi.org/10.1016/j.ijhydene.2016.08.093.

[346] X. Guo, A. Traitangwong, M. Hu, C. Zuo, V. Meeyoo, Z. Peng, C. Li, Carbon Dioxide Methanation over Nickel-Based Catalysts Supported on Various Mesoporous Material, Energy and Fuels. 32 (2018) 3681–3689. https://doi.org/10.1021/acs.energyfuels.7b03826.

[347] S.N. Bukhari, C.C. Chong, L.P. Teh, D.V.N. Vo, N. Ainirazali, S. Triwahyono, A.A. Jalil, H.D. Setiabudi, Promising hydrothermal technique for efficient CO2 methanation over Ni/SBA-15, Int. J. Hydrogen Energy. 44 (2019) 20792–20804. https://doi.org/10.1016/j.ijhydene.2018.07.018.

[348] L. Xu, F. Wang, M. Chen, H. Yang, D. Nie, L. Qi, X. Lian, Alkaline-promoted Ni based ordered mesoporous catalysts with enhanced low-temperature catalytic activity toward CO2 methanation, RSC Adv. 7 (2017) 18199–18210. https://doi.org/10.1039/c7ra01673e.

[349] S. Ratchahat, M. Sudoh, Y. Suzuki, W. Kawasaki, R. Watanabe, C. Fukuhara, Development of a powerful CO2 methanation process using a structured Ni/CeO2 catalyst, J. CO2 Util. 24 (2018) 210–219. https://doi.org/10.1016/j.jcou.2018.01.004.

[350] Y. Yu, Y.M. Chan, Z. Bian, F. Song, J. Wang, Q. Zhong, S. Kawi, Enhanced performance and selectivity of CO2 methanation over g-C3N4 assisted synthesis of Ni-CeO2 catalyst: Kinetics and DRIFTS studies, Int. J. Hydrogen Energy. 43 (2018) 15191–15204. https://doi.org/10.1016/j.ijhydene.2018.06.090.

[351] F. Wang, M. Wei, D.G. Evans, X. Duan, CeO2-based heterogeneous catalysts toward catalytic conversion of CO2, J. Mater. Chem. A. 4 (2016) 5773–5783. https://doi.org/10.1039/c5ta10737g.

[352] E.M. Köck, M. Kogler, T. Bielz, B. Klötzer, S. Penner, In situ FT-IR spectroscopic study

of CO2 and CO adsorption on Y2O3, ZrO2, and yttria-stabilized ZrO2, J. Phys. Chem. C. 117 (2013) 17666–17673. https://doi.org/10.1021/jp405625x.

[353] J.K. Kesavan, I. Luisetto, S. Tuti, C. Meneghini, G. Iucci, C. Battocchio, S. Mobilio, S. Casciardi, R. Sisto, Nickel supported on YSZ: The effect of Ni particle size on the catalytic activity for CO2 methanation, J. CO2 Util. 23 (2018) 200–211. https://doi.org/10.1016/j.jcou.2017.11.015.

[354] X. He, H. Yang, A novel strategy to the synthesis of Na3YSi2O7 from natural palygorskite, Appl. Clay Sci. 101 (2014) 339–344. https://doi.org/10.1016/j.clay.2014.08.025.

[355] L. Ilieva, A.M. Venezia, P. Petrova, G. Pantaleo, L.F. Liotta, R. Zanella, Z. Kaszkur, T. Tabakova, Effect of Y modified ceria support in mono and bimetallic Pd-Au catalysts for complete benzene oxidation, Catalysts. 8 (2018). https://doi.org/10.3390/catal8070283.

[356] J. Liu, Z. Zhao, J. Wang, C. Xu, A. Duan, G. Jiang, Q. Yang, The highly active catalysts of nanometric CeO2-supported cobalt oxides for soot combustion, Appl. Catal. B Environ. 84 (2008) 185–195. https://doi.org/10.1016/j.apcatb.2008.03.017.

[357] E. Paparazzo, Use and mis-use of x-ray photoemission spectroscopy Ce3d spectra of Ce2O3 and CeO2, J. Phys. Condens. Matter. 30 (2018). https://doi.org/10.1088/1361-648X/aad248.

[358] P. Burroughs, A. Hamnett, A.F. Orchard, G. Thornton, Satellite Structure in theX-Ray Photoelectron Spectra of some Binary and Mixed Oxides of Lanthanum and Cerium, J. Chem. Soc., Dalt. Trans. (1976) 1686–1698.

[359] E.J. Preisler, O.J. Marsh, R.A. Beach, T.C. McGill, Stability of cerium oxide on silicon studied by x-ray photoelectron spectroscopy, J. Vac. Sci. Technol. B Microelectron. Nanom. Struct. 19 (2001) 1611–1618. https://doi.org/10.1116/1.1387464.

[360] B. Xu, Q. Zhang, S. Yuan, M. Zhang, T. Ohno, Synthesis and photocatalytic performance of yttrium-doped CeO2 with a porous broom-like hierarchical structure, Appl. Catal. B Environ. 183 (2016) 361–370. https://doi.org/10.1016/j.apcatb.2015.10.021.

[361] X. Du, D. Zhang, L. Shi, R. Gao, J. Zhang, Morphology dependence of catalytic properties of Ni/CeO2 nanostructures for carbon dioxide reforming of methane, J. Phys. Chem. C. 116 (2012) 10009–10016. https://doi.org/10.1021/jp300543r.

[362] M.M. Najafpour, S. Mehrabani, R. Bagheri, Z. Song, J.R. Shen, S.I. Allakhverdiev, An aluminum/cobalt/iron/nickel alloy as a precatalyst for water oxidation, Int. J. Hydrogen Energy. 43 (2018) 2083–2090. https://doi.org/10.1016/j.ijhydene.2017.12.025.

[363] M. Boaro, F. Giordano, S. Recchia, V.D. Santo, M. Giona, A. Trovarelli, On the mechanism of fast oxygen storage and release in ceria-zirconia model catalysts, Appl. Catal. B Environ. 52 (2004) 225–237. https://doi.org/10.1016/j.apcatb.2004.03.021.

[364] M.C. Biesinger, B.P. Payne, L.W.M. Lau, A. Gerson, R.S.C. Smart, X-ray photoelectron spectroscopic chemical state Quantification of mixed nickel metal, oxide and hydroxide

systems, Surf. Interface Anal. 41 (2009) 324–332. https://doi.org/10.1002/sia.3026.

[365] J. Zhou, H. Ma, C. Liu, H. Zhang, W. Qian, W. Ying, Ni Based Catalysts Supported on Ce Modified MgAl Spinel Supports for High Temperature Syngas Methanation, Catal. Letters. 149 (2019) 2563–2574. https://doi.org/10.1007/s10562-019-02868-7.

[366] Z. Bian, Y.M. Chan, Y. Yu, S. Kawi, Morphology dependence of catalytic properties of Ni/CeO2 for CO2 methanation: A kinetic and mechanism study, Catal. Today. 347 (2020) 31–38. https://doi.org/10.1016/j.cattod.2018.04.067.

[367] L. Xue, C. Zhang, H. He, Y. Teraoka, Catalytic decomposition of N2O over CeO2 promoted Co3O4 spinel catalyst, Appl. Catal. B Environ. 75 (2007) 167–174. https://doi.org/10.1016/j.apcatb.2007.04.013.

[368] N. Wang, K. Shen, X. Yu, W. Qian, W. Chu, Preparation and characterization of a plasma treated NiMgSBA-15 catalyst for methane reforming with CO2 to produce syngas, Catal. Sci. Technol. 3 (2013) 2278–2287. https://doi.org/10.1039/c3cy00299c.

[369] J. Ashok, M.L. Ang, P.Z.L. Terence, S. Kawi, Promotion of the Water-Gas-Shift Reaction by Nickel Hydroxyl Species in Partially Reduced Nickel-Containing Phyllosilicate Catalysts, ChemCatChem. 8 (2016) 1308–1318. https://doi.org/10.1002/cctc.201501284.

[370] I. Atribak, A. Bueno-López, A. García-García, Role of yttrium loading in the physico-chemical properties and soot combustion activity of ceria and ceria-zirconia catalysts, J. Mol. Catal. A Chem. 300 (2009) 103–110. https://doi.org/10.1016/j.molcata.2008.10.043.

[371] F.J. Perez-Alonso, I. Melián-Cabrera, M. López Granados, F. Kapteijn, J.L.G. Fierro, Synergy of FexCe1-xO2 mixed oxides for N2O decomposition, J. Catal. 239 (2006) 340–346. https://doi.org/10.1016/j.jcat.2006.02.008.

[372] N.S. Arul, D. Mangalaraj, P.C. Chen, N. Ponpandian, P. Meena, Y. Masuda, Enhanced photocatalytic activity of cobalt-doped CeO2 nanorods, J. Sol-Gel Sci. Technol. 64 (2012) 515–523. https://doi.org/10.1007/s10971-012-2883-7.

[373] M. Burbano, S.T. Norberg, S. Hull, S.G. Eriksson, D. Marrocchelli, P.A. Madden, G.W. Watson, Oxygen vacancy ordering and the conductivity maximum in Y2O3-Doped CeO2, Chem. Mater. 24 (2012) 222–229. https://doi.org/10.1021/cm2031152.

[374] J.B. Wang, Y.L. Tai, W.P. Dow, T.J. Huang, Study of ceria-supported nickel catalyst and effect of yttria doping on carbon dioxide reforming of methane, Appl. Catal. A Gen. 218 (2001) 69–79. https://doi.org/10.1016/S0926-860X(01)00620-2.

[375] G. Munteanu, P. Petrova, I. Ivanov, L.F. Liotta, Z. Kaszkur, T. Tabakova, L. Ilieva, Temperature-programmed reduction of lightly yttrium-doped Au/CeO2 catalysts: Correlation between oxygen mobility and WGS activity, J. Therm. Anal. Calorim. 131 (2018) 145–154. https://doi.org/10.1007/s10973-017-6475-1.

[376] G. Zhou, H. Liu, K. Cui, A. Jia, G. Hu, Z. Jiao, Y. Liu, X. Zhang, Role of surface Ni and Ce species of Ni/CeO_2 catalyst in CO_2 methanation, Appl. Surf. Sci. 383 (2016) 248–252. https://doi.org/10.1016/J.APSUSC.2016.04.180.

[377] J. Ashok, M.L. Ang, S. Kawi, Enhanced activity of CO2 methanation over Ni/CeO2-ZrO2 catalysts: Influence of preparation methods, Catal. Today. 281 (2017) 304–311. https://doi.org/10.1016/j.cattod.2016.07.020.

[378] H. Liu, X. Zou, X. Wang, X. Lu, W. Ding, Effect of CeO2 addition on Ni/Al2O3 catalysts for methanation of carbon dioxide with hydrogen, J. Nat. Gas Chem. 21 (2012) 703–707. https://doi.org/10.1016/S1003-9953(11)60422-2.

[379] D. Zhao, Q. Huo, J. Feng, B.F. Chmelka, G.D. Stucky, Nonionic triblock and star diblock copolymer and oligomeric sufactant syntheses of highly ordered, hydrothermally stable, mesoporous silica structures, J. Am. Chem. Soc. 120 (1998) 6024–6036. https://doi.org/10.1021/ja974025i.

[380] O.C. Gobin, Y. Wan, D. Zhao, F. Kleitz, S. Kaliaguine, Mesostructured silica SBA-16 with tailored intrawall porosity part 1: Synthesis and characterization, J. Phys. Chem. C. 111 (2007) 3053–3058. https://doi.org/10.1021/jp0635765.

[381] K. Flodström, H. Wennerström, C. V. Teixeira, H. Amenitsch, M. Lindén, V. Alfredsson, Time-resolved in situ studies of the formation of cubic mesoporous silica formed with triblock copolymers, Langmuir. 20 (2004) 10311–10316. https://doi.org/10.1021/la0482958.

[382] S.M.L. Dos Santos, K.A.B. Nogueira, M. De Souza Gama, J.D.F. Lima, I.J. Da Silva Júnior, D.C.S. De Azevedo, Synthesis and characterization of ordered mesoporous silica (SBA-15 and SBA-16) for adsorption of biomolecules, Microporous Mesoporous Mater. 180 (2013) 284–292. https://doi.org/10.1016/j.micromeso.2013.06.043.

[383] Q. Zhang, M. Wang, T. Zhang, Y. Wang, X. Tang, P. Ning, A stable Ni/SBA-15 catalyst prepared by the ammonia evaporation method for dry reforming of methane, RSC Adv. 5 (2015) 94016–94024. https://doi.org/10.1039/c5ra18845h.

[384] N. Wang, X. Yu, K. Shen, W. Chu, W. Qian, Synthesis, characterization and catalytic performance of Ce-SBA-15 supported nickel catalysts for methane dry reforming to hdrogen and syngas, Int. J. Hydrogen Energy. 37 (2012) 19–30. https://doi.org/10.1016/j.ijhydene.2011.03.138.

[385] A. Albarazi, P. Beaunier, P. Da Costa, Hydrogen and syngas production by methane dry reforming on SBA-15 supported nickel catalysts: On the effect of promotion by Ce0.75Zr 0.25O2 mixed oxide, Int. J. Hydrogen Energy. 38 (2013) 127–139. https://doi.org/10.1016/j.ijhydene.2012.10.063.

[386] M. Chotirach, S. Tungasmita, D. Nuntasri Tungasmita, S. Tantayanon, Titanium nitride promoted Ni-based SBA-15 catalyst for dry reforming of methane, Int. J. Hydrogen Energy. 43 (2018) 21322–21332. https://doi.org/10.1016/j.ijhydene.2018.09.205.

[387] A.S. Al-Fatesh, Y. Arafat, A.A. Ibrahim, H. Atia, A.H. Fakeeha, U. Armbruster, A.E. Abasaeed, F. Frusteri, Evaluation of Co-Ni/Sc-SBA–15 as a novel coke resistant catalyst for syngas production via CO2 reforming of methane, Appl. Catal. A Gen. 567 (2018) 102–111. https://doi.org/10.1016/j.apcata.2018.09.012.

[388] S. Daneshmand-Jahromi, M.R. Rahimpour, M. Meshksar, A. Hafiz, Hydrogen Production from Cyclic Chemical Looping Steam Methane Reforming over Yttrium Promoted Ni/SBA-16 Oxygen Carrier, Catalysts. 7 (2017) 1–21. https://doi.org/10.3390/catal7100286.

[389] S. Zhang, S. Muratsugu, N. Ishiguro, M. Tada, Ceria-doped Ni/SBA-16 catalysts for dry reforming of methane, ACS Catal. 3 (2013) 1855–1864. https://doi.org/10.1021/cs400159w.

[390] Zahra Taherian, A. Khataee, Y. Orooji, Nickel-based nanocatalysts promoted over MgO-modified SBA-16 for dry reforming of methane for syngas production: Impact of support and promoters, J. Energy Inst. (2021). https://doi.org/10.1016/j.joei.2021.04.005.

[391] K. Świrk, P. Summa, D. Wierzbicki, M. Motak, P. Da Costa, Vanadium promoted Ni(Mg,Al)O hydrotalcite-derived catalysts for CO2 methanation, Int. J. Hydrogen Energy. (2021). https://doi.org/https://doi.org/10.1016/j.ijhydene.2021.02.172.

[392] X. Wang, L. Zhu, Y. Liu, S. Wang, CO2 methanation on the catalyst of Ni/MCM-41 promoted with CeO2, Sci. Total Environ. 625 (2018) 686–695. https://doi.org/10.1016/j.scitotenv.2017.12.308.

[393] G. Du, S. Lim, Y. Yang, C. Wang, L. Pfefferle, G.L. Haller, Methanation of carbon dioxide on Ni-incorporated MCM-41 catalysts: The influence of catalyst pretreatment and study of steady-state reaction, J. Catal. 249 (2007) 370–379. https://doi.org/10.1016/j.jcat.2007.03.029.

[394] H. Li, J. Ren, X. Qin, Z. Qin, J. Lin, Z. Li, Ni/SBA-15 catalysts for CO methanation: effects of V, Ce, and Zr promoters, RSC Adv. 5 (2015) 96504–96517. https://doi.org/10.1039/c5ra15990c.

[395] N. Abdullah, N. Ainirazali, H. Ellapan, Structural effect of Ni/SBA-15 by Zr promoter for H2 production via methane dry reforming, Int. J. Hydrogen Energy. (2020). https://doi.org/10.1016/j.ijhydene.2020.07.060.

[396] H. Wan, X. Li, S. Ji, B. Huang, K. Wang, C. Li, Effect of Ni Loading and CexZri-xO2 Promoter on Ni-Based SBA-15 Catalysts for Steam Reforming of Methane, J. Nat. Gas Chem. 16 (2007) 139–147. https://doi.org/10.1016/S1003-9953(07)60039-5.

[397] C.C. Chong, L.P. Teh, H.D. Setiabudi, Syngas production via CO2 reforming of CH4 over Ni-based SBA-15: Promotional effect of promoters (Ce, Mg, and Zr), Mater. Today Energy. 12 (2019) 408–417. https://doi.org/10.1016/j.mtener.2019.04.001.

[398] C. Liu, J. Zhou, H. Ma, W. Qian, H. Zhang, W. Ying, Antisintering and High-Activity Ni Catalyst Supported on Mesoporous Silica Incorporated by Ce/Zr for CO Methanation, Ind. Eng. Chem. Res. 57 (2018) 14406–14416. https://doi.org/10.1021/acs.iecr.8b03254.

[399] Y. Kathiraser, J. Ashok, S. Kawi, Synthesis and evaluation of highly dispersed SBA-15 supported Ni-Fe bimetallic catalysts for steam reforming of biomass derived tar reaction, Catal. Sci. Technol. 6 (2016) 4327–4336. https://doi.org/10.1039/c5cy01910a.

[400] Q. Zhang, M. Wang, T. Zhang, Y. Wang, X. Tang, P. Ning, A stable Ni/SBA-15 catalyst prepared by the ammonia evaporation method for dry reforming of methane, RSC Adv. 5 (2015) 94016–94024. https://doi.org/10.1039/c5ra18845h.

[401] R. Gómez-Reynoso, J. Ramírez, R. Nares, R. Luna, F. Murrieta, Characterization and catalytic activity of Ni/SBA-15, synthesized by deposition-precipitation, Catal. Today. 107–108 (2005) 926–932. https://doi.org/10.1016/j.cattod.2005.07.152.

[402] N. Wang, W. Chu, T. Zhang, X.S. Zhao, Synthesis, characterization and catalytic performances of Ce-SBA-15 supported nickel catalysts for methane dry reforming to hydrogen and syngas, Int. J. Hydrogen Energy. 37 (2012) 19–30. https://doi.org/10.1016/j.ijhydene.2011.03.138.

[403] Q.H. Dongyuan Zhao, Jianglin Feng, G.D.S. Nicholas Melosh, Glenn H. Fredrickson, Bradley F. Chmelka, Triblock Copolymer Syntheses of Mesoporous Silica with Periodic 50 to 300 Angstrom Pores, Science (80-.). 279 (1998) 548–552. https://doi.org/10.1126/science.279.5350.548.

[404] K. Wang, X. Li, S. Ji, X. Shi, J. Tang, Effect of CexZr1-xO2 Promoter on Ni-Based SBA-15 Catalyst for Steam Reforming of Methane, Energy Fuels. 23 (2009) 25–31. https://doi.org/https://doi.org/10.1021/ef800553b.

[405] D. Xia, Y. Chen, C. Li, C. Liu, G. Zhou, Carbon dioxide reforming of methane to syngas over ordered mesoporous Ni/KIT-6 catalysts, Int. J. Hydrogen Energy. 43 (2018) 20488–20499. https://doi.org/10.1016/j.ijhydene.2018.09.059.

[406] U. Oemar, Y. Kathiraser, M.L. Ang, K. Hidajat, S. Kawi, Catalytic Biomass Gasification to Syngas over Highly Dispersed Lanthanum-Doped Nickel on SBA-15, ChemCatChem. 7 (2015) 3376–3385. https://doi.org/10.1002/cctc.201500482.

[407] V. Shanmugam, R. Zapf, S. Neuberg, V. Hessel, G. Kolb, Effect of ceria and zirconia promotors on Ni/SBA-15 catalysts for coking and sintering resistant steam reforming of propylene glycol in microreactors, Appl. Catal. B Environ. 203 (2017) 859–869. https://doi.org/10.1016/j.apcatb.2016.10.075.

[408] L. Ilieva, A.M. Venezia, P. Petrova, G. Pantaleo, L.F. Liotta, R. Zanella, Z. Kaszkur, T. Tabakova, Effect of Y modified ceria support in mono and bimetallic Pd-Au catalysts for complete benzene oxidation, Catalysts. 8 (2018) 283. https://doi.org/10.3390/catal8070283.

[409] G. Pantaleo, V. La Parola, F. Deganello, R.K. Singha, R. Bal, A.M. Venezia, Ni/CeO2 catalysts for methane partial oxidation: Synthesis driven structural and catalytic effects, Appl. Catal. B Environ. 189 (2016) 233–241. https://doi.org/10.1016/j.apcatb.2016.02.064.

[410] M. Kang, E.D. Park, J.M. Kim, J.E. Yie, Manganese oxide catalysts for NOx reduction with NH3 at low temperatures, Appl. Catal. A Gen. 327 (2007) 261–269. https://doi.org/10.1016/j.apcata.2007.05.024.

[411] F. Larachi, J. Pierre, A. Adnot, A. Bernis, Ce 3d XPS study of composite Ce x Mn 1-x O 2-y wet oxidation catalysts, Appl. Surf. Sci. 195 (2002) 236–250. https://doi.org/10.1016/S0169-4332(02)00559-7.

[412] J. Yang, R. Wang, L. Yang, J. Lang, M. Wei, M. Gao, X. Liu, J. Cao, X. Li, N. Yang, Tunable deep-level emission in ZnO nanoparticles via yttrium doping, J. Alloys Compd. 509 (2011) 3606–3612. https://doi.org/10.1016/j.jallcom.2010.12.102.

[413] G. Zhou, H. Liu, K. Cui, A. Jia, G. Hu, Z. Jiao, Y. Liu, X. Zhang, Role of surface Ni and Ce species of Ni/CeO2 catalyst in CO2 methanation, Appl. Surf. Sci. 383 (2016) 248–252. https://doi.org/10.1016/j.apsusc.2016.04.180.

[414] H.D. Setiabudi, C.C. Chong, S.M. Abed, L.P. Teh, S.Y. Chin, Comparative study of Ni-Ce loading method: Beneficial effect of ultrasonic-assisted impregnation method in CO2 reforming of CH4 over Ni-Ce/SBA-15, J. Environ. Chem. Eng. 6 (2018) 745–753. https://doi.org/10.1016/j.jece.2018.01.001.

[415] D. Li, L. Zeng, X. Li, X. Wang, H. Ma, S. Assabumrungrat, J. Gong, Ceria-promoted Ni/SBA-15 catalysts for ethanol steam reforming with enhanced activity and resistance to deactivation, Appl. Catal. B Environ. 176–177 (2015) 532–541. https://doi.org/10.1016/j.apcatb.2015.04.020.

[416] S.M. Sidik, S. Triwahyono, A.A. Jalil, M.A.A. Aziz, N.A.A. Fatah, L.P. Teh, Tailoring the properties of electrolyzed Ni/mesostructured silica nanoparticles (MSN) via different Ni-loading methods for CO2 reforming of CH4, J. CO2 Util. 13 (2016) 71–80. https://doi.org/10.1016/j.jcou.2015.12.004.

[417] U. Oemar, Y. Kathiraser, L. Mo, X.K. Ho, S. Kawi, CO2 reforming of methane over highly active La-promoted Ni supported on SBA-15 catalysts: Mechanism and kinetic modelling, Catal. Sci. Technol. 6 (2016) 1173–1186. https://doi.org/10.1039/c5cy00906e.

[418] S. Sahebdelfar, M. Takht Ravanchi, Carbon dioxide utilization for methane production: A thermodynamic analysis, J. Pet. Sci. Eng. 134 (2015) 14–22. https://doi.org/10.1016/j.petrol.2015.07.015.

[419] B. Lu, K. Kawamoto, Direct synthesis of highly loaded and well-dispersed NiO/SBA-15 for producer gas conversion, RSC Adv. 2 (2012) 6800–6805. https://doi.org/10.1039/c2ra20344h.

[420] B. Lu, K. Kawamoto, Preparation of monodispersed NiO particles in SBA-15, and its enhanced selectivity for reverse water gas shift reaction, J. Environ. Chem. Eng. 1 (2013) 300–309. https://doi.org/10.1016/j.jece.2013.05.008.

[421] T. Zurrer, K. Wong, J. Horlyck, E.C. Lovell, J. Wright, N.M. Bedford, Z. Han, K. Liang, J. Scott, R. Amal, Mixed-Metal MOF-74 Templated Catalysts for Efficient Carbon Dioxide Capture and Methanation, Adv. Funct. Mater. 31 (2020) 2007624. https://doi.org/10.1002/adfm.202007624.

[422] M.A.A. Aziz, A.A. Jalil, S. Triwahyono, R.R. Mukti, Y.H. Taufiq-Yap, M.R. Sazegar,

Highly active Ni-promoted mesostructured silica nanoparticles for CO2 methanation, Appl. Catal. B Environ. 147 (2014) 359–368. https://doi.org/10.1016/j.apcatb.2013.09.015.

[423] Q. Zhang, T. Zhang, Y. Shi, B. Zhao, M. Wang, Q. Liu, J. Wang, K. Long, Y. Duan, P. Ning, A sintering and carbon-resistant Ni-SBA-15 catalyst prepared by solid-state grinding method for dry reforming of methane, J. CO2 Util. 17 (2017) 10–19. https://doi.org/10.1016/j.jcou.2016.11.002.

[424] D. Liu, X.Y. Quek, W.N.E. Cheo, R. Lau, A. Borgna, Y. Yang, MCM-41 supported nickel-based bimetallic catalysts with superior stability during carbon dioxide reforming of methane: Effect of strong metal-support interaction, J. Catal. 266 (2009) 380–390. https://doi.org/10.1016/j.jcat.2009.07.004.

[425] M. Meshksar, M.R. Rahimpour, S. Daneshmand-Jahromi, A. Hafizi, Synthesis and application of cerium-incorporated SBA-16 supported Ni-based oxygen carrier in cyclic chemical looping steam methane reforming, Catalysts. 8 (2018) 1–17. https://doi.org/10.3390/catal8010018.

[426] M. Romeo, K. Bak, J. El Fallah, F. Le Normand, L. Hilaire, XPS Study of the reduction of cerium dioxide, Surf. Interface Anal. 20 (1993) 508–512. https://doi.org/https://doi.org/10.1002/sia.740200604.

[427] S. Watanabe, X. Ma, C. Song, Characterization of structural and surface properties of nanocrystalline TiO2-CeO2 mixed oxides by XRD, XPS, TPR, and TPD, J. Phys. Chem. C. 113 (2009) 14249–14257. https://doi.org/10.1021/jp8110309.

[428] P.I. Ravikovitch, A. V. Neimark, Density functional theory of adsorption in spherical cavities and pore size characterization of templated nanoporous silicas with cubic and three-dimensional hexagonal structures, Langmuir. 18 (2002) 1550–1560. https://doi.org/10.1021/la0107594.

[429] M. Kruk, C.M. Hui, Supporting information: Thermally induced transition between open and closed spherical pores in ordered mesoporous silicas, J. Am. Chem. Soc. 130 (2008) 1. https://doi.org/10.1021/ja0749035.

[430] D. Zhao, Q. Huo, J. Feng, B.F. Chmelka, G.D. Stucky, Nonionic triblock and star diblock copolymer and oligomeric sufactant syntheses of highly ordered, hydrothermally stable, mesoporous silica structures, J. Am. Chem. Soc. 120 (1998) 6024–6036. https://doi.org/10.1021/ja974025i.

[431] H. Liu, H. Wang, J. Shen, Y. Sun, Z. Liu, Promotion effect of cerium and lanthanum oxides on Ni/SBA-15 catalyst for ammonia decomposition, Catal. Today. 131 (2008) 444–449. https://doi.org/10.1016/j.cattod.2007.10.048.

[432] M.N. Kaydouh, N. El, A. Davidson, S. Casale, H. El, P. Massiani, N. El Hassan, A. Davidson, S. Casale, H. El Zakhem, P. Massiani, Effect of the order of Ni and Ce addition in SBA-15 on the activity in dry reforming of methane, Comptes Rendus - Chim. 18 (2015) 293–301. https://doi.org/10.1016/j.crci.2015.01.004.

[433] O.C. Gobin, Y. Wan, D. Zhao, F. Kleitz, S. Kaliaguine, Mesostructured silica SBA-16 with tailored intrawall porosity part 1: Synthesis and characterization, J. Phys. Chem. C. 111 (2007) 3053–3058. https://doi.org/10.1021/jp0635765.

[434] J.K. Kesavan, I. Luisetto, S. Tuti, C. Meneghini, C. Battocchio, G. Iucci, Ni supported on YSZ: XAS and XPS characterization and catalytic activity for CO2 methanation, J. Mater. Sci. 52 (2017) 10331–10340. https://doi.org/10.1007/s10853-017-1179-2.

[435] M. Lorenz, M. Schulze, Reduction of oxidized nickel surfaces, Surf. Sci. 454–456 (2000) 234–239. https://doi.org/10.1016/S0039-6028(00)00145-X.

[436] A. Berlich, Y.C. Liu, H. Morgner, Growth of nickel nanoparticles on NiO/Ni(0 0 1): Evidence of adsorbed oxygen on metal particles by metastable induced electron spectroscopy (MIES), Surf. Sci. 602 (2008) 3737–3744. https://doi.org/10.1016/j.susc.2008.10.014.

[437] X. Jiang, X. Li, J. Wang, D. Long, L. Ling, W. Qiao, Three-dimensional Mn-Cu-Ce ternary mixed oxide networks prepared by polymer-assisted deposition for HCHO catalytic oxidation, Catal. Sci. Technol. 8 (2018) 2740–2749. https://doi.org/10.1039/c8cy00212f.

[438] B. Jenewein, M. Fuchs, K. Hayek, The CO methanation on Rh/CeO2 and CeO2/Rh model catalysts: A comparative study, Surf. Sci. 532–535 (2003) 364–369. https://doi.org/10.1016/S0039-6028(03)00095-5.

[439] C. De Leitenburg, A. Trovarelli, J. Kašpar, A temperature-programmed and transient kinetic study of CO2 activation and methanation over CeO2 supported noble metals, J. Catal. 166 (1997) 98–107. https://doi.org/10.1006/jcat.1997.1498.

[440] M. Ricken, J. Nölting, I. Riess, Specific heat and phase diagram of nonstoichiometric ceria (CeO2-x), J. Solid State Chem. 54 (1984) 89–99. https://doi.org/10.1016/0022-4596(84)90135-X.

[441] J. Van De Loosdrecht, A.M. Van Der Kraan, A.J. Van Dillen, J.W. Geus, Metal-support interaction: Titania-supported and silica-supported nickel catalysts, J. Catal. 170 (1997) 217–226. https://doi.org/10.1006/jcat.1997.1741.

[442] A. Westermann, B. Azambre, M.C. Bacariza, I. Graça, M.F. Ribeiro, J.M. Lopes, C. Henriques, I. Grac, M.F. Ribeiro, Insight into CO2 methanation mechanism over NiUSY zeolites: An operando IR study, Appl. Catal. B Environ. 174–175 (2015) 120–125. https://doi.org/10.1016/j.apcatb.2015.02.026.

[443] A.E. John L.Falconer, Adsorption and methanation of carbon dioxide on a nickel/silica catalyst, J. Catal. 62 (1980) 280–285.

[444] C. Liang, L. Zhang, Y. Zheng, S. Zhang, Q. Liu, G. Gao, D. Dong, Y. Wang, L. Xu, X. Hu, Methanation of CO2 over nickel catalysts: Impacts of acidic/basic sites on formation of the reaction intermediates, Fuel. 262 (2020) 116521. https://doi.org/10.1016/j.fuel.2019.116521.

[445] P.A.U. Aldana, F. Ocampo, K. Kobl, B. Louis, F. Thibault-Starzyk, M. Daturi, P. Bazin, S. Thomas, A.C. Roger, Catalytic CO2 valorization into CH4 on Ni-based ceria-zirconia. Reaction mechanism by operando IR spectroscopy, Catal. Today. 215 (2013) 201–207. https://doi.org/10.1016/j.cattod.2013.02.019.

References

Publications and conferences

Publications

1. **Chao Sun**, Katarzyna Świrk, Dominik Wierzbicki, Monika Motak, Teresa Grzybek, and Patrick Da Costa*. On the effect of yttrium promotion on Ni-layered double hydroxides-derived catalysts for hydrogenation of CO_2 to methane. International Journal of Hydrogen Energy, 46(2021), 12169-12179.

2. **Chao Sun***, Jugoslav Krstic, Vojkan Radonjic, Miroslav Stankovic, Patrick da Costa*. The Effect of Ni Precursor Salts on Diatomite Supported Ni-Mg Catalysts in Methanation of CO_2. [Materials Science Forum, ISSN: 1662-9752, Vol. 1016, pp 1417-1422, 2021.

3. Claudiu Rizescu, **Chao Sun**, Ionel Popescu, Adriana Urdă*, Patrick Da Costa, and Ioan-Cezar Marcu*. Hydrodeoxygenation of benzyl alcohol on transition-metal-containing mixed oxides catalysts derived from layered double hydroxide precursors. Catalysis Today 366(2021), 235-244.

4. **Chao Sun**, Patricia Beaunier, Valeria La Parola, Leonarda F. Liotta*, and Patrick Da Costa*. Ni/CeO_2 Nanoparticles Promoted by Yttrium Doping as Catalysts for CO_2 Methanation. ACS Applied Nano Materials. 2020, 3, 12, 12355–12368.

5. **Chao Sun***, Patricia Beaunier, and Patrick Da Costa*. Effect of ceria promotion on the catalytic performance of Ni/SBA-16 catalysts for CO_2 methanation. Catalysis Science & Technology, 10(2020): 6330-6341.

6. **Chao Sun**,* Patrick Da Costa. Heterogeneous Catalysis: Materials and Applications. Elsevier chapter III 2021. (under review)

7. **Chao Sun***, Katarzyna Świrk, Ye Wang, Katharina Scheidl, Dag Werner Breiby, Magnus Rønning, Changwei Hu, Patrick Da Costa*. Tailoring yttrium content on NiCe/SBA-15 mesoporous silicas for CO_2 methanation. Catalysis today. (Under review)

8. Katarzyna Świrk, **Chao Sun**, Sandra Casale, Patrick Da Costa, Magnus Rønning. Unraveling the effect of well-dispersed nickel species in mesoporous KIT-6 for CO_2 reforming reaction. RKMC, submitting.

9. **Chao Sun**, Katarzyna Świrk, Ye Wang, Magnus Rønninb, Changwei Hu, Patrick Da Costa. Yttrium Promoted Mesoporous SBA-16 Material Supported Ni catalysts for CO_2 Methanation. Catalysis Communication. (Under submitting)

Conference

1. Claudiu Rizescu, **Chao Sun**, Ionel Popescu, Adriana Urdă, Patrick Da Costa, Ioan-Cezar Marcu. Cu-containing ex-LDH mixed oxide catalysts for the hydrodeoxygenation of benzyl alcohol. Young Researchers' International Conference on Chemistry and Chemical Engineering (YRICCCE III), online platform, 2021. 4/5 June 2021

2. **Chao Sun**, M. Stankovic, Patrick Da Costa. The Effect of Ni Precursor Salts on Diatomite Supported Ni-Mg Catalysts in Methanation of CO_2 International Conference on Processing & Manufacturing of Advanced Materials (Thermec 2020/2021), May 10, 2021, Vienna, Austria.

3. Katarzyna Świrk, **Chao Sun**, Sandra Casale, Patrick Da Costa, Magnus Rønning. Unraveling the effect of well-dispersed nickel species in mesoporous KIT-6 for CO2 reforming reaction. 12nd

International Conference on Reaction Kinetics, Mechanisms and Catalysis. 19 -22 May 2021, Budapest, Hungary.

4. **Chao Sun**, Ye Wang, Katarzyna Świrk, Magnus Rønning, Changwei Hu, Patrick Da Costa. Tailoring yttrium content on NiCe/SBA-15 mesoporous silicas for CO_2 methanation. 15th International conference on materials chemistry (MC15) online, July 12, 2021, Royal Society of Chemistry (RSC), UK.

5. **Chao Sun**, Patricia Beaunier, Patrick Da Costa. Effect of ceria promotion on the catalytic performance of Ni/SBA-16 catalysts for CO_2 methanation. 11th International Conference on Environmental Catalysis (ICEC 2020), September 6, 2020, Manchester, UK.

6. **Chao Sun**, Katarzyna Świrk, Dominik Wierzbicki, Monika Motak, Teresa Grzybek, Patrick Da Costa. On the effect of yttrium promotion on Ni-layered double hydroxides-derived catalysts for hydrogenation of CO_2 to methane. 14th International Conference on Advanced Nano Materials, (ANM2019), July 17, 2019, Lisbon, Portugal.

Annexes

Annex. 1. The titration set-up for precipitation (a) and Polytetrafluoroethylene (PTFE) lined hydrothermal autoclave (b) for syntheses of mesoporous materials.